The synthesis of metallic nanoparticles by femto-second laser ablation

Lim, Han Leong

2008

Lim, H. L. (2008). The synthesis of metallic nanoparticles by femto-second laser ablation. Doctoral thesis, Nanyang Technological University, Singapore.

https://hdl.handle.net/10356/14257

https://doi.org/10.32657/10356/14257

The Synthesis of Metallic Nanoparticles by Femto-Second Laser Ablation

LIM HAN LEONG

School of Mechanical and Aerospace Engineering

A thesis submitted in to Nanyang Technological University

in fulfilment of the requirements for the degree of

Doctor of Philosophy

2008

Acknowledgment

The writer hopes to express his appreciation to his first supervisor, Professor Bryan Ngoi Kok Ann, for all the opportunities he had given him for this research.

The writer wishes to show his gratitude to his second supervisor, Associate Professor David Lee Butler, who had believed in him all these time . In addition, the writer would like to express his appreciation to Asst Prof David for sharing his invaluable assistance and his constant encouragement throughout the last one year.

Also, the writer likes to share his gratefulness to his wife, Ms Claris Lim , who stood by him in his most difficult time and her constant support during this research.

In additional, the writer would take the opportunity to show his thanks to Dr. Zheng Hong Yu of SIMTech for sharing his experiences and knowledge .
The writer would like to say thanks all the staff of SIMTECH for sharing their facilities. Also, the writer would like to extend his gratitude to the staff of PEN center for assisting him for past years.

Table of Contents

Acknowledgement …… i

Table of contents …… ii

Summary…… viii

List of Figures…… ix

List of Tables …… . xvi

List of Equations …… xviii

List of Symbols ……..xxiv

1. INTRODUCTION 1

1.1 Background 1

1.2 Objective 2

1.2.1 Scope 2

1.2.2 Significance of the Research..... 3

1.3 Outline of Thesis 3

2. LITERATURE REVIEW 5

2.1 Nanoparticle Application..... 5

2.1.1 Next-generation computer chips..... 6

2.1.2 Low-cost flat-panel displays 6

2.1.3 High energy-density batteries..... 7

2.1.4 High-sensitivity and high-selectivity sensors……..7

2.1.5 More durable, highly functional aerospace components ... 7

2.1.6 Ceramics with superior formability..... 8

2.1.7 Better weapons systems for armour and anti-armour applications..... 8

2.1.8 Better and future weapons platforms 9

2.1.9 Tougher and harder cutting tools 9

2.2.10 High-power magnetic devices 9

2.2.11 More effective, better filtering pollution control devices ... 10

2.1.12 Fuel-efficient automobiles 10

2.1.13 More durable, biocompatible biomaterials …….. 10

2.1.14 Propellants 11

2.1.15 Advanced Munitions 11

2.1.16 Textiles Application 12

2.2 Various methods of generating nanoparticles 13

2.2.1 Naked Flame Plasma 14

2.2.2 Radio Frequency Induced Plasma 15

2.2.3 Chemical Reaction - Precipitation in Liquid Phase 18

2.2.4 Chemical Reaction - Precipitation in Sol-Gel 19

2.2.5 Chemical Reaction - Sintering In Gas-Phase 21

2.2.6 Thermal Decomposition 24

2.2.7 Thermal Reaction 26

2.2.8 Continuous Laser Vaporization Condensation 27

2.2.9 Femto Second Laser 30

2.3 Mechanism of nanoparticle formation of ultra short pulse laser synthesize 37

2.4 Characterization of nanoparticles 42

2.4.1 Collection of nanoparticles 43

2.4.2 Measurement of nanoparticles 45

2.5 Summary 49

3. THEORETICAL MODEL DEVELOPMENT 52

3.1 Parameters of studies 52

3.1.1 Laser Power 54

3.1.2 Pressure 57

3.1.3 Temperature 59

3.1.4 Flow rate 60

3.1.5 Target material 62

3.1.6 Carrier Gas 63

3.2 Development of model 64

3.2.1 The Process of Nanoparticle Formation 65

3.2.2 The Model 73

3.3 Comparison with Contemporary Model 108

3.4 Summary 116

4. EXPERIMENTS AND RESULTS 117

4.1 Equipment 117

4.1.1 Estimate of Collection Efficiency 122

4.2 Procedure 125

4.3 Metrology 127

4.3 Design of Experiment 133

4.3.1 Physical Constants 133

4.3.2 Fractional Factorial Design 134

4.3.3 Analysis of Variance (ANOVA) Test 135

4.3.4 Experimental Trails Trials 136

4.4 Simulation Model Data 138

4.4.1 Simulation model data of various Laser Power 138

4.4.2 Simulation model data of various Pressure 141

4.4.3 Simulation model data of various Temperature 143

4.4.4 Simulation model data of various Flow Rate 146

4.4.5 Simulation model data of various Target Material..... 148

4.4.6 Simulation model data of various Carrier Gas 151

4.5 Experimental Results 153

4.5.1 Experimental results of various Laser Power..... 154

4.5.2 Experimental results of various Pressure 157

4.5.3 Experimental results of various Temperature 159

4.5.4 Experimental results of various Flow Rate 162

4.5.5 Experimental results of various Target Material..... 164

4.5.6 Experimental results of various Carrier Gas 167

4.6 Summary..... 168

5. DISCUSSION..... 169

5.1 Effect of Laser Power 170

5.1.1 Comparison between model and experimental diameter mean of Laser Power variation 170

5.1.2 Comparison between model and experimental standard deviation of Laser Power variation..... 173

5.1.3 Nanoparticle population distribution obtained by various Laser Powers..... 175

5.2 Effect of Pressure..... 179

5.2.1 Comparison between model and experimental diameter mean of Pressure variation..... 179

5.2.2 Comparison between model and experimental diameter standard deviation of Pressure variation 182

5.2.3 Nanoparticle population distribution obtained by various Pressure 184

5.3 Effect of Temperature 187

5.3.1 Comparison between model and experimental diameter mean of Temperature variation 187

5.3.2 Comparison between model and experimental diameter standard deviation of Temperature variation 190

5.3.3 Nanoparticle population distribution obtained by various Temperature 191

5.4 Effect of Flow Rate 195

5.4.1 Comparison between model and experimental diameter mean of Flow Rate variation 195

5.4.2 Comparison between model and experimental diameter standard deviation of Flow Rate variation 198

5.4.3 Nanoparticle population distribution obtained by various Flow Rate 200

5.5 Effect of Target Material 203

5.5.1 Comparison between model and experimental diameter mean of Target Material variation 206

5.5.2 Comparison between model and experimental diameter standard deviation of Target Material variation 211

5.5.3 Nanoparticle population distribution obtained by various Target Material 214

5.6 Effect of Carrier Gas 217

5.6.1 Comparison between model and experimental diameter mean of Carrier Gas variation 218

5.6.2 Comparison between model and experimental diameter standard deviation of Carrier Gas variation 221

5.6.3 Nanoparticle population distribution obtained by various Carrier Gases 222

5.6 Correlation between Model Data and Experimental Results 224

5.7 Summary 225

6. CONCLUSION 226

6.1 Achievement of Objectives 226

6.2 Knowledge Gained 227

6.3 Suggested Future Work 231

6.3.1 Coagulation and Coalescence 231

6.3.2 Metal Target Material 232

6.3.3 Correction factor for Carrier Gas 233

6.3.4 Partial Use of the Model 233

6.3.5 Relation between mode and mean 234

REFERENCE 235

Summary

Nanoparticles are generally used to indicate particles with dimensions less than 100 nanometers. With such fine dimensions, a great proportion of atoms or molecules are exposed on the total surface. Metal existing as nano-scale particles have special properties never discover before when they were bulk material of micro-scale and above.

A list of nanoparticles application was discussed in the report, including its industrial potential and commercial value. Literature review was done on established processes of nanoparticle synthesis. The review had taken in account the principle of each process, their advantages and limitations, their yield quantities and qualities. Most of these processes are limited by the specific chemical reaction equations and equipments, know as recipes. Usually, these different recipes are not inter-changeable for different materials. To overcome this short fall, in recent, there has been great interest to explore the use of physical and mechanical methods.

Laser process does not share these same problems. The very same set of equipment could be used to synthesize many materials without the concern of the recipes. The final nanoparticles material and start material could be the same. The use of femto second laser ablation had gained much interest in current research around the globe. With its short pulse width, femto second laser is able to deliver the necessary energy to process the precursor material, yet fast enough not to affect its properties. However, the actual mechanism and sub-processes of femto second laser ablation to syntheses nanoparticle has not been fully explained before. A model was proposed by the writer, in the attempt to describe the process of metallic nanoparticles synthesize in aerosol form. A series of experiments runs were conducted to verify the model. The accuracy and robustness of the model were discussed together with its limitation. The report ended with suggestions for future works to improve further on the model limitation.

List of Figures

Figure 2- 1 Different Methods of Nanoparticle Synthesis 13
Figure 2- 2 Schematic of CF-CVC Process [10] 14
Figure 2- 3 Experimental setup for investigation of particle formation during PECVD of α-SiO2 using a VLPDMA..... 16
Figure 2- 4 Schematic laser ablate gas-to-particle conversion process 37
Figure 2- 5 Temporal evolution of vapour phase particle growth. 39
Figure 2- 6 Schematic diagram of formation of oxide nanoparticles 40
Figure 2- 7 A typical ionization chamber 44
Figure 2- 8 Scanning Electron Microscope. 45
Figure 2- 9 Transmission Electron Microscope 46
Figure 2- 10 Differential Mobility Analyzer 49
Figure 3- 1 The comparison of size distributions by different fluences, a) 1.9J/cm^2 and b) 3.8J/cm^2, plotted by Ozawa et al..... 55
Figure 3- 2 Histograms for collected nano-particles generated by LAM on a plate in air for gold particles irradiated by 249 nm laser at fluence (a) 3.1 J J/cm^2, (b) 6.2 J/cm^2 and (c) 10.0 J/cm^2. 56
Figure 3- 3 Mean nanoparticle size versus pressure for argon, nitrogen and helium with a laser fluence of 2.4 J/cm^2. 58
Figure 3- 4 Size distribution of generated TiO_2 nanoparticle measured by Low Pressure Differential Mobility Analyst and electrometer 58
Figure 3- 5 Maxwell-Boltzmann probability distribution for the speed of molecules of gas with two temperature T_1 and T_2..... 59
Figure 3- 6 Schematic of the nanoparticle formation. 61
Figure 3- 7 Mean nanoparticle diameter against variuos pressure for argon, nitrogen and helium wiht a laser flunce of 2.4 J/cm^2 as reported by Nichols et al 64
Figure 3- 8 Drude Model for Metal 66
Figure 3- 9 Laser Irradiation on Metal Material 70
Figure 3- 10 Cations lose its binding and break away from bulk material 71
Figure 3- 11 Nucleation occurs when monomers cluster together. 71
Figure 3- 12 Separation of atoms into monomers and nuclei 72
Figure 3- 13 Temperature-density phase diagram typical for metals. 77
Figure 3- 14 Growth and shrinking of clusters and notation used in this text... 87
Figure 3- 15 Discrete size distribution for clusters formed by homogeneous nucleation 91

Figure 3- 16 Serway Model of Collision 96
Figure 3- 17 Schematic Diagram of formation of oxide nanoparticle with graph of temperature against time..... 97
Figure 3- 18 Progress of mapping function..... 107
Figure 4- 1 Schematic setup of the equipment and instruments..... 118
Figure 4- 2 Cross section view of the internal of the six-way cross head. .. 120
Figure 4- 3 Focused Aerosol Impactor 121
Figure 4- 4 Zone of nanoparticles deposition in inner wall of tubing. 122
Figure 4- 5 Collection efficiency versus Stokes number curves fro nanoparticles of diameter 54 nm , (a) d_n/d_c =0.51 ; (b) d_n/d_c =2.10 124
Figure 4- 6 EDS spectrum graph of Titanium nanoparticle collected on TEM grid. 128
Figure 4- 7 EDS spectrum graph of Zinc nanoparticle collected on TEM grid 128
Figure 4- 8 EDS spectrum graph of Nickel nanoparticle collected on TEM grid 128
Figure 4- 9 EDS spectrum graph of Iron nanoparticle collected on TEM grid 129
Figure 4- 10 EDS spectrum graph of Copper nanoparticle collected on TEM grid 129
Figure 4-11 TEM images of Ti nanoparticles synthesised under pressure 26kPa, temperature 297.3K, argon flow rate 0.60SLM ,ablated by 198mW laser at (a) x350K , (b) x500K , (c) x875K magnification. 130
Figure 4- 12 TEM images of Ti nanoparticles synthesised under pressure 44kPa, temperature 297.3K, argon flow rate 0.60SLM, ablated by 198mW laser. 131
Figure 4- 13 TEM images of Ti nanoparticles synthesised under pressure 32kPa, temperature 297.3K, argon flow rate 0.60SLM, ablated by 255mW laser. 131
Figure 4- 14 TEM images of Ti nanoparticles synthesised under pressure 31kPa, temperature 324.3K, argon flow rate 0.60SLM, ablated by 218mW laser. 131
Figure 4- 15 TEM images of Zn nanoparticles synthesised under pressure 32kPa, temperature 297.3K, argon flow rate 0.60SLM, ablated by 224mW laser. 132
Figure 4- 16 TEM images of Ti nanoparticles synthesised under pressure 34kPa, temperature 297.3K, nitrogen flow rate 0.60SLM, ablated by 220mW laser. 132

Figure 4- 17 TEM images of Ti nanoparticles synthesised under pressure 31kPa, temperature 297.3K, argon flow rate 0.80SLM, ablated by 210mW laser. 132

Figure 4- 18 .... Graph of simulation data of nanoparticle population distribution vs. diameter range of experiment 1: Laser Power of 143mW.. 138

Figure 4- 19 .... Graph of simulation data of nanoparticle population distribution vs. diameter range of experiment 2 : Laser Power of 198 mW 139

Figure 4- 20 .... Graph of simulation data of nanoparticle population distribution vs. diameter range of experiment 3 : Laser Power of 255 mW 139

Figure 4- 21 .... Graph of simulation data of nanoparticle population distribution vs. diameter range of experiment 4 : Laser Power of 363 mW 140

Figure 4- 22 .... Graph of simulation data of nanoparticle population distribution vs. diameter range of experiment 5 : Laser Power of 433 mW 140

Figure 4- 23 .... Graph of simulation data of nanoparticle population distribution vs. diameter range of experiment 6 : Pressure of 26 KPa..... 141

Figure 4- 24 .... Graph of simulation data of nanoparticle population distribution vs. diameter range of experiment 7 : Pressure of 34 KPa..... 141

Figure 4- 25 .... Graph of simulation data of nanoparticle population distribution vs. diameter range of experiment 8 : Pressure of 39.5 KPa.... 142

Figure 4- 26 .... Graph of simulation data of nanoparticle population distribution vs. diameter range of experiment 9 : Pressure of 44 KPa..... 142

Figure 4- 27 .... Graph of simulation data of nanoparticle population distribution vs. diameter range of experiment 10 : Pressure of 52 KPa..... 143

Figure 4- 28 .... Graph of simulation data of nanoparticle population distribution vs. diameter range of experiment 11 : Temperature 297.3 K .. 143

Figure 4- 29 .... Graph of simulation data of nanoparticle population distribution vs. diameter range of experiment 12 : Temperature 203.3 K .. 144

Figure 4- 30 .... Graph of simulation data of nanoparticle population distribution vs. diameter range of experiment 13 : Temperature 214.3 K .. 144

Figure 4- 31 .... Graph of simulation data of nanoparticle population distribution vs. diameter range of experiment 14 : Temperature 324.3 K .. 145

Figure 4- 32 .... Graph of simulation data of nanoparticle population distribution vs. diameter range of experiment 15 : Temperature 336.3 K .. 145

Figure 4- 33 .... Graph of simulation data of nanoparticle population distribution vs. diameter range of experiment 16 : Flow Rate 0.3 SLM..... 146

Figure 4- 34 .... Graph of simulation data of nanoparticle population distribution vs. diameter range of experiment 17 : Flow Rate 0.4 SLM..... 146

Figure 4- 35 .... Graph of simulation data of nanoparticle population distribution vs. diameter range of experiment 18 : Flow Rate 0.6 SLM..... 147

Figure 4- 36 .... Graph of simulation data of nanoparticle population distribution vs. diameter range of experiment 19 : Flow Rate 0.8 SLM..... 147

Figure 4- 37 .... Graph of simulation data of nanoparticle population distribution vs. diameter range of experiment 20: Flow Rate 1.0 SLM..... 148

Figure 4- 38 .... Graph of simulation data of nanoparticle population distribution vs. diameter range of experiment 21 : Target Material Titanium….148

Figure 4- 39 .... Graph of simulation data of nanoparticle population distribution vs. diameter range of experiment 22 : Target Material Iron..... 149

Figure 4- 40 .... Graph of simulation data of nanoparticle population distribution vs. diameter range of experiment 23 : Target Material Nickel . 149

Figure 4- 41 .... Graph of simulation data of nanoparticle population distribution vs. diameter range of experiment 24 : Target Material Copper 150

Figure 4- 42 .... Graph of simulation data of nanoparticle population distribution vs. diameter range of experiment 25 : Target Material Zinc 150

Figure 4- 43 .... Graph of simulation data of nanoparticle population distribution vs. diameter range of experiment 26 : Helium gas 151

Figure 4- 44 .... Graph of simulation data of nanoparticle population distribution vs. diameter range of experiment 27 : Argon gas..... 151

Figure 4- 45 .... Graph of simulation data of nanoparticle population distribution vs. diameter range of experiment 28 : Nitrogen gas..... 152

Figure 4- 46 Graphs of experimental results of nanoparticle population distribution vs. diameter range of experiment 1 : Laser Power of 143mW..... 154

Figure 4- 47 Graph of experimental results of nanoparticle population distribution vs. diameter range of experiment 2 : Laser Power of 198 mW..... 155

Figure 4- 48 Graph of experimental results of nanoparticle population distribution vs. diameter range of experiment 3 : Laser Power of 255 mW..... 155

Figure 4- 49 Graph of experimental results of nanoparticle population distribution vs. diameter range of experiment 4 : Laser Power of 363 mW..... 156

Figure 4- 50 Graph of experimental results of nanoparticle population distribution vs. diameter range of experiment 5 : Laser Power of 433 mW..... 156

Figure 4- 51 Graph of experimental results of nanoparticle population distribution vs. diameter range of experiment 6 : Pressure of 26 KPa 157

Figure 4- 52 Graph of experimental results of nanoparticle population distribution vs. diameter range of experiment 7 : Pressure of 34 KPa 157

Figure 4- 53 Graph of experimental results of nanoparticle population distribution vs. diameter range of experiment 8 : Pressure of 39.5 KPa 158

Figure 4- 54 Graph of experimental results of nanoparticle population distribution vs. diameter range of experiment 9 : Pressure of 44 KPa 158

Figure 4- 55 Graph of experimental results of nanoparticle population distribution vs. diameter range of experiment 10 : Pressure of 52 KPa 159

Figure 4- 56 Graph of experimental results of nanoparticle population distribution vs. diameter range of experiment 11 : Temperature 297.3 K..... 159

Figure 4- 57 Graph of experimental results of nanoparticle population distribution vs. diameter range of experiment 12 : Temperature 203.3 K..... 160

Figure 4- 58 Graph of experimental results of nanoparticle population distribution vs. diameter range of experiment 13 : Temperature 214.3 K..... 160

Figure 4- 59 Graph of experimental results of nanoparticle population distribution vs. diameter range of experiment 14 : Temperature 324.3 K..... 161

Figure 4- 60 Graph of experimental results of nanoparticle population distribution vs. diameter range of experiment 15 : Temperature 336.3 K..... 161

Figure 4- 61 Graph of experimental results of nanoparticle population distribution vs. diameter range of experiment 16 : Flow Rate 0.3 SLM..... 162

Figure 4- 62 Graph of experimental results of nanoparticle population distribution vs. diameter range of experiment 17 : Flow Rate 0.4 SLM..... 162

Figure 4- 63 Graph of experimental results of nanoparticle population distribution vs. diameter range of experiment 18 : Flow Rate 0.6 SLM..... 163

Figure 4- 64 Graph of experimental results of nanoparticle population distribution vs. diameter range of experiment 19 : Flow Rate 0.8 SLM..... 163

Figure 4- 65 Graph of experimental results of nanoparticle population distribution vs. diameter range of experiment 20 : Flow Rate 1.0 SLM..... 164

Figure 4- 66 Graph of experimental results of nanoparticle population distribution vs. diameter range of experiment 21 : Target Material Titanium 164

Figure 4- 67 Graph of Experimental Results of nanoparticle population distribution of experiment 22 : Target Material Iron 165

Figure 4- 68 Graph of experimental results of nanoparticle population distribution vs. diameter range of experiment 23 : Target Material Nickel 165

Figure 4- 69 Graph of experimental results of nanoparticle population distribution vs. diameter range of experiment 24 : Target Material Copper 166

Figure 4- 70 Graph of experimental results of nanoparticle population distribution vs. diameter range of experiment 25 : Target Material Zinc 166

Figure 4- 71 Graph of experimental results of nanoparticle population distribution vs. diameter range of experiment 26 : Helium gas. 167

Figure 4- 72 Graph of experimental results of nanoparticle population distribution vs. diameter range of experiment 27 : Argon gas .. 167

Figure 4- 73 Graph of experimental results of nanoparticle population distribution vs. diameter range of experiment 28 : Nitrogen gas ……....168

Figure 5- 1 Graph of diameter mean of model and experimental vs. variation in Laser Power. 171

Figure 5- 2 Graph of diameter mean differences vs. variation in Laser Power ……....173

Figure 5- 3 Graph of standard deviation of model and experimental diameter vs. variation in Laser Power. 174

Figure 5- 4 Graph of diameter standard deviation differences vs. variation in Laser Power. 175

Figure 5- 5 Histogram Graphs of nanoparticle population obtained from simulation model data and experimental results of Laser Power at (a)143mW, (b)198mW, (c)255mW, (d)363mW, (e)433mW.. 177

Figure 5- 6 Graph of diameter mean of model and experimental vs. variation in Pressure. 180

Figure 5- 7 Graph of diameter mean differences vs. variation in Pressure. 181

Figure 5- 8 Graph of standard deviation of model and experimental diameter vs. variation in Pressure 182

Figure 5- 9 Graph of diameter standard deviation differences vs. variation in Pressure 183

Figure 5- 10 Histogram graphs of nanoparticle population obtained from simulation model data and experiments results of Pressure (a) 26KPa, (b) 34KPa, (c) 39.5KPa, (d) 44KPa, (e) 52KPa. 185

Figure 5- 11 Graph of diameter mean of model and experimental vs. variation in Temperature 188

Figure 5- 12 Graph of diameter mean difference vs. variation in Temperature ……189

Figure 5- 13 Graph of standard deviation of model and experimental diameter vs. variation in Temperature 190

Figure 5- 14 Graph of diameter standard deviation difference vs. variation in Temperature 191

Figure 5- 15 Histogram graphs of nanoparticle population obtained from simulation model data and experiments results of Temperature (a) 297.3K, (b) 303.3K, (c) 314.3K, (d) 424.3 K, (e) 336.3K. ... 193

Figure 5- 16 Graph of diameter mean of model and experimental vs. variation in Flow Rate 196

Figure 5- 17 Graph of diameter mean difference vs. variation in Flow Rate . 198

Figure 5- 18 Graph of standard deviation of model and experimental diameter vs. variation in Flow Rate 199

Figure 5- 19 Graph of diameter standard deviation difference vs. variation in Flow Rate 200

Figure 5- 20 Histogram graphs of nanoparticle population obtained from simulation mold data and experiments results of Flow Rate (a) 0.3 SLM , (b) 0.4 SLM, (c) 0.6 SLM, (d) 0.8 SLM, (e)1.0 SLM. 201

Figure 5- 21 Graph of diameter mean vs. variation in atomic binding energy206

Figure 5- 22 Graph of diameter mean vs. variation in molecular volume..... 207

Figure 5- 23 Graph of diameter mean of model and experimental vs. variation in Target Material 209

Figure 5- 24 Graph of diameter mean difference vs. variation in Target Material 211

Figure 5- 25 Graph of standard deviation of model and experimental diameter vs. variation in Target Material 212

Figure 5- 26 Graph of diameter standard deviation difference vs. variation in Target Material 213

Figure 5- 27 Histogram graphs of nanoparticle population obtained from simulation model data and experimental results of Target (a) Titanium , (b) Iron, (c) Nickel, (d) Copper, (e) Zinc 215

Figure 5- 28 Graph of diameter mean of model and experimental vs. variation in Carrier Gas..... 218

Figure 5- 29 Graph of diameter mean of model and experimental vs. variation in Carrier Gas..... 220

Figure 5- 30 Graph of standard deviation of model and experimental diameter vs. variation in Carrier Gas..... 221

Figure 5- 31 Graph of diameter standard deviation difference vs. variation in Carrier Gas..... 222

Figure 5- 32 Histogram graphs of nanoparticle population obtained from simulation data and experiments results of Carrier Gas (a) Helium, (b) Nitrogen, (c) Argon. 223

Figure 6- 1 Graphs of diameter difference between Model and Experiments vs. diameter mean..... 232

List of Tables

Table 1- 1 Range of parameters within scope of model 2
Table 2- 1 Characteristics of different lasers 29
Table 2- 2 Properties of Radioactive material commonly used for ionization . 44
Table 2- 3 Methods of nanoparticles synthesizing by plasma. 50
Table 2- 4 Methods of nanoparticles synthesizing by chemical reaction. 50
Table 2- 5 Methods of nanoparticles synthesizing by plasma. 51
Table 2- 6 Methods of nanoparticles synthesizing by laser. 51
Table 3- 1 Variable parameters of models and their methods of control and measure. 114
Table 4- 1 List of minimum and maximum values of variable terms to Stokes Number. 125
Table 4- 2 Table of different levels of the 4 parameters under ANOVA test. 135
Table 4- 3 The parameters and the levels of for ANOVA test. 135
Table 4- 4 Matrix of series of experiments conducted 136
Table 5-1 Table of paired Z-test of diameter mean difference of Laser Power variation of two tails trial test at 95% confidence limit. 172
Table 5-2 Table of skew of the histogram graphs of difference of Laser Power variation. 176
Table 5-3 Table of paired Z -test of diameter mean difference of Pressure variation of two tails trial test at 95% confidence limit. 181
Table 5-4 Table of skew of the histogram graphs of difference of Pressure variation. 184
Table 5-5 Table of paired Z -test of diameter mean difference of Temperature variation of two tails trial test at 95% confidence limit.. 189
Table 5-6 Table of skew of the histogram graphs of difference of Pressure variation. 192
Table 5- 7 Table of paired Z -test of diameter mean difference of Flow Rate variation of two tails trial test at 95% confidence limit.. 197
Table 5-8 Table of skew of the histogram graphs of difference of Pressure variation. 201
Table 5- 9 Physical Properties of Metal Elements 204
Table 5- 10 Table of t-test of diameter mean difference of Target Material variation of two tails trial test at 95% confidence limit.. 210
Table 5-11 Table of skew of the histogram graphs of difference of Pressure variation. 214

Table 5- 12 Physical Properties of Gas Elements 217

Table 5- 13 Table of paired Z-test of diameter mean difference of Carrier Gas variation of two tails trial test at 95% confidence limit.. 219

Table 5- 14 Table of skew of the histogram graphs of difference of Pressure variation. 223

Table 5- 15 Summary of t-test on diameter mean and standard deviation of model data and experiential results 225

Table 6- 1 Range of the six parameters used in model. 227

List of Equations

$M(OH)_X \rightarrow H_2O + MO$ Equation 2- 1..... 25

$M_2O_X \rightarrow M + O_2$ Equation 2- 2..... 25

$M_{2(}SO_{4)X} \rightarrow M_2O_Y + x\ SO_2$ Equation 2- 3..... 25

$M_2S_X + H_2 \rightarrow M + H_2S$ Equation 2- 4..... 25

$MCl_X \rightarrow M + Cl_2$ Equation 2- 5..... 25

$E(x) = E(0)\ \exp[-\frac{x}{l_s}]$ for x > 0 Equation 3- 1..... 80

$l_s = \frac{c}{\omega K}$ Equation 3- 2..... 80

$n \approx K = \left(\frac{\omega_{pe}}{2\omega}\right)^{1/2}$ Equation 3- 3..... 81

$A = 1 - R \approx \frac{2}{n} - \frac{1}{n^2}$ Equation 3- 4..... 81

$T_e = (\varepsilon_b + \varepsilon_{esc})$ Equation 3- 5..... 81

$(\varepsilon_b + \varepsilon_{esc}) = \frac{4}{3}\frac{AI_0 t_p}{l_s n_e}$ Equation 3- 6..... 81

$F_{th} \equiv I_0 t_p \approx \frac{3}{4}(\varepsilon_b + \varepsilon_{esc})\frac{l_s n_e}{A}$ Equation 3- 7..... 82

$F_{th} \equiv I_0 t_p \approx \frac{3}{8}(\varepsilon_b + \varepsilon_{esc})\frac{cn_e}{\omega}$

$\equiv \frac{3}{8}(\varepsilon_b + \varepsilon_{esc})\frac{\lambda n_e}{2\pi}$ Equation 3- 8..... 82

$c_e(T_e) n_e \frac{\delta T_e}{\delta t} = -\frac{\delta Q}{\delta x}$ Equation 3- 9..... 82

$Q = -AI_0\ exp\left(-\frac{2x}{l_s}\right)$ Equation 3- 10..... 82

$d_{ev} = \frac{l_s}{2} ln\left(\frac{F}{F_{th}}\right)$ Equation 3- 11..... 83

$n_t = d_{ev} \times n_a \times S_a$ Equation 3- 12..... 83

$S = \frac{P_A}{P_S(T)}$ Equation 3- 13..... 84

$S = \frac{P_I}{P_S(T)}$ Equation 3- 14..... 85

$\frac{dN_t}{dt} = \beta_{i-1} N_{i-1}(t) - \alpha_i N_i(t) + \alpha_{i+1} N_{i+1}(t)$ Equation 3- 15..... 87

$J_{i+1/2} = \beta_i N_i - \alpha_{i+1} N_{i+1}$ Equation 3- 16..... 88

$\beta s_{i-1} n_{i-1} = \alpha_i s_i n_i$ Equation 3- 17..... 88

$\beta = \frac{p_1}{\sqrt{2\pi mkT}}$ Equation 3- 18..... 89

$\alpha_i = \frac{p_s}{\sqrt{2\pi mkT}} \exp\left[\frac{4\sigma v_m}{dkT}\right]$ Equation 3- 19..... 89

$\frac{n_{i-1}}{n_i} = \frac{1}{S} \exp\left[\frac{2\sigma v_m \left(\frac{4}{3}\pi / v_m\right)^{1/3}}{i^{1/3} kT}\right]$ Equation 3- 20..... 89

$\frac{n_i}{n_S} = S^i \exp\left[\frac{-3\sigma v_m \left(\frac{4}{3}\pi / v_m\right)^{1/3} i^{2/3}}{kT}\right]$ Equation 3- 21..... 90

$d^* = 4\left[\frac{\sigma V_1}{k\,T\,ln(S)}\right]$ Equation 3- 22..... 92

$\frac{n_c}{n_1} = exp\left[\frac{-16\,\pi\,\sigma^3\,V_1^2}{3\,(kT)^3\,(ln(S)^2)}\right]$ Equation 3- 23..... 92

$$v_g = \frac{(m_g + m_1)v_1' - m_1 v_1}{m_g}$$ Equation 3- 24..... 94

$$\sum_{1}^{i=k} v_g^{(i)} = \frac{(m_1)v_1^{(k+1)} - m_1 v_1^{(0)}}{m_g}$$ Equation 3- 25..... 95

$$v_g = \frac{n_1}{Z}\frac{m_1}{m_g} v_{th}$$ Equation 3- 26..... 95

$$Z'_{gl} = \pi d_{gl}^{\ 2} < v_{rel} > \frac{n_g}{V}\frac{n_1}{V}$$ Equation 3- 27..... 96

$$Z_{gl} = \pi d_{gl}^{\ 2} v'_g \frac{n_g}{V} \times 10^{-5} \quad \text{or} \quad \frac{Z_{gl}}{v'_g} = \pi d_{gl}^{\ 2} \frac{n_g}{V} \times 10^{-5}$$ Equation 3- 28 97

Total system energy before collision = kinetic energy + surface energy

= $\frac{1}{2} m_1 (\upsilon_1)^2 - \pi (d_1)^2 \sigma - \pi (d_n)^2 \sigma$.....

Equation 3- 29..... 98

Total system energy after collision = $\frac{1}{2} (m_{n+1})(\upsilon'_{n+1})^2 - \pi (d_{n+1})^2 \sigma + \varepsilon$.....

Equation 3- 30..... 98

$$\tfrac{1}{2} m_1 (v_1)^2 = \tfrac{1}{2}(m_1 + m_n)(v'_{n+1})^2 + \varepsilon_a - \pi\sigma d_1^2 \left[\sqrt[3]{(n+1)^2} - 1 - \sqrt[3]{(n)^2}\right]$$ .....

Equation 3- 31..... 99

$$v_H \le \sqrt{\frac{2}{m_1}(\varepsilon_a + \pi\sigma d_1^2)}$$ Equation 3- 32..... 99

$\frac{1}{2} (m_n)(\upsilon'_n)^2 + \frac{1}{2} (m_1)(\upsilon'_1)^2 + \varepsilon_a = \frac{1}{2} m_1 (\upsilon_1)^2$ Equation 3- 33..... 100

$$v_L \ge \sqrt{\frac{2\varepsilon_a}{m_1}}$$ Equation 3- 34..... 100

$$\sqrt{\frac{2\varepsilon_a}{m_1}} \le v_1 \le \sqrt{\frac{2}{m_1}(\varepsilon_a + \pi\sigma d_1^2)}$$ Equation 3- 35..... 101

$$v_1 = v'_g Z_{gl} \frac{m_g}{m_l}$$ Equation 3- 36..... 101

$$v'_{gL} = \frac{1}{Z_{g1}}\frac{m_1}{m_g} v_L \quad \text{or} \quad v'_{gL} = \sqrt{\frac{v'_{gL}}{Z_{g1}}\frac{m_1}{m_g} v_L}$$ Equation 3- 37..... 101

$$v'_{gH} = \frac{1}{Z_{g1}} \frac{m_1}{m_g} v_H \quad \text{or} \quad v'_{gH} = \sqrt{\frac{v'_{gH}}{Z_{g1}} \frac{m_1}{m_g} v_H}$$ Equation 3- 38..... 101

$$\frac{dN}{dv} = 4\pi \left(\frac{m_g}{2\pi kT}\right)^{3/2} v^2 \exp\left(-\frac{mv^2}{2kT}\right)$$ Equation 3- 39..... 101

$$\Rightarrow \quad \frac{\delta V}{\delta n} = \frac{m_A}{\rho N_A}$$ Equation 3- 40..... 102

$$Z_{c1} = \langle v_{rel} \rangle \pi d^2 \frac{n_1}{V} \frac{n_c}{V}$$

$$\frac{\delta n}{\delta t} = \langle v_{rel} \rangle \pi d^2 \frac{n_1}{V} \frac{n_c}{V}$$ Equation 3- 41..... 103

$$\Rightarrow \quad \frac{\delta n}{\delta t} = \sqrt{2} v_1 \pi d^2 \frac{1}{V} \left[(n_1) \times p(n_1)\right]^2 \times 10^{-2}$$ Equation 3- 42..... 104

$$\int \delta d = \int 2\sqrt{2} \frac{m_A}{\rho N_A} \frac{v_1}{V} \left[(n_1) \times p(n_1)\right]^2 \times 10^{-2} \ \delta t$$ Equation 3- 43..... 104

$$d = 2\sqrt{2} \frac{m_A}{\rho N_A} \frac{v_1}{V} \left[(n_1) \times p(n_1)\right]^2 \times 10^{-2} \times t + d*$$ Equation 3- 44..... 105

$$\frac{dn_k}{dt} = \left(\frac{dn_k}{dt}\right)_{nucl} + \left(\frac{dn_k}{dt}\right)_{coag}$$ Equation 3- 45..... 108

$$I_k = n_{k-1} s_{k-1} \beta - n_k s_k \alpha_k$$ Equation 3- 46..... 109

$$I_k = n^e_{k-1} s_{k-1} \beta \left[\frac{n_{k-1}}{n^e_{k-1}} - \frac{n_k}{n^e_k}\right]$$ Equation 3- 47..... 109

$$\left(\frac{dn_k}{dt}\right)_{nucl} = I_k - I_{k+1}$$ Equation 3- 48..... 109

$$I = \beta \Big/ \int_0^\infty \frac{dk}{nS}$$

$$= 2\left[\frac{p_1}{(2\pi mkT)^{1/2}}\right] \left(n_1 v_m^{2/3}\right) \left[\frac{\sigma v_m^{2/3}}{kT}\right]^{1/2} \exp\left[-\frac{16\pi\sigma^3 v_m^2}{3(kT)^3 (\ln S)^2}\right]$$ Equation 3- 49..... 109

$$\beta(v_k, v_m) = 2\pi (D_k + D_m)(d_k + d_m)$$ Equation 3- 50..... 110

$$\beta(v_k, v_m) = \left(\frac{3}{4\pi}\right)^{1/6} \left(\frac{6kT}{\rho}\right)^{1/2} \left(\frac{1}{v_k} + \frac{1}{v_m}\right)^{1/2} \left(v_k^{1/3} + v_m^{1/3}\right)^2$$ Equation 3- 51..... 110

$$\left(\frac{dn_k}{dt}\right)_{coag} = \frac{1}{2}\sum_{i+j=k}\beta(v_i,v_j)n_i n_j - n_k\sum_{i=1}^{\infty}\beta(v_i,v_k)n_i$$ Equation 3- 52 110

$$\frac{d(vol)}{dt} = \frac{2\pi D d_p (vol_m)(p_1 - p_d)}{kT}$$ Equation 3- 53..... 110

$$\frac{d(vol)}{dt} = \frac{\alpha\,\pi\, d_p^2 (vol_m)(p_1 - p_d)}{(2\pi\, m\, k\, T)^{1/2}}$$ Equation 3- 54..... 111

$$M_x(r,t) = \int_0^{\infty} n_d d_p{}^x\, d(d_p)$$ Equation 3- 55..... 111

$$M_0(r,t) = \int_0^{\infty} n_d\, d(d_p) = N_{\infty}(r,t)$$ Equation 3- 56..... 111

$$M_1(r,t) = \int_0^{\infty} n_d d\, d(d_p)$$ Equation 3- 57..... 112

$$\overline{d} = \frac{\int_0^{\infty} n_d d\, d(d_p)}{\int_0^{\infty} n_d d(d_p)} = \frac{M_1}{M_0}$$ Equation 3- 58..... 112

$$\pi M_2(r,t) = \pi\int_0^{\infty} n_d d^{\,2} d(d_p) = \sum A$$ Equation 3- 59..... 112

$$\frac{\pi M_3}{6}(r,t) = \frac{\pi}{6}\int_0^{\infty} n_d d^{\,3} d(d_p) = \sum V$$ Equation 3- 60..... 112

$$\overline{V} = \frac{\sum V}{N_{\infty}} = \frac{\pi M_3}{6 M_0}$$ Equation 3- 61..... 112

$$R = \frac{\pi d_t \times R_a}{\pi \frac{d_t^2}{4}}$$ Equation 4- 1..... 123

$$\underline{S} = 0.178\frac{\dot{m}\,\rho_P d_P C_O^3}{p_0 d_n^3}$$ Equation 4- 2..... 123

$$d \propto (ln(F))^3$$ Equation 5-1……170

$$d \propto (\ln(P))^3$$ Equation 5- 2……170

$d \propto P$ Equation 5- 3..... 179

$d \propto T$ Equation 5- 4..... 187

$d \propto \frac{1}{f}$ Equation 5- 5..... 195

$d \propto \left(d_1 + d_g\right)^2 \cdot \frac{1}{\rho} \cdot \frac{1}{m_1} \cdot \left(\frac{n_a}{k}\right)^3 \cdot \left[\ln \frac{1}{\left(\varepsilon_b + \varepsilon_{esc}\right)\left(n_e\right)}\right]^3$ Equation 5- 6..... 203

$d \propto \left(d_1 + d_g\right)^2$ Equation 5- 7..... 217

$d \propto N_a$ Equation 5- 8..... 217

List of Symbols

c	speed of light
c_e	specific heat of the valance (conductive) of electrons
C_O	speed of sound
D	coefficient of diffusion
d_1	diameter of monomer
d_1	diameter of monomer
d_{ev}	depth of crater per laser pulse ablation
d_g	diameter of gas molecule
d_n	diameter of nanoparticles
d_n	diameter of nozzle
D_k	diffusion coefficient of cluster of size k
d_p	diameter of particle
$E(x)$	is the electrical field due to laser at distance x
F	laser irradiated fluence
F_{th}	threshold laser fluence
K	imaginary part of refractive index
k	Boltzmann Constant
l_s	field penetration (or absorption) length (skin-depth)
$\dot{m}$	mass flow rate of carrier gas

m	molecular mass (atomic mass)
m	mass of molecule
m_1	molecular mass of monomer
m_1	mass of monomer
m_g	molecular mass of carrier gas molecule
m_g	mass of gas molecule
N	Refractive index
$N(\upsilon_g)$	number of gas molecule with velocity υ_g
n_1	concentration count of monomers
n_a	number of atoms per unit volume
N_A	Avogadro number
N_a	atomic number of element
n_c	concentration count of nuclei
n^e_k	the particle number concentration for size class k at equilibrium
n_g	number of gas molecules / atoms
n_i	concentration count of cluster containing i atoms (i-mer)
$N_i(t)$	the number concentration of clusters containing *i* atoms (*i*-mer) at time *t*
n_k	the particle number concentration for size class k
n_t	amount of metal material ablate per pulse
$p(n_1)$	the probability of monomer with velocity υ_1
p_0	up-stream pressure of nozzle

P_1	partial pressure exert by monomer
p_1	partial pressure exert by monomer
p_1	partial pressure of monomer
P_A	partial pressure exert by metal A vapour
p_d	equilibrium vapour pressure above a drop of diameter d_p
p_s	vapour pressure above a flat surface of liquid
$P_S\ (T)$	saturation vapour at temperature T
Q	total energy flux absorbed by the metal
S	saturation ratio
S_a	laser spot area
s_i	surface area of cluster containing i atoms (i-mer)
T	absolute temperature
T_e	electron temperature energy
V	volume of channel
$\overline{V}$	average volume of particles disperse in the an aerosol
v_m	molecular volume of liquid
υ'_{gH}	corresponding higher limit velocity of the gas molecule.
υ'_{gL}	corresponding lower limit velocity of the gas molecule.
υ_1	velocity of monomer
$\upsilon_1^{(z)}$	velocity of monomer after z^{th} collision
υ_g	velocity of gas molecule

$\upsilon_g^{(z)}$	velocity of carrier gas molecule after z^{th} collision
υ_H	higher limit velocity of monomer for successful adhesive impact.
υ_L	lower limit velocity of monomer for successful adhesive impact.
υ_{rel}	relative velocity of monomer and nuclei
υ^{th}	threshold velocity require for successful adhesive impact
$<\upsilon_{rel}>$	is the relative velocity of monomer and gas molecule
vol	is the volume of particle
vol_m	is the volume of single molecule
x	distance form the surface of metal
Z	number of collision between gas and monomers molecules
Z_{c1}	number of collision between monomer and nuclei per unit volume per second
Z_{g1}	number of collision between monomer and gas molecules per unit volume per second
α_i	the reverse rate constant for evaporation of a monomer from an *i*-mer
β_i	the forward rate constant for condensation of a monomer by an *i*-mer
$\beta(\upsilon_k,\upsilon_m)$	frequency function
$\bar{d}$	average diameter of particles disperse in the an aerosol
ε_b	binding energy
ε_{esc}	work function

λ	laser wavelength
ρ_P	density of nanoparticles
σ	surface energy
σ	surface tension
ω	laser frequency in radian
ΣA	total surface area of all particles disperse in the an aerosol
ΣV	total volume of all particles disperse in the an aerosol
$\frac{\delta n}{\delta t}$	rate of monomers absorb by a growing nucleus
$\frac{\delta d}{\delta t}$	diameter growth rate of nanoparticle
$\left(\frac{dn_k}{dt}\right)_{nucl}$	rate of particle formation due to homogeneous nucleation (formation of critical size embryo with diameter d*)
$\left(\frac{dn_k}{dt}\right)_{coag}$	describes the coagulation mechanism,
$\left(\frac{dn_k}{dt}\right)_{grow}$	the growth by condensation.

1. Introduction

1.1 Background

The term nanoparticle is generally used to indicate particles with dimensions less than 100 nanometers. One nanometer is one billionth of a meter. Express in numbers :

1 nm = 10^{-9} m or 1,000,000,000 nm = 1 m.

For a simple comparison, a human hair is about 50,000 nm in diameter, while a smoke particle is about 1,000 nm in diameter. The smallest nanoparticle, only a few nanometers in diameter, contains only a few thousand atoms. These particles possess properties that are entirely different from their parent materials.

Nanoparticles have been under investigation in the recent years due to their novel physical, chemical and mechanical properties. They have been studied for use as catalysts, fuel cells, pigments, gas absorbers and a host of other applications. Their uniqueness arises from their high ratio of surface area to volume. It has been well established that these 'far from equilibrium' materials exhibit novel mechanical properties such as much higher yield and tensile ultimate strength. Strength increases on the order of 15 times that of bulk material have been reported [1,2,3]. Hardness values and compressive yield strengths have also been improved However, there may be a compromise in tensile modulus and elongation as one reduces the particle size below a diameter of ~100 nm. This compromise has led to many theories about the nature of consolidated nanoparticles, including similarities to metallic glasses and amorphous-crystalline behavior.

Nanoparticles can make metals stronger and harder, give ceramics enhanced ductility and formability enable normally insulating materials to conduct heat or electricity and make protective coatings transparent. In short, nanoparticles allow industries to re-engineer many existing products and design novel new products/processes that function at unprecedented levels.

Furthermore, engineering the size, morphology, and composition of the particle, we can selectively control electrical, optical, chemical, mechanical, magnetic properties of nanoparticles. After developing materials in this near-atomic size range, engineers can combine and exploit the properties of the nanoparticle surface atoms to create new substances with enhanced or entirely different properties from their parent materials.

1.2 Objective

The aim of this research is to establish a model of metallic nanoparticle formation in a gaseous medium. The model will be expressed as a function of parameter of a controlled environment of temperature, pressure, chamber gas type, gas flow rate, and target material. Following, a system is to be designed and built to verify the validity of model.

1.2.1 Scope

The model developed in this research is limited to the application of ultra short pulse laser irradiation onto metallic target material. Six key parameters will be studied in this research. Each of the parameters in the model is restricted to only a range as stated in table 1-1 that follows. Only the physical dimensions of the nanoparticles are of interesting this study.

Table 1- 1 Range of parameters within scope of model

Pressure	100 ~ 900 mBar
Laser Power	0 ~ 600 mW

Temperature	20 ~ 60 ^{0}C
Flow rate	0.1 ~ 1.0 SLM
Target material	Ti, Cu , Fe, Zn , Ni
Carrier Gas	N_2 , He , Ar

1.2.2 Significance of the Research

The research project is to develop a uncomplicated and straight forward model that could help predict the size and distribution population of nanoparticles synthesized under the condition of femto second laser ablation on metal target in a low vacuum chamber. Nanoparticles generated in gas media have many advantages but some pitfall as well. The nanoparticles generated are not of a single size, but of various sizes and with a spread of population distribution.

Currently, most of the existing models for nanoparticles formed in gaseous media were proposed by aerosol scientists. These models are expressed in term of particle count concentration, diffusion with time domain factor, surface tension, viscosity etc. Values and information of these terms are often not easily available. In addition, there are very little instruments able to measure and quantify these values directly.

The proposed model is a stochastic function expressed in terms of common industrial parameters and material properties values. Parameters used to express the model could be quantified without difficulty with existing instruments. These parameters include pressure, temperature, laser power, mass flow rate, common material properties of metals and gas.

The mean value of the model of stochastic function offers the expected average value of the nanoparticles. The variance of the model gives a good estimate of the spread of the population size distribution.

1.3 Outline of Thesis

This thesis records the development of a novel model to predict the size of the nanoparticle synthesized from femto second laser in a low vacuum chamber. The key strength of this model is that it is expressed in term of parameters common to the real industrial world. Secondly, the model utilizes less computation resources as compare to contemporary model.

Chapter 2 of the thesis gives an extensive literature review of the various methods of generating nanoparticles. This is followed by a description of each of the sub-processes of the mechanism of the formation of the nanoparticles in a gaseous medium. Lastly, it discusses the various characterization practices employed by the research community. The chapter concludes with the presentation of the method of characterization used in this research.

Chapter 3 is the development of the model. The basic fundamentals of the nanoparticle formation process from the field of aerosol science are revisited. The six parameters used in the model are reviewed and explain as how they will influence the outcome of the diameter. The assumptions of the proposed model are stated. Finally, the chapter ends with the development of the model proper.

Chapter 4 comprises of all the experiment equipment, procedures and results. Both results from stimulation model data and experimental results are included.

Chapter 5 analyses the collected data. It demonstrates how each of the parameters influences the outcome of the diameter. Verification of the developed model is done as well.

Chapter 6 concludes the thesis with a section suggesting future work in this field of research.

2. Literature Review

The chapter begins with various applications of nanoparticles, giving examples of current commercial usage and providing some future potential areas of usage identified by industry. Next the chapter will review the various methods of nanoparticle generation reported. More in depth studies into each methods were discussed, including their nanoparticles yield, suitable materials to be synthesized, and each of their strengths and limitations.. The chapter further elaborates one of the methods by laser ablation in gaseous medium to have a unique advantage. Laser ablation allows the same material of nanoparticles to be same of the start off material. A model is proposed to explain this method. The method is divided into 6 sub-processes : (i) irradiation (ii) ablation (iii) nucleation (iv) growth (v) coalescence / coagulation and (vi) agglomeration. Further details on the mechanism of each sub-process are explained. The chapter ends with some of the current characterization techniques and the one which this research is based on is highlighted.

2.1 Nanoparticle Application

Nanoparticles offer radical breakthroughs in areas such as materials and manufacturing. Three characteristics of nanoparticles that give rise to their unique properties：

1. Nanoparticles are at a dimension close to if not smaller than normal crystal grain size. In other words, every nanoparticle itself is almost near prefect single crystal structure.
2. Physically, it offers very high surface area to volume ratio. With such high ratio, nanoparticles have a very large effective surface area for chemical reaction which bring about (i) faster reaction rate, (ii) and more effective reaction of all the reactants.

3. At such a tiny size, the nanoparticles do not possess any of the imperfections of bulk material due to grain boundaries. The absence of grain boundaries makes the material harder and faster in electron transport across the whole material.

With these unique characteristics, nanoparticles are able to offer a whole new world of material properties not found before. It has found new applications in the field of electronics, medicine and healthcare, environment and energy, chemical and pharmaceutical, biotechnology and agriculture, computation and information technology as well as in national security. Following are some of the applications of nanoparticles.

2.1.1 Next-generation computer chips [4]

It had been an on-going goal for the microelectronics industry to miniaturize components such as transistors, resistors, and capacitors and thus lead to an overall reduction in circuit size. By shrinking these components, the microprocessors that house them can run much faster, enabling computations at far greater speeds. It is expected that new nano-scale materials will help the industry overcome these barriers by providing manufacturers with ultra-high purity nanoparticles as starting materials with better thermal conductivity, and longer-lasting, durable interconnections.

2.1.2 Low-cost flat-panel displays [4]

Flat-panel displays represent a huge market in the laptop (portable) computers industry. By synthesizing nano-size phosphors crystalline particles, the resolution of these display devices can be greatly enhanced, and the manufacturing costs can be significantly reduced. Also, the flat-panel displays constructed out of nanoparticles possess much higher brightness and contrast than conventional ones due to their enhanced electrical and magnetic properties.

2.1.3 High energy-density batteries [4]

Conventional and rechargeable batteries are used in almost all applications that require electric power. The energy density (storage capacity) of these batteries is quite low requiring frequent recharging and their life span is short as well. Nanoparticle materials synthesized by sol-gel techniques are good candidates for separator plates in batteries because of their foam-like (aero-gel) structure which can hold considerably more energy than conventional ones. Furthermore, nickel-metal hydride (Ni-MH) batteries made of nanoparticles nickel and metal hydrides are envisioned to require far less frequent recharging and to last much longer because of their larger surface area and enhanced physical, chemical, and mechanical properties.

2.1.4 High-sensitivity and high-selectivity sensors [4]

Sensors employ their sensitivity to the changes in various parameters that they are designed to measure. Some of the more common measured parameters are electrical resistivity, chemical activity, magnetic permeability, thermal conductivity, and capacitance. All of these parameters depend greatly on the microstructure (grain size) of the materials employed in the sensors. A change in the sensor's environment is manifested by the sensor material's chemical, physical, or mechanical characteristics, which can be exploited for measurement. The rate and the extent of this reaction are greatly increased by a decrease in the grain size. Thus sensors composed of nanoparticles are made extremely sensitive to the changes in their environment. Typical applications for sensors made out of nanoparticles are smoke detectors, ice detectors on aircraft wings, automobile engine performance sensor.

2.1.5 More durable, highly functional aerospace components [4]

One of the important properties required of the aircraft components is the fatigue strength, which decreases with the component's age. By making the

components out of stronger materials, the product life of the aircraft is greatly increased. The fatigue strength increases with a reduction in the grain size of the material. Nanoparticle materials provide such a significant reduction in the grain size over conventional materials that the fatigue life is increased by an average of 200-300%. Furthermore, components made of nanoparticles are stronger and can operate at higher temperatures; aircraft can fly faster and more frequently.

2.1.6 Ceramics with superior formability [4]

Ceramics are very hard, brittle, and difficult to machine and lead to much discouragement from users exploiting their other beneficial properties. However, with the discovery of reduction in grain size, ceramics has been rendered to become super-plastic. These populous and ultra fine grains are made possible by pressing and sintering them into various shapes at high temperatures from nanoparticles. These ceramics possess good formability and machinabilty combined with excellent physical, chemical, mechanical and specially thermal properties.

2.1.7 Better weapons systems for armour and anti-armour applications [4]

Currently, defense forces are using depleted-uranium (DU) projectiles (penetrators) due to its unique self-sharpening mechanism on impact with hardened targets and enemy armoured vehicles. However, DU has residual radioactivity, and hence is a toxic (carcinogenic) explosive and thus even lethal to the personnel who handle them. Nano-crystalline tungsten heavy alloys, sensitized from tungsten and other heavy metal nanoparticles, offer themselves with another self-sharpening mechanism because of their unique deformation characteristics of grain-boundary sliding, but without all the hazard of handling.

2.1.8 Better and future weapons platforms [4]

Extensive researches had been conducted on rail guns as a preferred projectile mechanism other than conventional fire arms. The rails need to be very good conductors of electricity, and to be strong and rigid so that the rail-gun does not sag while firing and buckle under its own weight. However, rail-gun made out of copper wear out much too quickly due to the erosion of the rails by the hypervelocity projectiles and they lack high-temperature strength. To over frequent barrel replacement, a composite material made of tungsten, copper, and titanium diboride nanoparticles is being evaluated as a potential candidate. This alloy of nanoparticles possesses the requisite electrical conductivity, adequate thermal conductivity, excellent high strength, high rigidity, hardness, and wear / erosion resistance.

2.1.9 Tougher and harder cutting tools [4]

Cutting tools sinter from nanoparticle will comprise of nano-crystalline. These nano-crystalline structure give rise to superior material strength. Employing this technique on traditional materials such as tungsten carbide, tantalum carbide, and titanium carbide, these material are now much harder, more wear-resistant, more erosion-resistant, and last longer as compare with their conventional (large-grained) counterparts.

2.2.10 High-power magnetic devices [4]

The strength of a magnet is measured in terms of coactivity and saturation magnetization values. These values increase with a decrease in the grain size and an increase in the specific surface area (surface area per unit volume of the grains) of the grains. It has been shown that magnets made from nanoparticles of yttrium-samarium-cobalt possess very unusual magnetic properties due to their extremely large surface area.

2.2.11 More effective, better filtering pollution control devices [4]

Nanoparticles exhibit an extremely large surface area to volume ratio. Hence, they are very active in terms of their chemical, physical, and mechanical properties. Due to their enhanced chemical activity, nanoparticles can be used as catalysts to react with such noxious and toxic gases as carbon monoxide and nitrogen oxide in automobile catalytic converters and power generation equipment to prevent environmental pollution arising from burning gasoline and coal.

2.1.12 Fuel-efficient automobiles [4]

Currently, automobile engines waste considerable amounts of gasoline by not completely combusting the gas; thereby contributing to environmental pollution. The conventional spark plug electrodes with defective and worn-out are not able to burn the gasoline completely and efficiently. Nanoparticles coated material are stronger, harder, more wear-resistant and erosion-resistant, These new electrodes render the spark plugs longer-lasting and combust fuel far more efficiently and completely.

Also, automobiles waste significant amounts of energy by losing the thermal energy generated by the engine, especially in diesel engines. Hence, if engine cylinders (liners) are to be coated with zirconia - alumina mixed nanoparticles ceramics, they will retain heat much more efficiently and result in complete and efficient combustion of the fuel.

2.1.13 More durable, biocompatible biomaterials [4]

In today's practice, medical implants, such as orthopedic implants and heart valves, are made of titanium and stainless steel alloys. These alloys are primarily used in humans because they are bio-compatible, i.e., they do not adversely react with human tissue. For an implant to effectively mimic a natural

human bone, the surrounding tissue must penetrate the implants thereby affording the implant with the required strength. Yet, these materials are relatively impervious. However, zirconia ceramic sintered from nanoparticles is hard, wear-resistant, corrosion-resistant and bio-compatible.

Nanoparticle ceramics synthesized by sol-gel techniques can also be made porous into aerogels, which can withhold up to 100 times their weight. Silicon carbide (SiC) is a candidate material for artificial heart valves primarily due to its low weight, high strength, extreme hardness, wear resistance, inertness (SiC does not react with biological fluids), and corrosion resistance.

2.1.14 Propellants [5]

High-burn rate propellants burn predictably at high pressures, enabling specific impulse gains through higher nozzle expansion ratios. Aluminum in nanoparticles sizes is currently being used to formulate the next-generation of solid rocket propellants. Development work is underway in hybrid, liquid, and gel -based propellants. Nano-aluminum-based propellants have been shown to meet strict military requirements for minimum-smoke qualification.

2.1.15 Advanced Munitions [5]

Aluminum nanoparticle based primers are superior in aspects such as ignition firing, priming load requirements, high reaction rates and low temperature performance. Lead-free, nano-aluminum based primers are environmentally being preferred to the conventional toxic munitions primers. *Advanced Energetic Materials* such as super-thermal dynamites are formed by combining nano-aluminum and nano-formulated oxidizers. Aluminum nanoparticles is being developed to be next-generation warheads and advanced explosives.

2.1.16 Textiles Application [6]

Colloidal antimony pentoxide is a nanoparticle dispersant used as a flame retardant synergist with halogenated flame retardants. The nano-size dispersant offers the advantages that conventional antimony trioxide systems can not provide. In automotive upholstery, it is able to give a clear transparent coating on deep dark colors without any settling. In tent coating, it allows easier coating and wider range of colours, and increase flame retardant in denier fibers. In terms of process, nano-colloidal do not clog spray guns, nor settle down.

All in all, the interest in nanoparticle research has grown tremendously during the last decade. This interest stems from the different and often superior properties of nanoparticles, as compared to bulk material. For instance nanoparticles are chemically very reactive, making them attractive for catalyst and sensor applications. As faster and therefore smaller electronic circuits are wanted the building blocks need to be smaller. However, an inexpensive method to produce nanoparticles in large quantities is still lacking for most materials. [7]

Nanoparticles can be prepared through different routes, for instance liquid-phase routes and gas-phase, i.e. aerosol routes. In liquid-phase routes, such as the sol–gel technique, the starting point is a solution of the precursors in a solvent. After the chemical reactions have taken place, the material needs to be processed, e.g. dried and milled, before obtaining a usable powder. During the processing, especially the milling, the powder can be contaminated. The purity of the product is also dependent on the purity of the precursors [8]

2.2 Various methods of generating nanoparticles

In recent years, many methods of synthesizing nanoparticles have been invented and perfected with each offering its own unique advantage. However, each method is still unable to breakthrough their own inherent limitations. As a result, the research and industrial communities around the globe are faced with a situation of a wide variety of synthesizing methods, but each method could only synthesize a very little number of materials. This is due to the constraint of that each of these methods can only generate a limited choice of nanoparticle materials. In general, all these methods can be classified into four main categories according to the physical mechanism of the process.

(i) Plasma ,
(ii) Chemical reaction ,
(iii) Thermolysis and
(iv) Laser

From these four main categories, we can further sub-divide them into nine methods according to different classifications of each category, as can be seen in figure 2-1. The different methods of synthesizing will be discussed further in the following sub-sections.

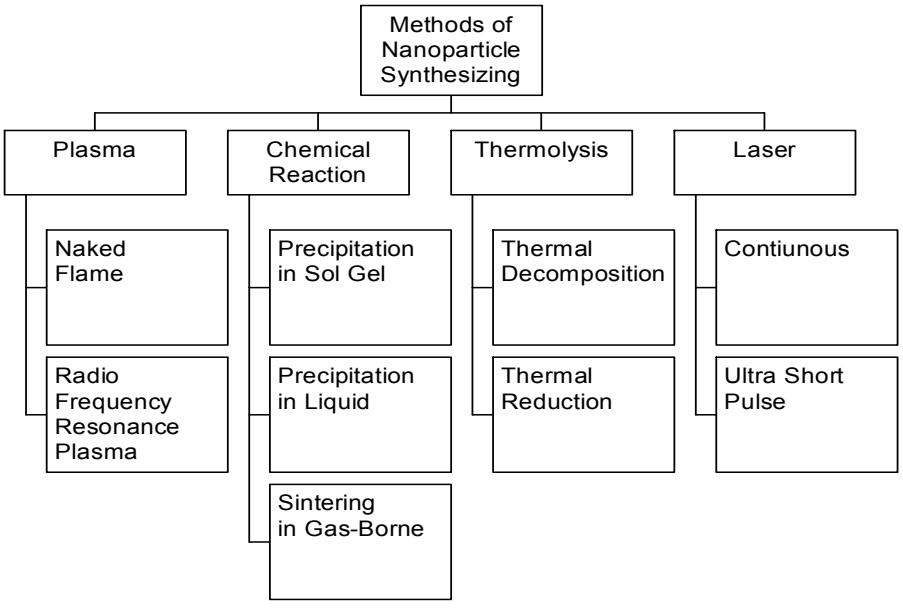

Figure 2- 1 Different Methods of Nanoparticle Synthesis

2.2.1 Naked Flame Plasma

Naked flame plasma is characterized by a high electron density of 10^{21} to 10^{26} $m^{-3.}$ In the naked flame plasma, different chemical precursors undergo chemical change in the ambience of a plasma flame. Due to the extreme condition, desired materials are formed, yet not allowed to grow into sizable grains. [9]

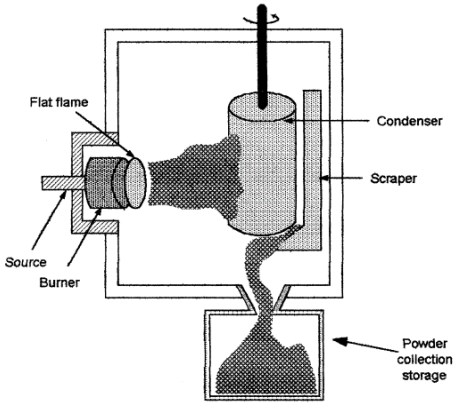

Figure 2- 2 Schematic of CF-CVC Process [10]

One of the more common hybrids of flame plasma synthesis is *Combustion Flame – Chemical Vapour Condensation* **CF-CVC.** In this process, a stable flat flame is generated by burning a fuel and oxygen mixture. Chemical precursors, introduced along with combustibles, experience rapid thermal decomposition in the hot zone of the flame. Since the temperature profile, gas phase residence time and precursor concentration are uniform across the entire surface of the burner, the effect is to generate a beam of essentially mono-dispersed nanoparticles. Pyrolysis occurs in the thin hot zone. Clusters are formed and nanoparticles condense as the temperature of the gas falls off sharply. In the low pressure flat flame, the temperature profile across the entire burner surface is uniform [10], which leads to a narrow particle size distribution. [11,12,13 ,14]

Till now, material reported being successful generated by plasma flame includes [9,10,11,12,13,14]:

- aluminum trioxide (Al_2O_3),
- cobalt oxide (CoO , Co_3O_4),
- silicon dioxide (SiO_2),
- vanadium oxide (V_2O_5),

Most of the nanoparticles are spherical and dense, with an average size of 35 nm and with a range of 10 to 60 nm. Yield rates can reach as high as 40 grams per hours [15]. However, with the use of CV-CVC, it is possible to achieve an average size of 16nm with a range of 10 to 35 nm. [13,14,15]

In most cases of the plasma flame process, the plasma is kept at atmospheric pressure, which results in sintering of the particles that collide with each other. This in turn, leads to aggregation of primary particles. CF-CVC, on the other hand, uses low pressure stagnation point flame. It offers several advantages. Firstly, high flame radical concentration can be maintained at lower temperatures. Consequently, precursor decomposition temperature is lowered, resulting in less aggregation of primary particles. Secondly, the residence time of particles in the CF-CVC process is much smaller than that of the atmospheric flame process, since the pressure in the CF-CVC process is 35 times smaller. Thirdly, the inherent uniformity of the stagnation flow environment, coupled with the increasing strength of the thermophoretic force as compared to the drag force at low pressure, suggests that particles that condense at different radial locations will experience similar trajectories, and thus time / temperature histories. [16]

2.2.2 Radio Frequency Induced Plasma

Unlike the former process, high frequency induced plasma gains its energy from high frequency waves emitted onto the gas mixture itself. The wave is generated either by capacitive or inductive coupling, maintained by a time varying magnetic field operating between 3 to 30 MHz. Most commonly used frequencies today are in the range of microwaves. Most of the processes are

undertaken in inert gas such as nitrogen, helium or argon. However, in some cases, in the effort to prevent oxidation, the use of hydrogen had been reported.

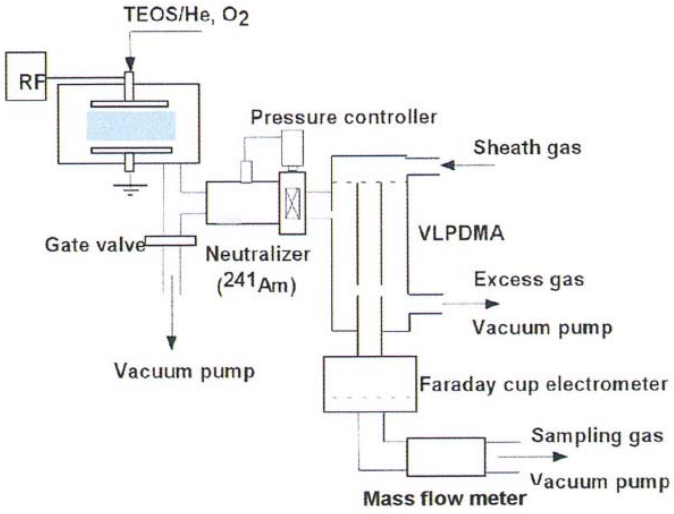

Figure 2- 3 Experimental setup for investigation of particle formation during PECVD of α-SiO_2 using a VLPDMA.

The precursors within the plasma are subjected to rapid heating followed by evaporation, and, in some cases, even thermal dissociation. In either way, re-condensation takes place in a very short time, usually in hundredths or thousandths of a second. The short time span denies the particles the opportunity to grow resulting in very fine nano-scale particles. In some cases, precursors under the intense heat of the plasma may break down forming free radicals. The free radicals recombine into nanoparticles as they descend down the cooled column. the generated nanoparticles are collected at the end of the assembly. [17,18,19,20]

Most of the materials generated are ultra-pure metal, most common being

- iron , (Fe)
- zinc, (Zn)
- copper , (Cu)
- silver, (Ag) .

For dielectric materials, high frequency induced plasma has been preferred to process chemicals with group III and IV cations, such as

- silicon carbonitride, (SiCN)
- silicon dioxide , (SiO_2)
- aluminum (III) oxide , (Al_2O_3)
- aluminum nitride , (AlN)

In the range of rare earth, it covers the whole 16 elements, more commercially popular are

- Yttrium (Y)
- Europium (Eu)
- Cerium (Ce)
- Lanthanum (La) [21]

One of the benefits of high frequency induced plasma is that the same equipment can yield very different qualities of nanoparticles, depending on the type of gas used, pressure, and temperature and flow rate. In a typical plasma of argon gas, the feed is at 3 m^3 per hour, temperature of 850^{O}C and pressure of 63 MPa, it was reported that a mean diameter of 500nm and standard deviation of 300nm was achieved.[22]

As mentioned above, the greatest advantage of high frequency induced plasma is that it is able to produce a wide range of nanoparticle material. Furthermore, it able to generate different sizes of nanoparticles just by altering the four main parameters; (i) plasma gas type , (ii) pressure of the chamber , (iii) temperature of the reactor, and (iv) flow rate of the gas mixture. However, little research has been reported on the influence of each parameter. Furthermore, to attain stability and repeatability of narrow range distribution of nanoparticle sizes had proven to be quite a challenge among industries.

2.2.3 Chemical Reaction - Precipitation in Liquid Phase

In any chemical reaction, the set of precursors or starting material are unique only to each intended final material. The precursors are mixed in calculated proportions and mixed in a liquid medium such as water or alcohol. To ensure homogenous mixing, ball milling, ultrasonication, or even simple blending can be performed. During the mixing, a chemical reaction occurs and precipitation is produced. [23,24,25,26] The resulting product is collected either by filtration or evaporation. However, due the nature of the fine dimension nanoparticles, the preferred method is evaporation. Following which, the residue undergoes a secondary process such as calcination. [27,28,29,30].

Likewise, precipitation in the liquid phase covers a good range of chemicals. However, these chemicals must be insoluble in the solvent medium. Currently, most materials are biased towards the polar solvent of water due to its stability and abundance. Though possible to precipitate pure elements out from chemical mixture, precipitation in liquid phase is commonly reserved for chemicals that cannot withstand the thermal stresses of plasma such as

- Calcium carbonate, ($CaCO_3$)
- Silicon nitrite, (Si_3N_4)
- Titanium nitrite , (TiN)
- Zinc sulphite , (ZnS)

In addition, precipitation in the liquid phase could produce oxides which are more thermally stable, for example

- Zinc oxide, (ZnO)
- Titanuim dioxide , (TiO_2)
- Copper oxide , (CuO)
- Cerium Oxide , (CeO) [31]

The variation in particle size generated by the precipitation in the liquid phase can be wide ranging from 20 to 60 nm for a well-controlled environment with a

mean of 30 nm. It has been reported that the distribution may not be symmetrical but slightly skew towards the lower end. [30]

Reactive precipitation involves four fundamental processes; (i) mixing-limited reaction, (ii) nucleation, (iii) growth, and (iv) aggregation. [32] The greatest challenge of this method arises during the stage of *growth*. It is the period when nuclei of few molecules in the range of angstroms (Å) begin to grow into nanoparticles. If left unchecked, these nuclei will quickly grow into particles above 100 nm and follow by clustering of these particles into aggregation.

Unlike plasma, precipitation can be carried out in an ambient environment and can be easily setup without much expensive equipment. Energy consumed comes mainly from the chemical reaction itself. Because of its low start up and operational costs, precipitation in liquid phase has often been preferred.

2.2.4 Chemical Reaction - Precipitation in Sol-Gel

The sol-gel process is a wet chemical synthesis. It is similar to the precipitation except that it is more complex and has sol-gel as solvent medium. It consists of a series of processes in the order of (i) gelation , (ii) precipitation and (iii) hydrothermal.

The precursors are calculated in required proportions before mixing. Unlike the previous process in liquid, sol-gel precipitation uses two different mediums, both organic and polar, rather than only one medium.[33,34] The mixture is well mixed by means of blending or ultrasonic mixing. The mixture is left to cure or age to form a *gel*. Occasionally, some hybrid of the process may require the aging environment to remain at an elevated temperature. After the gel medium is developed, the more viscous gel portion is separated from the more fluid portion. The gel medium next undergoes chemical reaction of precipitation. [35 , 36]. Precipitation is usually aided by external energy such as heat or ultraviolet light. In some practice of this method of precipitation, one of the precursors is kept separated initial, while the other precursors are exposed to

the external energy. The two portions of these precursors are later mixed together after the energy exposure. Nanoparticles are formed *in situ* in the gel medium. To further process the nanoparticles in the gel, the gel mixture may undergo more thermal processing to achieve the desired material. [37,38,39,40]

As the nanoparticle is synthesized in a gel medium, it is possible to achieve geometric shapes other than spherical nanoparticles, such as cubic, monoclinic (needle) or even tetragonal. Some of the materials that could be harvested by this method includes pure elements like,

- Silver , (Ag)
- Germanium , (Ge)
- Gold, (Au)

Even simple dielectric salts, consisting of a cation and anion, could be synthesized by sol-gel precipitation. Some of the reported salts include,

- Titanium Dioxide , (TiO_2)
- Zinc Oxide , (ZnO)
- Iron (III) Oxide , (Fe_2O_3)
- Cadmium Sulphide , (CdS)
- Copper Chloride, (CuCl)
- Cadmium Tellurides, (CdTe)
- Lead Sulphide, (PbS)

and even complex salt like Zinc Ferrate , ($ZnFe_2O_4$) [38,39,41,42]

Typical sizes of particles precipitated in sol gel are under 50 nm with distribution less then 20nm. It had been reported that a diameter range of between 4 to 10 nm and mean diameter of 5 nm was achieved [40,41,42,43].

The greatest limitation of precipitation in Sol-Gel is the long lead time. Though the actual precipitation hours could have been very short, but the preparation of gelation and post process, such as hydrothermal, could take up very long hours. Prior to any gelation process, a blending step is carried out to achieve a uniform mix, which would easily take up half to two hours. Following that is the

gelation process which occurs over a period of two hours to twenty-four hours. After which, general post processing could consume an additional four hours.

However, such lengthy time is not much of concern to yield rate if the process is employed by shear volume of mass production. Though the lead time is fixed, the volume is independent. Thus if the volume of the batch is huge enough, the problem of yield could be overcome. The second advantage of precipitation in Sol-Gel is that nanoparticles are synthesized in the gel medium, thus there is little opportunity for the particles to agglomerate. The use of a disperser could be eliminated. Thirdly, as particles are suspended in the gel, there will be no need to spend extra resources on storage medium for transportation, handling and storage of nanoparticle from location to location.

2.2.5 Chemical Reaction - Sintering In Gas-Phase

The gas evaporation method is one of the simplest techniques known to produce particles less than 100 nm in size. Extensive studies on metallic particles [44] began in Japan with the stimulation of the Kubo effect [45] which appears predominately in the case of particle sizes less than 100 nm. The evaporated vapour is subsequently cooled and condenses in the gas atmosphere, i.e. solid particles are obtained directly from a gas cloud. The production of compounds such as oxides and sulfides in smoke particles has been of interest as laboratory experiments on dust formation. [46,47]

Gas phase based methods of nanoparticle synthesis have inherent advantages over wet processes because they can be used to produce purer nanoparticles. However, gas phase syntheses at high concentrations that are necessary for the practical fabrication of nano-structured materials present serious difficulties in terms of controlling the size, morphology, crystalline phase, and composition, which ultimately determines the properties of the nano-structured materials. To master such aerosol based technologies we should understand not only the mechanisms of generation, growth, and deposition of nanoparticle, but also the fundamental nature of heat and fluid flow occurring during the synthesis. In gas

phase synthesis process, the final product is determined by fluid mechanics and particle dynamics within a few milliseconds at the early stages of the process. Within this short time frame, three major formation mechanisms dominate the particles formation; (i) chemical reaction (ii) coagulation (iii) coalescence. [48,49,50,51]

In initial stages of chemical reaction, the precursor leads to the formation of product monomers by nucleation. Following, the particles grow by more reactions between precursors on the surface of the newly formed particles. In the next stage, particles float in the gas medium in random order and collide with each other resulting in coagulation. Progressing further, these coagulates fuse together, coalescence occurs to form nanoparticles. [52,53,54]

This type of process is basically dominated by chemical reactions. Chemical reactions are not only restricted to only displacement precipitations but include reduction, oxidation, hydrolysis, direct combination and other less common reactions. For this reason, the final materials from gas-phase synthesis are usually normally ionic compounds rather than pure element. Some of reported compound manufactured by this method are listed below,

- Zirconia , (ZrO_2)
- Indium Tin Oxide, (ITO)
- Yttrium Sulphide Zinc , (YSZ)
- Mollium Dioxide , (MoO_2)
- Molybdenum Sulphide, (PbS)
- Lead Selenium , (PbSe)
- Lead Tellurium , (PbTe)
- Mercury Sulphide, (HgS)
- Mercury Selenium, (HgSe)
- Mercury Tellurium, (HgTe) [55]

Till date, the best practices of chemical reaction gas phase in the industry are able to yield a mean of 20 nm and a range of 120 nm. However, laboratories

had achieved diameter mean of 5nm with a diameter range of 10 nm only. [52,53,54,55]

Sintering in gas-phase was first achieved in the powder making industries. During then, it was used to generate powders for chemical, petroleum, plastics and even food industries. The size of the powder then was as large as a few thousand microns. Today, however, technologies demand even more minuet dimension in the nanometer scale. Sintering in gas-phase does have its advantages as being an established and stable process. Unfortunately, as the dimension of the particle decreases, the cost of production increases exponentially, as more resources are employed to suppress its size growth. The yield rate, fortunately on the other hand, is not significantly affected by these additional controls. Major advantages of aerosol routes are high purity, narrow particle size distribution and good thermal stability as they are already synthesized at high temperature. Furthermore no liquid waste is produced.

In the gas-phase, particles can be prepared either by a chemical or a physical pathway. In the chemical pathway a precursor compound is usually introduced into a tubular flow reactor either as droplets or as vapour. Following thermal decomposition, particles are formed through nucleation and they grow by condensation and agglomeration. A major drawback of this method is that precursors, which are expected to have a specified vapour pressure and be stable below the reaction temperature, are difficult to find. These precursors also tend to be expensive. [8] The physical pathway will be discussed further in later sections. In the evaporation–condensation technique material is evaporated by heating. This can easily be achieved using a tubular flow reactor. As the vapour cools, super-saturation leads to nucleation and particle growth. In such a system the residence time and cooling rate can easily be controlled. This allows for a good control of the particle size and morphology. The system is very simple as it can be operated at atmospheric pressure [53]. A major drawback of this method is that high enough temperatures are needed to evaporate the materials. This limits the materials that can be processed.

2.2.6 Thermal Decomposition

Thermal decomposition, or *calcinations*, is a very ancient technique known for thousands of years. In simple terms, thermal decomposition is just to introduce heat energy to the precursor compound material, raise it to an elevated temperature such that the compound breaks down into its composite elements or a simpler compound. In the application of nanoparticle synthesizing, thermal decomposition is usually utilized as one of the stages in a series of processes, seldom as a lone process by itself. [56,57,58,59]

Prior to thermal decomposition, the precursors are prepared into nano scale particles, suspended in an inert handling medium. Ideal choices of handling medium include non-reactive sol-gel, liquid or even gas. The handling medium serves as two purposes. Firstly, it prevents agglomeration of the newly formed nanoparticles. Secondly, it helps to remove the unwanted by-products yield simultaneously during the decomposition. These by-products are removed either by reacting or adsorbing to the handling medium. The unwanted by-products are usually small molecular compounds such as water, oxygen, carbon dioxide, and any forms of sulphide, nitride, fluoride and chloride. [60,61,62,63]

The variety of the materials able to be processed by this method is less than thermal reaction, the next method to be discussed later. Nevertheless, thermal decomposition is still able to produce a good range of material as shown below,

- Lead , (Pb)
- Silver, (Ag)
- Mercury, (Hg)
- Chromium, (Cr)
- Zinc, (Zn)
- Tin, (Sn)
- Bismuth, (Bi)
- Copper, (Cu)
- Nickel, (Ni)

These nanoparticles are created by one of the following decomposition reactions (noted that the equations are not balanced).

$M(OH)_X \rightarrow H_2O + MO$ **Equation 2- 1**

$M_2O_X \rightarrow M + O_2$ **Equation 2- 2**

$M_{2(}SO_{4)X} \rightarrow M_2O_Y + x\ SO_2$ **Equation 2- 3**

$M_2S_X + H_2 \rightarrow M + H_2S$ **Equation 2- 4**

$MCl_X \rightarrow M + Cl_2$ **Equation 2- 5**

The size and the distribution range of the nanoparticle yield are very much dependent on the precursor nanoparticles. The sizes of the final nanoparticles are usually between 10 % and 30 % less of the precursor. The reduction in size is explained by the loss of mass by the precursor during the decomposition. During the decomposition, small molecules are disassociated from the precursor. The range of the distribution, nevertheless, seldom alters from the precursor, unless sintering of the nanoparticles occurs. The effects of flame temperature on variations of particle size, number density, and morphology have been studied. In the experiments reported by Mansoo Choi, the temperature is controlled by the flow rate of the H_2 fuel. As the flow rate of H_2 increased, the primary particle diameters of silica aggregates initially decreased however, further increases in the H_2 flow rate caused the diameters of the primary particles to increase and the aggregate particles to become spherical. Variations of number density, volume fraction, and fractal dimension of silica aggregates were determined for different H_2 flow rate and different axial distances. [64]

Thermal decomposition is a simple process without much need of expensive equipment. Its simplicity and low cost had made it attractive to be considered often before other methods. However, thermal decomposition does not aid in the control of the size and distribution range of the nanoparticle synthesis thus

making it unable to function as a stand-alone method. It is used mainly as a final process in multi-process methods to synthesis nanoparticles.

2.2.7 Thermal Reaction

Likewise, thermal reaction is usually utilized as one of the final stages in a series of processes though it can generate nanoparticles alone. Unlike thermal decomposition, more chemicals are added into the precursors to form the final product. More often, small molecules are combined into the precursors in the chemical reaction. Similar to thermal decomposition, prior to thermal reaction, the precursors are prepared into nano-scale particles, suspended in an inert handling medium. Ideal choices of handling medium include non-reactive sol-gel, liquid or even gas. In the same way, the handling medium also serves for two purposes, but with different reasons as compared to thermal decomposition. Firstly, just like previously, the medium prevents agglomeration of the newly formed nanoparticles. Secondly, it could serve as one of the reactant precursors, commonly provided in excessive proportion with respect to nanoparticle precursors. [65,66,67]

On the contrary to the thermal decomposition, thermal chemical reaction has a wider variety of chemical. Most common materials synthesized by this method are metallic hydroxides by the hydrolysis, oxides by oxidation, nitrides by nitration, pure elements by reduction, carbides by carbonization. Some industrial [68,69] examples are :

- Zinc oxide, (ZnO)
- Copper oxide, (CuO)
- Iron (II) oxide , (Fe_2O_3)
- Iron (III) oxide, (Fe_3O_4)
- Nickel oxide, (NiO)
- Titanium dioxide, (TiO_2)
- Silicon carbide, (SiC)
- Tin dioxide, (SnO_2)

- Calcium carbonate, ($CaCO_3$)
- Titanium nitride, (TiN)

Simplicity and wide material varieties are two main reasons that made thermal reaction attractive. However, like all other processes, its variety is constrained by the few limited reactions of the hydrolysis, oxidation, nitration, reduction and carbonization. Thermal reaction is usually confined to temperatures below 1000^0C and additional chemicals are only small molecules, such as water, carbon dioxide, oxygen, nitrogen, carbon…etc. Due the easily attainable conditions and abundance of raw material, thermal reaction is often one of the first few processes considered by industry.

2.2.8 Continuous Laser Vaporization Condensation

Continuous Laser Vaporization Condensation, as the names implies, involves two basic stages. The first stage is the vaporization of material; and the second stage is condensation of the vapour into fine nanoparticle. It can be further divided by the type of pressure chamber used. Generally, there is the lower pressure technique, *high vacuum laser vaporization condensation (*HVLVC) and the higher pressure technique; *laser vaporization controlled condensation* (LVCC). The LVCC process involves continuous or short pulsed (nanosecond and less pulse width) laser vaporization of single or multiple targets into a selected gas mixture in a convective atmosphere in a diffusion cloud chamber The large temperature gradient between the bottom and top portions of the chamber results in a steady convection current. The convection could be can be further enhanced under high pressure (≈103 Torr) and a large temperature gradient ($\Delta T \approx 200^0$C) conditions. In HVLVC, a high-vacuum chamber of less than few Torr is used; a flow rate of few litres per hour is maintained. Equivalent temperature gradient is achieved easily despite the difference in other physical conditions. [70,71,72,73]

Laser ablation has proven to be an excellent means for producing nanoparticles [74] and nano-structured thin films [75] of high purity. Particularly

advantageous is the ease with which particle sizes produced by ablation can be adjusted by varying process parameters. From these studies, it is known that the mean particle size as well as the distribution are strongly dependent on the choice of gas type and pressure.[76]

Typical laser ablation experiments are carried out from flat targets in a chamber maintained well below atmospheric pressure (1to 50 Torr), therefore little is known about the behaviour of laser-induced nanoparticle formation in dynamic systems near atmospheric pressure [75].

The method of laser ablation of microparticles (LAM) [77] has been shown to produce a nearly monodispersed distribution of nanoparticle in contrast to the rather broadly distributed particle sizes observed for the ablation of flat targets. In LAM, a shock wave is launched by dielectric breakdown. Nanoparticles are then formed by homogeneous nucleation behind this shock within the expanding microparticle. Under the usual process conditions, only 10–50% of the heat of vaporization of the microparticles is required for nanoparticle formation because of the traveling-wave nature of the shock process.[75]

In all the laser techniques, a fine beam of laser is focused onto the target material. Light energy is converted in to heat energy upon absorption of the laser. The intense heat energy melts the surface of the target, and vapourize the melts. Only a small amount of the target material is vapourized. Commonly, a plasma arc is ignited and rapidly propagated in the reverse direction to the laser beam and in the transverse direction. The plasma cloud rapidly expands away from the liquid surface, and a *laser-supported combustion wave* (LSCW) occurs with the propagating plasma [78,79,80]. The LSCW velocities are found to be typical in the range of a few 10 ~ 100 m/s. Therefore the vapour particles will escape away from the surface with the same order of the velocity which is thought to be much higher than that of evaporation in inductive resource heating. It is reported that the moving velocity of the vapour particles in traditional gas condensation method is the same order of ambient gas convection, which ranges from 0.01 to 1.0 m/s. The high temperature vapour particles were condensed by quenching in inert gas ambient when they

departed from the plasma arc. Thus the nanoparticles are formed and harvested. The nanoparticles could be transported into storage medium or direct deposition on surface [81,82,83,84].

When preparing particles by this physical pathway, the composition of the material is the same before and after processing. Particles can be prepared in the gas phase for instance by laser ablation or evaporation–condensation technique. In laser ablation, material is evaporated and ionised using a laser beam. Particle formation takes place when the vapour cools. The system becomes both expensive and complex, as a laser is needed. Another drawback of this method is that the production rates are small.[85]

Contemporary, a wide range of lasers could be used for short pulse and continuous *laser vaporization condensation*. Another method for classification is to sub-divide them into three main groups based on their excitation medium: (i) Excimer, (ii) Nd:YAG and (iii) CO_2 . Below is a table that summarises each of their characteristics. [86]

Table 2- 1 Characteristics of different lasers

Laser	**Wavelength (nm)**	**Pulse Width (ns)**	**Fluence (J cm^{-2})**	**Threshold Fluence (J cm^{-2})**	**Rep. Rate (Hz)**
Excimer	248 ~ 355 UV range	25	0.24	0.027	10
Nd:YAG	400 ~ 1046 visible light range	46.7	1.70 ~ 5.10	0.12	3000
CO_2	≈ 9.3 X 10^3 IR range	120	5.54 ~ 7.83	3.6	500

With such intensity of energy focused onto such a small area of few mm^2, the localized energy applied on the target is very great. In most cases it is able to melt and vaporize almost any material. Due to its ability to vaporize almost any material, *continuous laser vaporization condensation* is commonly used on

materials that have very high latent heat of vaporization, such as materials of pure metal elements, and materials with ionic–covalent bonds. Thus *continuous laser vapourization condensation* is believed to be able to synthesis almost any material. [87]

Under controlled environment of LVCC or HVLVC, the nanoparticle yield could achieve a narrow distribution range of 5 nm diameter with a mean diameter of 12 nm.

Unlike all other processes described earlier, in which final materials are very dependent on the chemical reactions known and the availability of the precursor chemical, CLVC uses the exact same materials as precursor as the indented final material nanoparticle.

However, the yield rate of *continuous laser vaporization condensation* is very low as compared to the others (about 0.2g/hr). A second limitation is the restriction of the material variety. Though it was mentioned above it was believed that *Continuous Laser Vaporization Condensation* is able to synthesis almost any material, it is restricted to mainly materials with metallic and ionic–covalent bonds. Other materials with weak intermolecular bonding may be found to be non-compatible with *Laser Vaporization Condensation.* Its high energy concentration may prove too much for other materials and cause decomposition or even ignition. [76,80,83,85,86,87]

2.2.9 Femto Second Laser

Like the former laser method, *Femto Second Laser* synthesizing, consists of two main stages; firstly ablation of material followed by condensation of the vapour into fine nanoparticles.

However, there are two major differences. Firstly, the mechanism of vaporizing the material is not by melting but by ablation. It is a process whereby material undergoes phase change from solid directly to gaseous. Because *Femto*

Second Laser has a pulse width in the order of femto seconds (1fs = 10^{-15}s), it will not have the sufficient time needed to penetrate beneath the surface of the target material. Nevertheless, its intense energy is fast enough just to affect the surface of the material via ablation. Secondly, lower pressure is preferred to aid gaseous phase formation and prevent agglomeration.

For any chemical reaction to occur or any structural changes of material, the time taken is in the order of pico-seconds (10^{-12} s) and above. *Femto Second Laser*, on the other hand, has a pulse width of femto second (10^{-15} s) - much shorter than any possible time of reaction. In other words, it is theorized to be able to synthesis any nanoparticle material from its bulk material precursor, without affecting its properties. Also, the short time pulse concentrates the laser energy onto the material so fast that energy is hardly dispersed, thus making it able to ablate a wide range of materials.

On the femto second time scale, energy can be deposited into matter faster than needed for the system to react, leading to confinement of ultra high quantities of energy. This pushes the matter into a state of extreme non-equilibrium and can lead into material ejection from the target by process of ablation. There have been various interpretations of ablation in different types of material, each with its unique processes. However, experiments have shown that different matters all behave roughly the same when irradiated by a femto second laser [87, 88]. An exclusive property of femto second that the author would like to exploit. Though, it had been proven by numerous experiments by many researchers before that for metal, pulse laser as short as nanosecond could generate nanoparticles. But the mechanism of ablation would have been very different for all the other pulse laser of different time frame from that of the femto second. The author had chosen to model the femto second laser in hope that the proposed model could serve as a basis for future model that explains ablation of femto second laser on other material as well.

More than often, plasma is associated with femto second laser ablation. And almost all natural and laboratory plasmas are sources of nanoparticles. [89] The plasma produced by pulsed-laser ablation using short laser pulses has been

shown to be an efficient tool to produce small particles in the nanometer size-range. [90,91,92]

The interaction of femto-second pulses with metals implies a change in the ablation mechanism due to not only the absence of equilibrium between electrons and lattice-ions during the pulse, but also because the heating is too large and fast. The principle characteristic of femto-second pulses, which makes them advantageous for metal treatment, is that the pulse duration is shorter than the equilibration time, about 1 to 10 ps between electron and lattice-ions subsystems. In addition, the time needed for the electron heat diffusion to reach the optical penetration depth is several orders of magnitude longer than the pulse duration. [93]

In general, material ablation is connected with one or several of the following processes [94]

1. relatively slow heating leads to equilibrium melting and evaporation (thermal evaporation);
2. Coulomb explosion takes place as a result of the repulsive forces between the ions if electrons escape from the target first;
3. escaped electrons pull the ions off the target (electrostatic ablation);
4. fast heating causes material expansion (non-equilibrium thermal ablation);
5. very fast energy absorption leads to the development of mechanical stress (mechanical fragmentation in the stress confinement regime).

From the time-scales of the processes during the ultrashort pulse ablation described above, it is evident that a laser pulse in the order of pico-seconds interacts with many transient states of the metal, following the fourth path of non-equilibrium thermal ablation. Often, it is accompanied with the fifth path of mechanical fragmentation. For the even longer nano-second laser ablation with the first path of thermal evaporation. The nanosecond laser not only interacts with metal, but as well as with the expanding plume and the ambient gas plasma. Most of the limitations in applications of nano-second and pico-second laser pulses can be understood from these basic considerations. Relative to the femto-second, the energy deposition is much slower, so that the thermal

diffusion of the lattice is significant and cannot be neglected. The electrons and the ions can be considered to be in equilibrium during the nano-second and pico-second ablation processes. The longer the pulse, the deeper and wider is the laser affected zone, which will affect the microstructures of nanoparticles formed and the target left behind. The threshold fluence that is necessary for the material removal metal ablation is inversely proportional to the pulse length of laser. Typically, the femto-second threshold fluence values are about one order of magnitude lower than the nanosecond ones.

In nano-second and pico-second ablation the target surface can be heated up to temperatures close to the critical point, which can result in explosive boiling [88]. Due to the long duration of the ablation process, melting cannot be avoided. The plume expansion is complicated by plasma absorption of the laser light, which in turn reduces the efficiency of the energy deposition into the target (plasma shielding).

The time scales of the processes during the femto-second laser ablation enable very efficient energy deposition into the sample and the material does not seem to be removed through the classical melting and evaporation route. In addition, the post-heating of the plume can be neglected so that the risk of the fractional evaporation during the ablation process itself is minimized.

When femto-second laser is used, the equilibrium thermal evaporation, which is a very slow surface process, is definitely not the basic ablation mechanism. For the observation of the second mechanism (Coulomb explosion), a charge separation at the surface is required. Although metals have large electron mobility, the ultra short time frame of interaction prevents these electrons to have the necessary screening effect, as explained above. The third mechanism (electrostatic ablation), plays a role only if the electron energy overcomes the sum of the work function and the binding energy [95]. This ablation occurs only at the very beginning and therefore be responsible for the ejection of only a small fraction of all ablated material. To accurately investigate the contributions of the two remaining mechanisms, a microscopic model is required [96,97]. However, the development of such a model for laser fluences needed for the

plasma generation is rather complicated, the major difficulty being the absence of the knowledge about the interaction potential. The use of the one dimensional model gives a possibility approximate information about the these ablation process. [91] So, the second mechanisms may be used as the basis in building model for the case of femto-second interaction with metals.

As reported further by *Perez and Lewis*, the basic mechanisms leading to ablation are still subject to debate, largely because theoretical modeling is difficult. Indeed, absorption of a large quantity of energy on such short timescale induces many different processes. Hence, the details of the complex non-thermal processes which occur shortly after the absorption of the pulse are not expected to play a crucial role in the material removal. Ablation should thus be dominated by processes occurring on a mesoscopic scale. Taking advantage of this simplifying factor, we can identify the relevant ablation mechanisms for low fluences[98]. It had been shown that nanoparticles formation by femto-second laser ablation involves four different processes : (i) spallation, (ii) homogeneous nucleation, (iii) fragmentation and (iv) vapourization , which sometimes occur simultaneously at different positions. [99]

After the metallic material had been successfully vapourized , the sequential process is to condense these vaporized into ultra fine solid particles. The fundamental of femto-second laser synthesis is to quench these vapours with very high temperature difference. In a very short time, nucleation occurs and the crucial challenge is to suppress these nuclei from over-growing into micron-size powder.

The first successful analysis of vapor condensation was done by *Yu. P. Raizer* in 1960. He applied the analysis based on the classical nucleation theory to formation of cosmic dust proposed by Zeldovich earlier in 1942. This combined effort became to known as Zeldovich-Raizer (ZR) theory later. [100] Recently this theory has been used to be used widely as the basis to calculate the size distribution function of nanoparticles produced during condensation of vapor into vacuum. [101,102,103]

In most cases, femto-second laser ablation was performed at relatively low gas pressure of inert or reactive gas. During expansion and cooling, condensation starts within the ablated vapor. If left uncheck over a period of time, the condensed particles undergo further multiple collisions with ambient gas molecules, leading to the stabilization of the nano-clusters. [104] The size of these nanoparticles and the nano-clusters are affected by the laser parameters: fluence, wavelength, pulse duration and by the ambient gas conditions: pressure, nature and flow parameters. Condensation of nanoparticles within the laser-induced vapor plume is a common phenomenon in pulse laser ablation and was also observed in numerous pulsed laser deposition experiments, as reported in the review by *Chen* as early as 1994. [105]

The purity of the nanoparticles depends primarily on that of the carrier gas and the target material. Since the laser beam is focused on the target, contamination by materials released from other parts of the apparatus is less likely. The handling of the solid metal target is easier and often less hazardous than using metal organic compounds or compounds containing chlorine or fluorine. Laser ablation allows control over the ablated mass by varying pulse energy and frequency. As reported, *Ullmann* and his team had attempted to measure the mass of material ablated by simple weighing the collected aerosol of nanoparticles and the target. Nanoparticles of different materials can be easily generated by changing the target material. [106] Under a controlled environment in the chamber, nanoparticles yield could achieve the same narrow distribution range of 5 nm with a mean less than 5 nm. A foreseen advantage of *Femto Second Laser* is that it is able to synthesis any material without the restriction of the availability of chemical reaction known. However, its greatest limitation is still its relatively low yield like all other laser methods.

Beside pure metal nanoparticles, oxides of metal nanoparticles could be synthesized by the same techniques. A certain amount of laser energy can be absorbed by the vapour that superheats and ionizes it. If a reactive gas, for example, oxygen which is found in abundance in air, is present, then a chemical reaction occurs. The energy of chemical reaction of the metal vapour with oxygen is similar to the energy required for evaporation. More laser energy

will be absorbed by the vapour to form the plasma. To superheat the vapour to 23,000 K, the maximum temperature of the plasma [107] requires about the same amount of energy as for the other two processes. Further ionization of the plasma may increase this value. In order to avoid this, laser irradiation is inclined at an angle with respect to the direction of plasma plume. By far the greatest part of the pulse energy is reflected (>95%) while a small amount is used to warm the target. The reflected energy is absorbed in the ablation chamber. The ablation chamber is not significantly warmed by the reflected energy, because of the comparatively large volume of the chamber and convective cooling by gas flows. Thus, it can be deduced that laser ablation is not efficient. However, the simplicity, versatility and stability of nanoparticles production by this method still make it very popular. This is especially so as these are important features for laboratory generation of aerosols. [105]

The basic mechanisms leading to ablation are still subject to debate; largely because theoretical modeling is difficult [95].The absorption of a large quantity of energy in an ultra short time scale induces many different processes. Most of the classical physics models are not able to give a full description of both the ablation and the formation of nanoparticles. Most of the recent models proposed were mainly based on *molecular dynamics model* technique. One good representative of such model was performed by *Amoruso et al.* in 2005. They constructed a molecular dynamic model to predict the ablation behaviour of aluminum. Their model was verified against actual experiments [108].

The laser ablation process has often been described by *Scuderi et al.* as a thermal de-sorption model, which considers the ablation as a rather slow layer-by layer sublimation of monomers from the target surface [109]. Many researchers had used the *Zeldovich–Raizer* condensation model to explain the formation of nanoparticles in the aerosols. However, the common thermal de-sorption and condensation model of *Zeldovich–Raizer* condensation model itself is insufficient to account for the whole population of nanoparticles formed. The *Zeldovich–Raizer* condensation model accounts only for the formation of an individual particle. Only a detailed molecular-level simulation can provide a complete description of the nanoparticles formation process at population level,

as explained by *Itina et al*. in their paper published in 2007. [103] One of the possible approaches for such simulations is to combine the *molecular dynamics* technique with the *direct simulation Monte Carlo method.* This combination allows one to properly account for both the processes of cluster ejection and their following evolution during the laser plume expansion as a result of the gas-phase collisions Some of the representive researchers using such an approach are, *Zhigilei et al.* in 2000, *Bird* in 1994, *Itina et al.* in 2002, *Zeifman et al.* in 2002, *Mizusek et al.* in 2001, and *Briehl et al.* in 1999 [110,111,112,113,114,115]. By using the combined model, the researchers were able to examine different types of collisions leading to nanoparticles formation.

2.3 Mechanism of nanoparticle formation of ultra short pulse laser synthesize

The total process of the nanoparticle formation could be further broken down into 6 sub-processes: (i) irradiation (ii) ablation (iii) nucleation (iv) growth (v) coalescence / coagulation and (vi) agglomeration. A schematic of laser ablation gas-to-particle conversion process is show below in figure 2-4.

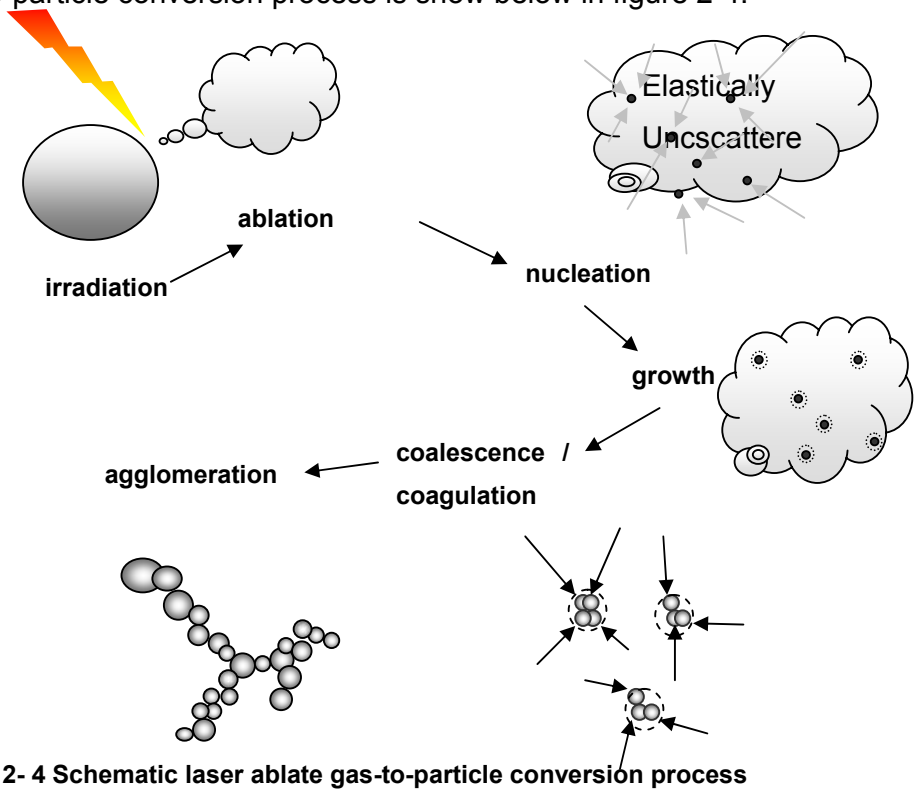

Figure 2- 4 Schematic laser ablate gas-to-particle conversion process

Firstly, the ultra short pulse laser is irradiated onto the target. The laser energy is absorbed by the target material. Because of the high energy intensity and the ultra short time pulse, the material changes phase from solid to gaseous in the process of *ablation*. Because of the nature of femto second laser, a plume is formed incident to the irradiation. Ablation follows to form a vapour of the target material. The difference in pressure and short time span, creates a localized zone of supersaturate vapour. This vapour is later used in the creation of nanoparticles. Physical properties of this supersaturated vapour have great influence on the shapes and dimensions of nanoparticles to be materialized.

Following on from irradiation and ablation is the process of gas–to–particle conversion which is quite common to many other methods of nanoparticle generation. In the gas-to-particle conversion, a supersaturated vapour of a gaseous species forms new particles. The supersaturated vapour is formed either as a result of chemical reactions, e.g. thermolysis of a metal containing species that form metal oxide molecules with a very low saturated vapour pressure, or as a result of physical processes such as cooling that reduces the vapour pressure of condensable species.

One of the undesirable by products of this method is that the volatile precursor or intermediate products can evaporate and form additional particles by gas-to-particle conversion. This would lead to a bimodal size distribution. In the formation of product particles with such desired properties as morphology, porosity, crystallinity etc., controlling the reactor conditions is of high importance. The classes of materials produced by the method include inorganic materials such as metals, simple metal oxides, complex metal oxides, and monoxides, as well as organic materials. [116, 117,118,119]

In the ultra short pulse laser ablation, the supersaturation of gaseous species then leads to the formation of new particles by homogeneous nucleation as shown in figure 2-4. Usually processes such as particle collisions, vapour condensation on particles, coalescence, and agglomeration are caused by the high particle concentrations resulting from the gas-to-particle conversion. A

relatively narrow particle size distribution, in terms of a geometric standard deviation of around σ_g<1.5 is typically obtained. [120]

The rate of particle coalescence has a significant impact on the final morphology observed. The temporal evolution of nanoparticle growth in a gas-phase process is depicted schematically in figure 2-5. This process of undesired coalescence often results in chained agglomerates of small particles. While the desirable morphologies are spherical, soft agglomerates may also been formed by intra-particle agglomeration, if post-agglomeration is not control. Since coalescence (sintering) processes are generally occurring simultaneously or subsequent to nucleation, the ability to predict the time scales and basic physics behind sintering of nanoparticles could be very useful in the construction of aerosol models that account for particle shapes [121] .

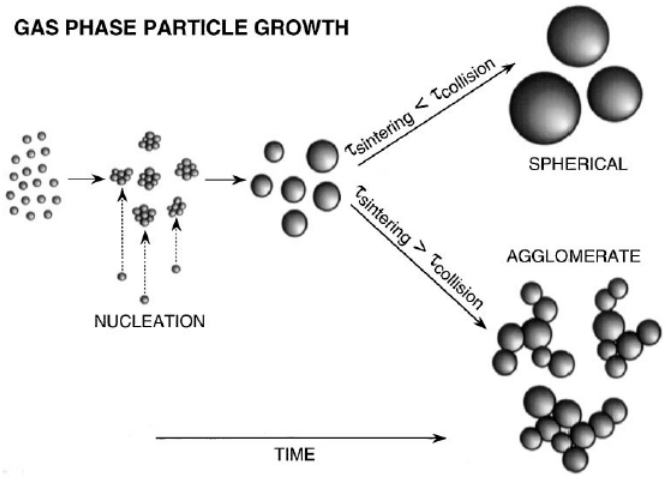

Figure 2- 5 Temporal evolution of vapour phase particle growth. [119]

Often aerosol researchers who are interested in materials processing direct much of their effort towards minimizing agglomeration [122,123]. The essence of the problem involves a competition between the time for particle-to-particle collisions and the rate of particle coalescence. If the collision time is long relative to the characteristic sintering (agglomeration) time, then spherical particles will be grown, since, on average, a particle doublet will have coalesced before another particle is encountered. If however (as is so often the

case) collisions between particles occurs faster than coalescence, chain aggregates similar in morphology to that formed in soothing flames are produced. [124]

$\tau_{sintering} < \tau_{collision} \Rightarrow$ spherical particle

$\tau_{sintering} > \tau_{collision} \Rightarrow$ agglomerate [124]

Naturally, both number concentration count and temperature are important variables in defining characteristic times for collision and sintering, respectively.

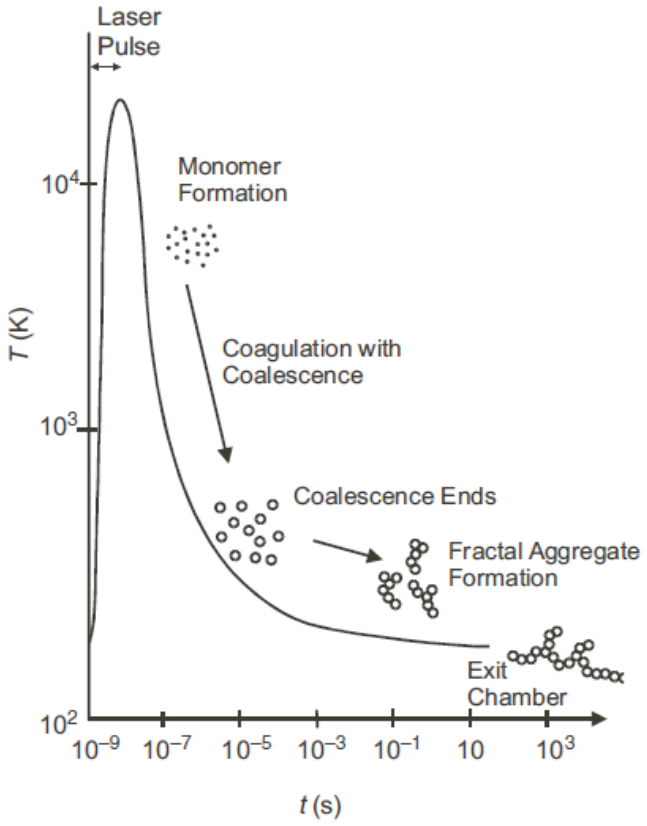

Figure 2- 6 Schematic diagram of formation of oxide nanoparticles [106]

Figure 2-6 illustrates the formation of titanium nanoparticles with respect to the time domain as reported by *Marc Ullmann et al*. [106]. Monomer formation occurs when the gas has cooled to the point where the oxide dissociation ends. Coalescence continues during a period of rapid quenching and ends at about the same time. Hence particles of similar size are produced; these form aggregates with a fractal dimension of 1.7–1.9 by cluster–cluster collision.

The driving force for coalescence is the minimization of the surface free energy, brought about from a gradient in the chemical potential. While agglomeration is generally found to be important in the solid-phase (because it is relatively slow), liquid-phase processes can have a large impact on the resulting morphology of multi-component clusters [125].

In general, these models employ concepts of viscous flow, diffusion processes and evaporation / condensation as mechanisms for sintering [126]. During coalescence, the surface area of the particle decreases, resulting in a heat release associated with the resulting lower surface energy. In a growth process particle heating competes with heat transfer by conduction to the cooler carrier gas and radiation. To grow the largest primary particles one should operate at low pressures and or high volume loadings. [127]

It was shown that since these particles coalesce by the mechanism of solid state diffusion which is an extremely sensitive function of temperature, the temperature increase within the particle has an important effect on the dynamics of coalescence. In fact, it was shown by *Lehtinen and Zachariah* that for silicon nanoparticles coalescence, the effect reduced in some cases the coalescence time by 1 to 2 orders of magnitude and that heat transfer rate played a critical role. Below a critical gas temperature, all the generated heat release is conducted to the surrounding gas, whereas above the critical temperature a sharp increase in particle temperature is observed, and with it a significant deduction in coalescence time.[125]

If the gas temperature is high enough, the particle temperature increase due to heat release from coalescence will be faster than the heat transferred to the surroundings. This will increase the diffusion coefficient and, hence, the coalescence rate—which will increase the temperature. If the gas temperature is low, conduction and radiation will dominate, and thus the particle temperature will always stay at the gas temperature.[106]

Koch and Friedlander proposed a model that suggested the use of high temperature will result in aggregation of monomers. More will be discussed in the next chapter. Taking the heat increase into account, temperature enables particles to grow to 1000 times of their initial volume. If one wishes to grow large primary particles without using excessively high gas temperatures then this could be achieved using very high loadings together with low pressures.[119]

To master such aerosol based technologies one should understand not only the mechanisms of generation and growth of nanoparticles, but also the fundamental nature of heat and fluid flow occurring during the synthesis. In addition, one requires the development of methodology to transport and deposit particles at specific locations of interest.

Particle nucleation, nucleus growth, coagulation / coalescence, and agglomeration when coupled with the fluid mechanics, heat transfer, and mass transfer would determine the size distribution and morphology, of the nanoparticles formed. Nanoparticles often form chain-like aggregates when generated at high concentrations. If allowed to grow, these aggregates then coalesce to become an isolated particle. It is well known that the size and morphology of particles are determined by the competition between collision and the coalescence of particles.

2.4 Characterization of nanoparticles

Through the years several methods had been developed by the research communities to characterize the physical dimension of nanoparticle. Due to the extremely small nature of these nanoparticles, characterization had often been divide into two stages: (i) collection ; (ii) measurement.

2.4.1 Collection of nanoparticles

As these particles are in the scale of nanometers, which make it very difficult to handle and position often, some other properties of the nanoparticle could be modified by external source to aid in the sample collection of the particle. Common practice include changes it movement velocity (both in direction and speed), electrical charge, coating with a thin layer of another material.

Movement velocity

This method is usually used in light fluid as carrying medium, more so often in carrying gas. The fluid is forced to travel at laminar flow with the desired velocity, thus carrying the nanoparticle along with the same velocity. The nanoparticles have a different mass which is proportional to the physical dimension of the particle. In such flows, with all the nanoparticles traveling in the same velocity, different nanoparticles will have different momentum, directly proportional to their mass, which in turn depends on their dimensions. Understanding the relation between the momentum and the physical dimension, these nanoparticles could be sorted out into their various sizes to be collected. [128]

Electrical charge

In order for the nanoparticles to be classified and collected by an electrical field, the nanoparticle must be first ionized. Ionization is best done in an ion generation chamber and the particle is carried in a gas medium. A radio-active material is kept in the chamber. As the carrier gas with nanoparticle is passed through the chamber, the radiation emitted from the material irradiates onto the nanoparticle giving them charges. Different types of radioactive material emit different radiation. Below in table 2-2 is the commonly used radioactive material. The α-radiation carries positive charge while β-radiation carries negative charge. [129,130,131]

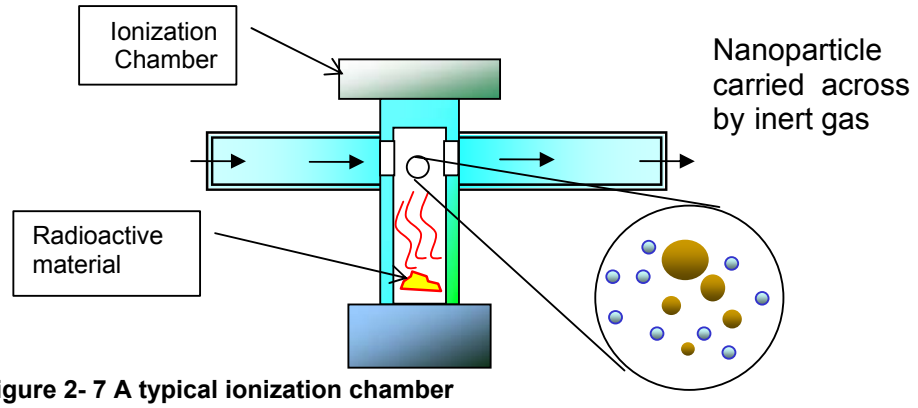

Figure 2- 7 A typical ionization chamber

Table 2- 2 Properties of Radioactive material commonly used for ionization

Radioactive Material	Half Life	Radiation Type	Energy (MeV)
^{63}Ni	100 years	β	0.065
^{90}Sr	27.7 years	β	0.546
^{90}Y	2.7 days	β	2.18
^{85}Kr	10.76 years	β γ	0.67 0.514
^{241}Am	458.6 years	α	5.49
^{210}Po	138.4 days	α	5.30

Coating with a thin layer of another material

At the nano-scale, the finer particles are unable to be detected by the current automated optical inspection (AOI) machine. Current AOI rely heavily on electro-magnetic wave from spectrum of the visible light range and Couple Charged Device (CCD) camera as sensors for imaging. As the wavelength of these visible wave are already at few hundreds nanometer, they had proven to be quite unreliable to image nanoparticle of size of 20 nanometers and below. A simple direct approach is to coat this nanoparticle with a thin layer of liquid. By the principle of the Kelvin Effect, each nanoparticle, irrespective of their diameters, can be coated with the same uniform thickness. The thickness of the liquid film can be controlled by the saturation ratio of the partial pressure of the vapour of liquid to the saturation pressure of the liquid. [129,130,131]

2.4.2 Measurement of nanoparticles

The physical dimensions can be measured directly by the use of SEM (scanning electron microscope) FESEM (field emission scanning electron microscope) TEM (transmission electron microscope), SPM (Scanning Probe Microscope), AFM (atomic force microscopy) and STM (scanning tunneling microscopy). Alternatively, there had reports of the measure of other physical properties of the nanoparticle to reflect back the physical dimension of the nanoparticle, such as APS (aerodynamics particle sizing), OPC (optical particle counter), MDA (mobility differential analyzer) and diffusion battery.

SEM - Scanning Electron Microscope

Due to the fine dimension of nanoparticle, to facilitate direct measurement, either a shorter wavelength is used for imaging or high velocity electrons beam is used. The SEM system is made up of (i) an electron gun , (ii) several condenser lenses, (iii) an aperture , (iv) scan coils , (v) secondary electron detector , (vi) backscatter electron detector , (vii) electron backscattered diffraction detector (viii) X-ray energy dispersive spectrometer (XEDS) detector (ix) scintillator, (x) and photon-multiplier. Figure 2-8 shows a schematic diagram of a SEM. [132,133]

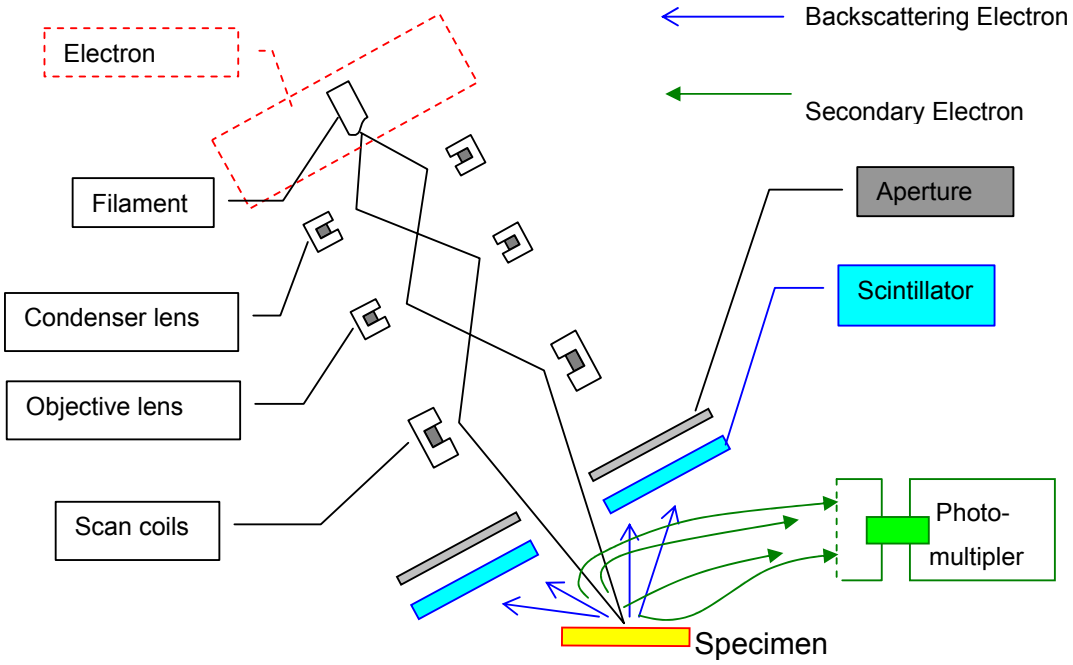

Figure 2- 8 Scanning Electron Microscope.

FESEM - Field Emission Scanning Electron Microscope

The field-emission environmental scanning electron microscope (ESEM-FEG) represents several important advances in scanning electron microscopy. Whereas conventional scanning electron microscopy requires a relatively high vacuum in the specimen chamber to prevent atmospheric interference with primary or secondary electrons, an FESEM may be operated with a lower vacuum (up to 10 Torr of vapour pressure) in the specimen chamber. [134]

TEM - Transmission Electron Microscope

Like the SEM and FESEM, the TEM works in a high vacuum chamber. Similarity, TEM employs an electron gun, and depends on an electron beam as illumination. The only difference is that the electrons are made to penetrate the specimen. The specimen has to be thin (a few micron) in order for the electron to be transmitted through it. [128,129,130,131,135]

An TEM is made up of (i) an electron gun , (ii) condenser lenses, (iii)aperture , (iv) objective lens , (v) objective aperture, (vi) projective lenses , (vii) phosphor screen electron backscattered diffraction detector (viii) X-ray energy dispersive spectrometer (XEDS) detector and (ix) couple charged device (CCD).

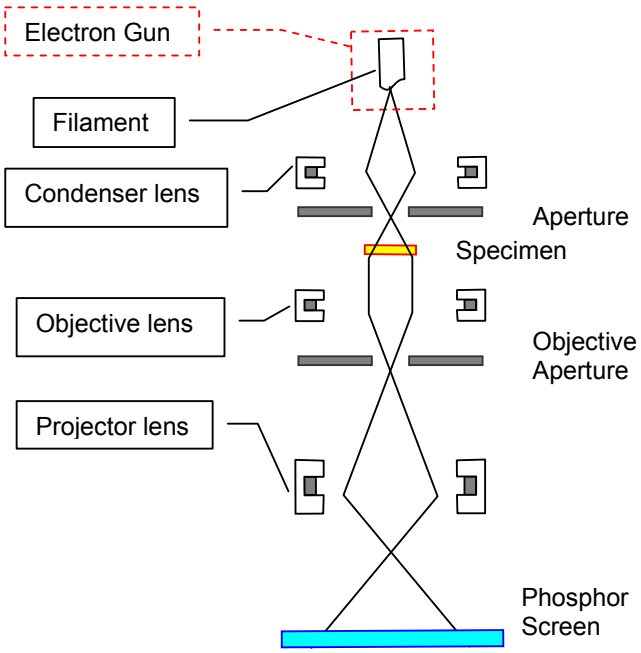

Figure 2- 9 Transmission Electron Microscope

SPM - Scanning Probe Microscope

Scanning Probe Microscope (SPM) utilizes automated atomic force microscopy (AFM) and scanning tunneling microscopy (STM) techniques had been used to measure surface characteristics for semiconductor wafers, lithography masks, magnetic media, CDs/DVDs, biomaterials, optics, and other samples up to 20 mm in diameter. Most of these instruments have a laser spot alignment system and the ability to change scanning techniques without tools. These features offer great flexibility and ease of use. In additional to measuring the size of the nanoparticles, the SPM could be use to determine the shape of the nanoparticles as well. [61,62]

Scanning Probe Microscopy belongs to the family of microscopy where a sharp probe is scanned across a surface and interactions between the probe tip and samples are monitored. The two primary forms of SPM consist of:

- Scanning Tunneling Microscopy (STM)
- Atomic Force Microscopy (AFM) (also called Scanning Force Microscopy (SFM)) , which is further divided into 3 primary modes of AFM:
    1. Contact Mode AFM
    2. Non-contact Mode AFM
    3. Tapping Mode™ AFM

APS - Aerodynamics Particle Sizing

The aerosol of nanoparticle and carrier gas is channeled into a nozzle, which accelerates the nanoparticle. After the nozzle, the smaller nanoparticle continues to flow closely to the velocity of the carrier gas, while the larger nanoparticles will lag behind. This results in a difference in relative velocity between the nanoparticle and carrier gas. The higher the relative velocity, the longer the settling time and thus the larger the nanoparticle size. Using the time difference in settling time and time interval for collection, one could determine the dimensions of the nanoparticles. [128]

OPC - optical particle counter

An optical particle counter could measure both the size and number concentration of the nanoparticle in a limited size and range. It uses the principle of light scattering. A stream of aerosol, nanoparticle and carrier gas is flown past a highly focused light beam. The intense light beam is flashed onto the beam. The nanoparticle reflects the flash light and scatters the reflected light across the chamber. This scattered light are received by a photo-detector and converted into electronic signal. The number of counts of the signal gives the concentration count, while the amplitude of the signal gives the nanoparticles size. The light power that an individual particle scatters is a function of its sizes, refractive index, and shape. With the development of laser, more intense light is achieved and thus the finer the nanoparticle could be measured. [128,129,130,131,136]

DMA - Differential Mobility Analyzer

The Differential Mobility Analyzer (DMA) is a device that can be used to sort nanoparticles according to size while keeping them suspended in carrier gas. Figure 2-10 shows a schematic diagram of a DMA. The first step in this technique is to apply an electric charge to the particles. It is difficult to put more than one charge on small particles; as a result, most of the particles will be either uncharged or have a single charge. Only the positively charged particles are sorted by the DMA while all of the others are lost.

After charging, the particles enter the DMA were they are allowed to migrate into a clean sheath air flow under the influence of an electric field (see the Figure 2-10 below). The rate of migration depends on the electrical mobility of the particles; mobility, in turn, depends on both the size and electrical charge of the particle. If all the particles have the same charge, then particles of a given mobility will all be of the same size. Since the particles migrate at different rates, they are spread out through the sheath air according to mobility. Then withdrawing a portion of the sheath air flow separates a narrow range of particle mobilities from the rest of the aerosol. To measure a size distribution, the differential mobility analyzer (DMA) is scanned over a range of particle mobilities by varying the applied field; until this is done the number

concentrations in each range of mobilities are measured. This can then be converted to a size distribution by using the distribution of charges produced by the charger and the known relation between mobility and size. [128,129,130,131,109]

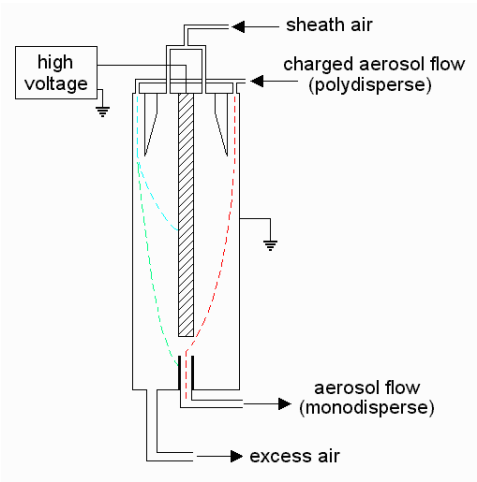

Figure 2- 10 Differential Mobility Analyzer

Diffusion Battery

There are several types of diffusion batteries. They are differential by their shape, mainly as rectangular channel and parallel circular plate. The plates are mesh of metal of different density. A series of these plates are placed after in the path of the aerosol flow. The denser, i.e higher mesh number, are placed in front of the flow. The larger nanoparticles are trapped onto the denser plates in front, while the finer nanoparticle travels down to be trapped by the less dense plates. The plates are removed and measurements are done on them to review the nanoparticle size and distribution.[137, 138,139]

2.5 Summary

Various methods of generating nanoparticles were discussed in this chapter. These methods are summarized in tables 2- 3 to 2-6 below. A short discussion of the mechanism of nanoparticle formation by ultra short pulse laser has been presented. Following, the literature review presented various method of characterization of the nanoparticles. In the next chapter, a novel model of

explaining the mechanism of the formation of the nanoparticles by femto-second laser ablation will be presented.

Table 2- 3 Methods of nanoparticles synthesizing by plasma.

Methods	Advantages	Limitation	Material	Yield
Plasma – Naked Flame	Atmospheric pressure Short reside time	High temperature	Al_2O_3, Co_3O_4, SiO_2 ,V_2O_5	Mean 35 nm Range 10 ~ 60 nm 40 g / hr
Plasma – RF Resonance	Versatile to be used for many material of same equipment Able to control yield type by parameter changes	Capital equipment needed	Fe , Zn, Cu, Ag, SiCN, SiO_2, Al_2O_3 , AlN	Mean 500nm Range +/- 300 nm

Table 2- 4 Methods of nanoparticles synthesizing by chemical reaction.

Methods	Advantages	Limitation	Material	Yield
Chemical reaction – Precipitation in Sol Gel	Carried out in normal environment Little or no energy consumption Simple set up	Fixed recipe	Ag ,Ge, Au, TiO_2, ZnO, Fe_2O_3, CdS, CuClTiN, CdTe, PbS, $ZnFe_2O_4$, Y , Eu, Ce, La	Mean 50 nm Range 30 ~ 70 nm
Chemical reaction – Precipitation in Liquid	Carried out in normal environment Little or no energy consumption	Fixed recipe	$CaCO_3$, Si_3N_4 TiN, SZn, ZnO, TiO_2, CuO, CeO	Mean 30 nm Range 20 ~ 60 nm
Chemical reaction – Sintering in Gas-Borne	Purer material yield	Fixed recipe Difficult to control size, morphology , crystalline phase.	ZrO_2 ,ITO, YSZ, MoO2 PbS, PbSe, PbTe, HgS HgSe,HgTe	Mean 5 to 10 nm Range 10 ~ 120 nm

Table 2- 5 Methods of nanoparticles synthesizing by plasma.

Methods	Advantages	Limitation	Material	Yield
Thermolysis – Decomposition	Simple and direct.	Many impurities Fixed recipe	Pb, Ag, Hg, Cr, Zn, Sn Bi, Cu ,Ni	Dependent on precursor
Thermolysis – Reduction	Simple and direct.	Many impurities Fixed recipe	ZnO, CuO Fe_2O_3, Fe_3O_4 NiO, TiO, SiC SnO_2, $CaCO_3$ TiN	Dependent on precursor

Table 2- 6 Methods of nanoparticles synthesizing by laser.

Methods	Advantages	Limitation	Material	Yield
Laser - Continuous	Purer material yield	Capital equipment needed Control environment	Almost All	Parameter control
Laser- Ultra Short Pulse	Purer material yield	Capital equipment needed Control environment	Almost All	Parameter control

3. Theoretical Model Development

In this chapter, a theoretical model is developed to explain for the formation of nanoparticle using laser ablation. The different parameters which have a significant influence on the formation of the nanoparticle are identified and a model based on these parameters is proposed and developed. The proposed model is later compared with some contemporary models used in the aerosol research communities.

3.1 Parameters of studies

Till date, there has been many reports and papers published about the phenomena of nanoparticle synthesis utilizing the ultra short pulse laser as their energy source. Though many had performed experiments with various parameters, especially (i) Laser Power, (ii) Pressure, (iii) Temperature, (iv) Flow rate, (v) Target material, and (vi) Carrier Gas, very few comprehensive models have been offered to explain the phenomena. Many, instead, have given qualitative explanations, with little quantitative discussion.[75, 106,140,141,142,143,144,145,146,147,148,149,150] Though, some attempted to model the phenomena, they were only partial descriptions of the whole process. [136,151,152,153]

The author will attempt here to develop a model that can explain the phenomena of how each of the following parameters: (i) Laser Power, (ii) Pressure, (iii) Temperature, (iv) Flow rate, (v) Target material, and (vi) Carrier Gas; will affect the mean and distribution spread of the nanoparticle diameter formed. Unlike most of the former partial models, the author aims to develop a model, comprising of a direct relationship between these parameters and the nanoparticles diameter yield. These six parameters were drawn from the references of prior works of other researchers which had established them to

be some of the most significant influencing factors in nanoparticles formation by femto second laser ablation.[[129,130,131, 154]]

As previously explained in section 2.3, the mechanism of nanoparticle formation by ultra short pulse laser synthesis can be further broken down into 6 sub -processes of:

- *irradiation* of the target metal material to transfer energy to the solid phase target, resulting in highly excited atoms of the metal.,
- *ablation* of the solid phase metal into vapour,
- *nucleation* of the metal vapour to form stable nuclei, or seed, to facilitate further growth of the particles,
- *growth* of the nuclei occurs as it attracts more vapour towards itself, adhering and fusing together,
- *coalescence* of these grown nuclei accelerate the growth process into micro-scale particles.
- *agglomeration* of these nanoparticles is inevitable due to its nano-scale size, eventually into clusters of nanoparticles.

By natural occurrence, the formation of nanoparticles does not yield a discrete single diameter nanoparticle population, but rather a range of sizes spread over a continuous distribution. A desirable yield with a high commercial value would be expected to have a narrow size range and distribution.

The basis of the formation of nanoparticle is dependent on the following:

- the amount of monomer, single atom entities, present in the system,
- the kinetic energy, thermal energy possessed by these monomers,
- the probability of collision between these monomers, and
- the time allowed for the collision between these monomers.

The greater the amount of monomers and higher the level of energy they possess, the probability of collision and the longer time given the more likelihood for the nanoparticles to grow into larger sizes. Likewise, if the distribution spread of the monomer population increases, so will the size of the

nanoparticles. Of all the six parameters identified, whenever there is an increase in any or a combination of these factors, it will result in larger particle diameters with a larger distribution spread.

3.1.1 Laser Power

Laser power is the main source of the energy input into the system. It provides the energy to convert bulk metal into vaporous monomers. Thus the amount of laser power applied directly affects the amount of monomers generated. Another factor is the effectiveness the energy being transferred to the bulk material by laser irradiation. The effectiveness of the energy transfer in turn depends on the optics of the laser beam, the nature of the laser and the response of the target metal. The reaction outcome of different metals towards different type of laser will be discussed in the section *3.1.5 Target Material*.
The type of the laser can be characterized by the following:

- wavelength,
- oscillation frequency,
- amplitude,
- pulse width,
- pulse frequency, and
- polarization.

The optics layout, on the other hand, affects the focus and beam spot area.

A common unit of measurement for laser power is fluence, J/cm^2. Its relationship with the some of the other laser parameters, mentioned above, make it a useful quantification parameter.

$$\text{Fluence} = \frac{\int (\text{Power laser})\,(\text{number of pulse})\; d(\text{pulse width})}{d(\text{beam spot area})}$$

Figure 3 - 1

The higher the fluence, the more mass will be ablated and, in turn more vapour generated, which results in more monomers being formed. The concentration of monomers in a fixed volume is commonly referred as *loading.* When the loading is high, it increases the probability of collision between monomers, and results in larger diameter of nanoparticles with an increased distribution spread being formed. These phenomena had been reported independently by Heszler *et al* [155],.Veintemillas-Vergauer *et al* [156] , and Nicholas *et al* [75]

Experiments conducted by Ozawa *et al* [129] in 2001 displayed this relation and are shown in figure 3-1.

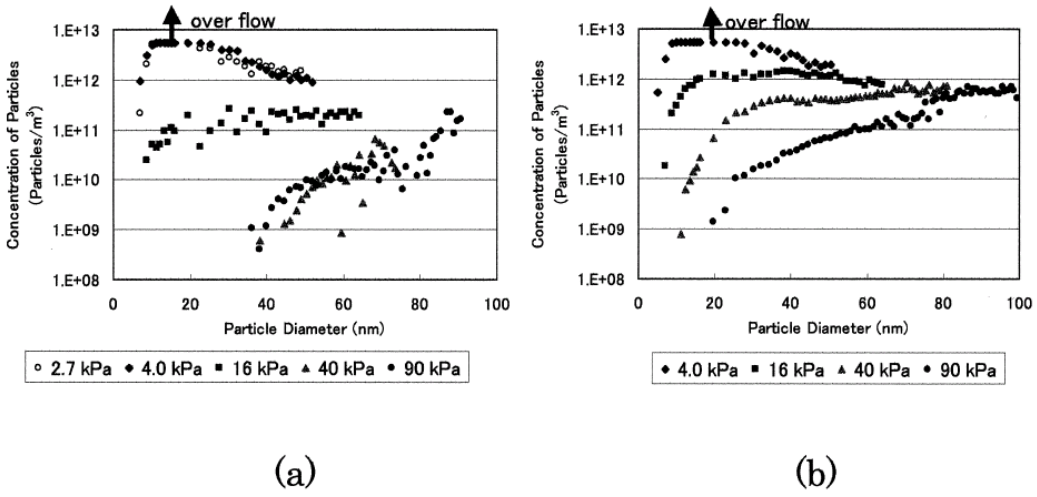

Figure 3- 1 The comparison of size distributions by different fluences, a) 1.9J/cm^2 and b) 3.8J/cm^2, plotted by Ozawa *et al* [101]

Before laser ablation could occur, the laser must first overcome several thresholds inherent in the metal itself. The use of femto-second laser, with its short pulse width helps to overcome the threshold for plasma formation in the metal and concentrates the shock heating in a shorter timeframe.

Similar, experiments of laser ablation had been conducted on metallic mirco-spheres in 1998 by the team leaded by *Cai*. [133] The team explored this methods as they believed that the process is more efficient than the ablation of surfaces because the use of micro-spheres decreases the threshold for plasma

formation in the material and concentrates the shock heating to a smaller volume than for surface ablation. Nevertheless, the same fundamental of physics for metallic nanoparticles formation from either flat surface target or mirco-spheres remain the same. It was found that the average diameter for gold nanoparticles increased the with laser fluence, from 80 nm at 3.1 J/cm^2 to 116 nm at 10 J/cm^2. They found that above the laser fluence required for formation of a plasma, two shock waves travel parallel and anti-parallel to the laser beam direction. The shock traveling away from the laser quickly leaves the droplet causing a plume on the shadow side of the droplet. In the shock traveling towards the laser, the density and temperature of the material grows rapidly, and behind this rapidly moving shock the pressure decreases rapidly and catastrophic condensation occurs. Similar to the experiments reported by *Carls et al.*, in 1988 [157,158].

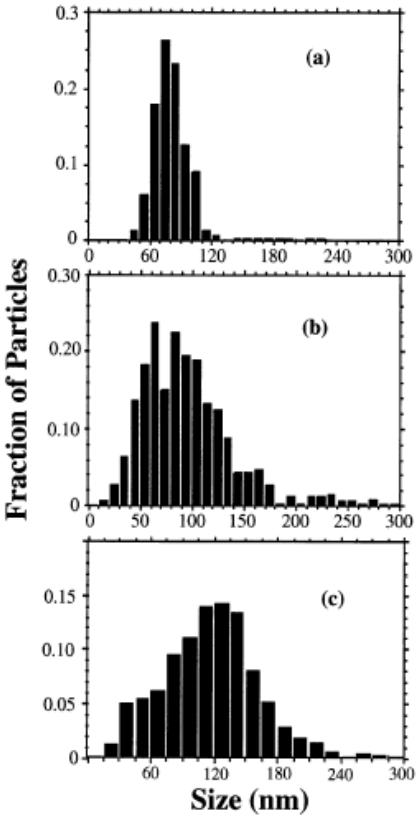

Figure 3- 2 Histograms for collected nano-particles generated by LAM on a plate in air for gold particles irradiated by 249 nm laser at fluence (a) 3.1 J J/cm^2, (b) 6.2 J/cm^2 and (c) 10.0 J/cm^2. [157]

Above on figure 3-2, is the graph of nanoparticles distribution generated by various level of laser fluence. It can be seen that the higher the laser flunce, the greater will be the average nanoparticles diameter. *Cai et al.* further explained that with higher laser fluence, the plasma forms at a much earlier time in the laser pulse, and therefore, it absorbed more laser energy to raise the density, temperature, and pressure. With more nanoparticles expected to be formed behind this stronger shock wave. *Cai et al.* further proposed that the limiting factors controlling the production rates for the laser ablation process is by knowing the mass of material ablated.

3.1.2 Pressure

During the process of nanoparticles formation from monomers, the monomers suspended in the aerosol are attracted to each other and integrate into nanoparticles. For the attraction to be successful and permanent, the monomers must first gain enough kinetic energy, or momentum, in order to attend an adhesion-collision between the growth nuclei and monomers. The nucleus is actually a collection or cluster of monomers. Complete description of the nucleus formation from monomers to nuclei will be explained in details later in section 3.2.2. Furthermore, the interaction between these single monomers to a cluster is further discussed in the same section. In turn, the monomers gain their kinetic energy from momentum exchange from collision with the carrier gas molecules. Thus, if the number of collisions between carrier gas molecules and monomers increases, so will the amount of kinetic energy transfer to monomer increase.

In accordance to the Ideal Gas Law, in the event of a pressure increase of the carrier gas, the number of gas molecules increases proportionally. This results in more bombardment from the gas molecules onto the monomers. These bombardments in turn increase the average momentum, and kinetic energy, of the monomers. With higher kinetic energy, more successful adhesion-collision occurs between monomers and growing cluster of monomers, known as nuclei.

The collected cluster of monomers fuses and leads to the formation of nanoparticles.

In other words, when the pressure of the carrier increases, so will the rate of nanoparticles growth rate, and so will be the number of different sizes of monomers clusters. As a result, pressure of the carrier gas has a positive effect on both the size of the nanoparticle diameter, as well as the spread distribution. This effect was represented by Nicholas *et al* [75] in figure 3-3,

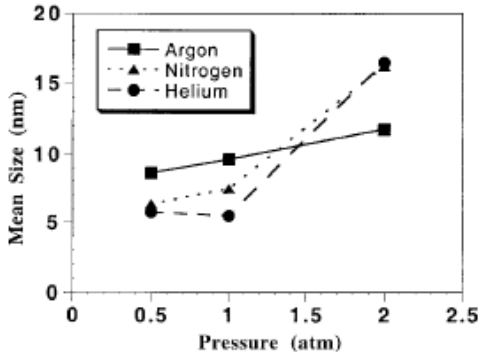

Figure 3- 3 Mean nanoparticle size versus pressure for argon, nitrogen and helium with a laser fluence of 2.4 J/cm^2. [75]

Similar results were obtained by Ozawa *et al* [129] as shown in figure 3.1. When the pressure was raised, the overall diameter becomes large. Likewise, observations were reported by Seto *et al.*[131] and shown in figure 3-4.

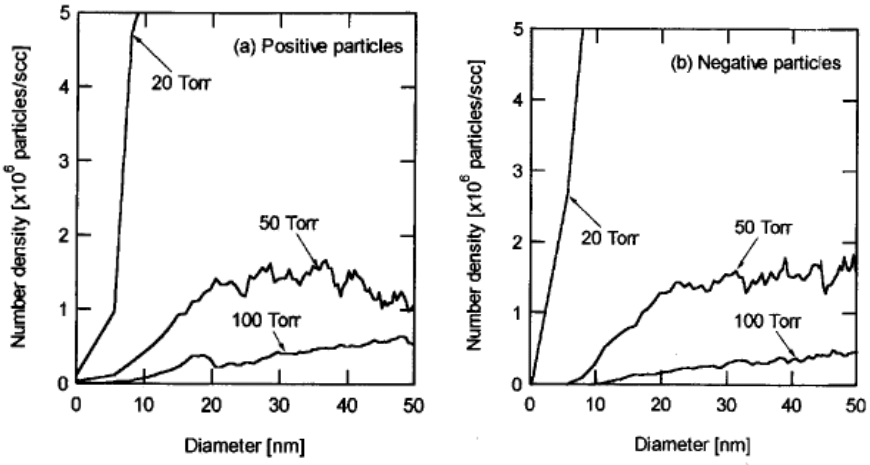

Figure 3- 4 Size distribution of generated TiO_2 nanoparticle measured by Low Pressure Differential Mobility Analyst and electrometer [131]

3.1.3 Temperature

As described by the *Maxwell-Boltzmann* probability distribution for the speed of molecules of gas, when the temperature of a system is elevated, two major changes occur to the distribution. As shown below in figure 3-5, the distribution become more evenly spread for higher temperatures, and the mean velocity increases with the temperature. During the formation of the nanoparticles, monomers are suspended in an aerosol system comprising of inert gas as the carrier. As the temperature of these gas molecules increases, so will the overall velocities of these molecules. Likewise, so will their momentum be raised .With greater momentum, more energy is transferred to the monomers each time the gas molecules interacts with the monomers. Details of the interaction will be explained further in the section 3.2.2 that follows. More monomers with higher kinetic energy will result in the formation of nanoparticles with larger diameters.

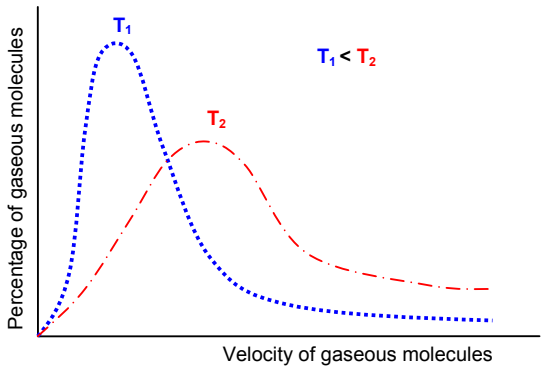

Figure 3- 5 *Maxwell-Boltzmann* probability distribution for the speed of molecules of gas with two temperature T_1 and T_2.

There have been very few publications regarding the relationship between temperature and the nanoparticle size and its distribution by the laser synthesizing method. However, reference can be drawn from other methods of nanoparticle synthesis described in the review paper by Choi [159]. In a flame reactor system, the effects of flame temperature on variations of particle size, number density, and morphology were studied. In the experiment, the flow rate of H_2 fuel was used as a means of controlling the temperature. When the flow

rate of H_2 fuel was increased so did the temperature of reactor. With a rise in temperature, primary particle diameters of the silica nanoparticles formed increased. On the other hand, if the temperature was lower, the average diameters were smaller. Also, reported by *Choi* was that nanoparticles formed was generally spherical. From this experiment, it could be derived that the temperature of the ambient has a direct positive relationship on the nanoparticle diameter formed.

3.1.4 Flow rate

Flow rate of the carrier gas in the system serves three purposes.

1. to dilute the loading, concentration count of monomers in the system,
2. to reduce the residual time of the monomers suspending in the system, and
3. to step up the rate of thermal dissipation of the aerosols.

In the event of the flow rate increasing, the probability of collision is diminished, and the mean and distribution spread of the nanoparticle diameter is accordingly lower.

It had been reported in experiments conducted by Backman *et al* [136] in 2002, that dilution of the aerosol system by increasing flow rate was able to reduce the geometric mean diameter of the nanoparticles. In their experiments, they used a tubular reactor to synthesis nanoparticles and control the flow rate by means of a mass flow controller. They explained that when the flow rate was lowered, the monomers had more time to collide and grow, resulting in larger but fewer particles.

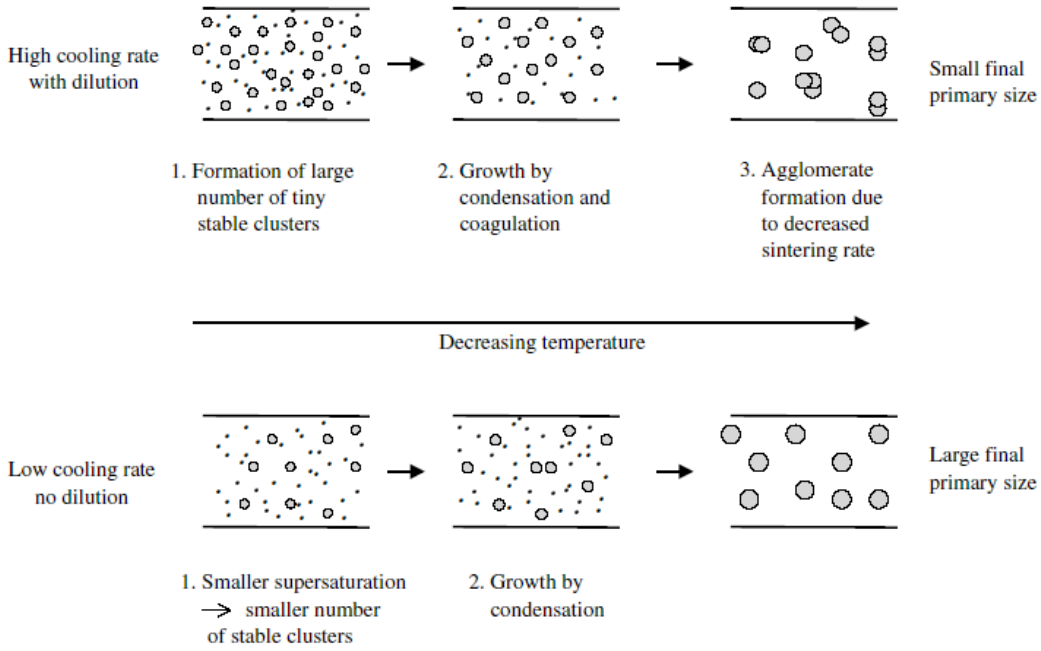

Figure 3- 6 Schematic of the nanoparticle formation.[151]

Backman *et al* presented a schematic of the nanoparticle formation shown in figure 3-6. In the first case of the experiments, where silver vapour was quenched with a higher flow rate of dilution gas, the system had a higher cooling rate. The end results achieved was an aerosol of high concentration of tiny clusters. As explained, these tiny clusters first grew mainly by process of condensation. Later when all vapour was consumed , they continued to grow by agglomeration. When the cooling by dilution is sufficient the agglomerated particles did not sinter and small nano-sized primary particles were obtained. [151]

On the other hand, in the undiluted case, the cooling rate was slow, larger and fewer primary particles are formed. The primary particles grew by a process of condensation. After which they continue to grow by condensation as long as there was vapour available. After this point, where most vapour had been exhausted, growth by agglomeration was still possible if the number concentration was high enough. However, as there is no cooling by carrier gas flow, temperature recorded was higher as compared to the diluted case and the formed agglomerates usually sintered to form spherical nanoparticles. [151]

3.1.5 Target material

Different target metals respond differently to the same laser which, in turn, determines the effectiveness of energy conversion of the laser power. The higher the effectiveness of the energy conversion, the more monomers will be generated, the higher the probability of collision, the larger the overall diameter of the nanoparticles. The effectiveness of laser energy conversion is dependent on the following:

i. the reflectance of the metal to different wavelength of laser, and
ii. the threshold fluence of the metal before any ablation could occur.

Both of the above factors are greatly influenced by the conduction electrons in the metal. These electrons absorb laser energy by a photoelectric process which takes place near the surface. The electrons behave as if they are free and that the light within the metal decays according to the formula given by the classical skin effect.[160] Details of classic skin effect will be accounted later in section 3.2. The higher the effectiveness of laser conversion, the more mass the metal will be ablated, the greater the number of monomers will be formed. With greater number of monomers suspended in the aerosols, the larger the diameter of the nanoparticle formed.

While, there has been very few publications of the direct effect of different metals on the size of nanoparticles; there have been many publications regarding the different metals and the mass ablated by femto-second laser. These reports are best represented by *Gonzales et al.* [161], *Yao et al.* [162] and *Ullmann et al.* [106]. Gonzales *et al.* examined the ablation rate of a wide range of metal across the periodic table under the same laser ablation condition. His team constructed empirical models to serve as future fabrication guidelines. *Yao et al*, studied the various mechanisms of laser material removal. *Ullmann et al.* conducted an experiment to explain that the amount of evaporated material is dependent on the amount of energy absorbed by the target, and is thus dependent on the material properties. The amount of material that

evaporates also depends on the reflectivity of the materials at the initial conditions. [106]

Laser ablation is the process of removing material from a solid surface by irradiating it with a laser beam. At low laser flux, the material is heated by the absorbed laser energy and evaporates or sublimates. At high laser flux, the material is typically converted to a plasma. Also of interest, *Ullmann et al.* further reported that another parameter that influences the amount of generated material is the enthalpy of evapouration [106]. However, this effect is only dominant for lasers with low flux. If an ultra short pulse laser, which by nature is considered to be high flux, is used instead, the influence of enthalpy of evaporation is very little. It is so because the influence is in turn affected by the thermal conductivity of the metal. As the pulse width of femto second laser is so small that it can be neglected.

3.1.6 Carrier Gas

The molecular size of the carrier gas has a significant influence on the nanoparticle diameter. The larger size molecules with bigger molecular volume boost the probability of collision between the carrier gas molecules and monomers. The larger molecules have more mass and possess higher momentum during collision. Both these factors intensify the momentum transfer to the monomers, which leads to more successful fission collisions, resulting in larger nanoparticle diameters.

This phenomena was observed by *Nichols et al*. [75] earlier. Referring to figure 3-7, when using helium as a buffer gas in their experiments, they obtained smaller nanoparticles than when using argon. They further explained that as the laser produced vapour and nanoparticles expand, they interact with the buffer gas. Helium is less effective at slowing the expansion of the vapour and the particulate cloud. When the vapour pressure was lower and nanoparticles density reduced, smaller particles were grown. On the other hand, the heavier

gas argon slows the expansion of the cloud more effective thus maintaining a higher density. Since the collision rate is larger at this higher density, particles grow to larger sizes.

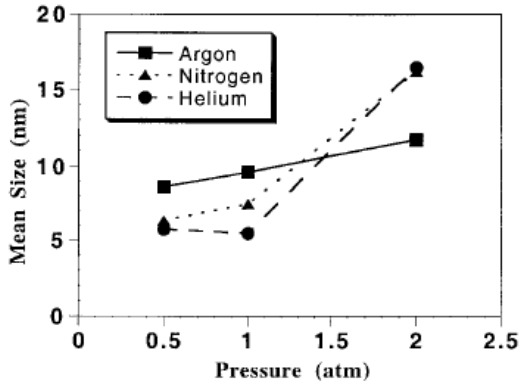

Figure 3- 7 Mean nanoparticle diameter against various pressure for argon, nitrogen and helium with a laser fluence of 2.4 J/cm^2 as reported by Nichols *et al* [75]

3.2 Development of model

As mentioned earlier, there have been many reports and papers published about the phenomena of nanoparticle synthesis utilizing femto second laser [128~131,142~150]. Though many have undertook experiments with various parameters, especially the six discussed above, very few comprehensive models have been offered to explain the phenomena. Instead, many researchers have given descriptive explanations, with little modeling discussions.[100~132] Though, some attempted to model the phenomena, they were, limited to only part of the whole process. [136,151,163,164,165,166,167]

The author will attempt here to develop a model that can explain the phenomena of how each of the discussed parameters, namely:

(i) Laser Power ,
(ii) Pressure,
(iii) Temperature,

(iv) Flow rate ,
(v) Target material , and
(vi) Carrier Gas,

will affect the mean value of the nanoparticle diameters and distribution spread of the diameters formed. Unlike most of the previous models, the author aims to develop a model, comprised of relative simple relationships between these parameters to the particle dimensions. As mentioned before in chapter 2 , most of current model and equation require at least one level of integration to obtain the particle dimensions. Also, the selected six parameters are either easily quantified with off-the-shelve instruments; or easily available in most free published data source.

The basis of the proposed model is to decompose the whole process itself, into the smallest possible entities. The basis of this approach is to identify the smallest fundamental entities of the system. The first step is to understand the behaviour of these elementary entities. Second step is to forecast how this behaviour will be affected when integrated as bulk material and thus enabling the prediction of the behaviour of material as a huge collective whole. Building on these behaviours, the sub–processes are re-constructed, and a model is built up with a bottom-up approach. With these, the author will attempt to forecast how these elementary entities integrate into larger entities, in the case of this research, the nanoparticles. In the progression of this effort, enabling the prediction of the diameters and distribution frequencies of the nanoparticles population synthesized.

3.2.1 The Process of Nanoparticle Formation

In this model, the monomer is identified as the fundamental entity. A monomer is a single molecule species. As it is single molecule, it does not possess the properties of phase and can be considered as either solid, liquid or gaseous phase.

Assumption 1

The target metal is assumed to compile closely to Drude metal model.

According to the Drude model, metal atoms have one, two or three electrons lying on the outer shell, which is relatively weakly attracted to the nucleus. [168].The atoms lose these outer shell electrons easily and results in cations and free electrons. The cations form an orderly array of lattice. The free electrons surround the lattice binding the cations together. The electro-attraction between the positive cations and negative electrons provides the binding force of the metallic material. While the rigid lattice structure gives metal its crystalline structure, the mobile electrons are responsible for ductile and malleable nature of metal and the binding force provides its tensile strength.

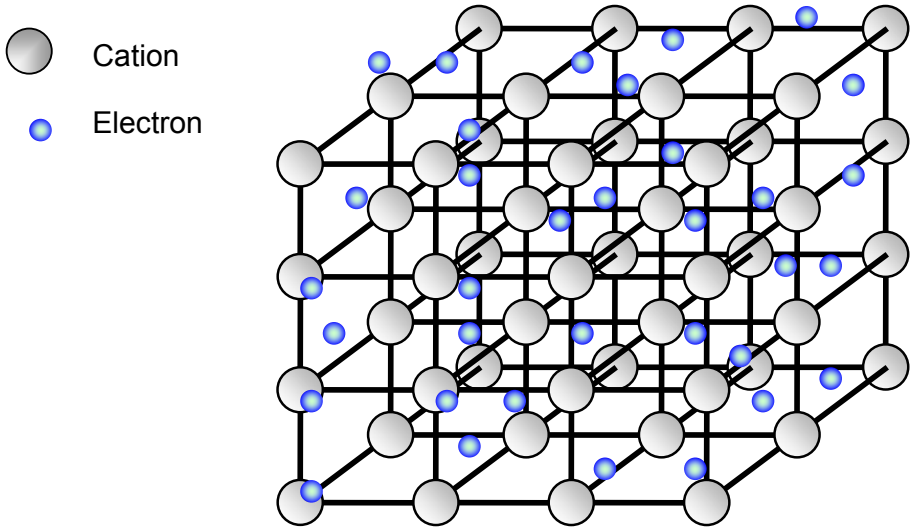

Figure 3- 8 Drude Model for Metal

Femto second laser ablation has also been the object of several theoretical investigations with different proposed model by each investigator teams. The process has been recognized as very complicated since it depends on both the processing conditions and the material properties. For a comprehensive description, one must take into account optical absorption, heat conduction,

phase transitions, evaporation kinetics, and, finally, fluid dynamics during vacuum expansion. In additional, the presence of nonlinear processes in the absorption of the laser energy and ultra-fast order-disorder transitions related to the high excitation of the electron of the metal must also be considered. The mechanism of the ablation process can be divided into four main basis of different models, namely,

(i) thermal,
(ii) thermo-mechanical,
(iii) photochemical, and
(iv) defect models.[169,170,171,172,173]

Generally, laser energy can be considered as a form of energy deposit into the metal. And the time frame of the deposition, which is the pulse width of the laser, is faster than the time metal can dissipated the energy by the classical channels of relaxation such as thermal or mechanical. As a result an overheating of the system is realized with the consequent development of critical pressure gradients. [108]

In this case of femto-second laser irradiated on metal, laser energy can cause direct bond breaking, and ejection of single atoms or molecules. The pulse durations of order of femto second are shorter than the characteristic times for electron energy loss in metals. [174] The most common utilized model is based on the assumption of two interacting systems : (i) electrons and (ii) lattice. Each system are characterized by different laser-induced initial temperatures and exchanging energy on different time scale. [175] Recent studies by *Stoian et al*. at irradiation intensities above the damage threshold have pointed out the potential of solid charging to induce an electrostatic disintegration of the surface following efficient photoelectron emission, thus occurrence of Coulomb explosion. [176] It is understood implicitly that fast thermalization within the electronic system occurs so that the two temperature model remains valid. Photons provided by the laser are necessary to overcome the potential barrier and to release the electron into the vacuum. Femto-second laser irradiation of metals is able to induce extremely high electronic temperatures, while the lattice remains cold for the time scales of interest. The time scale of interest for the considered process is less than 1 ps, so that electron-lattice relaxation may

be neglected and the lattice temperature is assumed to be constant. [177,178,179] In this specific region, rapid heating of the electronic system takes place and strong electron-lattice non-equilibrium is induced.

When a laser irradiates the surface of any solid, the laser energy may be absorbed. In metals the optical absorption is usually dominated by free carrier absorption, the electrons in the conduction band absorb photons and gain higher energy. Following absorption, the optical energy is transferred from electrons to phonons, this is when the expected lattice heating will occur. In metals the energy transfer from hot electrons to the initially cold lattice is usually described by a two-temperature model. However, the application of the two-temperature model has always been based on the assumption that the energy distributions of both electrons and phonons are thermal distributions each characterized by the electron temperature and the lattice temperature. A Fermi distribution is established in the electron system by electron–electron collisions. Yet, many models had taken the assumption that for time frame of absorption is shorter than the electronic thermalization time, electron temperature looses its meaning and the use of the two-temperature model is questionable.[180,]

The transient behavior of electrons and phonons in metals has been studied by *Rethfeld et al*. Instead, a microscopic approach was used that took into account the temporal evolution of the electron and phonon distribution functions and their changes due to laser absorption, electron– electron, and electron–phonon collisions. This approach allowed a detailed investigation of the influence of the individual collision processes even for highly non-equilibrium conditions. *Rethfeld et al*. found that for weak excitations, the energy transfer from the electrons to the lattice is delayed when the energy distribution of the laser-excited electrons is non-thermal. On the other hand, for stronger excitations, which leads to melting or ablation, thermalization occurs much more rapidly. And in these circumstances the electron–phonon coupling can properly described by the two-temperature model. [,182].

In order to remove an atom from metal by the means of a single laser pulse, one should deliver energy in excess of the binding energy of that atom. In other words, to ablate the same amount of material with a short pulse one should apply larger laser intensity approximately in inverse proportion to the pulse duration. At intensities above 10^{13} W/cm^2, ionization of practically any target material takes place early in the laser pulse time. Even for femto-second pulse to interact with a dielectric, almost full single ionization of the target occurs at the beginning of the laser pulse. Following ionization, the laser energy is absorbed by free electrons due to inverse Brehmstrahlung and resonance absorption mechanisms. More important is that it does not depend on the initial state of the target. Consequently, the interaction with both metals and dielectrics proceeds in a similar way which contrasts to the situation when a long pulse is where ablation of metals occurs at relatively low intensity compared with that for a transparent dielectric whose absorption is negligibly small. Another distinctive feature of the femto-second interaction mode is that the energy transfer time , in order of pico-seconds, from the electrons to ions by Coulomb collisions is significantly longer (picoseconds) that the laser pulse duration, in order of femto-second. Therefore, the conventional hydrodynamics motion does not occur during the femto-second interaction time. [183]

Gamaly et al. proposed in their paper that there are two forces in play for momentum transfer from the laser field and the energetic electrons to the ions in the absorption zone :

(i) firstly, due to the electric field of charge separation and

(ii) secondly ,due to the ponderomotive force.

The charge separation occurs if the energy absorbed by the electrons exceeds the *Fermi energy*. The *Fermi energy* could be estimated to be the sum of the *binding energy* and *work function*, so the electrons would have enough energy to escape from the bulk of the metal. The electric field of charge separation pulls the ions out of the metal atoms. At the same time, the ponderomotive force of the laser field in the skin layer pushes electrons deeper into the within of the lattice structure. In the same way, it builds up into the lattice structure a mechanism for ion acceleration. [95]

The proposed model by the author considers that when the laser is irradiated onto the metal target material, energy is converted to liberate the cations into numerous monomers. The laser energy is deposited onto both the cation lattice and mobile electrons, as shown in figure 3-9. The electron sub-system gained these energy and induced strong electron-lattice non-equilibrium. At this state, the electron energy level is raised to a highly excited state, enough to release itself from the matrix of bulk material, see figure 3-10. With the electron gone, positive charge cations are left behind. Concurrently, some of the excited electrons were driven deeper into the matrix of bulk material of lattice structure. This build up a zone of momentary localized of negative charge. The opposite charges repel each other and the cations are propelled off the matrix of bulk material of lattice structure as free atoms, as illustrated in figure 3-8. This phenomenon is commonly called *Coulomb Explosion.* Thus the *ablation* of the target metal. The free atoms in their very much despise and highly separated state cause the formation of the metal vapour.

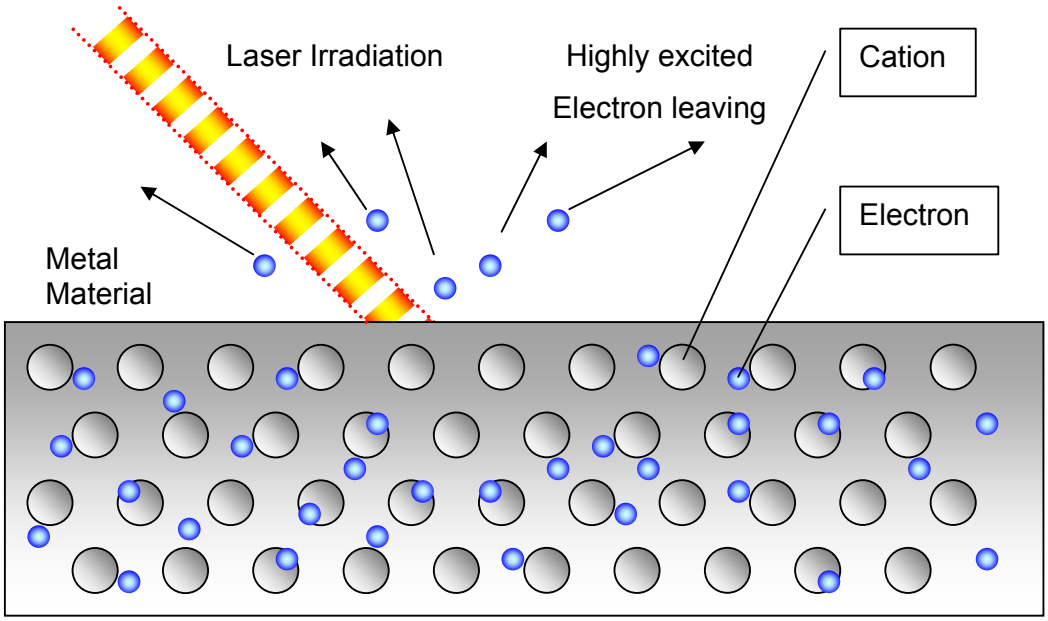

Figure 3- 9 Laser Irradiation on Metal Material

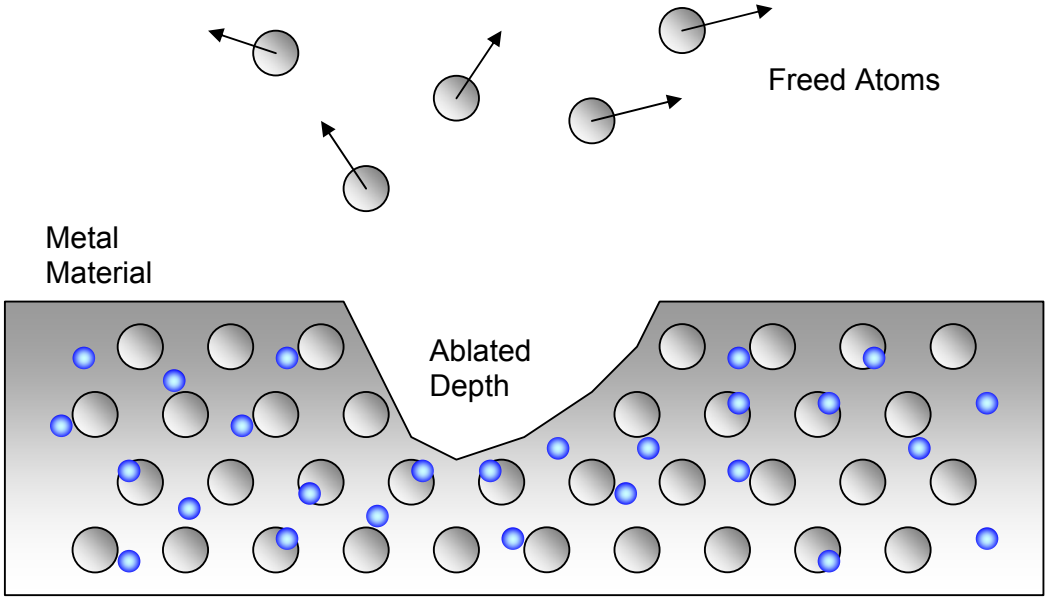

Figure 3- 10 Cations lose its binding and break away from bulk material

After ablation, the freed atoms may combine with the free electrons in the void to form back neutral charge single atom. Large populations of these atoms are formed by each single pulse, resulting in a large concentration count of atoms suspended in carrier gases. These single atoms entities are also commonly known as monomers. These single suspended atoms will be addressed as monomers hereafter. The monomers behave like an aerosol system, and they try to cluster together by Van der Waals attraction, as displayed on figure 3-11.

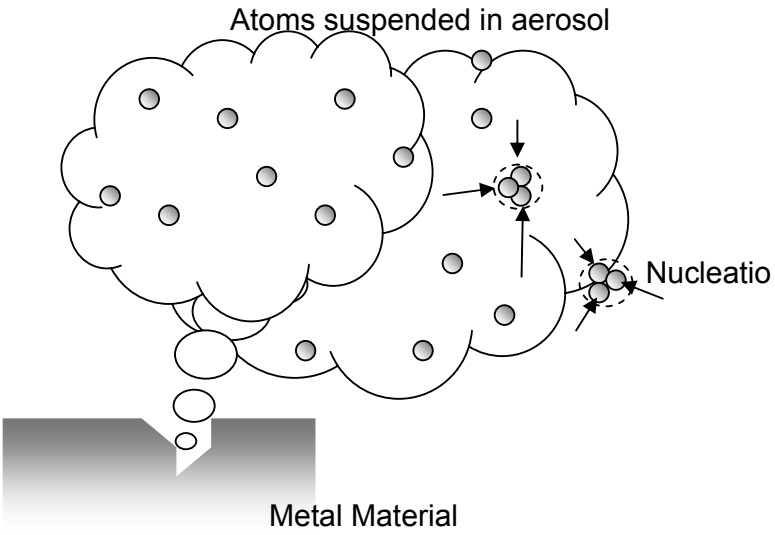

Figure 3- 11 Nucleation occurs when monomers cluster together.

In order to reach a more stable and lower energy level, these atoms attempt to cluster together to reduce their surface energy level. At any time, while one of the atoms is trying to condense itself to the cluster, there is an equal probability that another atom is trying to evaporate itself away from the cluster. The cluster has to nucleate to certain size to contain enough energy to remain stable, such that it is not able to evaporate away. The corresponding size is known as critical diameter. Once the cluster can achieve the critical diameter *nucleation* occurs.

If any cluster of smaller size, is not able to achieve the critical diameter, it will be too unstable to exits over time. Monomers will be constantly evaporating away from the cluster. In a very short period of time, only two types of entities exist in relative abundance in such aerosol system, (i) monomers and (ii) nuclei, as seen in figure 3-12 below. [184] The resulting nuclei *grow* into nanoparticles by absorbing more monomers onto themselves.

Assumption 2

The whole population of the atoms formed is assumed to stabilize into two populations. One population of the atoms that has successful achieved a critical diameter and have formed nuclei. The other population comprises of those atoms that are left behind and remain as monomers.

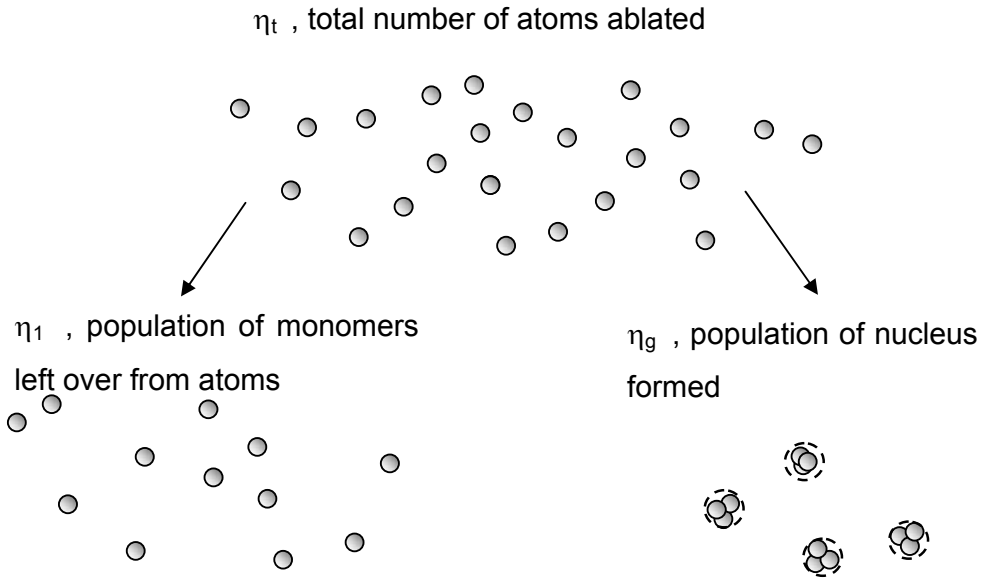

Figure 3- 12 Separation of atoms into monomers and nuclei

3.2.2 The Model

The model could be subdivided into 3 smaller segments, each segment dependent on the previous one.

- The first segment describes the process of *irradiation* of metal material. Laser energy is transferred to the solid metal, raising the metal atoms into highly excited sate, resulting in *ablation* of the solid metal into vapour.
- The second segment elucidates the *nucleation* process of the metal vapour to form stable nucleus, or *seed*, which in turn facilitate further growth of the particles. It also predicts the population of the nuclei and population of monomers.
- The third segment explain the *growth* of the nucleus as it attracts more monomers towards itself , where they adhere and fuse together into nano-scale particles.

Though, *agglomeration* of these nanoparticles is inevitable due to its miniature size, the model is limited only to the process of nucleus growth. The author did not attempt to model this process. Agglomeration is a time study process which much work has been done by aerosol scientist in the past years. [109,124,129,185,186,187]

The First Segment – Irradiation and Ablation

A large amount of work has been dedicated to the numerical study of laser material interactions. A few difference schemes have been reported in the past. The two-temperature model was first proposed by *Anisimov et al*. in 1974 [188]. *Anisimov* described the two-temperature model considers electrons and the lattice as two sub-systems. The laser energy is first absorbed by electrons and subsequently coupled to the lattice over a time period of several picoseconds. Recently, this model has been extended to compute solid-liquid and liquid-vapor phase change induced by a femto-second laser pulse. [123,189,190,191]

Generally, laser induced material removal can be broadly divided into two processes of: (i) surface evaporation and (ii) volumetric liquid-vapor phase transformation. [192]. Surface evaporation can occurs at any melted surface.

During normal pulse laser heating, however, surface evaporation normally accounts for a small fraction of the total material that is removed, since the high temperature state only lasts for a short period of time. In the case of ultra short time pulse such as nano-second second laser, the power is high and pulse is very short, the material removal mechanisms of volumetric phase transformation, also known as phase explosion pre-dominate. [193,194]. Within the ultra short time pulse and under intense energy irradiation, it is possible to raise the temperature above the boiling point of metal. Under these circumstances, both the volume and pressure of the metal increase tremendously, thus phase explosion occurs. During then the number of nucleation sites generated within the short heating duration is very few. Just prior to phase explosion, there exist a boundary of thermodynamic phase stability. The liquid is turned into a mixture of liquid and vapor through an explosive expansion. Therefore, phase explosion is often accompanied with melt expulsion. [95,195]

The physical phenomena in femto-second laser ablation, however, are much different than those in nano-second laser ablation. Due to the extremely short time frame of femto-second is much shorter than, the time required to transfer energy from the electron system to the lattice. This lead to a non-equilibrium between electrons and the lattice, resulting in electron emission. The localized high ion density results which can exceed the lattice stability limit and cause an non-thermal ablation commonly known as *Coulomb explosion.* [196,197]

It had been a common belief that because the mobility of electrons in metal is much higher than in dielectrics and semiconductors, the occurrence probability of localized high ion density is low. Thus, it was further believed that metal could rarely exceed the lattice stability limit and little Coulomb explosion happens in metal. Dielectrics and semiconductors, on the other hand, are believed to have much more significant non-thermal Coulomb explosion during

material removal, while non-thermal Coulomb explosion plays a minor role in metal. However, in 2001 *Gamaly et al.* proved otherwise in their published paper [95]. In their experiments, *Gamaly et al.* modeled a simulation of metal ablation based on electron emission, and conducted experiments to verified against their theoretical model. It was found that their model of Coulomb explosion holds for metal when the following two conditions were met :

(i) when the pulse width (pulse time frame) is very small, less than 100fs, and

(ii) the laser fluence irradiated onto the metal is close to the ablation thresholds.

A detailed understanding of the mechanism and the effects of ultra short pulse laser on metal ablation is essential to the successful implementation of laser ablation technology. The coupling of the intense electromagnetic energy of an ultra short laser pulse with metal is a very complex process. It could result in (i) melting , (ii) vaporization, (iii) ejection of electrons, atoms and ions, as well as (iv) shock wave formation and (v) plasma development [198]. To reduce the complexity of these interactions, the focuses were reduced to the final interest of outcome, the amount of the mass ablated. Following, the author offers a simplified model to explain the mechanism and the effects of ultra short pulse laser on metal ablation.

The absorption and reflection of electromagnetic energy on metal surface can be well explained by the classical Drude model [199]. The model describes metal to consist of two sub-systems, the (i) ridge cations lattice and (ii) mobile electrons. When electromagnetic energy (femto second laser in this research) is irradiated on metal, the energy is converted and diffused as heat into the metal. There exists two temperature diffusion modes: T_e (electron temperature) and T_l (lattice temperature). Note that the time scale of energy relation within the electron sub–system by electron-phonon coupling is much smaller than that for energy to transfer within the lattice sub-system [200,201]. Take, for example, the case of Copper, the electron relation time is of order 10^{-15} seconds , but the time for energy transfer for electron-phonon coupling is of order 10^{-12} seconds [155,161]. A similar finding was reported by *Tzuo* and *Pfautsch* in their recent

paper. From their calculations, it was found that phonons-electron relaxation time for metal is in the order of pico-second (10^{-12}) and electron-electron relaxation time is on the order of femto-second (10^{-15}). [202] With the use of femto-second laser, energy is only able to transfer across metal by electron temperature diffusion mode. As shown in the calculation and simulation by *Tzuo* and *Pfautsch* , the thermal relaxation by electrons could be neglected. As a result, the thermal diffusion mode within the lattice can be neglected.

In general, laser ablation keeps to a sequence of the following events:

(i) absorption of laser energy onto the target,
(ii) rapid (phase) transformation of the affected region,
(iii) ejection and separation of material from the target, and
(v) expansion of the plasma plume into the ambient.

Any electromagnetic wave in the form of a very ultra short pulse and within the range of visible light wavelength can interact effectively only with the electron subsystem of a metal. Pulse duration in the femto second range guarantees that processes number (ii) to (iv) to occur after the laser pulse is over [106]. Thermalization time of the electrons is of the order of 10^{-15} to 10^{-12} second [203]. Due to their low heat capacity, electrons can be heated to very high transient temperatures. On the other hand, the hot gas of free electrons within the lattice thermalizes in the range of 10^{-12} to 10^{-10} seconds, depending on the strength of electron - photon coupling [204]. Only after that, can any significant material removal take place. The mechanism governing the metal material removal by laser irradiation can be further divided into four types:

- direct vaporization,
- direct boiling,
- phase explosion (explosive boiling), and
- critical–point phase separation.

In this research, a femto second laser is used with the time scale of order 10^{-15}, which eliminates any possibility of time long enough for energy to be

transferred to the lattice. As a result, critical-point phase separation, an extreme form of ablation, prevails.

Critical-point phase separation

As discussed earlier, the time scale of the electron-phonon coupling is longer than the pulse width (time) of the femto second laser. The course of the phase transition should differ from the other mechanisms of (i) direct vapourisation , (ii) direct boiling, and (iii) phase explosion (explosive boiling). Figure 3-13 below shows a temperature-density phase diagram of a typical metal.

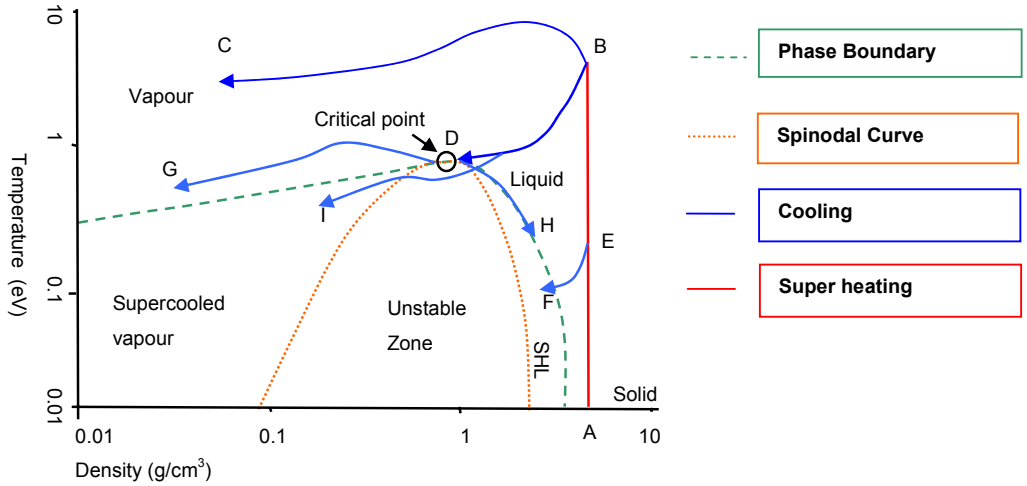

Figure 3- 13 Temperature-density phase diagram typical for metals. [204]

Several possible courses of the phase transitions caused by a femto-second laser pulse (arrows) are superimposed on the figure [205]. The green dashed line is the boundary between the one-phase and two-phase zone (bimodal). Orange dotted line is the spinodal curve. Spinodal is the boundary of extreme instability. Within this zone is the superheated liquid (SHL). Both blue and red solid lines schematically represent the two possible courses of phase transition during the femto-second laser ablation.

The heating rates of critical-point phase separation are extremely high, usually up to 10^{15} K/s. It causes the metal to heat up isochorically (constant volume) into a hot, highly pressurized (several GPa), fluid state with the temperature

close to or well above the critical temperature; represented by the red vertical solid line AB in figure 3-13 above. On the surface, some of the material will have enough energy to transform into the vapour phase directly shown by blue line AC. The terrific pressure built up is responsible for the formation of the shockwave that propagates away from the surface, this in turn result in an expansion of the layer away from the target. Note that until this point of time, the ambient pressure has little influence on the processes, since it is much lower than the pressure within the hot layer. The other portions of the subsequent layer of the material undergoes expansion, which is accompanied by adiabatic (no heat gain or loss) cooling shown by blue line BD. These portions that undergo this phase transformation, which is close to the critical point, see figure 3-13, could have several optional paths to achieve a more stable lower energy state.

- they could vapourize directly shown by line DG, or
- the vapour could reach the states of a superheated liquid shown by line DH, or
- the vapour move quickly across the unstable state to achieve supercooled vapour shown by line DI, or
- the material could directly reach a state of superheated liquid shown by line EF.

Eventually, all these materials will condense and lower their temperature over time to reach the ultimate stable state of a solid phase at point A, in the form either fine powder or bulk volume.

Though plasma is expected and observed during the experiment, its behaviour will not be discussed in this thesis. The detailed account for the process of the plasma formation is not within the scope of this work. The plasma formation and behaviour had been modeled by several researchers, and it was found that the three major factors that affect the plasma are (i) laser, (ii) pressure and (iii) target metal [168~172,180~182,185,190~194]. In the model proposed by the author, these three factors are taken in account during the stages of particle formation. The main purpose of the first part of the model is to determine the amount of

material which has been ablated and dispersed in the aerosol. The final objective of the proposed model is to explain how all the former mentioned six parameters affect the formation of nanoparticles. As thus, the author chose to simplify the process of plasma in the proposed model.

If an atom is to be removed from the bulk material, by means of any laser, an amount of energy in excess of the binding energy of that atom has to be delivered to the material. The total amount of energy of any laser irradiation is the combined product of the pulse width time and amplitude of the intensity. In other words, to ablate a certain amount of metal, with femto-second pulse duration, it is expected to apply a higher laser as compare with a nano-second pulse laser. Example, consider a laser with a pulse width of 100 fs and an intensity of approximate 10^{13}~10^{14} W/cm^2. The equivalent energy can be delivered by a laser of with a pulse width of 100 ns with an intensity of 10^8~10^9 W/cm^2 .

Explained earlier, the most distinctive feature of femto-second laser is that energy transfer time from electrons to ions (electron-phonons coupling) is significantly longer than the pulse duration. Thus conventional thermo-dynamics does not occur in femto-second laser ablation. The driving force behind ablation is the electric field of charge separation. The charge separation occurs when the energy absorbed by the electrons exceeds the *Fermi energy*. *Fermi energy* is a concept from quantum physics. In the context of metal, as in this thesis, it refers to the energy level of the highest occupied quantum state of the electrons in an atom at absolute zero temperature. *Fermi energy* of metal can be approximated by the sum of the *binding energy* ε_b and *work function* ε_{esc}. The electron *binding energy* ε_b is the measure of energy required to free an electron from their atomic orbits. The *work function* ε_{esc} is the minimum energy needed to remove an electron from an atom to a point outside the surface of the atom, such that the electron is no longer under the influence of the attraction force imposed by the atom. When the laser “deposit” sufficient energy onto the metal, the electrons could gain enough energy, exceeding the *Fermi energy* , to escape form the metal target. This results in formation of positive

cations. Simultaneously, electro-magnetic field from the subsequence laser pluses force some of the free electrons further deeper into the lattice structure, creating a partial negative charge zone. The electric field of charge separation is responsible for the pulling the ions out of the metal.

A rather simple and straightforward analytical set of explicit formulas can describe the ultra short pulse mode of laser-matter interaction. The main features of these formulas were developed more than 10 years ago *by Luther-Davies et al* [206]. These formulas, however, could work well for cases of the laser ablation at relatively moderate intensities near the ablation threshold for metals. [95]

Assumption 3

The intensity of laser irradiated on the metal target is relatively close to the threshold of the metal.

Skin Depth of Laser Penetration

When a femto-second laser is irradiated on the surface of a metal, only a very short length of the laser wavelength penetrates into the metal crystal structure. It is this short portion of the laser electron-magnetic wave per laser pulse that is responsible for the ablation. Thereafter the laser electron-magnetic wave decay exponentially within the depth of the metal. A proven expression could be used to show this relationship [207]

$$E(x) = E(0)\ \exp[-\frac{x}{l_s}] \quad \text{for } x > 0 \qquad \textbf{Equation 3- 1}$$

$$\Rightarrow \quad l_s = \frac{c}{\omega K} \qquad \textbf{Equation 3- 2}$$

where

	$E(x)$	is the electrical field due to laser at distance x
	l_s	field penetration (or absorption) length / skin-depth
	c	speed of light
	ω	laser frequency in radians
	λ	laser wavelength
	K	imaginary part of refractive index

and Refractive index $N = n + iK \approx n(1+i)$

However, in the case of metal, refractive coefficient could be expressed as

$$n \approx K = \left(\frac{\omega_{pe}}{2\omega} \right)^{1/2}$$ **Equation 3- 3**

and that Fresnel absorption coefficient is given as

$$\mathrm{A} = 1 - \mathrm{R} \approx \frac{2}{\mathrm{n}} - \frac{1}{\mathrm{n}^2}$$ **Equation 3- 4**

Where, A absorption of laser by the metal

R reflectance of laser by the metal, A =1 - R

ω_{pe} electron plasma frequency in radians, but in this case of metal , $\omega_{pe} >> \omega$

Laser Threshold of Metal

In order for ablation to occur, atoms within the bulk material of the metal must have enough energy to overcome the *ion binding energy* of the metal. Prior to that, the atom must be able to lose its valance electron. The amount of this energy equates to the minimum energy required by an electron to escape the metal. With these, we could set an energy condition for the laser ablation threshold for metal. When the laser irradiation penetrates the skin depth at a the surface at a distance x, such that x << l_s , the minimum energy transfer to the electron, electron temperature energy T_e, must be at least equal to the sum of binding energy ε_b and work function ε_{esc} . [208]

$$T_e = \left(\varepsilon_b + \varepsilon_{esc} \right)$$ **Equation 3- 5**

Proposed by *Gamaly et al.* in 1999 [207],

$$\left(\varepsilon_b + \varepsilon_{esc} \right) = \frac{4}{3} \frac{A I_0 t_p}{l_s n_e}$$ **Equation 3- 6**

where I_0 intensity of laser

t_p time of penetration

n_e number of electrons

The threshold laser fluence F_{th} for ablation of metals could be defined by

$$F_{th} \equiv I_0 t_p \approx \frac{3}{4}(\varepsilon_b + \varepsilon_{esc})\frac{l_s n_e}{A} \qquad \textbf{Equation 3- 7}$$

Combining equation 3-7 with equation 3-6,

$$F_{th} \equiv I_0 t_p \approx \frac{3}{8}(\varepsilon_b + \varepsilon_{esc})\frac{c n_e}{\omega} \equiv \frac{3}{8}(\varepsilon_b + \varepsilon_{esc})\frac{\lambda n_e}{2\pi} \qquad \textbf{Equation 3- 8}$$

Assumption 4

It is assumed that the density of metal is relatively stable throughout the laser ablation. In other words, the number density of valance (conductivity) electrons remains constant during the whole laser – metal interaction.

Material Ablation Rate

Under femto-second laser ablation, a shallow crater of depth d_{ev} is drilled by each pulse.

Assumption 5

The laser energy is transmitted to the metal target without any energy losses other than those factor discussed in the model.

Assumption 6

All energy of laser, other than those reflected by the metal surface, is absorbed by the metal to ablate the metal.

Under energy conservation law, energy conversion occurs only at the skin depth of the metal surface, i.e $x = d_{ev}$

$$c_e(T_e) n_e \frac{\delta T_e}{\delta t} = -\frac{\delta Q}{\delta x} \qquad \textbf{Equation 3- 9}$$

Integrating, $$Q = -AI_0 \exp\left(-\frac{2x}{l_s}\right) \qquad \textbf{Equation 3- 10}$$

where Q total energy flux absorbed by the metal

c_e specific heat of the valance (conductive) of electrons

x distance from the surface of metal

From equation 3-10 , put $x = d_{ev}$, and laser irradiated fluence $F = I_0 t$

$$d_{ev} = \frac{l_s}{2} ln\left(\frac{F}{F_{th}}\right) \qquad \textbf{Equation 3- 11}$$

Thus, the amount of material ablated per pulse n_t is given by expression

$$n_t = d_{ev} \times n_a \times S_a \qquad \textbf{Equation 3- 12}$$

where n_a number of atoms per unit volume

S_a laser spot area

From this expression, the number of atoms that are evaporated by femto-second laser irradiation can be easily determined.

Furthermore, the expression indicates that the amount of atoms evaporated by the femto-second laser is several magnitudes lower than that of a normal long pulse laser. As reported by Gamaly *et al.* [209], this effect eliminates the possibility of pulse laser deposition of thin films, in the form of tiny droplets and particles deposition on the approximate surface. Rode *et al.* [210] observed the same in their experiments.

Assumption 7

All the ablated mass is considered to have been transformed into vapour mass without loss by near deposition on the target surface.

The Second Segment – Nucleation

Saturation Ratio

After the ablation, the metal atoms are liberated into aerosol suspension of free atoms disperse in the carrier gas. These atoms will gain or lose kinetic energy from collisions between themselves and the carrier gas atoms / molecules. The

flow of the carrier is directed perpendicular to the direction of the plasma propagation.

Assumption 8

The metal vapour atoms, which eventually become monomers, are considered to have no momentum once they are suspended into the aerosol of carrier gas.

Assumption 9

Subsequent kinetic energy process by these atoms or monomers are obtained by the Brownian Random Motion collision between them and the carrier gas atoms / molecules.

The atoms will try to cluster together to form a collective of atoms. Each time, an atom joins a collective, there is an equal probability that another atom will leave the collective. There will reach a point when the collective possesses enough energy to retain atoms from leaving. When this happens, the cluster has attained its *critical diameter*, and then after *nucleation* would occur.

The atomic volume of metal is much larger than the atomic / molecular volume of the carrier gas. *Homogeneous nucleation* is the nucleation of vapour on embryos comprised of vapour molecules only, in absence of alien objects. A nucleation process that involves only one single type of species is known as *homomolecular*. In this research, the nucleation will be classified as *homogeneous-homomolecular, self nucleation*, as it has only metal vapour atoms in the aerosol, without any foreign nuclei or surface and no other alien vapor involved. [211]

Homogeneous-homomolecular, self nucleation occurs only in a *supersaturated vapour*. *Supersaturation* is a condition whereby the partial pressure P_A exerted by the metal *A* vapour exceed its saturation vapour P_S. The degree of supersaturation at temperature *T* is given by the *saturation ratio S*:

$$S = \frac{P_A}{P_S(T)} \qquad \textbf{Equation 3- 13}$$

If S < 1, the vapour is subsaturated, the concentration of single atoms is too dilute for any nucleation to occur.

At S = 1, the vapour is saturated, the system is at equilibrium. At any instance, one atom joins the collective, and another leaves. As a result no nucleation occurs.

When S > 1, the vapour is supersaturated. There are more atoms and monomers joining the collective then leaving, nucleation prevail. [212]

An unsaturated or saturated vapour can become saturated by any one or a combination of the three following conditions:

- isothermal compression (P_A increases),
- isobaric cooling ($P_S(T)$ decreases) or
- adiabatic expansion ($P_S(T)$ decreases faster than P_A).

In the case of this research the only species of concern are the single atoms, thus,

$$S = \frac{P_1}{P_S(T)} \qquad \textbf{Equation 3- 14}$$

It is worth mentioning that all the metals in the research have boiling points much higher than the temperature of the experiments. In other words, metals exist as solid phase under normal experiment condition, thus the saturation pressure will be very low and all species achieve nucleation easily.

Assumption 10

Nucleation of the atomic vapour is by homogeneous-homomolecular, self nucleation only, in the absence of any foreign particles

Classical theory of homogeneous - homomolecular self nucleation

Next, we need to determine the minimum size of the cluster when nucleation occurs, the diameter of this stable cluster is known as the *critical diameter for nucleation.* The expression was developed by aerosol scientists more than half century ago. The *classical theory of homogeneous homomolecular self nucleation* is based on a mixture of statistical and thermodynamic arguments. It can be approached from a kinetic view point, and relies heavily on the *capillary approximation*, wherein the bulk thermodynamics properties are used for these

clusters of all sizes. The following derivations of the critical diameter has been summarized from reference books by Friedlander [182] and Fuchs [213].

In most of the experiments conducted by various researchers, the femto-second laser is irradiated onto a target enclosure in a high vacuum (low pressure) chamber. As a result of the ablation, plasma will be formed. As the chambers do not have gas flow movement, the nanoparticles were synthesized in the plasma as the plasma propagates away from the target. In this research, the author had arranged the equipment as such that the monomers will be carried away from the plasma. As such the sub-process of nucleation could only occur in another space of volume away from the plasma zone. Details of the equipment set up and gas flow arrangement are described in detail later in chapter 4, section 4.1.

The basis for the classical kinetic approach starts with the assumption that clusters are formed by stepwise addition of monomers (or vapour atoms) and evaporate by losing single monomers. The change in concentration of the individual clusters is described by a rate equation that involves forward rate constants for addition of a monomer to a cluster and reverse rate constants for evaporation of a monomer from a cluster. A set of rate equations describe the change of concentrations of clusters of different sizes as a result of gain or loss of single atoms (monomers).

Also, in the experiment arrangement for this thesis, the carrier gas flow in a direction orthangonal to the propagation of the plamsa. As the monomers are carried outwards from the target in the plasma, they will be quenched by the carrier gas. The relativity huge volume of carrier to the plasma volume would be enough to default the monomers to that temperature of the carrier gas itself. The author realized the actual heat exchange and fluid dynamics between the plasma and carrier is a complex process. In the proposed model, this sub-process will be simplified by the following assumption.

Assumption 11

The temperatures of the clusters are constant and equal to the temperature of the background gas.

Assumption 12

For the development of the rate equation for cluster, the clusters grow and shrink only by acquisition or loss of a single atom. No coincident acquisition of two or more atoms and no collisions of clusters are taken into account. Also no fission of clusters into smaller clusters or evaporation of several atoms at the same time is taken into account.

The growth and shrinking mechanisms of clusters with the notation used in this development are shown below in figure 3-14.

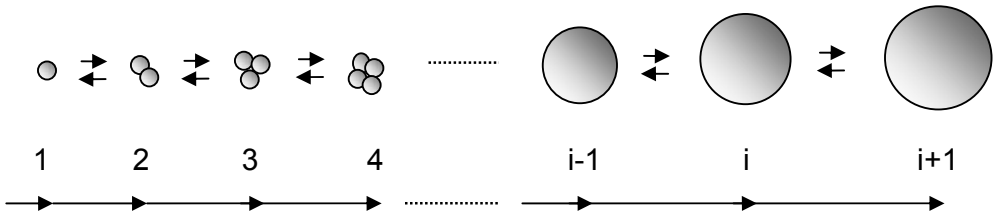

Figure 3- 14 Growth and shrinking of clusters and notation used in this text.

In order to formulate the rate equation for cluster growth and shrinking we define:

$N_i(t)$ the number concentration of clusters containing *i* atoms (*i*-mer) at time *t*

α_i the reverse rate constant for evaporation of a monomer from an *i*-mer

β_i the forward rate constant for condensation of a monomer by an *i*-mer

The rate equation describes the temporal change of the number concentration of the *i*-mers using forward and backward rate constants:

$$\frac{dN_t}{dt} = \beta_{i-1}N_{i-1}(t) - \alpha_i N_i(t) + \alpha_{i+1}N_{i+1}(t) \qquad \textbf{Equation 3- 15}$$

According to the above equation, the net rate at which clusters of size *i* grow into clusters of size *i+1* as $J_{i+1/2}$. The index *i+1/2* indicates that this rate is defined between cluster i and cluster i+1.

$$J_{i+1/2} = \beta_i N_i - \alpha_{i+1} N_{i+1} \qquad \textbf{Equation 3- 16}$$

This rate has a direction (indicated by a single arrow in figure 3-14). It is positive for net growing of clusters and is negative for net shrinking of clusters.

There is a condition by that the cluster achieves a state where the rate of monomer losses equal to that of monomer gains. At this state, the cluster is said to have achieved the critical diameter to form a stable nucleus, able for future continuous growth. To achieve the above mentioned state, a steady-state condition must be met, in which no accumulation of clusters of any cluster size, nor can any diminishing happen. So for all cluster sizes, the difference between growth out of this cluster size ($\beta_i N_i$) and evaporation into this cluster size ($\alpha_{i+1} N_{i+1}$),need to be the same.

Assumption 13

For any given monomer N_1 concentration (or saturation ratio S) it is assumed that the cluster distribution is at a steady state.

Thus the left and right hand sides of the rate equation 3-16 are both equal to zero (no net change in cluster concentration). This can only be obtained when all net fluxes between adjacent cluster sizes $J_{i+1/2}$ are equal to a single flux *J*, which is equal to the net production rate of new stable particles.

Critical diameter for nucleation

Critical diameter for nucleation is first achieved when the saturation ratio is equal to 1. At this condition, the rate of formation of N_i by condensation of the monomer on N_{i-1} is equal to the rate of loss of N_i by evaporation.

Translated into an equation, $\beta s_{i-1} n_{i-1} = \alpha_i s_i n_i$ **Equation 3- 17**

Where s_i surface area of cluster containing i atoms (i-mer)

n_i concentration of cluster containing i atoms (i-mer)

The expression for flux of condensing monomers can be obtained from the *kinetic theory of gas*.

$$\beta = \frac{p_1}{\sqrt{2\pi mkT}} \qquad \textbf{Equation 3- 18}$$

where p_1 partial pressure exert by monomer

m molecular mass (atomic mass)

k Boltzmann Constant

T temperature

A common assumption taken by aerosol science theorem is that all monomers that collide with the cluster of i-mer will adhere to it; there is no any inelastic collision.

The expression for evaporation flux can be given by the *Kelvin relationship* for the vapour pressure above a curved surface

$$\alpha_i = \frac{p_s}{\sqrt{2\pi mkT}} \exp\left[\frac{4\sigma v_m}{d kT}\right] \qquad \textbf{Equation 3- 19}$$

where p_s vapour pressure above a flat surface of liquid

σ surface tension

v_m molecular volume of liquid

substituting equation 3-18 and 3-19 into 3-17,

$$\frac{n_{i-1}}{n_i} = \frac{1}{S} \exp\left[\frac{2\sigma v_m \left(\frac{4}{3}\pi / v_m\right)^{1/3}}{i^{1/3} kT}\right] \qquad \textbf{Equation 3- 20}$$

Multiplying equation 3-20 successively for *i* to *i*=2,

$$\frac{n_1}{n_2}\frac{n_2}{n_3}\frac{n_3}{n_4}.....\frac{n_{i-2}}{n_{i-1}}\frac{n_{i-1}}{n_i}=\frac{1}{S^{i-1}}\exp\left[\frac{2\sigma v_m\left(\frac{4}{3}\pi/v_m\right)^{1/3}}{kT}\sum_{i=2}^{i}\frac{1}{i^{1/3}}\right]$$

in this case *i* is very large , i.e. $i \to \infty$

$$\sum_{i=2}^{i}\frac{1}{i^{1/3}}\approx\int_0^i\frac{dg}{i^{1/3}}=\frac{3}{2}i^{2/3}$$

Hence at the equilibrium distribution of nuclei, the expression is simplified to be,

$$\frac{n_i}{n_S}=S^i\exp\left[\frac{-3\sigma v_m\left(\frac{4}{3}\pi/v_m\right)^{1/3}i^{2/3}}{kT}\right]$$

Equation 3- 21

where $S = p_1 / p_S$

and $n_s = p_S / kT$

If the condition is unsaturated, S < 1 , n_i will be a monotonically decreasing function of *i* since the exponential always decreases with *i* . But when the condition is supersaturated, S > 1, as in the case of this research, n_i will reach a minimum value, as shown in figure 3-15 below.

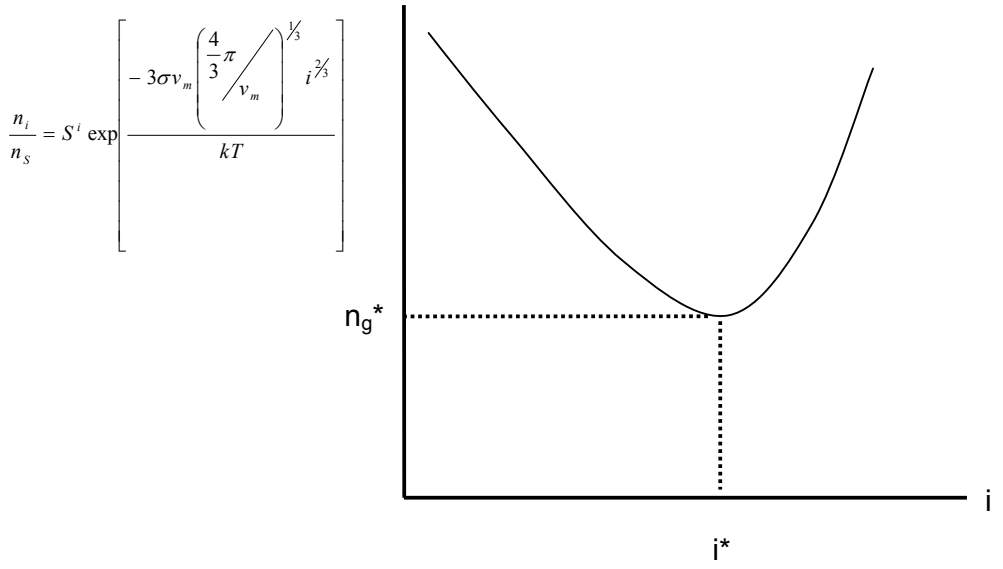

Figure 3- 15 Discrete size distribution for clusters formed by homogeneous nucleation .

When S > 1, an infinite mass of monomers must be present in aerosol at the equilibrium. Differentiating equation 3-20 with respect to *i* and setting $\frac{\delta n_i}{\delta i} = 0$, one could obtain the minimum number if *i* = *i*.* That is the smallest size a stable cluster of atoms could exist, and the corresponding diameter is the critical diameter of nucleation *d** , given by

$$d^* = 4\left[\frac{\sigma V_m}{k\,T\,ln(S)}\right]$$

However in this research,

- the volume of atom / molecule is equivalent to the volume of a monomer, $V_m = V_1$.
- Partial pressure p_1 exerted by the monomers are estimated to be in equivalent to the chamber pressure due the extremely small proportion of monomers volume as compared to that of a chamber.
- Saturation pressure p_s is taken to be equivalent to that of vapour pressure at the specific temperature.

- Surface tension is taken to be surface tension at the freezing point as the monomers are expected to solidified due to the fact that the temperature of the ambient are far below freezing point.

Thus after modification the critical diameter of nucleation *d** is altered to become

$$d^* = 4\left[\frac{\sigma V_1}{k\,T\,ln(S)}\right] \qquad \textbf{Equation 3- 22}$$

Proportional of nuclei to monomers population

By the same approach and substituting the value of equation of 3-22 into equation 3-21, we obtain the ratio of the number of nuclei to number of monomers.

$$\frac{n_c}{n_1} = exp\left[\frac{-16\,\pi\,\sigma^3\,V_1^{\,2}}{3\,(kT)^3\,(ln(S)^2)}\right] \qquad \textbf{Equation 3- 23}$$

where n_c concentration count of number of nuclei

n_1 concentration count of number of monomers

The Third Segment – Growth and Coalescence

When a laser electro magnetic wave is irradiated onto the metal surface, energy is transferred to the metal. Ablation occurs and free atoms of metal are liberated into the suspension of the carrier gas to form an aerosol system.

Assumption 14

All the vapour mass are considered to have been transformed into monomers only upon ablation, a species of entities of single atoms of the metal, without any losses by near deposition.

As discussed earlier, the aerosol monomers are allowed to nucleate to form the seeds for further nucleus growth. While some the monomers managed to cluster together to form a stable nucleus of critical diameter, majority of them remain as monomers.

Assumption 15

Only two types of the entities exist – monomers and particles with critical nucleation diameter. There exist no other clusters comprising of any other number of atoms (monomers)

Following homogenous-homo-molecules self nucleation, the seeds grow by collecting more monomers to themselves. These seeds expand by the adhesion of monomers colliding on to them.

Assumption 16

The effect of particle growth by coalescence and coagulation is much lesser than by the absorption of atomic vapour (monomer).

Assumption 17

Absorption of atomic vapour (monomer) is the only mechanism of nucleus growth.

Assumption 18

Loss of particles by deposition onto the side of chambers and channel are considered to be insignificant and neglected in the model.

Assumption 19

The monomers suspended in the aerosol possess no momentum. The monomers gain momentum from collision between the monomers and the Brownian random motion carrier gas atoms / molecule.

The momentum of the carrier gas atoms / molecules can be determined from the *Kinetic Theory of Ideal Gas*.

Assumption 20

All the assumptions as stated in the Kinetic Theory of Ideal Gas hold for this model, in which

1. *The molecules of gas are in constant random motion. They travel at high speed in straight lines unless they collide with the wall of the container or other molecules.*
2. *The molecules are separated by relatively large distances as compared to the diameter of the molecules, which is considered to be negligible.*
3. *The forces of attraction between molecules are negligible.*
4. *The temperature of molecules is a measure of the average kinetic energy of the molecules of gas.*

Momentum exchange of carrier gas atoms / molecules and monomers

Considering a monomer with initial velocity υ_1 , with molecular mass m_1 ; and a single carrier gas molecule of initial velocity υ_g , with molecular mass m_g . As the monomer molecular mass m_1 is much larger than carrier gas molecule mass m_g , the after velocity of both monomer and gas molecule will be the same υ_1' .

By conservation of momentum,

momentum before collision = momentum after collision

$$m_g v_g + m_1 v_1 = m_g v_1' + m_1 v_1'$$

$$v_g = \frac{(m_g + m_1)v_1' - m_1 v_1}{m_g} \qquad \textbf{Equation 3- 24}$$

As $m_1 >> m_g$, $(m_1 + m_g) \rightarrow m_1$,

After the first collision , $$v_g \approx \frac{(m_1)v_1' - m_1 v_1}{m_g}$$

After the second collision , $$v_g' \approx \frac{(m_1)v_1'' - m_1 v_1'}{m_g}$$

After the third collision , $$v_g'' \approx \frac{(m_1)v_1''' - m_1 v_1''}{m_g}$$

⋮ ⋮

After the k[th] collision , $$v_g^{(k)} \approx \frac{(m_1)v_1^{(k+1)} - m_1 v_1^{(k)}}{m_g}$$

Summation of all the momentum ,

$$\sum_{1}^{i=k} v_g^{(i)} = \frac{(m_1)v_1^{(k+1)} - m_1 v_1^{(0)}}{m_g} \qquad \textbf{Equation 3- 25}$$

Considering the boundary conditions,

when k = 0 , $\upsilon_1^{(0)} = \upsilon_1 = 0$

when at k+1, $\upsilon_1^{(k+1)} = \upsilon^{th}$.

where k is the number collisions, and υ^{th} is the final velocity or the threshold velocity of the monomer required for successful adhesive impact of a monomer onto a nucleus. The corresponding velocity of the gas molecules, υ_g, is determined by the *Kinetic Theory of Ideal Gas,*

$\upsilon_g = \upsilon_g' = \upsilon_g'' = \upsilon_g''' \ldots\ldots\ldots \upsilon_g^{(k-1)} = \upsilon_g^{(k)}$.

Thus, $$(k)v_g = \frac{(m_1)v_{th} - 0}{m_g}$$

$$\frac{Z}{n_1} v_g = \frac{(m_1)v_{th}}{m_g}$$

$$v_g = \frac{n_1}{Z}\frac{m_1}{m_g} v_{th} \qquad \textbf{Equation 3- 26}$$

Where, *Z* is the number of collisions between gas and monomers molecules.

The expression given by equation 3-26 describes the conversion of velocity from gas molecules to the velocity to monomers.

Collision frequency between gas and monomers molecules

Following the assumption of *Kinetic Theory of Ideal Gas*, all the molecules have point mass, and all collision between both gas and monomers molecules are perfect elastic.

The model proposed by Serway gave a good visualization for the collision.[214] If a monomer has a diameter d_1 , surrounded by a gas molecule of diameter d_g , the effective cross section for collision can be modeled by using a circle of radius d_{1g} to represent the molecule effective collision area, where $d_{1g} = \frac{d_1 + d_g}{2}$.

In time t , the circle would sweep out a volume as shown below in figure 3-16 , and the number of collisions between the monomer and gas molecule could be computed from the number of gas molecules in the volume.

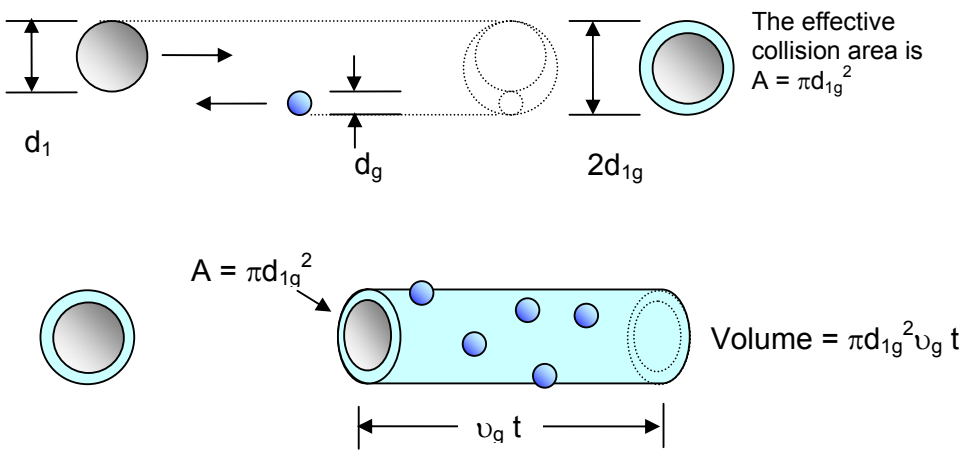

Figure 3- 16 Serway Model of Collision

As shown graphically in figure 3-16, the number of collisions between monomer and gas molecules per unit volume per second, Z'_{g1} , is given by

$$Z'_{g1} = \pi d_{g1}^{\ 2} < v_{rel} > \frac{n_g}{V}\frac{n_1}{V} \qquad \textbf{Equation 3- 27}$$

where $<\upsilon_{rel}>$ is the relative velocity of monomer and gas molecule

V volume of space where the nuclei grow

The monomers are assumed to be have zero initial momentum, and the velocity of the gas molecules υ_g is much higher than the carrier gas flow, i.e. $\upsilon_g >> \upsilon_1$. Thus, it is easy to approximate that the relative velocity between the monomer and the gas atoms / molecules to be the velocity of the gas atoms / molecules, i.e. $\langle\upsilon_{rel}\rangle \rightarrow \upsilon_g$ .It had been reported in the paper by *Ulmann et al.* [106] in 2002, the time scale for end of formation of monomer to the beginning of coalescence, which is also the time period of nucleus growth and coalescence, is in the order of 10^{-5} seconds. Following is a schematic representation of the process of the experiment conducted by *Ulmann et al.* in 2002. Reports of the similar time scale were published *Lehtien et al.* [215] in 2002 and also in 2001 [216] from a different approach to the study of collision processes.

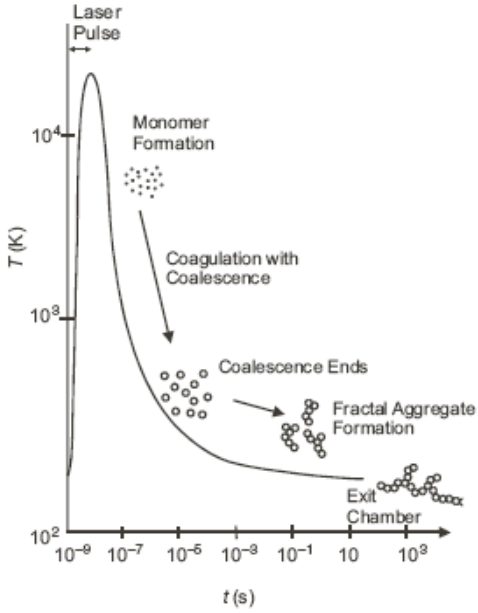

Figure 3- 17 Schematic Diagram of formation of oxide nanoparticle with graph of temperature against time [106]

Equation 3-27 could be modified to be explain the rate of collision of a single monomer Z_{g1} as

$$Z_{gl} = \pi\, d_{gl}{}^2 v'_g \frac{n_g}{V} \times 10^{-5} \quad \textbf{or} \quad \frac{Z_{gl}}{v'_g} = \pi\, d_{gl}{}^2 \frac{n_g}{V} \times 10^{-5} \qquad \textbf{Equation 3- 28}$$

where υ'_g is the modified velocity of gas atoms / molecules, which will be explained later in the chapter.

Perfect inelastic collision of monomers – adhesion

Consider two entities, one a monomer, another an n-mer. colliding together. The monomer has mass m_1 , diameter d_1 and surface energy $\pi(d_1)^2\sigma$, while the n-mer has mass m_n , diameter d_n and surface energy $\pi(d_n)^2\sigma$. Before the collision, the n-mer is relativity stationary and the monomer is traveling at a velocity υ_1, with kinetic energy $\frac{1}{2} m_1 (\upsilon_1)^2$

Total system energy before collision = kinetic energy + surface energy

$$= \frac{1}{2} m_1 (\upsilon_1)^2 - \pi(d_1)^2\sigma - \pi(d_n)^2\sigma$$

Equation 3- 29

In the case of perfect inelastic collision, the two monomers will fuse together after the collision to form an (n+1)-mer with mass m_{n+1}, diameter d_{n+1} and of velocity υ'_{n+1},

where $d_{n+1} = \sqrt[3]{(n+1)}d_1$ and $m_{n+1} = m_n + m_1$.

Total system energy after collision = kinetic energy + surface energy + heat lost

$$= \frac{1}{2} (m_{n+1})(\upsilon'_{n+1})^2 - \pi(d_{n+1})^2\sigma - \Delta h$$

Assumption 21

The thermal energy is used to convert in to bond energy of the two atoms and overcome the reduction in surface energy.

Total system energy after collision = $\frac{1}{2} (m_{n+1})(\upsilon'_{n+1})^2 - \pi(d_{n+1})^2\sigma + \varepsilon_a$

Equation 3- 30

where ε_a is the atomization energy

Assumption 22

No energy is lost or gained by the system during the collision. The momentum of the collision is conserved.

By Law of Conservation of Energy,

Total system energy after collision = Total system energy after collision

$\frac{1}{2}(m_{n+1})(\upsilon'_{n+1})^2 - \pi(d_{n+1})^2\sigma + \varepsilon_a = \frac{1}{2}m_1(\upsilon_1)^2 - \pi(d_1)^2\sigma - \pi(d_n)^2\sigma$

$\frac{1}{2}m_1(\upsilon_1)^2 = \frac{1}{2}(m_{n+1})(\upsilon'_{n+1})^2 - \pi(d_{n+1})^2\sigma + \varepsilon_a + \pi(d_1)^2\sigma + \pi(d_n)^2\sigma$

$$\tfrac{1}{2}m_1(v_1)^2 = \tfrac{1}{2}(m_1+m_n)(v'_{n+1})^2 - \pi\sqrt[3]{(n+1)^2}\,d_1^2\sigma + \varepsilon_a + 2\pi d_1^2\sigma + \pi\sqrt[3]{(n)^2}\,d_1^2\sigma$$

$$\tfrac{1}{2}m_1(v_1)^2 = \tfrac{1}{2}(m_1+m_n)(v'_{n+1})^2 + \varepsilon_a - \pi\sigma d_1^2\,[\sqrt[3]{(n+1)^2} - 1 - \sqrt[3]{(n)^2}]$$

Equation 3- 31

If velocity $\upsilon_1$is too great, the monomer will have sufficient kinetic energy to overcome the other adhesive forces to recoil away from the n-mer, and adhesion will not occur. There exists a *higher limit velocity* υ_H by which the condition of perfect inelastic adhesion collision is satisfied.

Noting that , $\frac{1}{2}(m_{n+1})(\upsilon'_{n+1})^2 \geq 0$ for all n, and $n \in \mathbf{Z^+}$

$[\sqrt[3]{(n+1)^2} - 1 - \sqrt[3]{(n)^2}] > 0$ for all n, and $n \in \mathbf{Z^+}$

$[\sqrt[3]{(n+1)^2} - 1 - \sqrt[3]{(n)^2}] > [\sqrt[3]{(n)^2} - 1 - \sqrt[3]{(n-1)^2}] > \ldots\ldots$
$\ldots\ldots > [\sqrt[3]{(3)^2} - 1 - \sqrt[3]{(2)^2}] > [\sqrt[3]{(2)^2} - 1 - \sqrt[3]{(1)^2}]$ for all n, and $n \in \mathbf{Z^+}$

To attain the higher limit of velocity υ_H, one would have to minimize the value $\frac{1}{2}(m_{n+1})(\upsilon'_{n+1})^2$, thus

- putting $\frac{1}{2}(m_{n+1})(\upsilon'_{n+1})^2 = 0$
- maximize the value of $[\sqrt[3]{(n+1)^2} - 1 - \sqrt[3]{(n)^2}]$, put $n \to \infty$
- as $n \to \infty$, $[\sqrt[3]{(n+1)^2} - 1 - \sqrt[3]{(n)^2}] \to [\sqrt[3]{(n)^2} - 1 - \sqrt[3]{(n)^2}] = -1$

from equation 3-30, $\frac{1}{2}m_1(v_H)^2 \leq \varepsilon_a - (-\pi\sigma d_1^2)$

$$v_H \leq \sqrt{\frac{2}{m_1}(\varepsilon_a + \pi\sigma d_1^2)}$$ **Equation 3- 32**

Perfect elastic collision of monomers – re-bounce

Consider the same two entities, one a monomer, another an n-mer colliding together. After the collision, the monomer and the n-mer will travel in opposite directions, the monomer with velocity υ'_1 , and the n-mer with velocity υ'_{n+1}. As no new energy will be created nor destroyed, there is no heat transfer. However, the monomer has to overcome the attraction force between itself and the n-mer.

Total system energy after collision

= kinetic energy + surface energy + attraction force

$= ½ (m_n)(\upsilon'_n)^2 + ½ (m_1)(\upsilon'_1)^2 - \pi(d_1)^2\sigma - \pi(d_n)^2\sigma + \varepsilon_a$

where ε_a atomization energy

by Law of Conservation of Energy,

Total system energy after collision = Total system energy after collision

$$½ (m_n)(\upsilon'_n)^2 + ½ (m_1)(\upsilon'_1)^2 = ½ m_1 (\upsilon_1)^2 - \pi(d_1)^2\sigma - \pi(d_n)^2\sigma - \pi(d_1)^2\sigma - \pi(d_n)^2\sigma + \varepsilon_a$$

$$½ (m_n)(\upsilon'_n)^2 + ½ (m_1)(\upsilon'_1)^2 + \varepsilon_a = ½ m_1 (\upsilon_1)^2 \qquad \textbf{Equation 3- 33}$$

As opposed to the case of adhesion impact, the collision is set for perfect re-bounce. If velocity $\upsilon_1$is too little, the monomer will not have sufficient kinetic energy to build the binding forces and it will recoil away from the n-mer. There exists a *lower limit velocity* υ_L by which the condition of perfect elastic re-bounce collision is satisfied.

Note that , $½ (m_n)(\upsilon'_n)^2 \geq 0$ for all n, and $n \in \mathbf{Z}^+$

and $½ (m_1)(\upsilon'_1)^2 \geq 0$

in the case of the lower limit of velocity υ_L , from equation3-32, $\varepsilon_a \leq ½ m_1 (\upsilon_L)^2$

$$v_L \geq \sqrt{\frac{2\varepsilon_a}{m_1}} \qquad \textbf{Equation 3- 34}$$

Combining both equations 3-32 and 3-33, the velocity of a monomer for successful adhesive impact can be determined to be within the limit of

$$\sqrt{\frac{2\varepsilon_a}{m_1}} \le v_1 \le \sqrt{\frac{2}{m_1}(\varepsilon_a + \pi\sigma d_1^2)} \qquad \textbf{Equation 3- 35}$$

As explained earlier the monomers have no momentum right after they are formed. All the momentum required for collisions are gained from carrier gas molecules impact. Knowing the frequency collision Z_{g1} and the higher limit velocity υ_H and lower limit of velocity υ_L of monomer; one could now determine the corresponding higher limit velocity υ'_{gH} and lower limit of velocity υ'_{gL} of the gas molecule,

$$v_1 = v'_g Z_{g1} \frac{m_g}{m_1} \qquad \textbf{Equation 3- 36}$$

therefore ,
$$v'_{gL} = \frac{1}{Z_{g1}}\frac{m_1}{m_g} v_L \quad \textbf{or} \quad v'_{gL} = \sqrt{\frac{v'_{gL}}{Z_{g1}}\frac{m_1}{m_g} v_L} \qquad \textbf{Equation 3- 37}$$

$$v'_{gH} = \frac{1}{Z_{g1}}\frac{m_1}{m_g} v_H \quad \textbf{or} \quad v'_{gH} = \sqrt{\frac{v'_{gH}}{Z_{g1}}\frac{m_1}{m_g} v_H} \qquad \textbf{Equation 3- 38}$$

Likewise the, the range of gas molecule velocities can be expressed by the inequality range, $\frac{1}{Z_{g1}}\frac{m_1}{m_g} v_L \le v'_g \le \frac{1}{Z_{g1}}\frac{m_1}{m_g} v_H$.

With these expressions, the distribution of monomer velocity can be reflected from the distribution of carrier gas velocity. Equation 3-34 provides a function to map the carrier gas velocity to monomer velocity. The velocity distribution of the carrier gas molecules can be easily represented by the Maxwell-Boltzmann Distribution given by the expression,

$$\frac{dN}{dv} = 4\pi\left(\frac{m_g}{2\pi kT}\right)^{3/2} v^2 \, exp\left(-\frac{mv^2}{2kT}\right) \qquad \textbf{Equation 3- 39}$$

where $N(\upsilon_g)$ number of gas molecule with velocity υ_g

υ_g velocity of gas molecule

m_g	mass of gas molecule
k	Boltzmann constant
T	absolute temperature

Assumption 23

A single monomer will have equal probability to interact with all the gas molecules. Each interaction is mutually independent and random. After each interaction, the gas molecules population will regain back the previous equivalent velocity distribution.

Growth rate of nanoparticles

The volume of a sphere V of diameter d is given by $V = \frac{\pi d^3}{6}$

$$\Rightarrow \quad \frac{\delta V}{\delta d} = \frac{\pi d^2}{2}$$

Also, the volume of a spherical nanoparticle can be expressed as follows

$$\begin{aligned} \text{volume} &= \frac{\text{mass}}{\text{density}} \\ &= \frac{\text{atomic mass}}{\text{nbr of moles}} \frac{1}{(\text{density})} \\ &= \frac{\text{number of atoms}}{\text{Avogadro number}} \frac{\text{atomic mass}}{(\text{density})} \end{aligned}$$

$$\frac{\text{volume}}{\text{number of atoms}} = \frac{1}{\text{Avogadro number}} \frac{\text{atomic mass}}{(\text{denisty})}$$

$$\Rightarrow \quad \frac{\delta V}{\delta n} = \frac{m_A}{\rho\, N_A} \qquad \textbf{Equation 3- 40}$$

The growth of the nanoparticles is by absorption of the monomers onto the nuclei. As the nuclei absorb more monomers, they grow into nanoparticles. The rate of monomers absorbed by a growing nucleus $\frac{\delta n}{\delta t}$ (into nanoparticle) is

equal to the rate of collision of monomers onto the nucleus. The total number of collisions between the nucleus and monomer Zc1 is given by

$$Z_{c1} = \langle v_{rel} \rangle \pi d^2 \frac{n_1}{V} \frac{n_c}{V}$$

$$\frac{\delta n}{\delta t} = \langle v_{rel} \rangle \pi d^2 \frac{n_1}{V} \frac{n_c}{V} \qquad \textbf{Equation 3- 41}$$

Where, Z_{c1} number of collision between monomer and nuclei per unit volume per second

υ_{rel} relative velocity of monomer and nuclei

n_c concentration count of nuclei

n_1 concentration count of monomers

V volume of growth channel

It was found that in the numerical simulation that the size of the nucleus is very close to a monomer. The values obtained from the expression in the model, equation 3-21, indicate that the size of a nucleus is close to a monomer. This comes as no surprise as the materials concerned are all metals. With their high freezing point, as compared to the ambience of the chamber, it is expected that a monomer itself could serve as a nucleus for growth.

Mathematically , $n_1 \Leftrightarrow n_c$

Assumption 24

Likewise, a nucleus (a single monomer) will have equal probability to interact with all the monomer in the growth channel. Each interaction is mutually independent and random. After each interaction, the monomer population will regain back the equivalent velocity distribution.

The model assumes there is continuous flow of monomers supplied into the growth channel. The laser is continuously irradiated onto the metal target, and the carrier gas is supplied uninterrupted. Each time a monomer is absorbed by the growing nanoparticle, it ceases to exist. For every monomer that is fused into a growing nanoparticle, it is replaced by an equivalent monomer from a continuous supply.

Assumption 25

The ratio of nuclei to monomers is so small that probability of nuclei interaction with each other is also very low. To simplify the model, the collision between growing nanoparticle is consider negligible.

The growing nanoparticle is effectively an i-mer, where i $\in$ $\mathbf{Z^+}$ and i is large. By analysis of momentum transfer in the early part, it can be determined that i-mer does not possess the necessary velocity for effective collision. Therefore, the relative velocity between the monomers and the growing nanoparticle is really the velocity of the monomer υ_1 multiple by a factor of $\sqrt{2}$.

Mathematically , $\sqrt{2}\upsilon_1 \Leftrightarrow \upsilon_{rel}$

In experiments conducted by *Ulmann et al.* in 2002 [106], and papers published by *Lehtnien et al.*[214,215], it had been indicated that process of such nanoparticle growth is in the order of 10^{-2} seconds.

Considering all the arguments above, equation 3-38 is modified to the following to reflect reality more accurately.

$$\Rightarrow \quad \frac{\delta n}{\delta t} = \sqrt{2}\nu_1 \pi d^2 \frac{1}{V}\left[(n_1)\times p(n_1)\right]^2 \times 10^{-2} \qquad \textbf{Equation 3- 42}$$

where $p(n_1)$ the probability of monomer with velocity υ_1

Integrating all the equation to obtain the growth rate equation ,

$$\frac{\delta d}{\delta t} = \frac{\delta d}{\delta V}\frac{\delta V}{\delta n}\frac{\delta n}{\delta t}$$

$$\frac{\delta d}{\delta t} = \frac{2}{\pi d^2}\frac{m_A}{\rho N_A}\sqrt{2}\nu_1 \pi d^2 \frac{1}{V}\left[(n_1)\times p(n_1)\right]^2 \times 10^{-2}$$

$$\frac{\delta d}{\delta t} = 2\sqrt{2}\frac{m_A}{\rho N_A}\frac{\nu_1}{V}\left[(n_1)\times p(n_1)\right]^2 \times 10^{-2}$$

$$\int \delta d = \int 2\sqrt{2}\frac{m_A}{\rho N_A}\frac{\nu_1}{V}\left[(n_1)\times p(n_1)\right]^2 \times 10^{-2} \ \delta t \qquad \textbf{Equation 3- 43}$$

Consider the boundary condition of the integration equation,

when t =0 , d= d* , the critical diameter of nucleation

when t = *t* , d=*d* , the final diameter of nanoparticle

$$d = 2\sqrt{2}\,\frac{m_A}{\rho\, N_A}\,\frac{v_1}{V}\left[(n_1)\times p(n_1)\right]^2\times 10^{-2}\times t + d^* \qquad \textbf{Equation 3- 44}$$

Recap of the Model

The model is divided into three segments: (i) ablation, (ii) nucleation, and (iii) growth.

In the first segment of the model explains the interaction between the laser and metal. It describes how the characteristics of the laser and properties of metal would determine the amount of metal which would be ablated into the ambience. The relation is given by

$$n_t = d_{ev}\times n_a \times S_a \qquad \textbf{Equation 3- 12}$$

where

$$d_{ev} = \frac{l_s}{2} ln\left(\frac{F}{F_{th}}\right) \qquad \textbf{Equation 3- 11}$$

The second segment is nucleation. It describes the how the metal vapour condenses into a nucleus. It is assumed that the metal vapour condenses into two types of entities. One is the nucleus, which is the seed to grow into nanoparticles in the later stage. The other is the vapour atoms that are left behind and remains as a single atom species known as monomers. Adopted from knowledge of aerosol science, an expression to determine the critical diameter for nucleation was given,

$$d^* = 4\left[\frac{\sigma\, V_1}{k\, T\, ln(S)}\right] \qquad \textbf{Equation 3-22}$$

and the ratio of the number of nuclei to number of monomers

$$\frac{n_c}{n_1} = exp\left[\frac{-16\,\pi\,\sigma^3\, V_1^{\,2}}{3\,(kT)^3\,\left(ln(S)^2\right)}\right] \qquad \textbf{Equation 3-23}$$

It is found later that the nucleus diameter is approximate to that of a monomer, and the ratio of n_c/n_1 is very low too. These imply that all the monomers found could serve as nucleus. This relates well to the real physical world, as metal has a very high melting point compared to the condition of the experiments.

The third segment of the model accounts for the growth process of the nuclei into nanoparticles. The monomers are taken to have zero inertial momentum. The nucleus grows by absorbing more monomers to itself to form a larger cluster of nanoparticle. The monomers gain their momentum from the carrier gas molecules. The energy of gas molecules are transferred to the monomers by collision. The gas molecules population are much larger than monomers, thus the numerous collision give the monomers their velocities required for collision. If the velocity is too low, an inelastic collision occurs. The monomer will not have sufficient energy to adhere itself to the cluster. Likewise, if the velocity is too high, an elastic collision occurs. The monomer will have sufficient energy to detach itself from the cluster. There exists a range of velocities for a successful adhesive impact,

$$\sqrt{\frac{2\varepsilon_a}{m_1}} \quad \leq \quad \upsilon_1 \quad \leq \quad \sqrt{\frac{2}{m_1}\left(\varepsilon_a + \pi\,\sigma\, d_1^2\right)}$$

A function is developed to map the velocity of the gas molecule to the velocity of the monomer,

$$v_1 = v'_g\, Z_{gl}\, \frac{m_g}{m_l} \qquad \textbf{Equation 3-26}$$

And the growth rate is given by

$$d = 2\sqrt{2}\,\frac{m_A}{\rho\, N_A}\,\frac{v_1}{V}\left[\left(n_1\right)\times p\left(n_1\right)\right]^2 \times 10^{-2} \times t + d^{*} \qquad \textbf{Equation3-44}$$

The distribution of the velocity of the gas molecules is given by the *Maxwell-Boltzmann Distribution*,

$$\frac{dN}{dv} = 4\,\pi\,(\frac{m_g}{2\,\pi\,kT})^{3/2}\, v^2\, exp(-\frac{mv^2}{2kT}) \qquad \textbf{Equation 3-39}$$

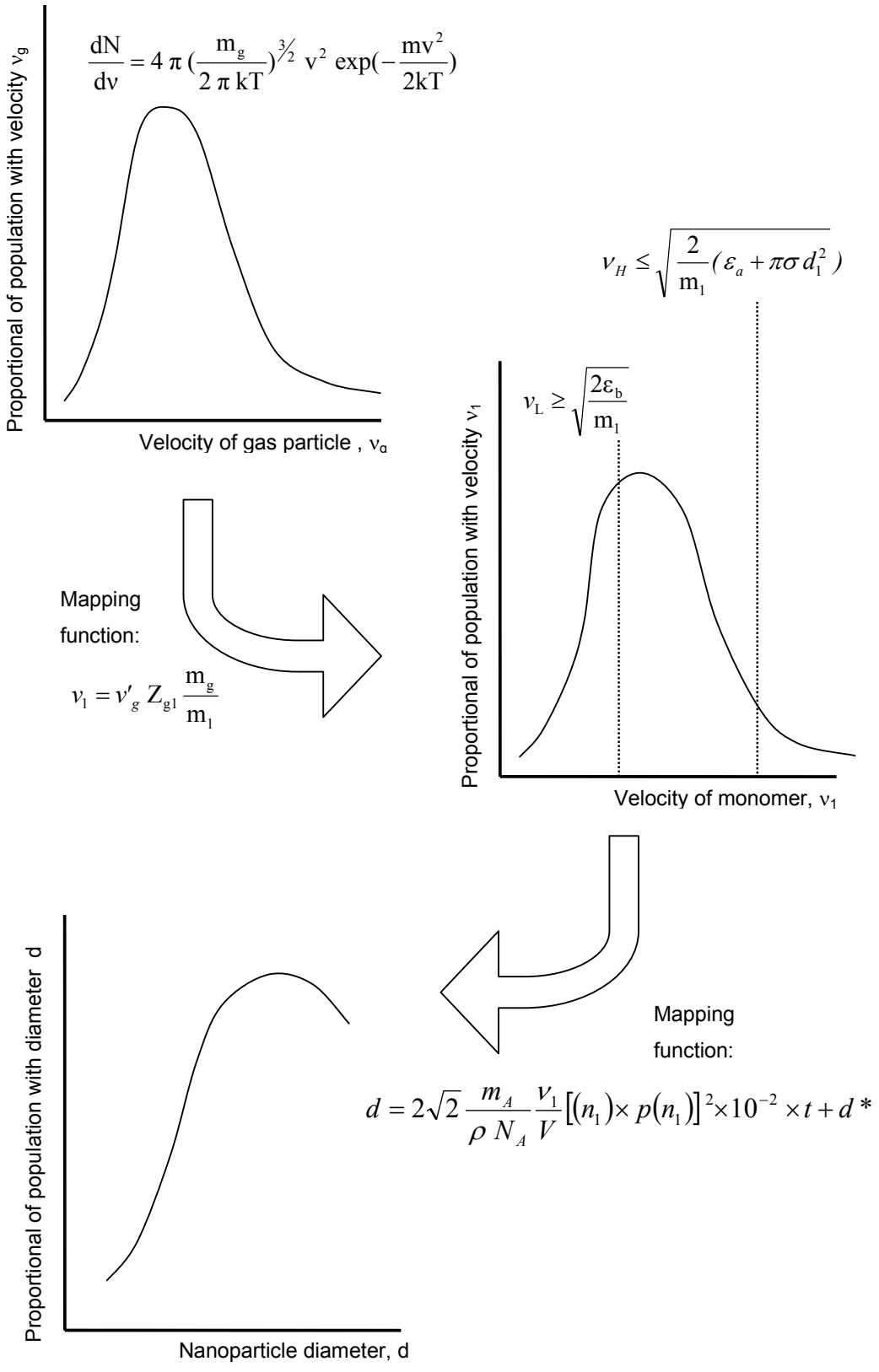

Figure 3- 18 Progress of mapping function

By mapping the distribution of the Maxwell-Boltzman Distribution, one could determine the size population distribution of the nanoparticles in the aerosol. Above in figure 3-18 is simple illustration of the process of function mapping described above.

3.3 Comparison with Contemporary Model

Currently, most of the models of nanoparticle formation are based on solving the aerosol general dynamic equation (GDE) in one-dimensional steady-state. a typical model as proposed by *Friedlander* [121] in 1977. Following which many others developed various deviations from it, such as *Pratsinis et al.* [217], , *McClurg et al.* [218], *Zhang et al.* [219] , and *Singh et al.* [220].

Below is a typical model as proposed by *Friedlander* in 1977. In his model, the GDE comprised of two main components, one to describe the mechanism of nucleation, the other explained coagulation.

The GDE for the discrete number concentration

$$\frac{dn_k}{dt} = \left(\frac{dn_k}{dt}\right)_{nucl} + \left(\frac{dn_k}{dt}\right)_{coag} \qquad \textbf{Equation 3- 45}$$

where n_k the particle number concentration for size class k

The first term $\left(\frac{dn_k}{dt}\right)_{nucl}$ at the right-hand side corresponds to particle formation due to homogeneous nucleation (formation of critical size embryo with diameter d*), the second term $\left(\frac{dn_k}{dt}\right)_{coag}$ describes the coagulation mechanism.

Homogeneous Nucleation

According to the Kelvin relation, the higher the saturation ratio, the smaller will be the diameter of the nucleus which can serve as a stable nucleus for particle

growth. When monomers begin to attach to nucleus, an non-equilibrium of the cluster distribution function exists, the difference is given by

$$I_k = n_{k-1} s_{k-1} \beta - n_k s_k \alpha_k \qquad \textbf{Equation 3- 46}$$

where β rate of nuclei pass form size k-1 to k by gaining a monomer

α_k rate of nuclei pass form size k to k-1 by loosing a monomer

I_k cluster current

Note that at equilibrium , $\beta n_{k-1} s_{k-1} = \alpha_k n_k s_k$

Substituting into equation 3-46 to eliminate α_k ,

$$I_k = n^e_{k-1} s_{k-1} \beta \left[\frac{n_{k-1}}{n^e_{k-1}} - \frac{n_k}{n^e_k} \right] \qquad \textbf{Equation 3- 47}$$

where n^e_k the particle number concentration for size class k at equilibrium

Thus the rate of change of number of clusters $\left(\frac{dn_k}{dt} \right)_{nucl}$,

$\left(\frac{dn_k}{dt} \right)_{nucl}$ = in from k-1 by gain of a monomer + in from k+1 by loss of a monomer - out from k-1 by lost of a monomer - out from k+1 by gain of a monomer

$$\left(\frac{dn_k}{dt} \right)_{nucl} = I_k - I_{k+1} \qquad \textbf{Equation 3- 48}$$

Where the value of I_k is given by ,

$$I = \frac{\beta}{\int_0^\infty \frac{dk}{nS}}$$

$$= 2 \left[\frac{p_1}{(2\pi m k T)^{1/2}} \right] \left(n_1 v_m^{2/3} \right) \left[\frac{\sigma v_m^{2/3}}{kT} \right]^{1/2} exp \left[- \frac{16 \pi \sigma^3 v_m^{\,2}}{3 (kT)^3 (\ln S)^2} \right] \qquad \textbf{Equation 3- 49}$$

Coagulation Mechanism

Particles smaller than 100 nm are believed to collide as result of Brownian motion. Consider a growing nanoparticle with diameter d_k, and another of diameter d_m. The collision frequency function $\beta(\upsilon_k,\upsilon_m)$ is obtained by

$$\beta(v_k,\upsilon_m)=2\pi(D_k+D_m)(d_k+d_m) \qquad \textbf{Equation 3- 50}$$

where D_k diffusion coefficient of cluster of size k

When the *Stokes-Einstein* relation holds for the diffusion coefficient, and that the cluster size is much smaller than the free mean path,

$$\beta(v_k,\upsilon_m)=\left(\frac{3}{4\pi}\right)^{1/6}\left(\frac{6kT}{\rho}\right)^{1/2}\left(\frac{1}{\upsilon_k}+\frac{1}{\upsilon_m}\right)^{1/2}\left(v_k^{1/3}+v_m^{1/3}\right)^2 \qquad \textbf{Equation 3- 51}$$

The rate of cluster change by coagulation is given by,

$$\left(\frac{dn_k}{dt}\right)_{coag}=\frac{1}{2}\sum_{i+j=k}\beta(v_i,v_j)n_in_j-n_k\sum_{i=1}^{\infty}\beta(v_i,v_k)n_i \qquad \textbf{Equation 3- 52}$$

The factor of ½ is added because each collision is counted twice in the summation.

Through the years more terms were added to the Equation 3-48 to improve the model to explain more different situations and to compensate for the deviation from real physical observation.

Growth Law

The model by Friedlander was expanded into more complex equations. In attempt to explain the phenomena of nanoparticle growth in aerosol, two limited conditions were imposed on to the model. It was considered that the growth rate of gas-to-particle conversion is in the case where the process of diffusion predominate, that is when particle diameter is much larger than free mean path,

$$\frac{d(vol)}{dt}=\frac{2\pi Dd_p(vol_m)(p_1-p_d)}{kT} \qquad \textbf{Equation 3- 53}$$

On the other hand, if the process of molecular bombardment is considered to be the predominate factor, that is when free mean path is much larger than particle diameter.

$$\frac{d(vol)}{dt} = \frac{\alpha \pi d_p^2 (vol_m)(p_1 - p_d)}{(2\pi m k T)^{1/2}} \qquad \textbf{Equation 3- 54}$$

where
- vol is the volume of particle
- vol_m is the volume of single molecule
- D coefficient of diffusion
- d_p diameter of particle
- p_1 partial pressure of monomer
- p_d equilibrium vapour pressure above a drop of diameter d_p
- m mass of molecule
- α the reverse rate constant for evaporation

Moment of Distribution Function

Integrating, either of the two above equations 3-53 and 5-54, with respect to time, the volume of the particle can be determined. However, this model is a time study equation, which gives the particle size over the period of fixed time. But these same expressions could be further used to estimate the distribution of the nanoparticles population. By integration of the nanoparticle size with a predetermined distribution function, we could obtain the moment of particle function. The various moments of the particle function could provide some very useful information of the particle population.

The general moment can be described by the equation,

$$M_x(r,t) = \int_0^\infty n_d d_p{}^x \, d(d_p) \qquad \textbf{Equation 3- 55}$$

where M_x is the order of moment

The ***zero moment*** , $M_0(r,t) = \int_0^\infty n_d \, d(d_p) = N_\infty(r,t)$, **Equation 3- 56**

is the total concentration of the particles in suspension in the system at given point of time t .

The *first moment*, $$M_1(r,t) = \int_0^\infty n_d d\, d(d_p)\,,$$ **Equation 3- 57**

if divided by the zero moment , will give an estimate of the average particle diameter, $$\overline{d} = \frac{\int_0^\infty n_d d\, d(d_p)}{\int_0^\infty n_d d\,(d_p)} = \frac{M_1}{M_0}$$ **Equation 3- 58**

The *second moment*, is proportional to the total surface area ΣA of all the particles, $$\pi M_2(r,t) = \pi \int_0^\infty n_d d^{\,2} d(d_p) = \sum A$$ **Equation 3- 59**

The ***third moment***, is proportional to the total volume ΣV of the all the particles,

$$\frac{\pi M_3}{6}(r,t) = \frac{\pi}{6}\int_0^\infty n_d d^{\,3} d(d_p) = \sum V$$ **Equation 3- 60**

And the average volume $\overline{V}$ of particle could be given by

$$\overline{V} = \frac{\sum V}{N_\infty} = \frac{\pi M_3}{6 M_0}$$ **Equation 3- 61**

Comparison

As shown, the contemporary models depend heavy on integration of various moments to determine many physical dimensional properties of the aerosol. These were the models developed later by researchers, with the best representation by *Pratsinis* [216],*McClurg et al*. [217] *, Zhang et al* [218], and *Singh et al* [219], were evolved from the one-dimensional aerosol general dynamic equation (GDE). Likewise, they all inherited the same problem of GDE. These models demand the perquisite knowledge of physical constant and variables such as partial pressure, diffusion coefficient at a particular temperature, equilibrium vapour pressure above a drop of diameter d_p . All of these are not

easily available in the real industrial engineering world. To compound these difficulties, equipment to perform a direct measurement and quantification of these parameters is very specialized and not readily available. Such conditions made these former models tedious to be applied to the industry.

The proposed model in this research, on the other hand, relies on physical variables such as laser power, absolute temperature, pressure of ambient, molar mass, time, and density. These variables are easily available in handbooks; and if not could be easily measured directly by different existing common equipment. A table of such equipment is listed in table 3-1. Secondly, the simulation of the contemporary model demands a great amount of computing resources to achieve the desired results. The proposed model in the research, on the other hand, had been formulated into a linear equation, in effort to achieve a effective computation. Thirdly, the parameters in the proposed model, are easily controlled by existing instruments accessible in the industry. The diameter of the nanoparticles is given by

$$d = 2\sqrt{2}\,\frac{m_A}{\rho\, N_A}\,\frac{\nu_1}{V}\left[(n_1)\times p(n_1)\right]^2\times 10^{-2}\times t + d^{*} \qquad \textbf{Equation 3-44}$$

and the distribution of the nanoparticle is obtain by mapping the *Maxwell-Boltzmann Distribution* ,

$$\frac{dN}{dv_g} = 4\,\pi\left(\frac{m_g}{2\,\pi kT}\right)^{3/2} v_g^{\,2}\; exp\left(-\frac{mv_g^{\,2}}{2kT}\right) \qquad \textbf{Equation 3-39}$$

with function, $$v_1 = v'_g\, Z_{gl}\,\frac{m_g}{m_l} \qquad \textbf{Equation 3-26}$$

where frequency of collisions is $$Z_{gl} = \pi\, d_{gl}^{\,2} v'_g\,\frac{n_g}{V}\times 10^{-5} \qquad \textbf{Equation3- 28}$$

The amount of monomers, $n_1=n_t$, in turn could be found by the relation

$$n_t = d_{ev}\times n_a \times S_a \qquad \textbf{Equation 3-12}$$

where $$d_{ev} = \frac{l_s}{2} ln\left(\frac{F}{F_{th}}\right) \qquad \textbf{Equation 3-11}$$

Below is a table of the variables called out in the model, with adjunct method and instruments of control and reading.

Table 3- 1 Variable parameters of models and their methods of control and measure.

Variable	**Quantifying / Measurement**	**Manipulate / Control**
d_{ev} , depth of ablation	(i) Determined by equation or (ii) direct measurement of AFM	Selection of metal material and laser type
F_{th} ,threshold laser fluence	Determined by equation	Selection of metal material and laser type
F , laser irradiated fluence	Power meter	Selection of laser type
n_a , number of atoms per unit volume	Determined by equation	Selection of metal material
S_a , laser spot area	Direct measurement	Optical focus setup of laser
l_s , field penetration / skin-depth	Determined by equation	Selection of metal material and laser type
n_g , number of gas molecules / atoms	Determined by equation	Selection of carrier gas , temperature, pressure,
V, volume of growth channel	Direct measurement by linear scale.	Physical size of the channel.
m_1 ,molecular mass of monomer	Available from handbook	Fixed physics constant
m_g ,molecular mass of gas	Available from handbook	Fixed physics constant
T , absolute temperature	Thermostat	Real time feedback control
K , Boltzmann Constant	Available from handbook	Fixed physics constant
t, time	Related to flow rate of carrier gas, mass flow meter	Mass flow controller
P, Pressure	Pressure gauge	Pressure valve

In recent years, several simulations had been undertaken on nanoparticles generation from laser ablation by researchers. The model commonly used was based on *molecular dynamics* combined with *direct simulation Monte Carlo* methods, acronym *MD-DSMC*. This approach is best represented by papers published by *T.E. Itina et la.*[221,222, 223], G. *Callies et al.*[224]. In their papers, the various researchers attempted to model the process of the nanocluster formation in a chamber. The chambers were either high vacuum or filled with inert gas. They used the *Zeldovich-Raizer* condensation model to help them in their simulation. However, there was little emphasis of plasma plume formation by laser ablation. The modeling of the nanocluster formation was concentrated more in the plasma plume space. The other two teams lead by both *Luk'yanchuk et al.* [225,226] and *Kuwata et la.* [227] paid more attention to the process of laser ablation in their papers. In additiona, detailed equations and numerical simulation were discussed as well.

Likewise these models described the phenomena of nanocluster formation in an enclosed chamber. On the other hand, the space of nanoparticles formation in the author's research is in a channel of steady gas flow, different from those researchers mentioned above. As a result, there is not an opportunity for a direct comparison between the model proposed by the author and those of the above mentioned researchers. Furthermore, all the *MD-DSMC* models took into consideration the time factor. The proposed model, however, describes a state of steady flow of carrier gas and therefore the time factor can be considered irrelevant.

Nevertheless, all models do share the common fundamental of using the *Zeldovich-Raizer* condensation model as a basis for nanoparticles formation. In the use of *MD-DSMC* models, on the other hand, researchers attempted to explain the relationship of one or few of the six parameters to the sizes of nanoparticles formed. The six parameters include, laser power, surrounding temperature, chamber pressure, flow rate of gas, target material and carrier gas type. The model proposed in this thesis also agreed well with each of these relationships to diameter of nanoparticle formed.

All in all, the model proposed in this research is to achieve the objective of improving computation efficiency by reducing computation steps, and converting integration equations into a linear equation. Concurrently, the author hopes to build the model to help translate scientific laboratory knowledge to easy applicable industrial technology for future uses.

3.4 Summary

The proposed model of this research was presented and discussed. Both its advantages and limitations were stated. A simple comparison of the proposed model was made with respect to several contemporary models. In the next chapter, experiments were conducted to verify the proposed model.

4. Experiments And Results

In this chapter, the equipment and experimental procedures are presented. Following, the data generated from the computer numerical simulation were documented. Results from the experiments described in the research were collected. An attempt to utilize the proposed model to account for all the observations from the experiments is made. Detailed comparisons of the two sets of data are made, and explanation of any differences is offered.

4.1 Equipment

In order to maintain a consistent sub-normal environment, a control chamber has to be employed for the process to be executed. The chamber must be able to both preserve and modify various levels of temperature, pressure, gas flow rate. The chamber is fixed with several feed-in and discharge channels to manipulate the ambience of the chamber. Figure 4-1 below, is a schematic of the setup of the equipment and instruments used in this research. The carrier gas was first pumped into an accumulator to aid in the regulation and preservation of the pressure of the carrier gas supply. In addition, the accumulator helped to buffer the large pressure variation of the gas supplied from liquid gas cylinders.

The rate of gas flow was managed by the mass flow control (2) supplied by MSK, model 1179A . The mass flow controller was linked to a MSK display console model 247. The unit is completed with a gas flow gauge (3). The reading from the gauge was looped back to the mass flow controller to provide a real time response. The mass flow controller has a self sealing function when no control signal is received from the control console. When not in use, the mass flow controllers provided a two way seal and confined the aerosol within the chamber. An electrical operated heating element (4) was coiled round the

chamber to provide heat energy to the chamber. A thermostat (5) was attached to the chamber to measure the temperature reading. The read out was responded back to a solid state reply which, in turn, controlled the current flow into the heating element. This design allowed for real-time control of temperature.

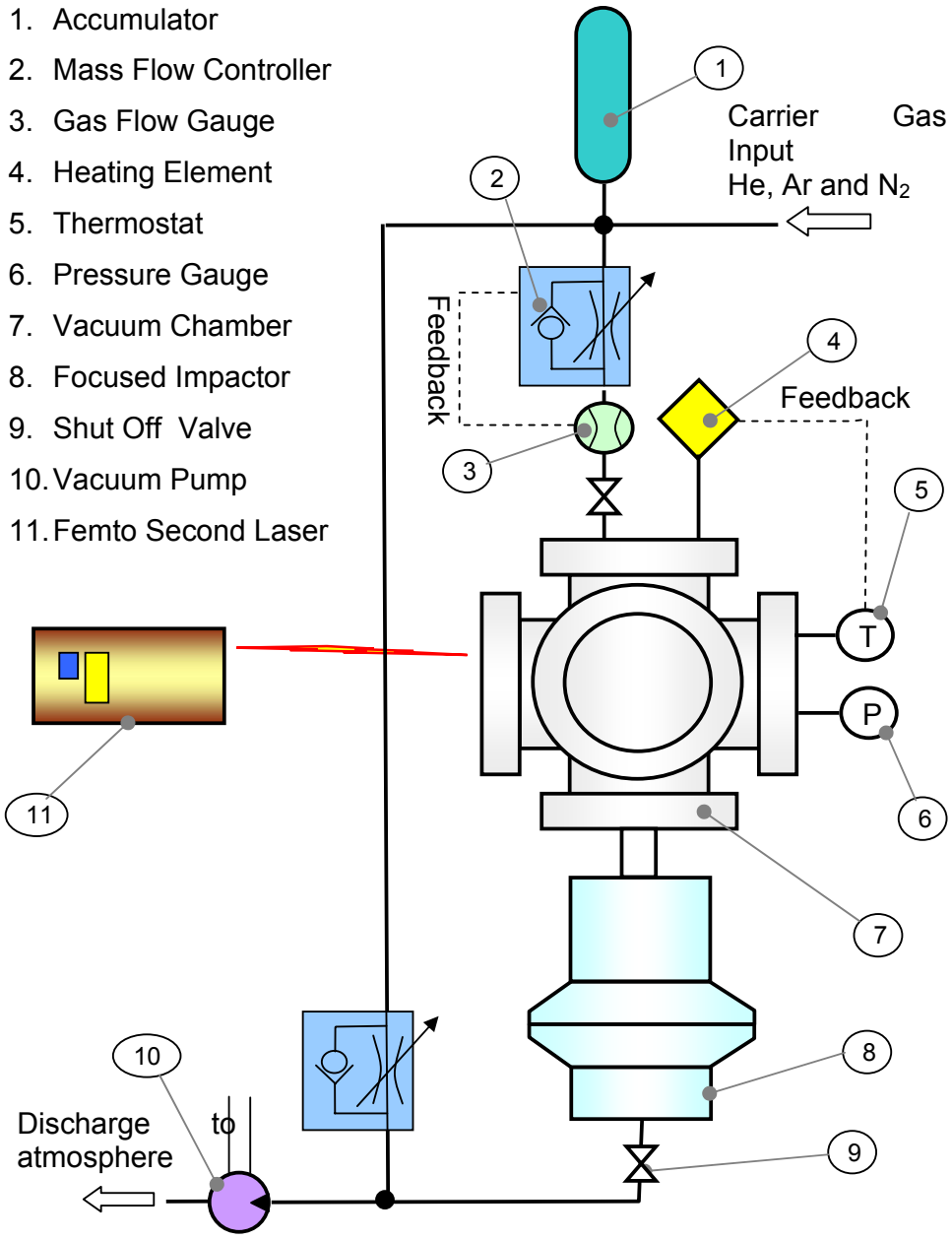

Figure 4- 1 Schematic setup of the equipment and instruments.

A pirani pressure gauge (6), manufactured by Pefiffer, model PK061705A, was used to indicate the pressure of the chamber. The pressure of the chamber was verified by counter balance check of the rate of gas inflow against the rate of gas pumped out by the vacuum pump (10), Pefiffer DU8.

The chamber itself was modified from a six-way cross head (7). The cross head was provide by MDS. Self design flanges were machined to cover five sides of the heads and one of the head was sealed with a quartz fused view port. The transparent view port provided the means for the laser to enter. The other flange cover facilitated the attachment of gauges and union bulk head for aerosol flow piping. All piping and tubing were supplied by Swagelok. The tubes were made of stainless steal and internally electroplated to give extremely smooth finishing to reduce deposition of nanoparticle on the tubing.

Figure 4-2 shows the internal of the chamber . The metal target pellets were held onto a rotating shaft. The pellets are supplied by Aexon. Five different materials of (i) Titanium, (ii) Nickel, (iii) Iron (iv) Copper and (v) Zinc, were used in the research. The pellets were all supplied as at least 99.9% pure. The femto second laser was irradiated on the pellet with beam directed horizontally. Due to geometry and position of the cylinder, the laser was effectively irradiated at an incline angle. The rotating motion ensured that the same location will not be irradiated continuously. A plume was formed as the laser irradiated on the metal. The plume contained plasma of monomers of the metal. The direction of the plume was orientated perpendicular to the direction of carrier gas flow.

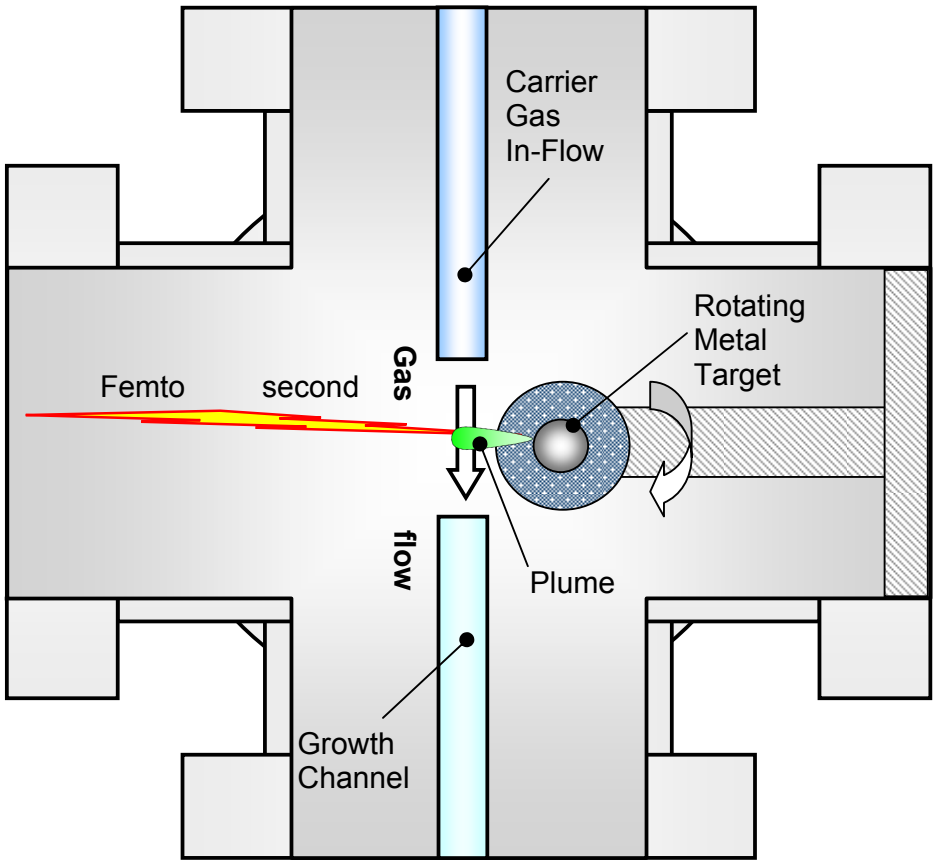

Figure 4- 2 Cross section view of the internal of the six-way cross head.

The top tubing directed the carrier gas into the chamber. The in-flowing carrier gas served two purposes; first to cool the monomers in the plumes to the ambient temperature of the chamber and secondly to carry the monomers into the growth channel. The monomers were directed in the growth channel where they coalesced into nanoparticles.

The aerosol of nanoparticles suspended in the carrier gas are fed into the *focused impactor.* A schematic diagram of the focused impactor is shown in figure 4-3 below.

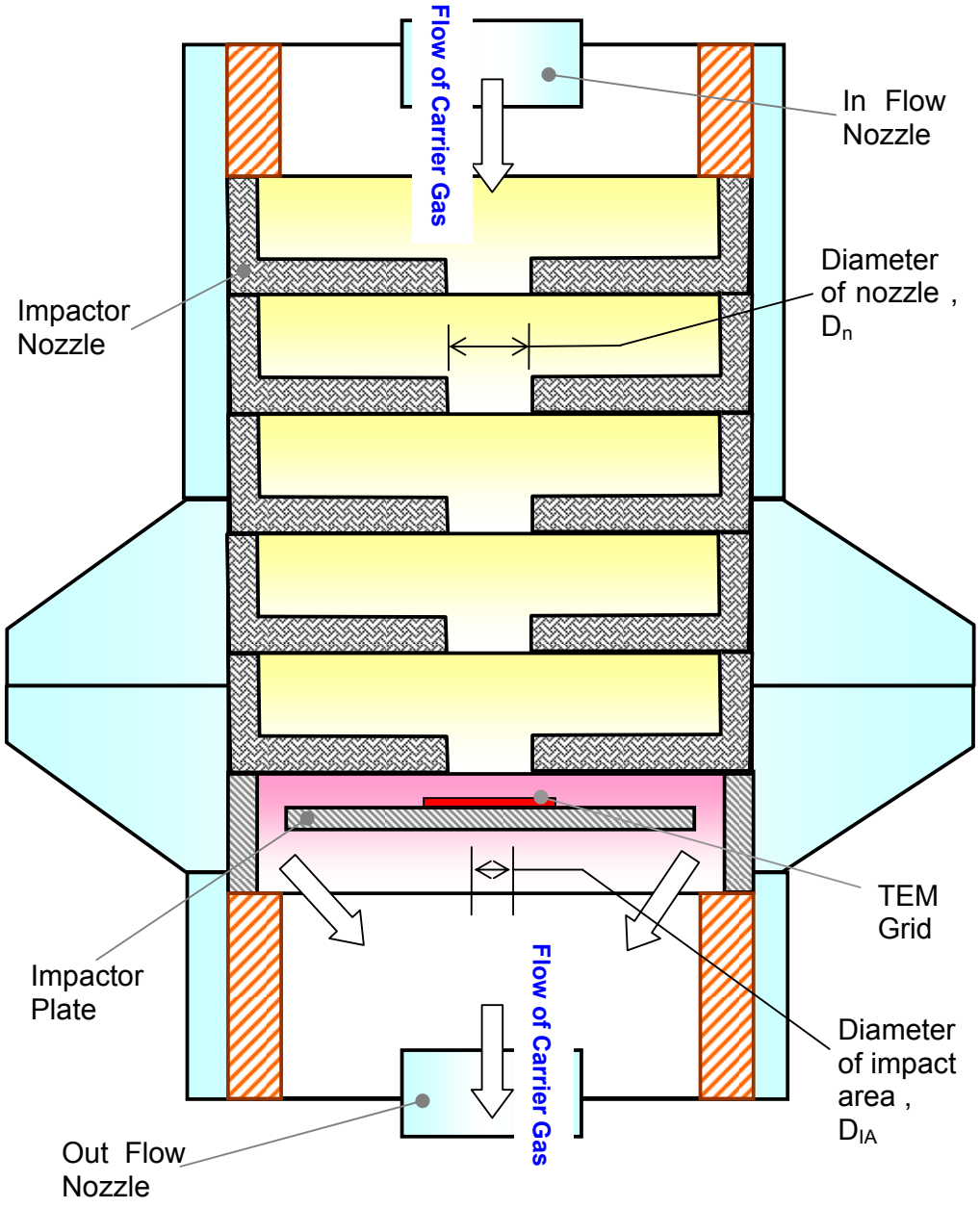

Figure 4- 3 Focused Aerosol Impactor

Unlike a common *impactor,* which has only one nozzle, the *focused impactor* has several nozzles, to help focus the stream of gas flow onto the target on the *impactor plate.* Different from the *multistage impactor*, where several sets of nozzles and impactor plates are stacked after one another, the *focus impactor* has only one impactor plate. The key feature of *focused impactor* is that the diameter of the area of impact D_{IA} is less than the area of the nozzle D_n. As

such, the nanoparticles in the aerosol could be collected on the target at minimium losses.[137,138,139] A TEM grid was used to collect the nanoparticles. The grids were supplied by Pacific Grid-Tech**.** They are pure thin carbon films coated grids. Thickness of the carbon film is about 35 nm, while the grid has 300 mesh. It has a diameter of 3.05mm and hole size of approximate 63 μm.

The exhausted carrier gas was next directed out of the impactor via the out flow nozzle. The nozzle was connected to a vacuum pump (11). The vacuum pump was responsible for creating the negative pressure point in the system, which in turn generate the low pressure and the direction of carrier gas flow. The vacuum pump is provided by Pefiffer Model 2309578. As it is driven by a single stage compressor, it has only one level of suction power. To enable various pressure levels and flow rates, another mass flow was included via a T-join. Through variation of the carrier gas in-flow, the effective displacement of the vacuum could be managed.

4.1.1 Estimate of Collection Efficiency

The tubing supplied by the Swagelok were all internally electroplated to give extremely smooth finishing to reduce deposition of nanoparticles onto the inner wall. The roughness was given as maximum of 0.25 μm. A good estimate of the percentage of nanoparticles losses due to wall deposited could be found from the calculation that follows. The zone of the inner wall with the roughness is the most likely place where the nanoparticles would be trapped during the transportation for the nanoparticles.

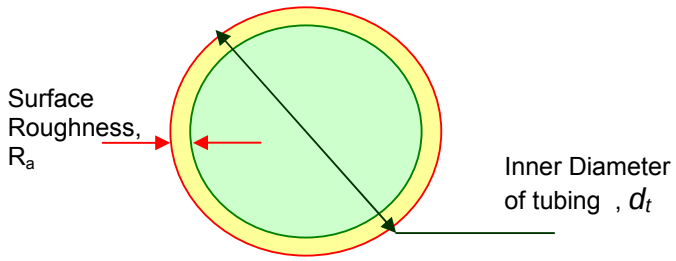

Figure 4- 4 Zone of nanoparticles deposition in inner wall of tubing.

The zone could be represented by the yellow zone show in figure 4-4 above. The effective cross-section area of the tubing that nanoparticles could be transport across free of deposition losses is represented by the green zone. The ratio of losses, *R*, could be quantified by dividing the area of yellow zone over the cross section area of inner tubing.

$$ratio\ of\ deposition\ losses = \frac{zone\ of\ rough\ surface}{cross-section\ area\ of\ inner\ tubing}$$

$$R = \frac{\pi d_t \times R_a}{\pi \frac{d_t^2}{4}} \qquad \textbf{Equation 4- 1}$$

Where d_t diameter of inner wall of tubing

R_a surface roughness of inner wall of tubing

$$R = \frac{4R_a}{d_t} = \frac{4 \times 0.25 \times 10^{-3}}{10.3} = 9.71 \times 10^{-3}\%$$

As show above estimate , the percentage is very low, thus satisfying the assumption made earlier.

The effectiveness of nanoparticles collection onto the TEM grid is very much dependent on the *Stokes Number* of carrier gas in the *focused impactor.* The higher the value of *Stokes Number*, the more effective the collection will be. As shown in figure 4-3, the *focused impactor* has several nozzles, which are in fact acting as focusing lenses to concentrate the flow of aerosol onto the TEM grid. This technique had been employed by several researchers before and its effectiveness had be quantified in the past as well. The best representative publications were by *L.Juan et al.* in 1998 [[228]] and *Liu et al.* in 1995.[[229]] . In paper by *Juan et al.*, the researchers recommended an equation to calculate the *Stokes Number* pertaining to the condition of *focused impactor.*

$$\underline{S} = 0.178 \frac{\dot{m} \rho_P d_P C_O^3}{p_0 d_n^3} \qquad \textbf{Equation 4- 2}$$

where	$\underline{S}$	Stokes Number
	$\dot{m}$	mass flow rate of carrier gas
	ρ_P	density of nanoparticles
	C_O	speed of sound
	p_0	up-stream pressure of nozzle (measured in Torr)
	d_n	diameter of nanoparticle
	d_n	diameter of nozzle
	d_c	diameter of collector (TEM grid)

Below in figure 4-5 are two graphs of *Collection Efficiency* against *Stokes Number*. The data were collected from experiments of *L.Juan et al.* In their experiments they include a repulsive voltage for other reasons not in concern in the research of this thesis. The only curves on the graph of interest will be the two with zero voltages. It had been found that as the Stokes number increase as the ratio of d_n/d_c decreases.[227] The ratio of d_n/d_c in the experiments of the thesis is 0.333. Thus from the graphs below, it can be conclude that if the Stokes number 0.12 can be attain above 0.12 , the collection efficiency achieve could be more than 90%.

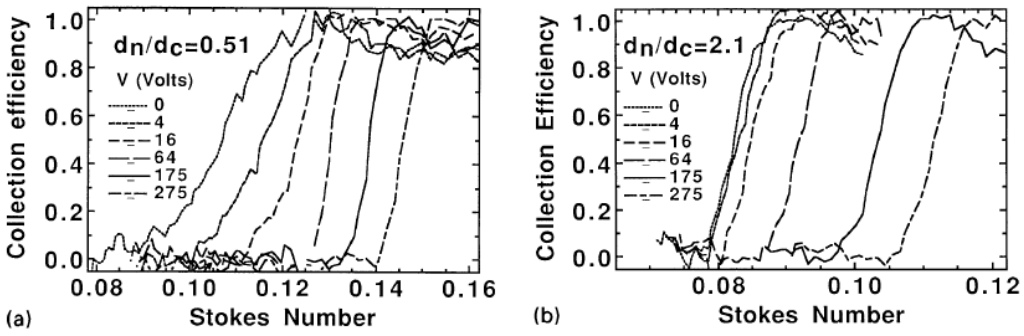

Figure 4- 5 Collection efficiency versus Stokes number curves fro nanoparticles of diameter 54 nm , (a) d_n/d_c =0.51 ; (b) d_n/d_c =2.10 . [227]

Considering all ranges of the six parameters, a table of the lowest and highest limit of the variables is shown below in table 4-1.

Table 4- 1 List of minimum and maximum values of variable terms to Stokes Number.

Symbol	Terms	units	Minimum	Maximum
$\dot{m}$	mass flow rate of carrier gas	Kg/sec	0.5953 He flowing at 0.2SLM	29.733333 Ar flowing at 1.0 SLM
ρ_P	density of nanoparticles	Kg/m^3	4500 Ti	8960 Cu
C_O	speed of sound	m/s	343 (constant)	343 (constant)
p_0	up-stream pressure of nozzle	Torr	195	390
d_n	diameter of nanoparticles	nm	1	100
d_n	diameter of nozzle	mm	1 (constant)	1 (constant)

With these values, it was found that the lowest possible value of Stokes number of the experiments in this thesis is 0.1265 and the highest possible value is 0.2831. Thus the *collection efficiency* of the *focused impactor* can be estimated to be higher than 90 %.

4.2 Procedure

Although the whole system used in the research was stationed in a class 100 clean room, extra precautions were taken to prevent alien object contamination. Before each experiment run the chamber had to be purged of impurities. The procedure described below were steps taken.

1. The intended target pellet was selected and placed onto the rotating shaft and intended carrier gas is hooked up into the system.
2. The TEM grid was placed on the impactor plate.
3. The heating element coil was turned and the chamber was maintained at 65^0C.

4. The top shut off valve was turned off and the bottom shut off valve was turned on. The chamber was evacuated of its gas contents by the vacuum pump.
5. The top shut off valve was turned on and the bottom shut off valve was turned off. The chamber was next filled with pressurized carrier gas cylinder via the accumulator.
6. Step 2 and step 3 were repeated two more cycles.

Following which, the actual experiment procedure commenced.

7. The desired flow rate was keyed into the top mass flow controller, temperature set in the thermostat, and laser power adjusted.
8. The vacuum pumped was started again with both shut off valves were turned on.
9. The desired carrier gas was introduced to the chamber at the controlled flow rate.
10. The pressure of the chamber was achieved by adjusting the bottom mass flow controller.
11. Once the chamber ambient was stabilized, the laser is irradiated onto the target for 5 minutes. The nanoparticle formed was impacted onto the TEM grid in the impactor.
12. The laser was blocked, the bottom shut off valve turned off and vacuum pump power switched off.

The last few steps were the collection of the TEM grid for measurement.

13. The top shut off valve remained opened to build up pressure in chamber until it equalized with the room pressure.

14. The TEM grid was removed from the impactor plate into a carrier container. A drop of isopropyl alcohol was placed onto the grid to minimized chemical reaction of the metal nanoparticle.

15. The TEM grid was keep in a sealed carrier before transporting to the TEM for measurement.

4.3 Metrology

The *transmission electron microscopy,* model JEM 2010 manufactured by JEOL was used to obtain images of the nanoparticle deposited on the grid. A machine vision system provided by Roper Scientific, model 780.J25HD was integrated into the TEM. The CCD camera in the machine vision system was used to acquire the images projected by the TEM. Two images were taken for each grid at two locations so as to obtain a non-biased sample presentation of the whole nanoparticle distribution population.

The software provided by the Gatan Inc, Digital MicroGraph 3.7.0, was used to analyze the images. Fifty particles in each image were isolated manually with the aid of the software to obtain their diameters. These raw data were collected for further analysis and discussion later.

The *transmission electron microscopy* (TEM) in used in the experiments is equipped with *Energy Dispersive X-ray Spectroscopy* (EDS). Each time an image was acquired, an analysis using EDS was followed. The two main aims of performing an EDS analysis were:

(i) To ensure the nanoparticles collected were still the same metal element as its target, and not other compounds of metal oxides, chloride, bromide or nitrides.

(ii) To ensure the nanoparticles being analyzed on the TEM grids were the nanoparticles intended in the experiments and not other alien objects deposited on the TEM grids.

In the figures below are some representative graphs of the EDS of the nanoparticle samples collected. One obvious common observation is that all graphs have a relative high reading of copper and carbon. This is expected as the TEM grids were made of copper and were coated with a thin film of carbon.

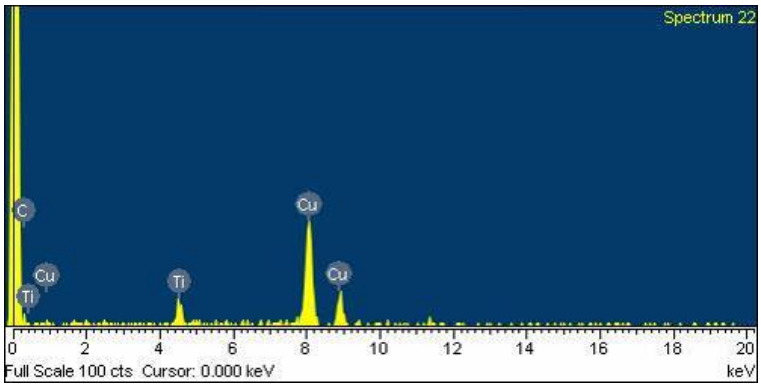

Figure 4- 6 EDS spectrum graph of Titanium nanoparticle collected on TEM grid.

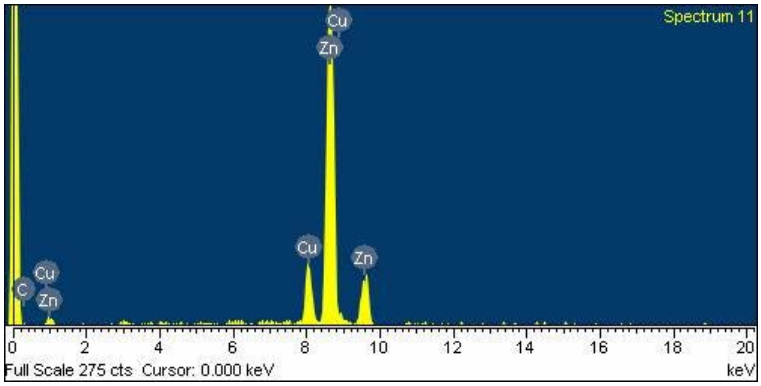

Figure 4- 7 EDS spectrum graph of Zinc nanoparticle collected on TEM grid

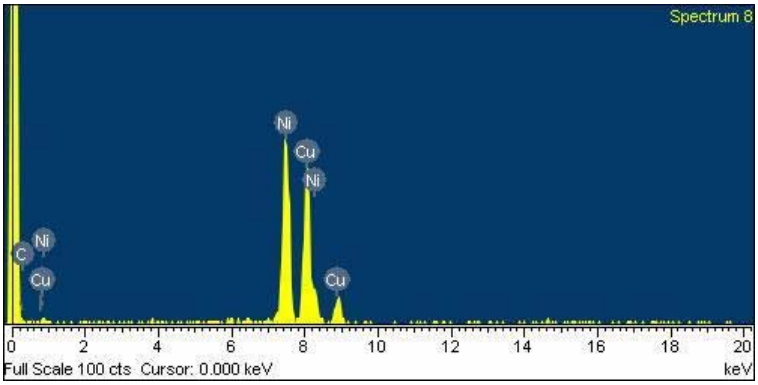

Figure 4- 8 EDS spectrum graph of Nickel nanoparticle collected on TEM grid

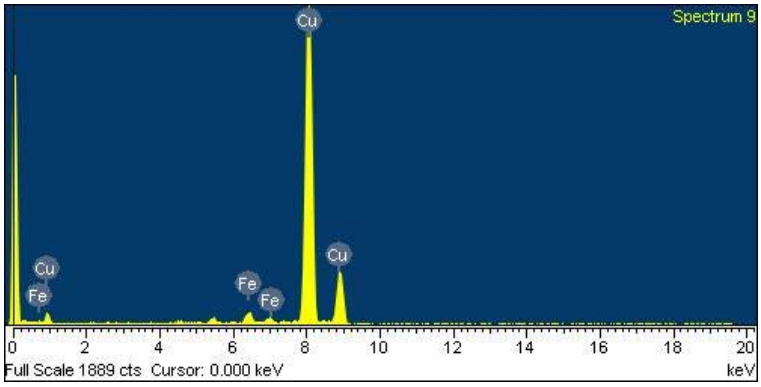

Figure 4- 9 EDS spectrum graph of Iron nanoparticle collected on TEM grid

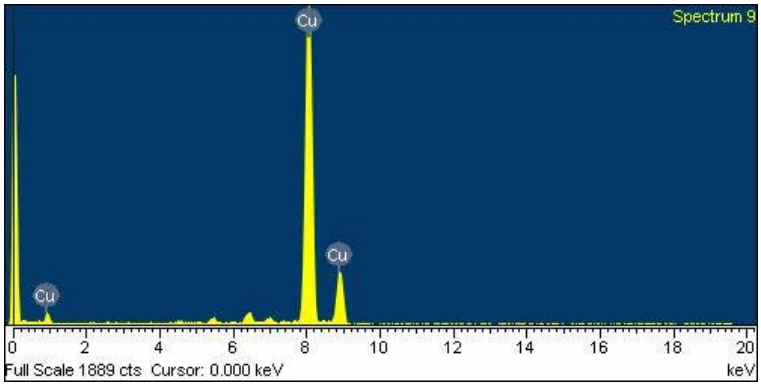

Figure 4- 10 EDS spectrum graph of Copper nanoparticle collected on TEM grid

Following are some of the images of nanoparticles on the TEM grids. In figure 4-11, the same area of imaging under went magnification at 350,000, 500,000 and 850,00 times respectively. Note that the higher the magnification, the smaller the field of view and lower the sharpness of the images. As a result, most of the images used for analysis were kept at 350,000 times magnification.

It was observed that the nanoparticles formed were all spherical. As sphere has one dimension of diameter, and will be the same no matter which orientation it is measured. Thus, measurement of the diameters from TEM images would be a reliable means of characterizing these nanoparticles.

(a)

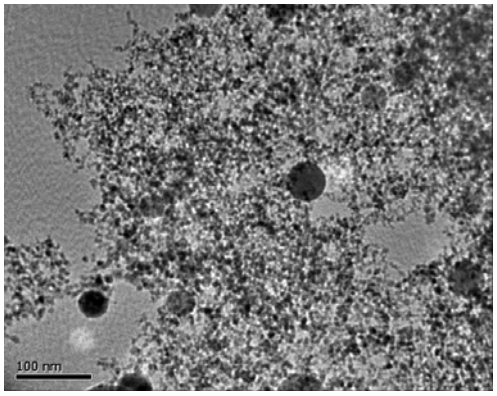

(b)

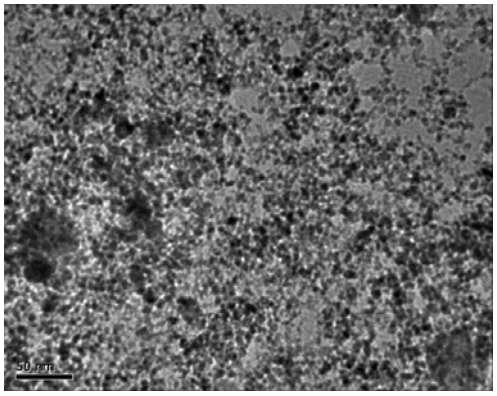

(c)

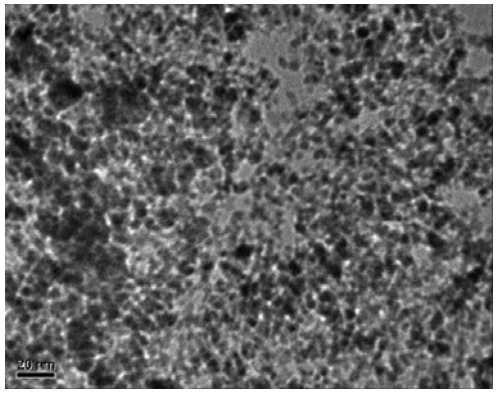

Figure 4-11 TEM images of Ti nanoparticles synthesized under pressure 26kPa, temperature 297.3K, argon flow rate 0.60SLM ,ablated by 198mW laser at (a) x350K , (b) x500K , (c) x875K magnification.

In figures 4-12 to 4-17 are samples of the images of nanoparticles synthesis under various conditions.

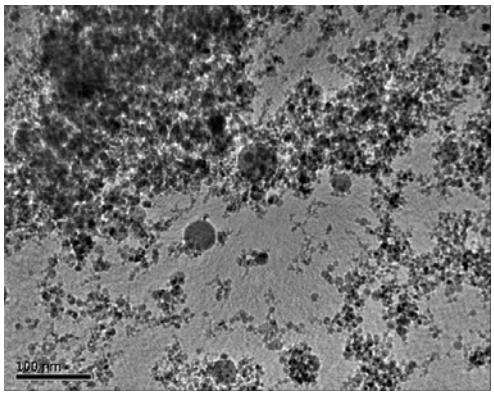

Figure 4- 12 TEM images of Ti nanoparticles synthesised under pressure 44kPa, temperature 297.3K, argon flow rate 0.60SLM, ablated by 198mW laser.

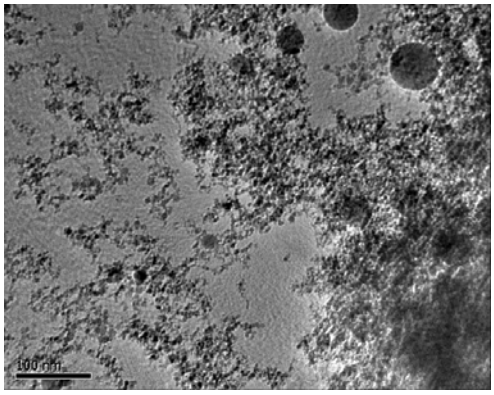

Figure 4- 13 TEM images of Ti nanoparticles synthesised under pressure 32kPa, temperature 297.3K, argon flow rate 0.60SLM, ablated by 255mW laser.

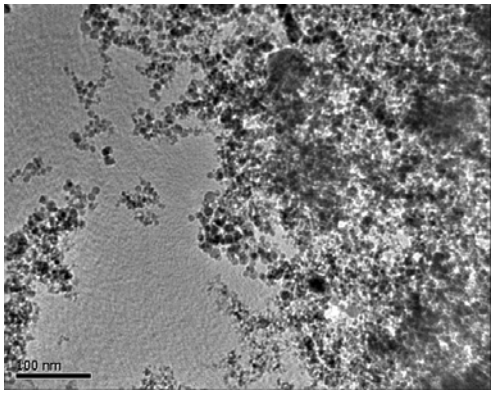

Figure 4- 14 TEM images of Ti nanoparticles synthesised under pressure 31kPa, temperature 324.3K, argon flow rate 0.60SLM, ablated by 218mW laser.

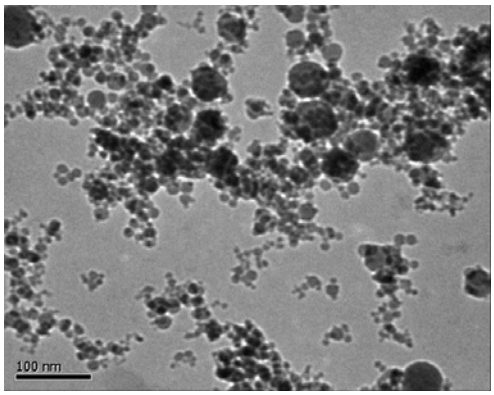

Figure 4- 15 TEM images of Zn nanoparticles synthesised under pressure 32kPa, temperature 297.3K, argon flow rate 0.60SLM, ablated by 224mW laser.

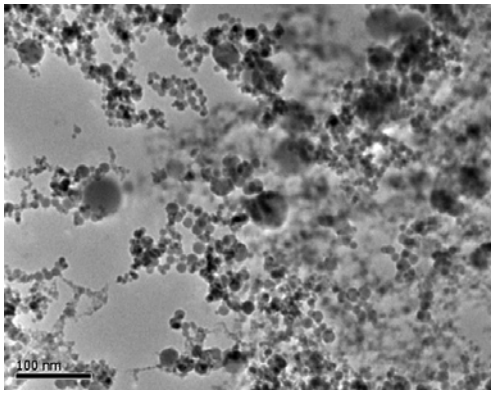

Figure 4- 16 TEM images of Ti nanoparticles synthesised under pressure 34kPa, temperature 297.3K, nitrogen flow rate 0.60SLM, ablated by 220mW laser.

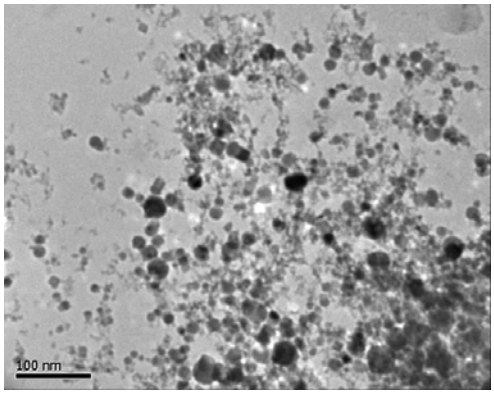

Figure 4- 17 TEM images of Ti nanoparticles synthesised under pressure 31kPa, temperature 297.3K, argon flow rate 0.80SLM, ablated by 210mW laser.

4.3 Design of Experiment

4.3.1 Physical Constants

As mentioned previously, the whole process of nanoparticle formation can be divided into three segments,

(i) Irradiation and Ablation ;

(ii) Nucleation ;

(iii) Growth and Coalescence.

and within these three segments are embedded several more sub-processes, which involve many other field of studies.

Irradiation and ablation demands the know-how of

- applied optics of laser path ,
- wave properties of laser,
- heat transfer,
- wave reflection and absorption,
- surface energy,
- Coulomb explosion .

Nucleation and rapid condensation of vapour require the understanding of

- heat transfer,
- diffusion,
- thermodynamics equilibrium,
- fluid flow control,
- nucleation,
- nucleus growth,

Consolidating all the above considerations and translated into engineering terms, the physical factors that are suspected to have an effect on the yield of the nanoparticles can be generalized into six parameters , namely :

(i) laser power of femto-second laser

(ii) temperature of ambient
(iii) pressure within the chamber
(iv) carrier gas flow rate
(v) types of metal target
(vi) types of carrier gas.

Incidentally, these six parameters are the same parameters of the proposed model.

4.3.2 Fractional Factorial Design

The six parameters can be considered as variable parameters that affects the yield condition of the nanoparticle. The yield properties can be quantified by

- mean diameter of nanoparticle,
- diameter distribution range .

The most simple and direct approach is to conduct *single variable parameter experiments* to determine which of the variable parameters are significant. Single variable parameter experiments requires one parameter to be varied while holding the others parameters constant. In the event of 5 different levels for each parameters are to conducted, the total number of runs of the whole research will be $6^5 = 7{,}776$, which is unrealistic and ineffective.

Alternative experimental approaches had to be considered. In replacement, *fractional factorial design experiment* will first be carried out. In *fractional factorial design*, a fraction of the total numbers of runs will be undertaken instead of all the 7,776 runs. To further reduce the number of runs, two parameters that were not able to be quantified were segregated from the original six. The two parameters considered were (v) types of metal target, and (vi) types of carrier gas.

As a result, only four parameters were left to conduct the *analysis of variance* (ANOVA) test.

4.3.3 Analysis of Variance (ANOVA) Test

ANOVA test was used to justifiy the significance of effects of the parameters on the formation of nanoparticles. Furthermore ANOVA test could identify if there is any correlation between these parameters. Table 4-2, shows the 16 preliminary experimental runs for the ANOVA test and in table 4-3 are the corresponding parameters and their different levels. The quantifying value for the ANOVA test was the mean diameters of the nanoparticles synthesized.

Table 4- 2 Table of different levels of the 4 parameters under ANOVA test.

Treatment	Laser Power	Temperature	Pressure	Flow Rate
1	-1	-1	-1	-1
2	-1	-1	-1	1
3	-1	-1	1	-1
4	-1	-1	1	1
5	-1	1	-1	-1
6	-1	1	-1	1
7	-1	1	1	-1
8	-1	1	1	1
9	1	-1	-1	-1
10	1	-1	-1	1
11	1	-1	1	-1
12	1	-1	1	1
13	1	1	-1	-1
14	1	1	-1	1
15	1	1	1	-1
16	1	1	1	1

Table 4- 3 The parameters and the levels of for ANOVA test.

Factors	Low (-1)	High (1)
Laser Power (mW)	143	433
Temperature (K)	297.3	336.3
Pressure (kPa)	26	52
Flow Rate (SLM)	0.3	0.8

At 10 % significant level ,the ANOVA indicated the following :

- All four parameters have significant influence on the mean diameters of the nanoparticles synthesized.
- The most significant being *Laser Power*, followed by *Pressure* , *Temperature* and *Flow Rate*.
- There exists a combined effect between *Pressure*, *Temperature* and *Flow Rate* on the mean diameter.
- *Laser Power*, on the other hand does not have any combined effect with any of the other 3 parameters.
- *Flow Rate* has a reverse effect to the mean diameter.

4.3.4 Experimental Trials

To further test the robustness, accuracy, repeatability and sensitivity of the model, additional experimental runs were designed and carried out. These results are later compared against the data from the model simulation. A direct but comprehensive matrix of experiments was designed with a total of six parameters in the model to verify. While holding all other parameters constant, one parameter will be varied to a different level. Pursuing this direction, the table below describes the design of the experiments.

Table 4- 4 Matrix of series of experiments conducted

Experiment Run Number	Temp-erature K	Pressure kPa	Flow Rate SLM	Laser Power mWatts	Target Material	Chamber Gas
1	297.3	32	0.60	143	Titanium	Argon
2	297.3	32	0.60	198	Titanium	Argon
3	297.3	32	0.60	255	Titanium	Argon
4	297.3	32	0.60	363	Titanium	Argon

Experiment Run Number	Temp-erature K	Pressure kPa	Flow Rate SLM	Laser Power mWatts	Target Material	Chamber Gas
5	297.3	32	0.60	433	Titanium	Argon
6	297.3	26	0.60	198	Titanium	Argon
7	297.3	34	0.60	198	Titanium	Argon
8	297.3	39.5	0.60	198	Titanium	Argon
9	297.3	44	0.60	198	Titanium	Argon
10	297.3	52	0.60	198	Titanium	Argon
11	297.3	31	0.60	218	Titanium	Argon
12	303.3	31	0.60	218	Titanium	Argon
13	314.3	31	0.60	218	Titanium	Argon
14	324.3	31	0.60	218	Titanium	Argon
15	336.3	31	0.60	218	Titanium	Argon
16	297.3	31	0.30	210	Titanium	Argon
17	297.3	31	0.40	210	Titanium	Argon
18	297.3	31	0.60	210	Titanium	Argon
19	297.3	31	0.80	210	Titanium	Argon
20	297.3	31	1.00	210	Titanium	Argon
21	297.3	32	0.60	224	Titanium	Argon
22	297.3	32	0.60	224	Iron	Argon
23	297.3	32	0.60	224	Nickel	Argon
24	297.3	32	0.60	224	Copper	Argon
25	297.3	32	0.60	224	Zinc	Argon
26	297.3	32	0.60	220	Titanium	Argon
27	297.3	32	0.60	220	Titanium	Helium
28	297.3	32	0.60	220	Titanium	Nitrogen

4.4 Simulation Model Data

Following in this section, the data obtained from the model simulation are plotted in graphs presented from figure 4-6 to 4–33. The graphs were plotted with population distribution vs. diameter range.

4.4.1 Simulation model data of various Laser Power

Experiment	1		
Laser Power (mW)	143	Pressure (Pa)	32,000
Carrier Gas	Argon	Flow Rate (SLM)	0.60
Target Material	Titanium	Temperature (K)	297.3

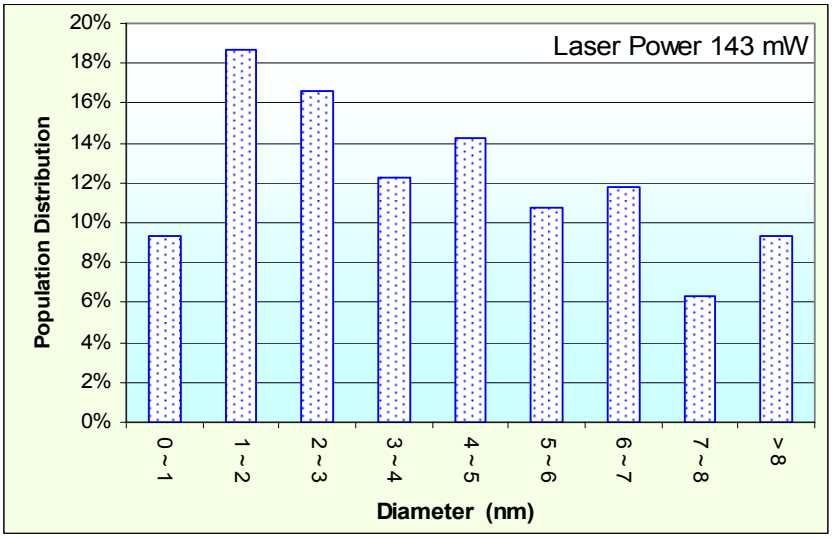

Figure 4- 18 Graph of simulation data of nanoparticle population distribution vs. diameter range of experiment 1: Laser Power of 143mW

Experiment	2		
Laser Power (mW)	198	Pressure (Pa)	32,000
Carrier Gas	Argon	Flow Rate (SLM)	0.60
Target Material	Titanium	Temperature (K)	297.3

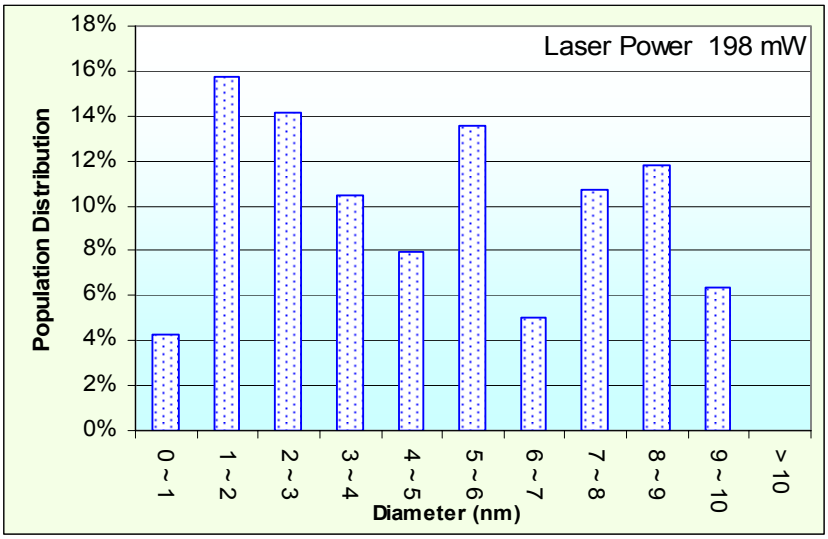

Figure 4- 19 Graph of simulation data of nanoparticle population distribution vs. diameter range of experiment 2 : Laser Power of 198 mW

Experiment	3		
Laser Power (mW)	255	Pressure (Pa)	32,000
Carrier Gas	Argon	Flow Rate (SLM)	0.60
Target Material	Titanium	Temperature (K)	297.3

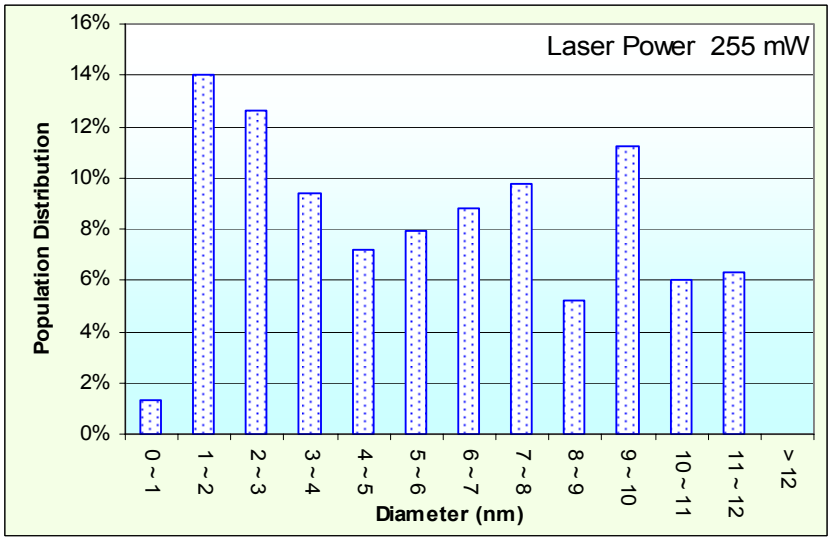

Figure 4- 20 Graph of simulation data of nanoparticle population distribution vs. diameter range of experiment 3 : Laser Power of 255 mW

Experiment	4		
Laser Power (mW)	363	Pressure (Pa)	32000.00
Carrier Gas	Argon	Flow Rate (SLM)	0.6
Target Material	Titanium	Temperature (K)	297.3

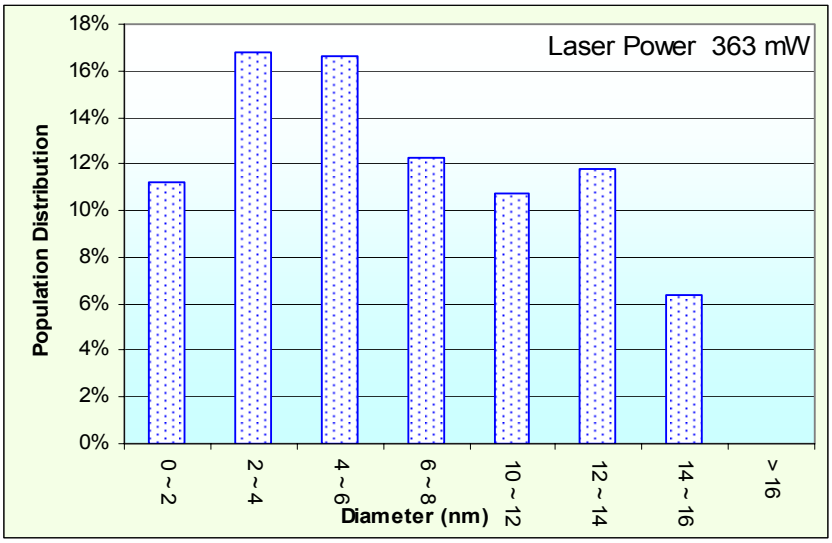

Figure 4- 21 Graph of simulation data of nanoparticle population distribution vs. diameter range of experiment 4 : Laser Power of 363 mW

Experiment	5		
Laser Power (mW)	433	Pressure (Pa)	32,000
Carrier Gas	Argon	Flow Rate (SLM)	0.60
Target Material	Titanium	Temperature (K)	297.3

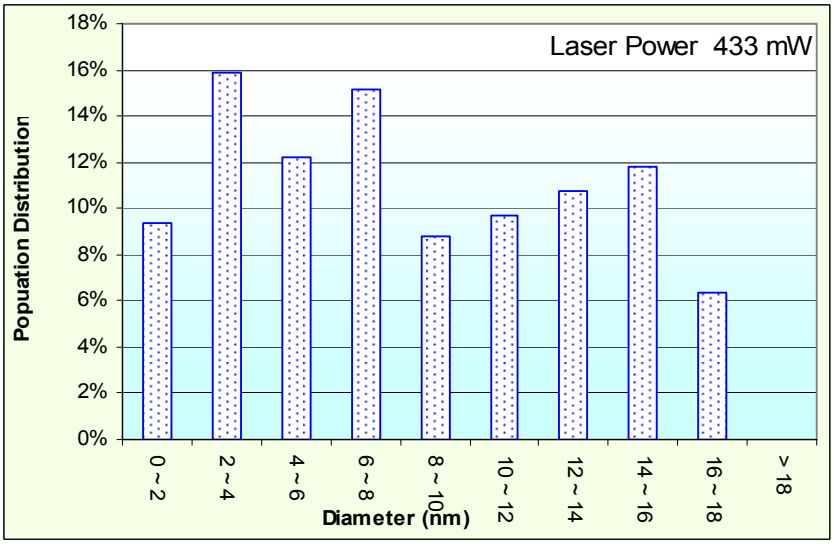

Figure 4- 22 Graph of simulation data of nanoparticle population distribution vs. diameter range of experiment 5 : Laser Power of 433 mW

4.4.2 Simulation model data of various Pressure

Experiment	6		
Laser Power (mW)	198	Pressure (Pa)	26,000
Carrier Gas	Argon	Flow Rate (SLM)	0.60
Target Material	Titanium	Temperature (K)	297.3

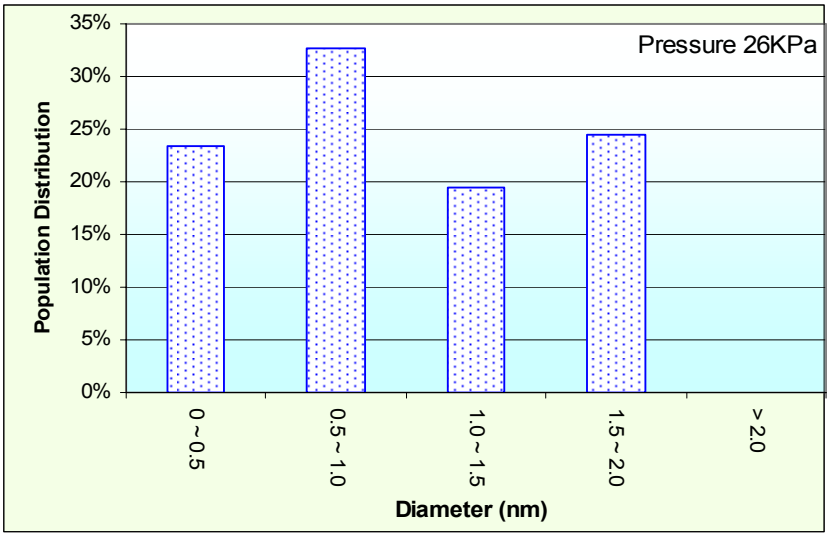

Figure 4- 23 Graph of simulation data of nanoparticle population distribution vs. diameter range of experiment 6 : Pressure of 26 KPa

Experiment	7		
Laser Power (mW)	198	Pressure (Pa)	34,000
Carrier Gas	Argon	Flow Rate (SLM)	0.60
Target Material	Titanium	Temperature (K)	297.3

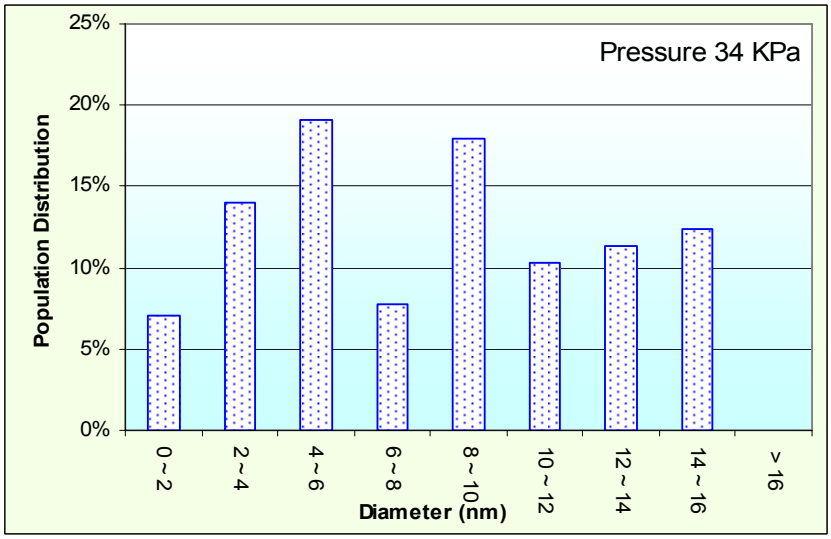

Figure 4- 24 Graph of simulation data of nanoparticle population distribution vs. diameter range of experiment 7 : Pressure of 34 KPa

Experiment	7		
Laser Power (mW)	198	Pressure (Pa)	39,500
Carrier Gas	Argon	Flow Rate (SLM)	0.60
Target Material	Titanium	Temperature (K)	297.3

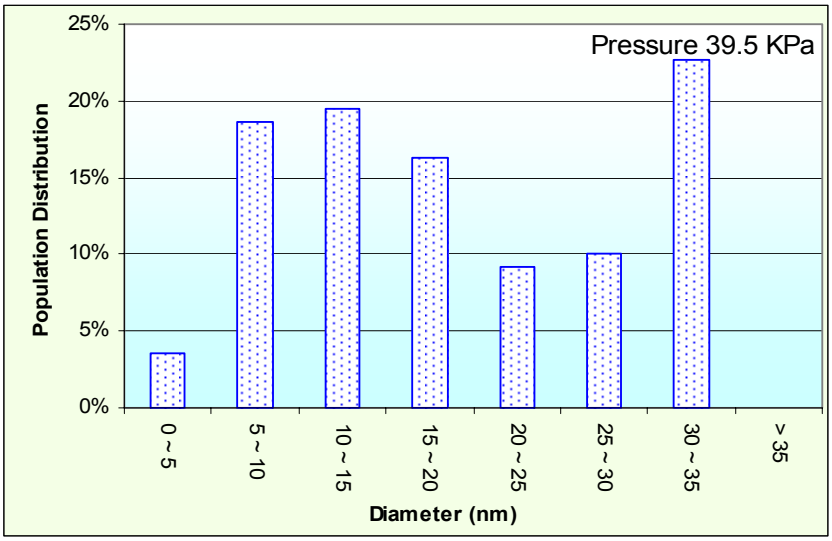

Figure 4- 25 Graph of simulation data of nanoparticle population distribution vs. diameter range of experiment 8 : Pressure of 39.5 KPa

Experiment	8		
Laser Power (mW)	198	Pressure (Pa)	44,000
Carrier Gas	Argon	Flow Rate (SLM)	0.6
Target Material	Titanium	Temperature (K)	297.3

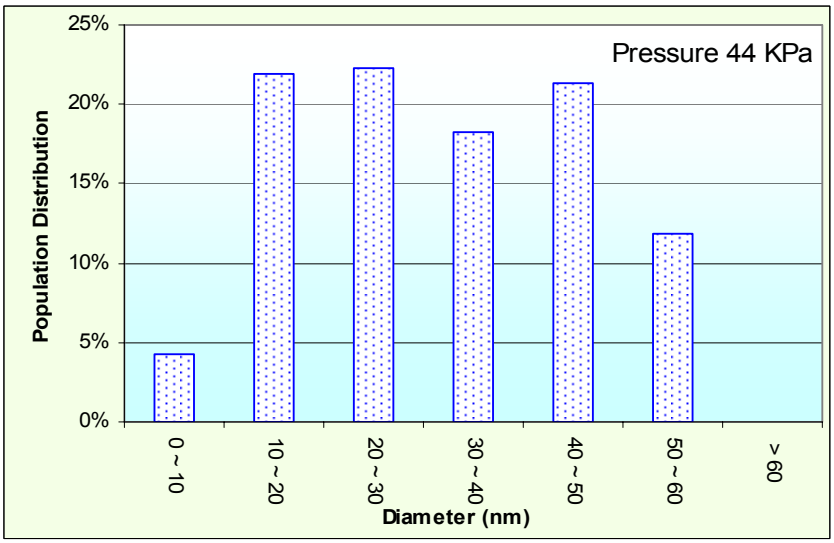

Figure 4- 26 Graph of simulation data of nanoparticle population distribution vs. diameter range of experiment 9 : Pressure of 44 KPa

Experiment	10		
Laser Power (mW)	198	Pressure (Pa)	52,000
Carrier Gas	Argon	Flow Rate (SLM)	0.60
Target Material	Titanium	Temperature (K)	297.3

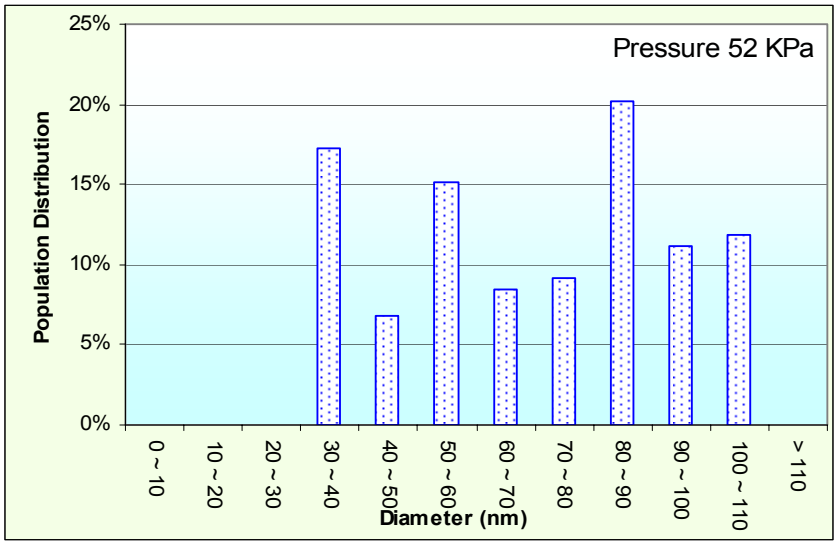

Figure 4- 27 Graph of simulation data of nanoparticle population distribution vs. diameter range of experiment 10 : Pressure of 52 KPa

4.4.3 Simulation model data of various Temperature

Experiment	11		
Laser Power (mW)	218	Pressure (Pa)	31,000
Carrier Gas	Argon	Flow Rate (SLM)	0.60
Target Material	Titanium	Temperature (K)	297.3

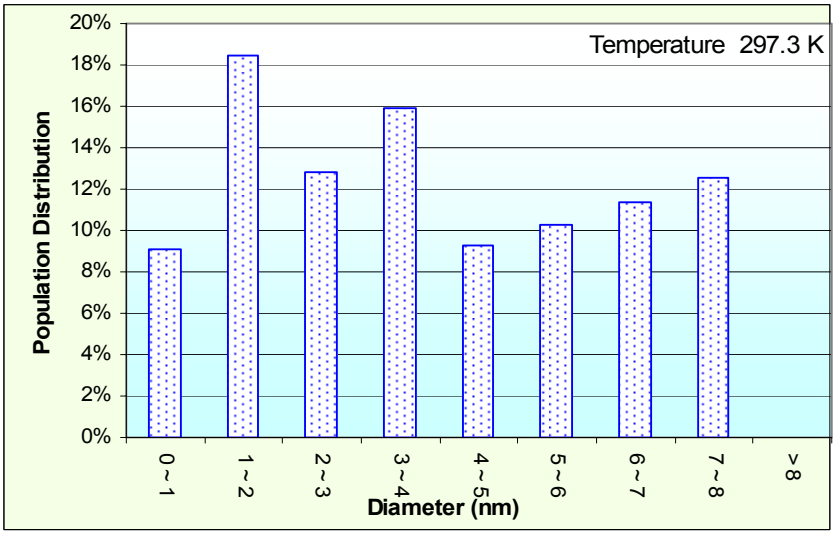

Figure 4- 28 Graph of simulation data of nanoparticle population distribution vs. diameter range of experiment 11 : Temperature 297.3 K

Experiment	12		
Laser Power (mW)	218	Pressure (Pa)	31,000
Carrier Gas	Argon	Flow Rate (SLM)	0.60
Target Material	Titanium	Temperature (K)	303.3

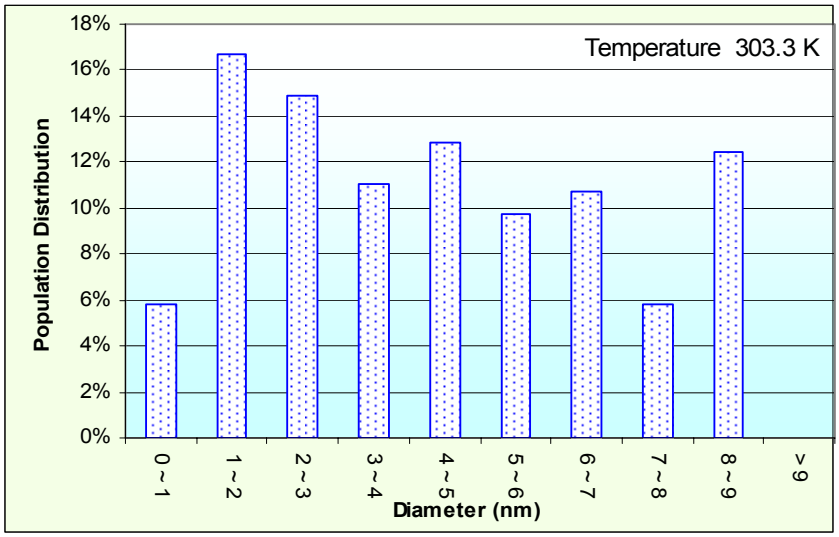

Figure 4- 29 Graph of simulation data of nanoparticle population distribution vs. diameter range of experiment 12 : Temperature 203.3 K

Experiment	13		
Laser Power (mW)	218	Pressure (Pa)	31,000
Carrier Gas	Argon	Flow Rate (SLM)	0.60
Target Material	Titanium	Temperature (K)	314.3

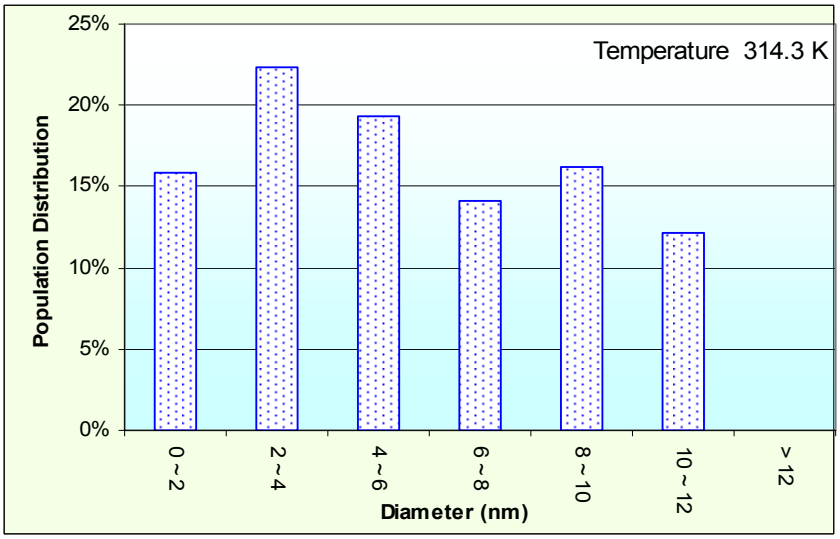

Figure 4- 30 Graph of simulation data of nanoparticle population distribution vs. diameter range of experiment 13 : Temperature 214.3 K

Experiment	14		
Laser Power (mW)	218	Pressure (Pa)	31,000
Carrier Gas	Argon	Flow Rate (SLM)	0.6
Target Material	Titanium	Temperature (K)	324.3

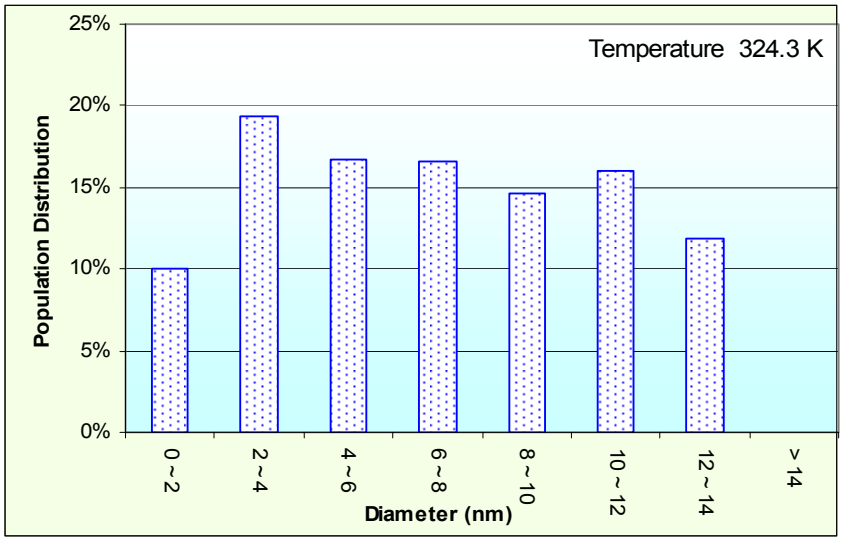

Figure 4- 31 Graph of simulation data of nanoparticle population distribution vs. diameter range of experiment 14 : Temperature 324.3 K

Experiment	15		
Laser Power (mW)	218	Pressure (Pa)	31,000
Carrier Gas	Argon	Flow Rate (SLM)	0.6
Target Material	Titanium	Temperature (K)	336.3

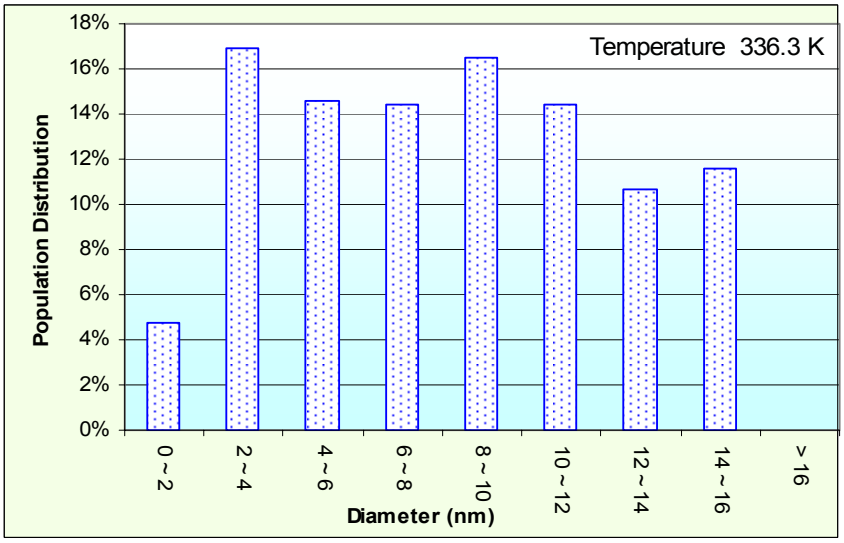

Figure 4- 32 Graph of simulation data of nanoparticle population distribution vs. diameter range of experiment 15 : Temperature 336.3 K

4.4.4 Simulation model data of various Flow Rate

Experiment	16		
Laser Power (mW)	210	Pressure (Pa)	31,000
Carrier Gas	Argon	Flow Rate (SLM)	0.3
Target Material	Titanium	Temperature (K)	297.3

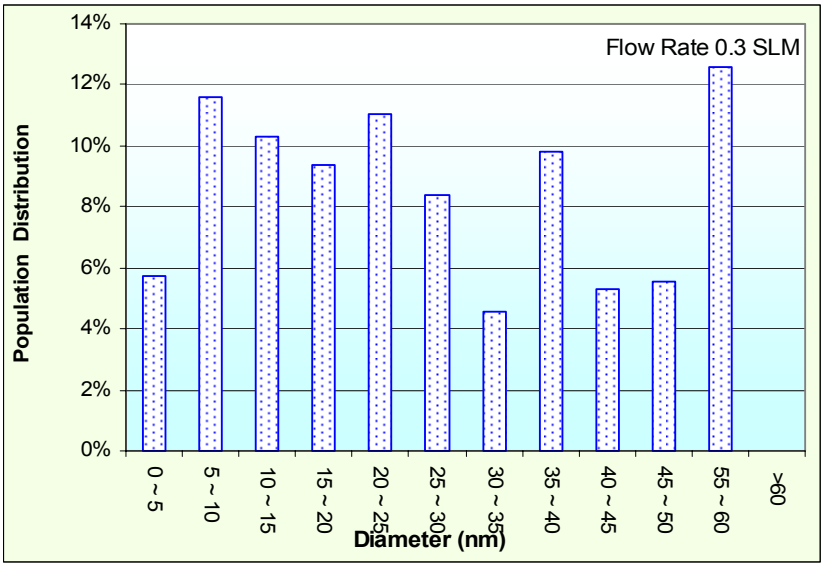

Figure 4- 33 Graph of simulation data of nanoparticle population distribution vs. diameter range of experiment 16 : Flow Rate 0.3 SLM

Experiment	17		
Laser Power (mW)	210	Pressure (Pa)	31,000
Carrier Gas	Argon	Flow Rate (SLM)	0.4
Target Material	Titanium	Temperature (K)	297.3

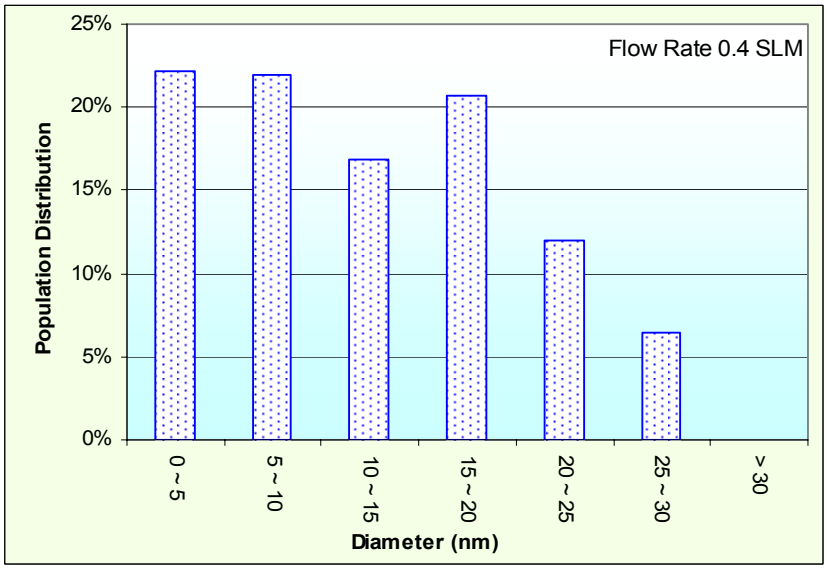

Figure 4- 34 Graph of simulation data of nanoparticle population distribution vs. diameter range of experiment 17 : Flow Rate 0.4 SLM

Experiment	18		
Laser Power (mW)	210	Pressure (Pa)	31,000
Carrier Gas	Argon	Flow Rate (SLM)	0.60
Target Material	Titanium	Temperature (K)	297.3

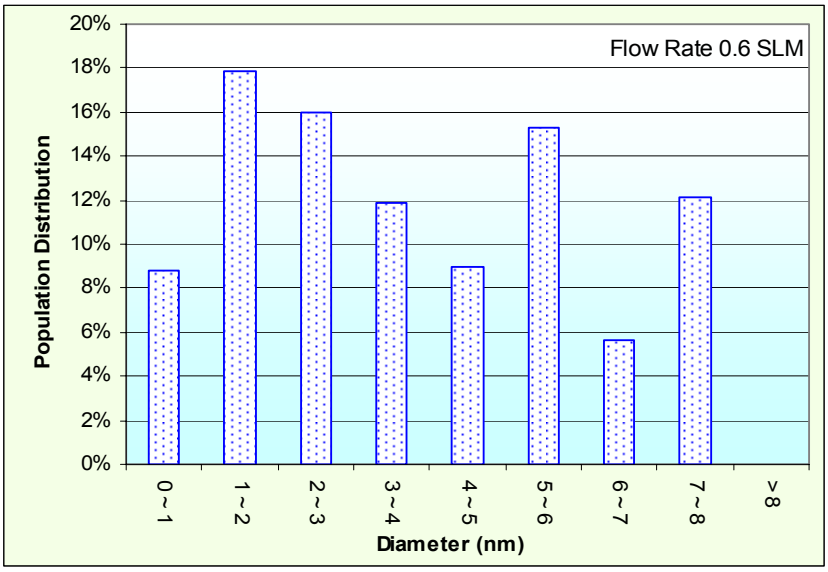

Figure 4- 35 Graph of simulation data of nanoparticle population distribution vs. diameter range of experiment 18 : Flow Rate 0.6 SLM

Experiment	19		
Laser Power (mW)	210	Pressure (Pa)	31,000
Carrier Gas	Argon	Flow Rate (SLM)	0.8
Target Material	Titanium	Temperature (K)	297.3

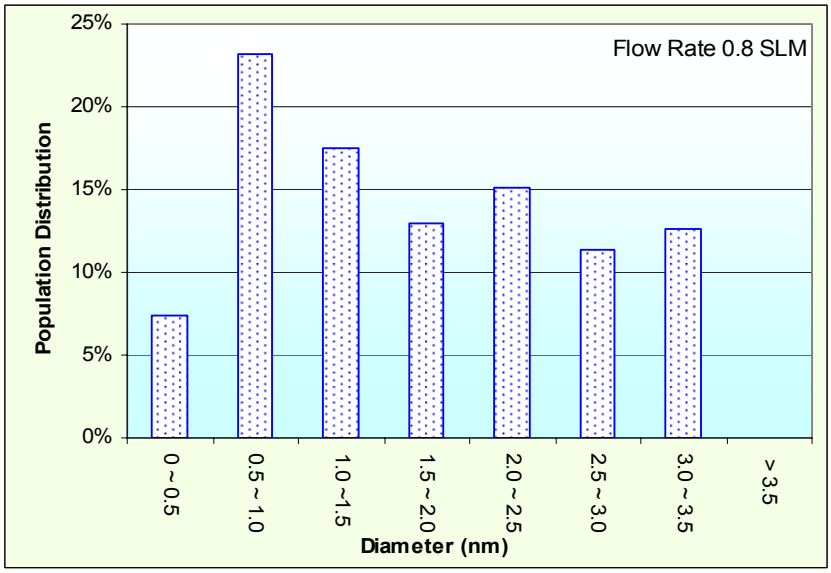

Figure 4- 36 Graph of simulation data of nanoparticle population distribution vs. diameter range of experiment 19 : Flow Rate 0.8 SLM

Experiment	20		
Laser Power (mW)	210	Pressure (Pa)	31,000
Carrier Gas	Argon	Flow Rate (SLM)	1
Target Material	Titanium	Temperature (K)	297.3

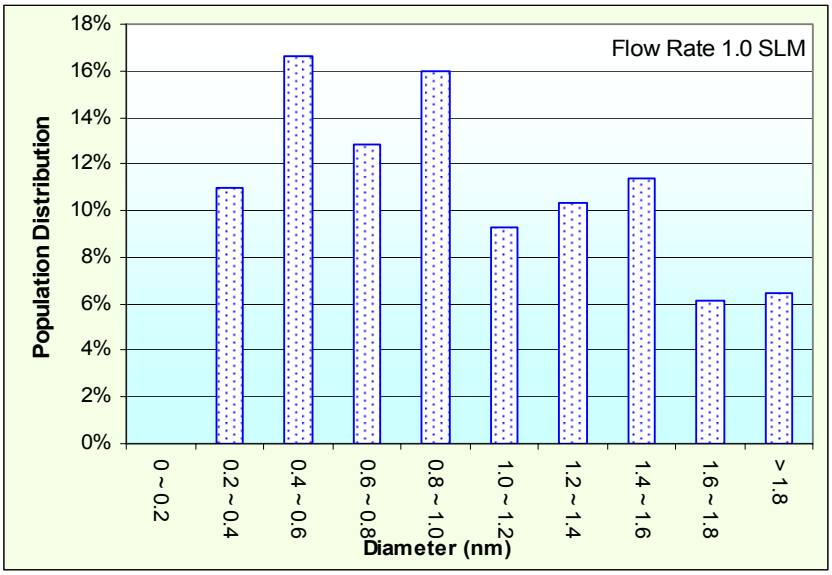

Figure 4- 37 Graph of simulation data of nanoparticle population distribution vs. diameter range of experiment 20: Flow Rate 1.0 SLM

4.4.5 Simulation model data of various Target Material

Experiment	21		
Laser Power (mW)	384	Pressure (Pa)	32,000
Carrier Gas	Argon	Flow Rate (SLM)	0.50
Target Material	Titanium	Temperature (K)	297.3

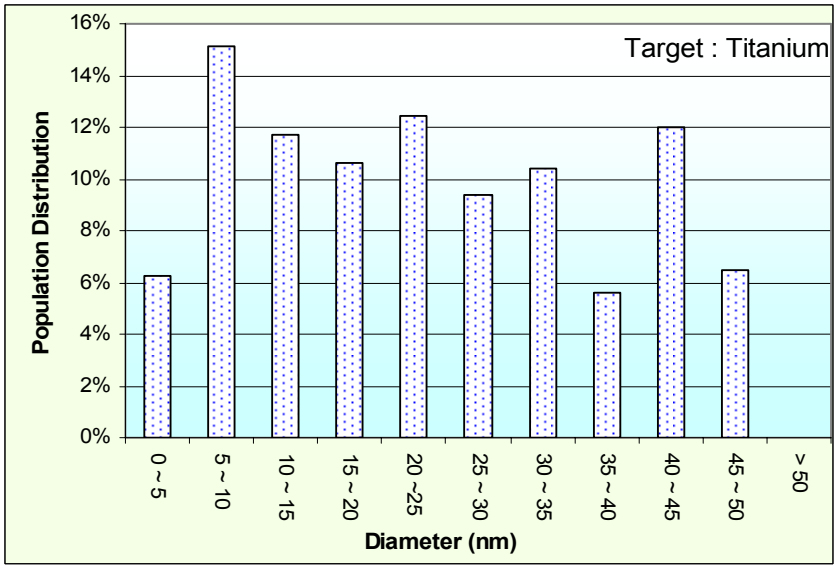

Figure 4- 38 Graph of simulation data of nanoparticle population distribution vs. diameter range of experiment 21 : Target Material Titanium

Experiment	22		
Laser Power (mW)	384	Pressure (Pa)	32,000
Carrier Gas	Argon	Flow Rate (SLM)	0.50
Target Material	Iron	Temperature (K)	297.3

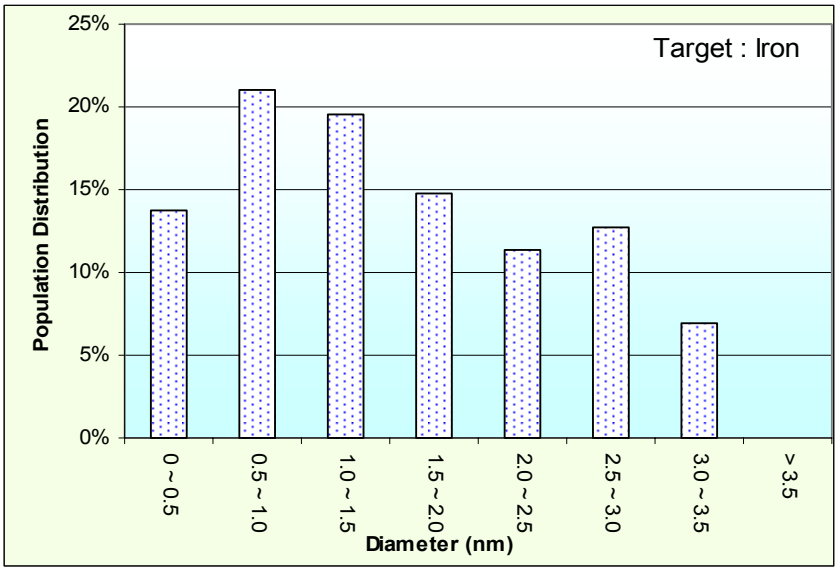

Figure 4- 39 Graph of simulation data of nanoparticle population distribution vs. diameter range of experiment 22 : Target Material Iron

Experiment	23		
Laser Power (mW)	384	Pressure (Pa)	32,000
Carrier Gas	Argon	Flow Rate (SLM)	0.50
Target Material	Nickel	Temperature (K)	297.3

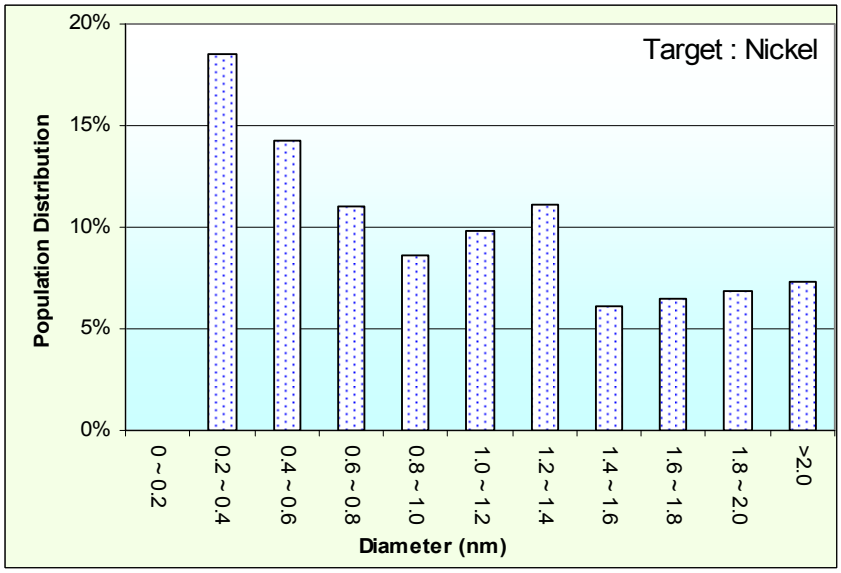

Figure 4- 40 Graph of simulation data of nanoparticle population distribution vs. diameter range of experiment 23 : Target Material Nickel

Experiment	24		
Laser Power (mW)	224	Pressure (Pa)	32000.00
Carrier Gas	Argon	Flow Rate (SLM)	0.6
Target Material	Copper	Temperature (K)	297.3

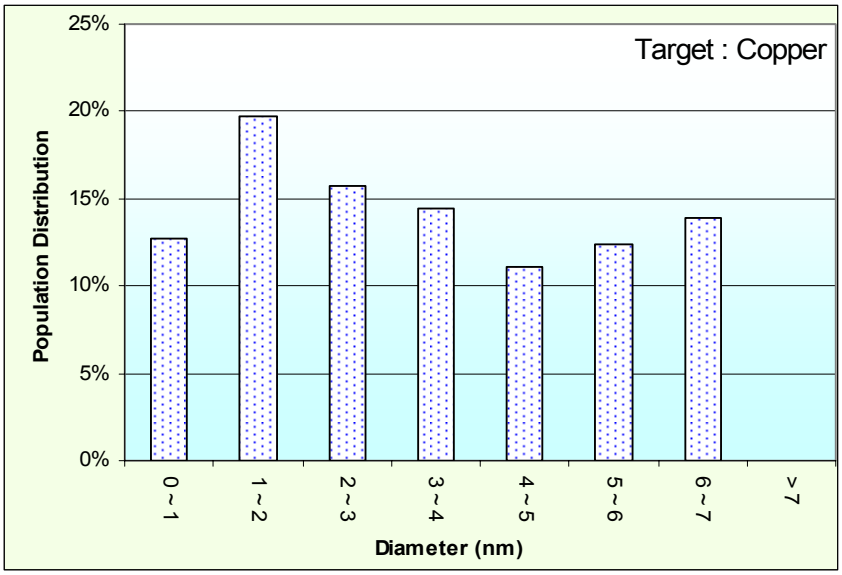

Figure 4- 41 Graph of simulation data of nanoparticle population distribution vs. diameter range of experiment 24 : Target Material Copper

Experiment	25		
Laser Power (mW)	224	Pressure (Pa)	32,000
Carrier Gas	Argon	Flow Rate (SLM)	0.60
Target Material	Zinc	Temperature (K)	297.3

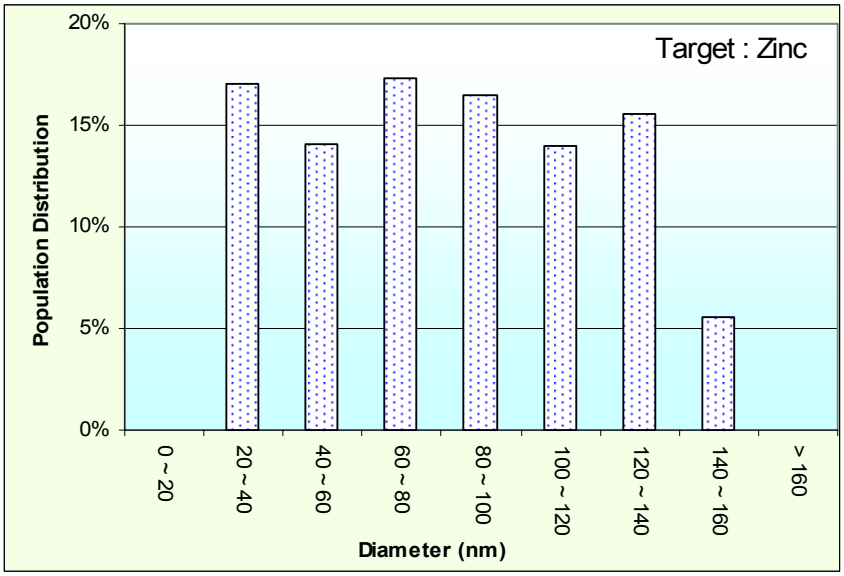

Figure 4- 42 Graph of simulation data of nanoparticle population distribution vs. diameter range of experiment 25 : Target Material Zinc

4.4.6 Simulation model data of various Carrier Gas

Experiment	26		
Laser Power (mW)	220	Pressure (Pa)	34,000
Carrier Gas	Helium	Flow Rate (SLM)	0.60
Target Material	Titanium	Temperature (K)	297.3

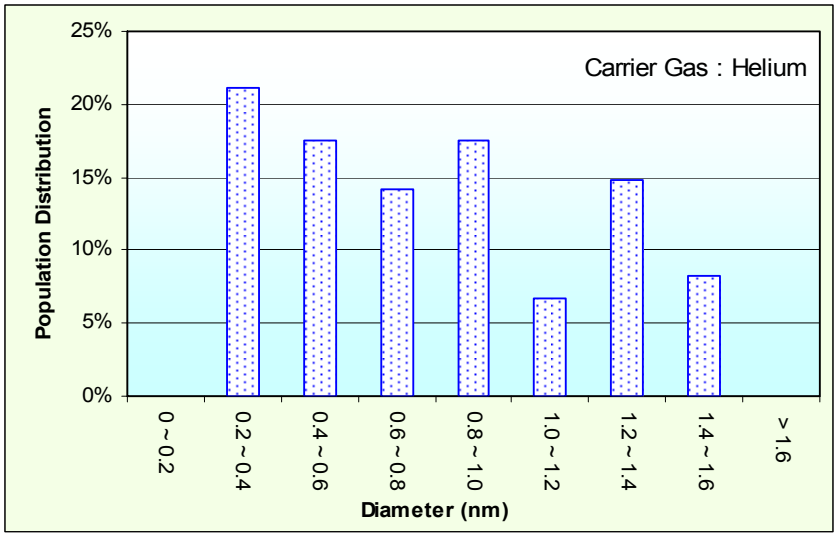

Figure 4- 43 Graph of simulation data of nanoparticle population distribution vs. diameter range of experiment 26 : Helium gas

Experiment	27		
Laser Power (mW)	220	Pressure (Pa)	34,000
Carrier Gas	Argon	Flow Rate (SLM)	0.60
Target Material	Titanium	Temperature (K)	297.3

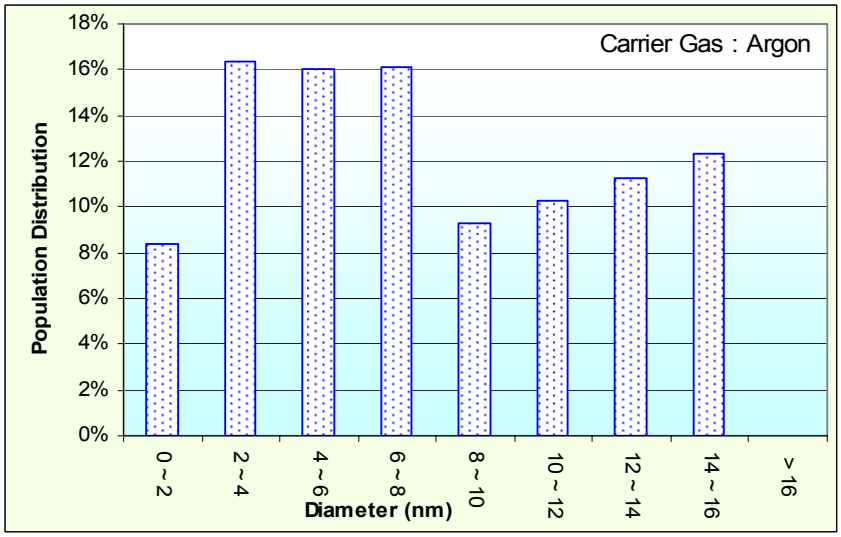

Figure 4- 44 Graph of simulation data of nanoparticle population distribution vs. diameter range of experiment 27 : Argon gas

Experiment	3		
Laser Power (mW)	220	Pressure (Pa)	34,000
Carrier Gas	Nitrogen	Flow Rate (SLM)	0.60
Target Material	Titanium	Temperature (K)	297.3

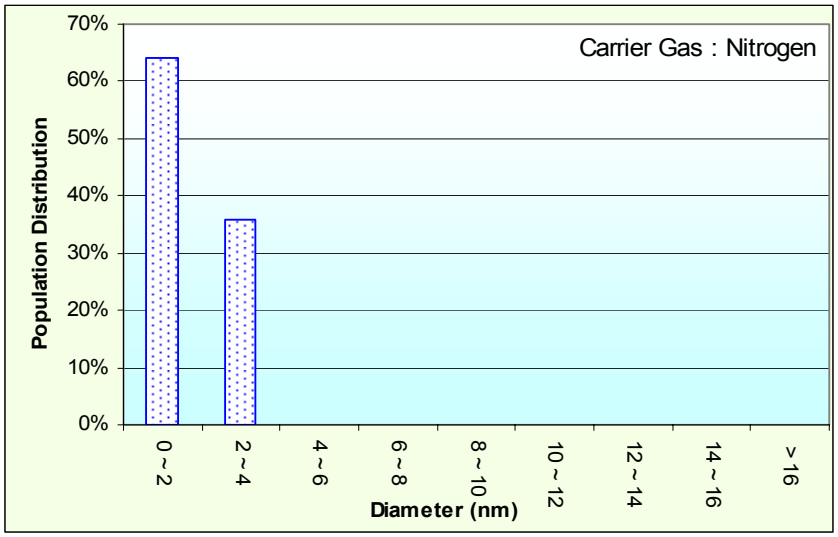

Figure 4- 45 Graph of simulation data of nanoparticle population distribution vs. diameter range of experiment 28 : Nitrogen gas

4.5 Experimental Results

Following in this section, the data obtained from the experimental results are plotted in graphs presented from figure 4 - 34 to 4 – 61. The graphs were plotted with population distribution vs. diameter range.

In view of the *Energy Dispersive X-ray Spectroscopy* (EDS) analysis, all the results obtained were satisfied the dual criterion of :

(i) nanoparticles collected still remained as the same metal as in their target, and

(ii) that the particles in the images were not alien objects.

However, there were some minute traces of oxygen in the EDS for some of the samples collected. This was especially so for those nanoparticles with very small diameters of below 10 nm. As the metal become smaller in size, the ratio of surface area to volume increases, so does their rate of reaction. Though much precaution were taken to prevent the samples from oxidation from the air once they were moved out of the chambers, but there were still a little “leak” in the system. But most important of all, the oxidation could not have happen during the synthesis process of the experiments because the chambers had been flushed out of almost all of the oxygen by the experimental preparation procedure described in section 4.2

Secondly, the ratio of empirical value of oxygen atoms to the metal atoms indicated that most of the nanoparticles were still metal. The empirical value of oxygen atom is obtained by dividing the mass of oxygen traces detected over the molar mass of oxygen. Likewise, the empirical value of metal is obtained by dividing the mass of metal traces detected over the molar mass of the metal. If all the metal had turned into oxide, the ratio of these empirical values will indicate the same ratio of the number of metal atoms to number of oxygen atoms in its oxide compound formula. Example for copper, its oxide is copper oxide (CuO). If most of the nanoparticles had been oxidized, then the obtained

ratio would be 1:1. Similar, if titanium had turned into titanium dioxide (TiO_2), the ratio would had been 1:2 . Ratios obtained in the experiments were much higher for the metal elements indicating most of the nanoparticles still remained as its original element metal

4.5.1 Experimental results of various Laser Power

Experiment	1		
Laser Power (mW)	143	Pressure (Pa)	32,000
Carrier Gas	Argon	Flow Rate (SLM)	0.60
Target Material	Titanium	Temperature (K)	297.3

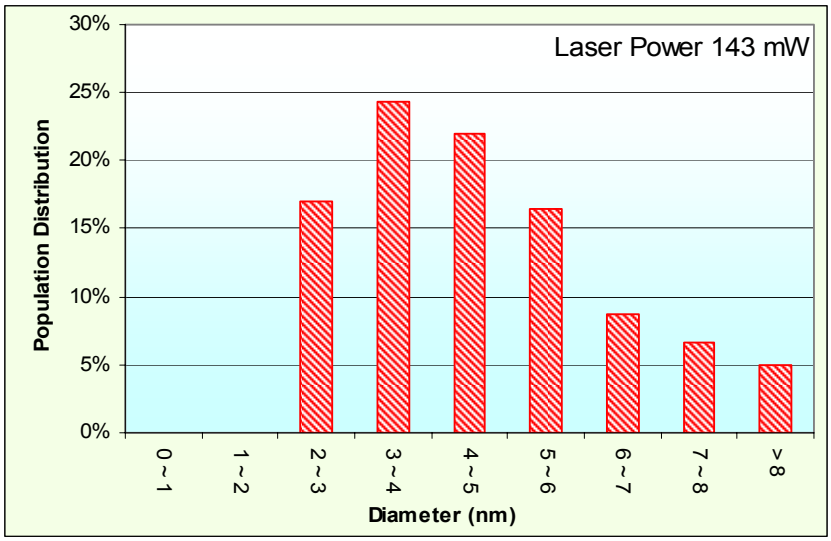

Figure 4- 46 Graphs of experimental results of nanoparticle population distribution vs. diameter range of experiment 1 : Laser Power of 143mW

Experiment	2		
Laser Power (mW)	198	Pressure (Pa)	32,000
Carrier Gas	Argon	Flow Rate (SLM)	0.60
Target Material	Titanium	Temperature (K)	297.3

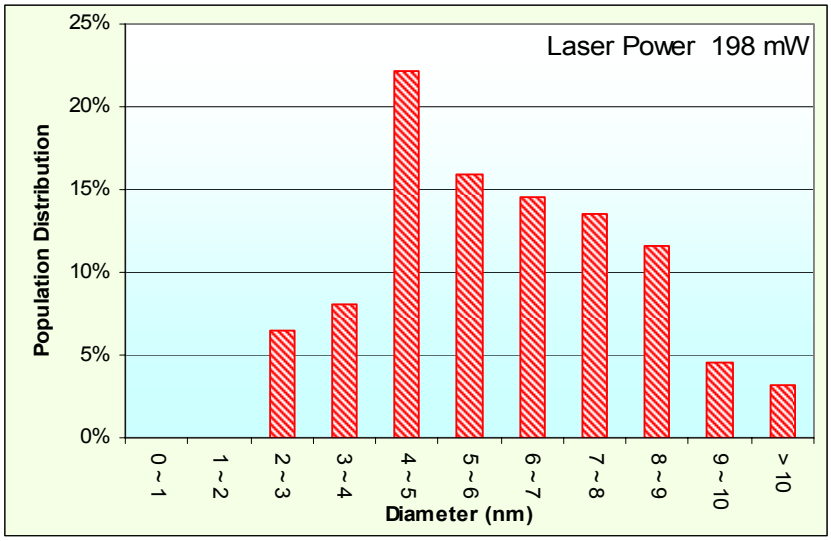

Figure 4- 47 Graph of experimental results of nanoparticle population distribution vs. diameter range of experiment 2 : Laser Power of 198 mW

Experiment	3		
Laser Power (mW)	255	Pressure (Pa)	32,000
Carrier Gas	Argon	Flow Rate (SLM)	0.60
Target Material	Titanium	Temperature (K)	297.3

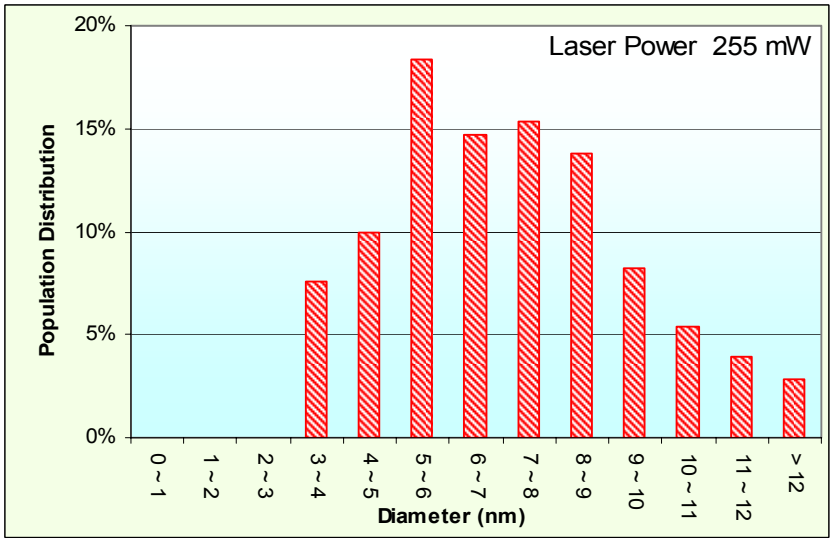

Figure 4- 48 Graph of experimental results of nanoparticle population distribution vs. diameter range of experiment 3 : Laser Power of 255 mW

Experiment	4		
Laser Power (mW)	363	Pressure (Pa)	32000.00
Carrier Gas	Argon	Flow Rate (SLM)	0.6
Target Material	Titanium	Temperature (K)	297.3

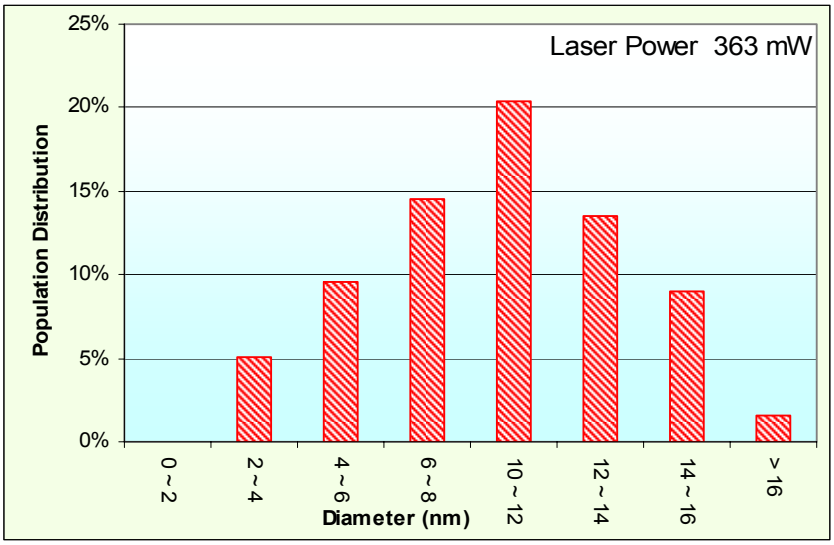

Figure 4- 49 Graph of experimental results of nanoparticle population distribution vs. diameter range of experiment 4 : Laser Power of 363 mW

Experiment	5		
Laser Power (mW)	433	Pressure (Pa)	32,000
Carrier Gas	Argon	Flow Rate (SLM)	0.60
Target Material	Titanium	Temperature (K)	297.3

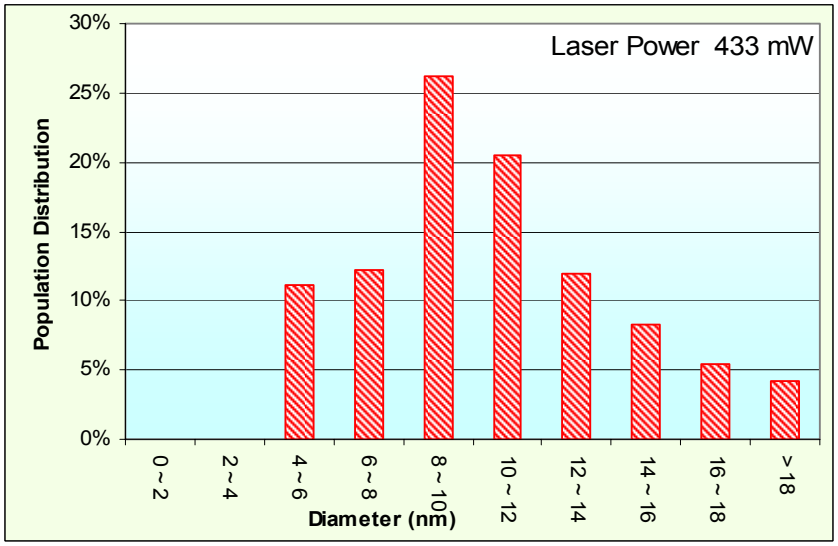

Figure 4- 50 Graph of experimental results of nanoparticle population distribution vs. diameter range of experiment 5 : Laser Power of 433 mW

4.5.2 Experimental results of various Pressure

Experiment	6		
Laser Power (mW)	198	Pressure (Pa)	26,000
Carrier Gas	Argon	Flow Rate (SLM)	0.60
Target Material	Titanium	Temperature (K)	297.3

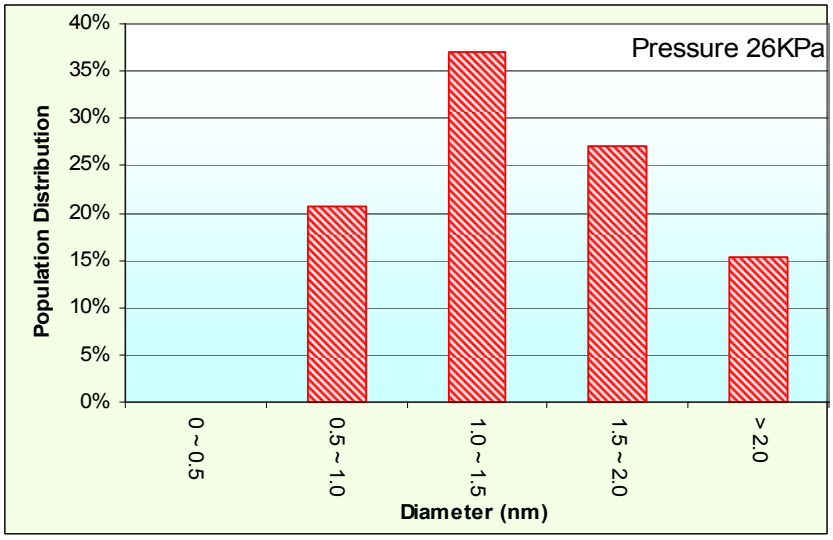

Figure 4- 51 Graph of experimental results of nanoparticle population distribution vs. diameter range of experiment 6 : Pressure of 26 KPa

Experiment	7		
Laser Power (mW)	198	Pressure (Pa)	34,000
Carrier Gas	Argon	Flow Rate (SLM)	0.60
Target Material	Titanium	Temperature (K)	297.3

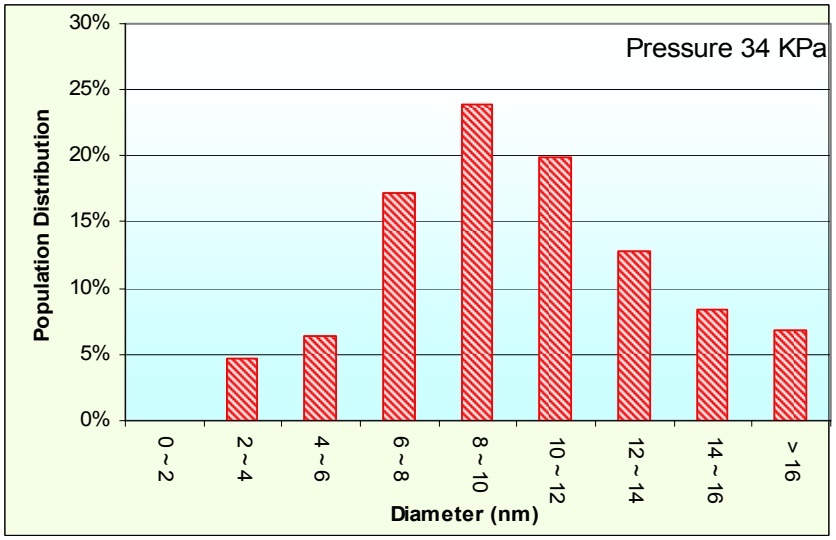

Figure 4- 52 Graph of experimental results of nanoparticle population distribution vs. diameter range of experiment 7 : Pressure of 34 KPa

Experiment	8		
Laser Power (mW)	198	Pressure (Pa)	39,500
Carrier Gas	Argon	Flow Rate (SLM)	0.60
Target Material	Titanium	Temperature (K)	297.3

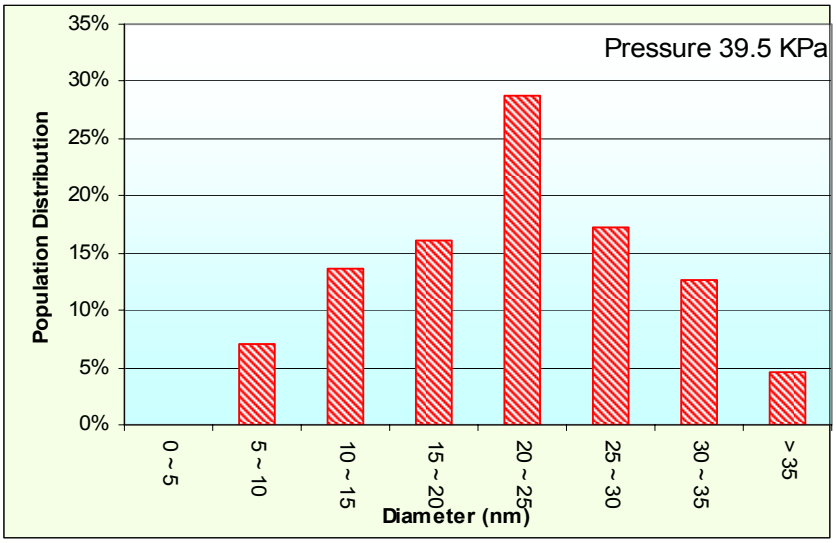

Figure 4- 53 Graph of experimental results of nanoparticle population distribution vs. diameter range of experiment 8 : Pressure of 39.5 KPa

Experiment	9		
Laser Power (mW)	198	Pressure (Pa)	44000.00
Carrier Gas	Argon	Flow Rate (SLM)	0.6
Target Material	Titanium	Temperature (K)	297.3

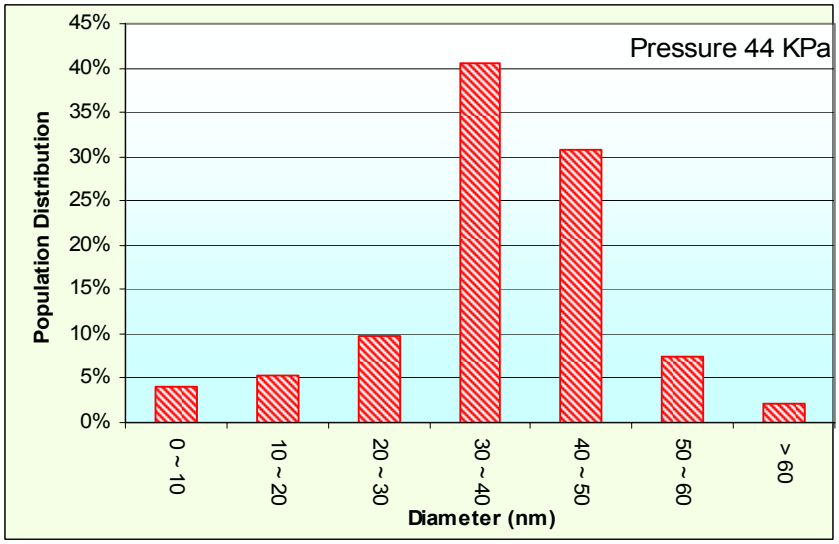

Figure 4- 54 Graph of experimental results of nanoparticle population distribution vs. diameter range of experiment 9 : Pressure of 44 KPa

Experiment	10		
Laser Power (mW)	198	Pressure (Pa)	52,000
Carrier Gas	Argon	Flow Rate (SLM)	0.60
Target Material	Titanium	Temperature (K)	297.3

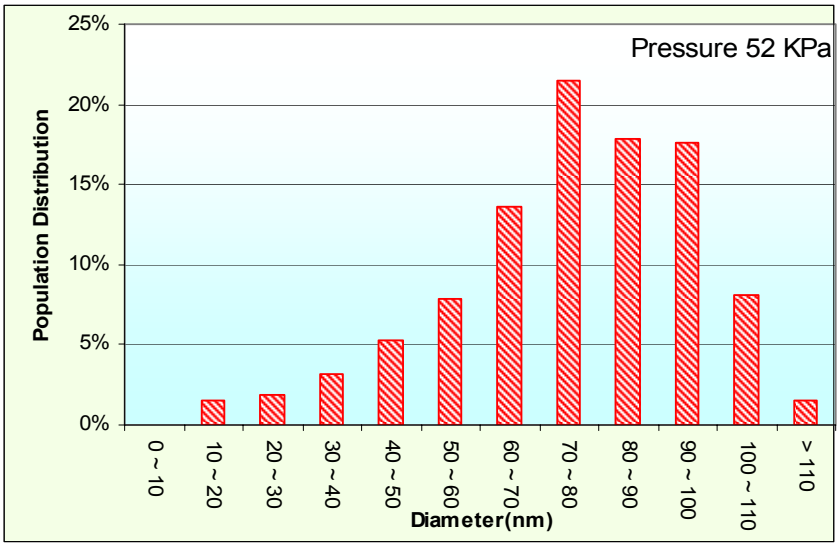

Figure 4- 55 Graph of experimental results of nanoparticle population distribution vs. diameter range of experiment 10 : Pressure of 52 KPa

4.5.3 Experimental results of various Temperature

Experiment	11		
Laser Power (mW)	218	Pressure (Pa)	31,000
Carrier Gas	Argon	Flow Rate (SLM)	0.60
Target Material	Titanium	Temperature (K)	297.3

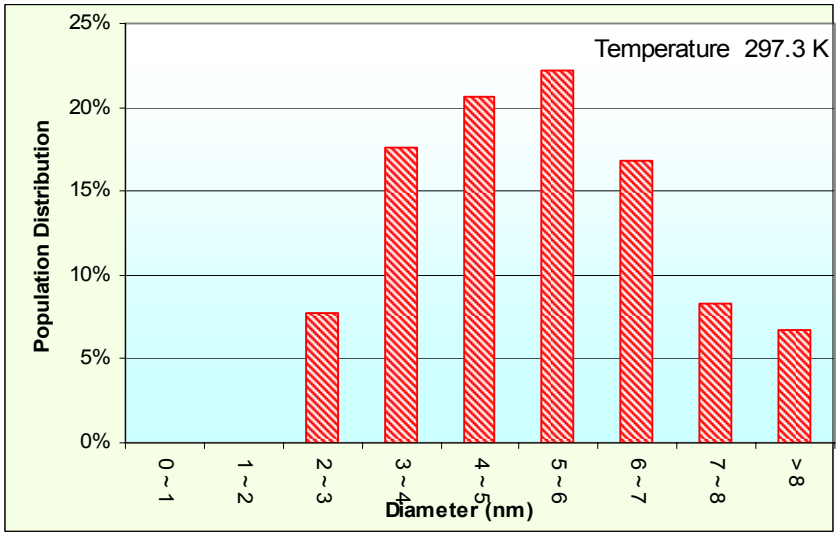

Figure 4- 56 Graph of experimental results of nanoparticle population distribution vs. diameter range of experiment 11 : Temperature 297.3 K

Experiment	12		
Laser Power (mW)	218	Pressure (Pa)	31,000
Carrier Gas	Argon	Flow Rate (SLM)	0.60
Target Material	Titanium	Temperature (K)	303.3

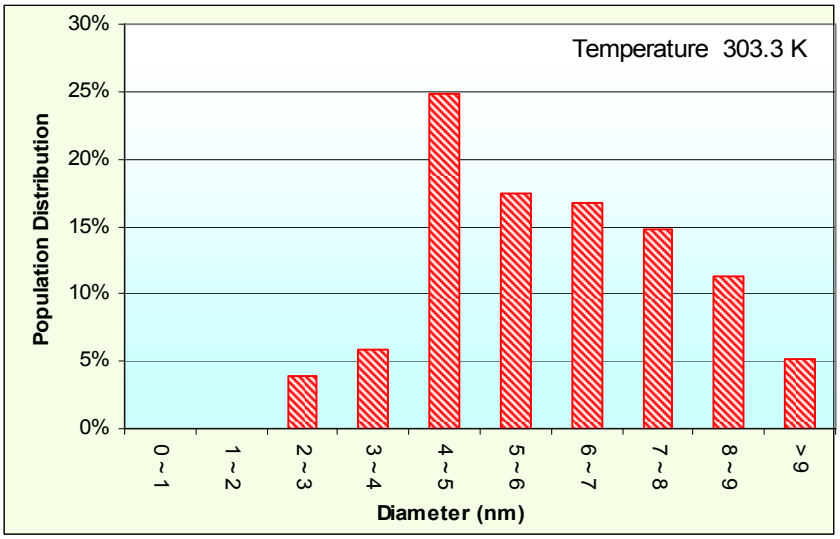

Figure 4- 57 Graph of experimental results of nanoparticle population distribution vs. diameter range of experiment 12 : Temperature 203.3 K

Experiment	13		
Laser Power (mW)	218	Pressure (Pa)	31,000
Carrier Gas	Argon	Flow Rate (SLM)	0.60
Target Material	Titanium	Temperature (K)	314.3

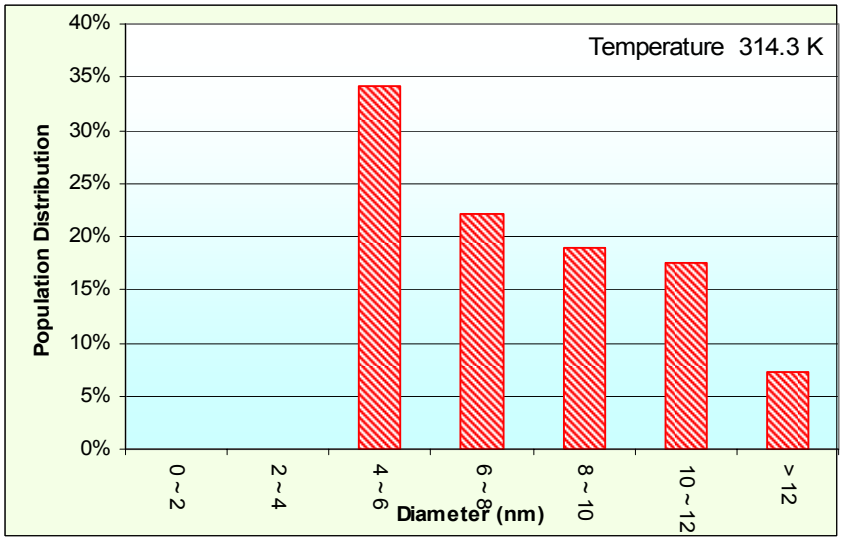

Figure 4- 58 Graph of experimental results of nanoparticle population distribution vs. diameter range of experiment 13 : Temperature 214.3 K

Experiment	14		
Laser Power (mW)	218	Pressure (Pa)	31000.00
Carrier Gas	Argon	Flow Rate (SLM)	0.6
Target Material	Titanium	Temperature (K)	324.3

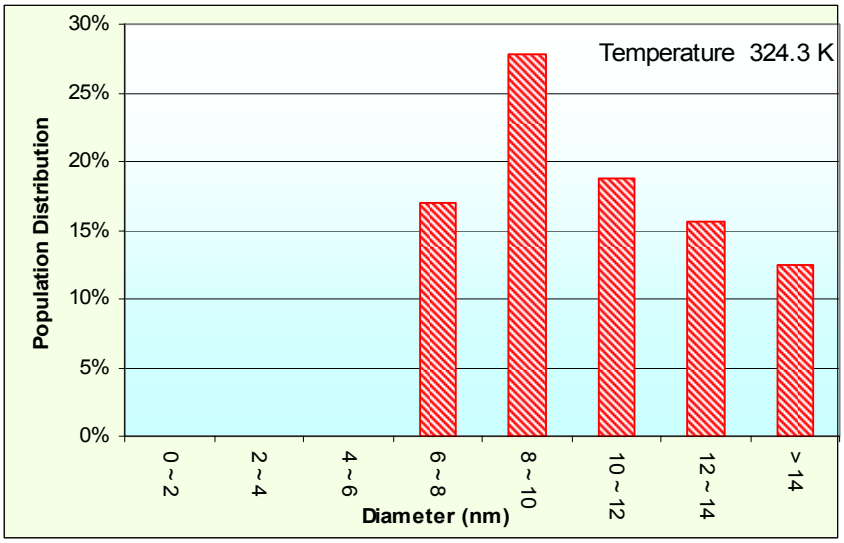

Figure 4- 59 Graph of experimental results of nanoparticle population distribution vs. diameter range of experiment 14 : Temperature 324.3 K

Experiment	15		
Laser Power (mW)	218	Pressure (Pa)	31000.00
Carrier Gas	Argon	Flow Rate (SLM)	0.6
Target Material	Titanium	Temperature (K)	336.3

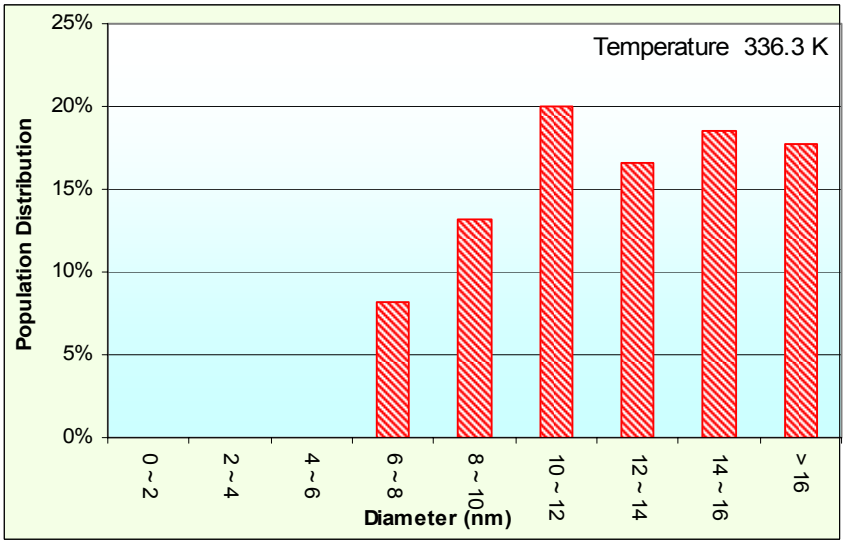

Figure 4- 60 Graph of experimental results of nanoparticle population distribution vs. diameter range of experiment 15 : Temperature 336.3 K

4.5.4 Experimental results of various Flow Rate

Experiment	16		
Laser Power (mW)	210	Pressure (Pa)	31,000
Carrier Gas	Argon	Flow Rate (SLM)	0.3
Target Material	Titanium	Temperature (K)	297.3

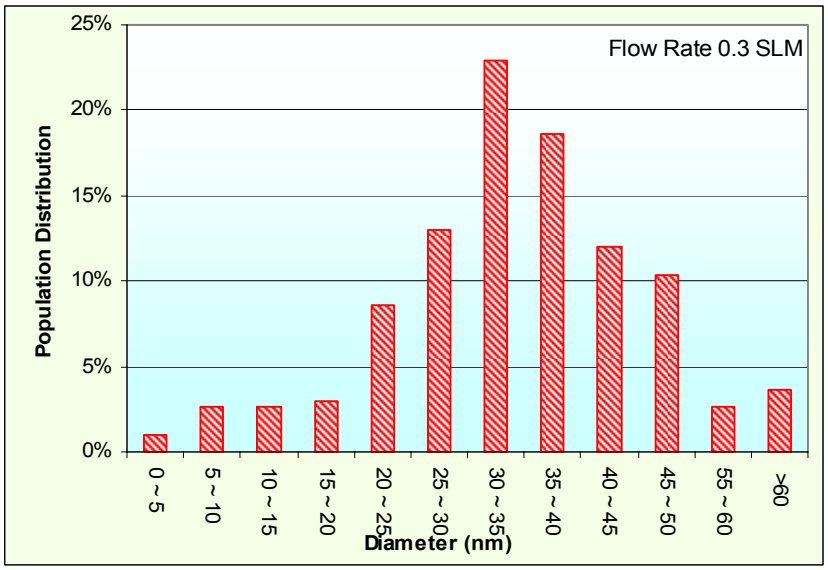

Figure 4- 61 Graph of experimental results of nanoparticle population distribution vs. diameter range of experiment 16 : Flow Rate 0.3 SLM

Experiment	17		
Laser Power (mW)	210	Pressure (Pa)	31,000
Carrier Gas	Argon	Flow Rate (SLM)	0.4
Target Material	Titanium	Temperature (K)	297.3

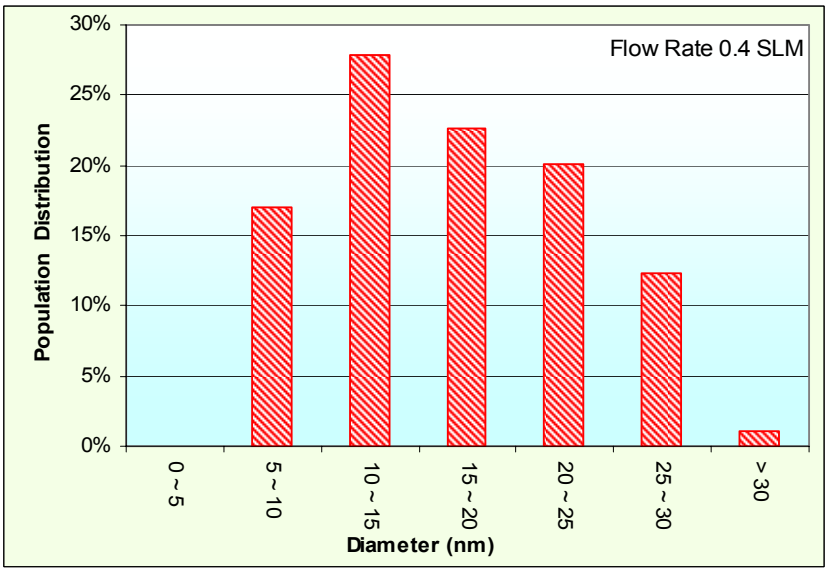

Figure 4- 62 Graph of experimental results of nanoparticle population distribution vs. diameter range of experiment 17 : Flow Rate 0.4 SLM

Experiment	18		
Laser Power (mW)	210	Pressure (Pa)	31,000
Carrier Gas	Argon	Flow Rate (SLM)	0.60
Target Material	Titanium	Temperature (K)	297.3

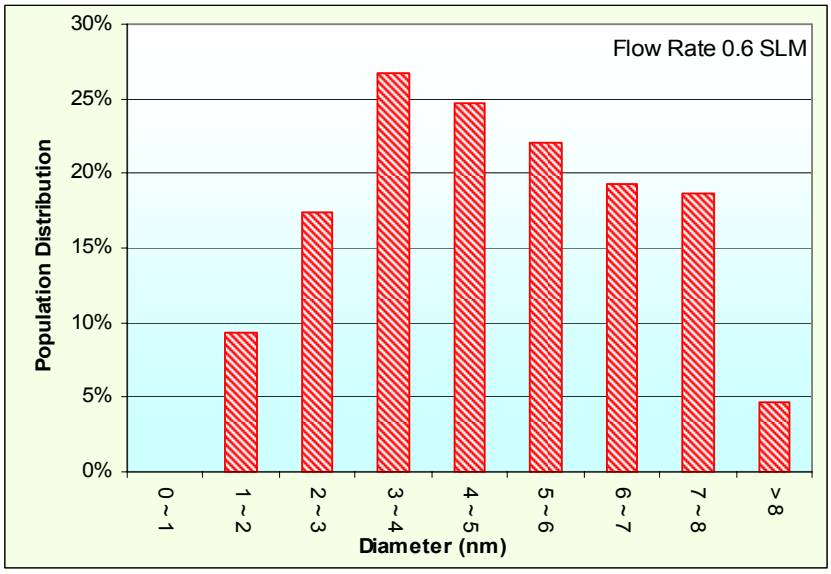

Figure 4- 63 Graph of experimental results of nanoparticle population distribution vs. diameter range of experiment 18 : Flow Rate 0.6 SLM

Experiment	19		
Laser Power (mW)	210	Pressure (Pa)	31,000
Carrier Gas	Argon	Flow Rate (SLM)	0.8
Target Material	Titanium	Temperature (K)	297.3

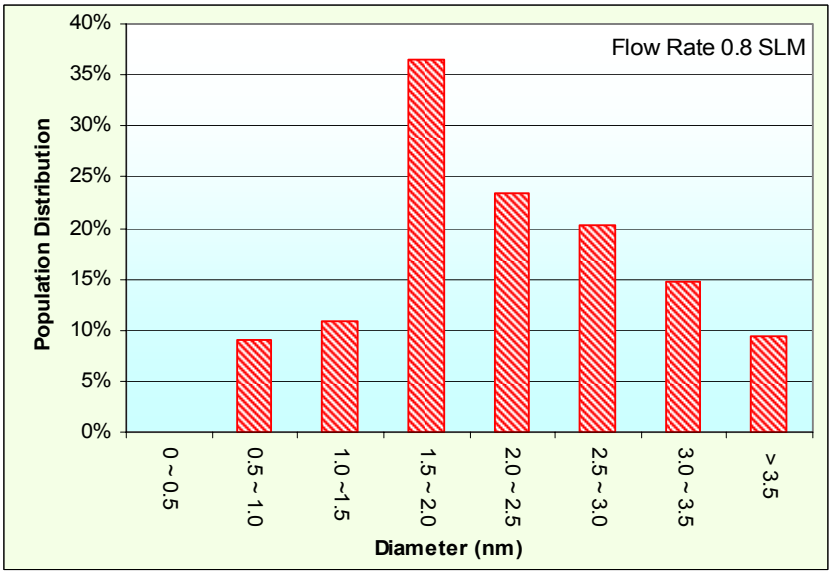

Figure 4- 64 Graph of experimental results of nanoparticle population distribution vs. diameter range of experiment 19 : Flow Rate 0.8 SLM

Experiment	20		
Laser Power (mW)	210	Pressure (Pa)	31,000
Carrier Gas	Argon	Flow Rate (SLM)	1
Target Material	Titanium	Temperature (K)	297.3

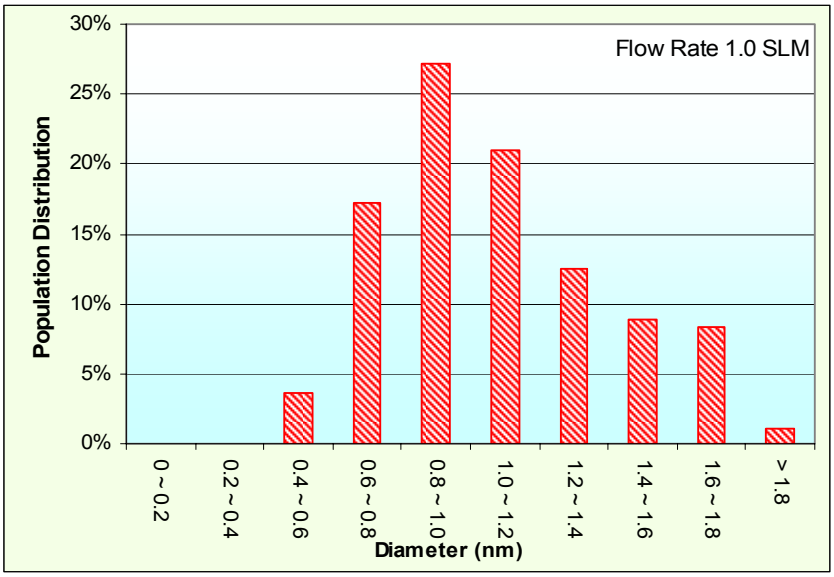

Figure 4- 65 Graph of experimental results of nanoparticle population distribution vs. diameter range of experiment 20 : Flow Rate 1.0 SLM

4.5.5 Experimental results of various Target Material

Experiment	21		
Laser Power (mW)	384	Pressure (Pa)	32,000
Carrier Gas	Argon	Flow Rate (SLM)	0.50
Target Material	Titanium	Temperature (K)	297.3

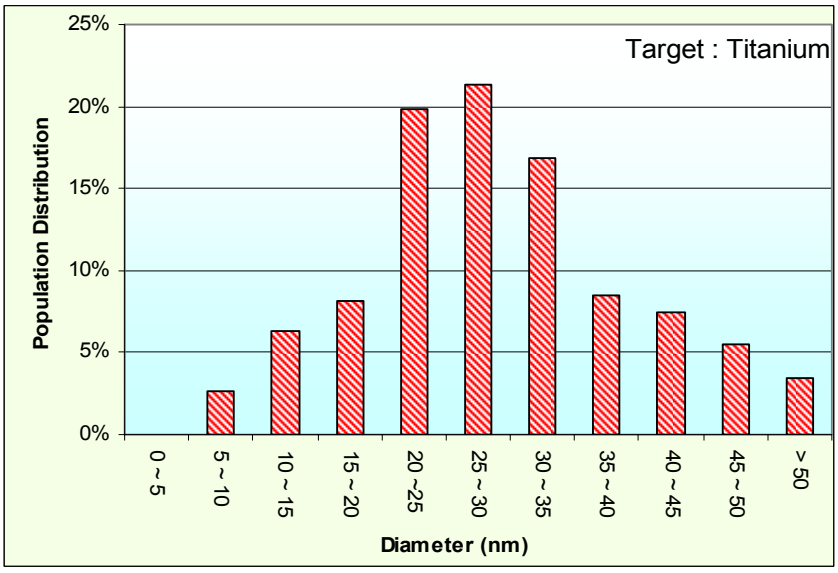

Figure 4- 66 Graph of experimental results of nanoparticle population distribution vs. diameter range of experiment 21 : Target Material Titanium

Experiment	22		
Laser Power (mW)	384	Pressure (Pa)	32,000
Carrier Gas	Argon	Flow Rate (SLM)	0.50
Target Material	Iron	Temperature (K)	297.3

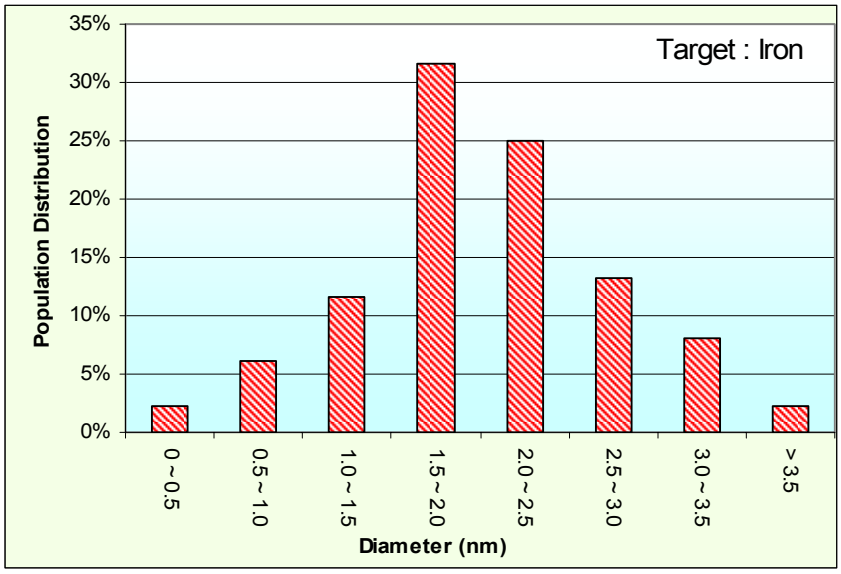

Figure 4- 67 Graph of Experimental Results of nanoparticle population distribution of experiment 22 : Target Material Iron

Experiment	23		
Laser Power (mW)	384	Pressure (Pa)	32,000
Carrier Gas	Argon	Flow Rate (SLM)	0.50
Target Material	Nickel	Temperature (K)	297.3

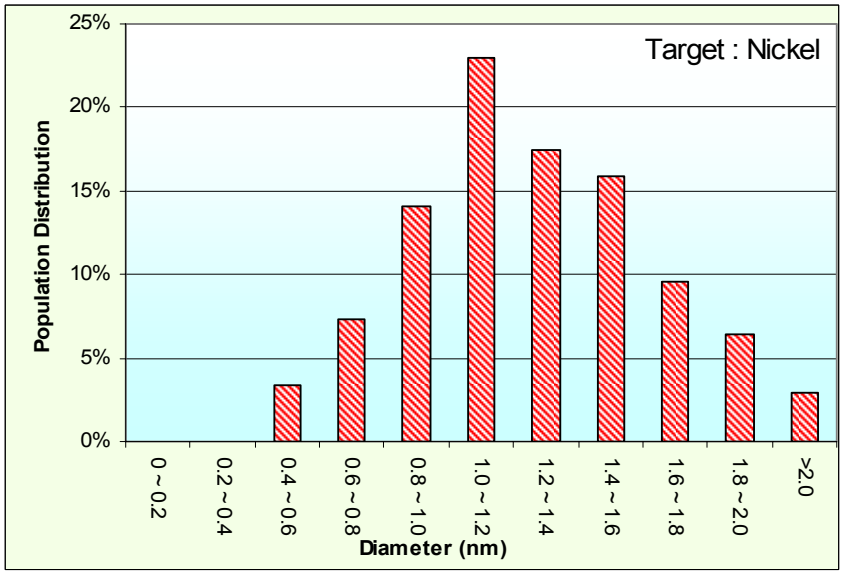

Figure 4- 68 Graph of experimental results of nanoparticle population distribution vs. diameter range of experiment 23 : Target Material Nickel

Experiment	24		
Laser Power (mW)	224	Pressure (Pa)	32000.00
Carrier Gas	Argon	Flow Rate (SLM)	0.6
Target Material	Copper	Temperature (K)	297.3

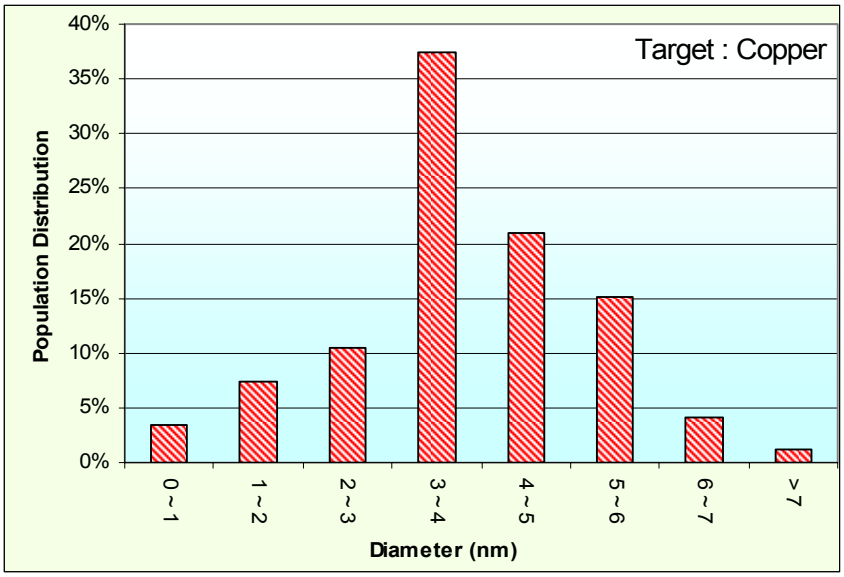

Figure 4- 69 Graph of experimental results of nanoparticle population distribution vs. diameter range of experiment 24 : Target Material Copper

Experiment	25		
Laser Power (mW)	224	Pressure (Pa)	32,000
Carrier Gas	Argon	Flow Rate (SLM)	0.60
Target Material	Zinc	Temperature (K)	297.3

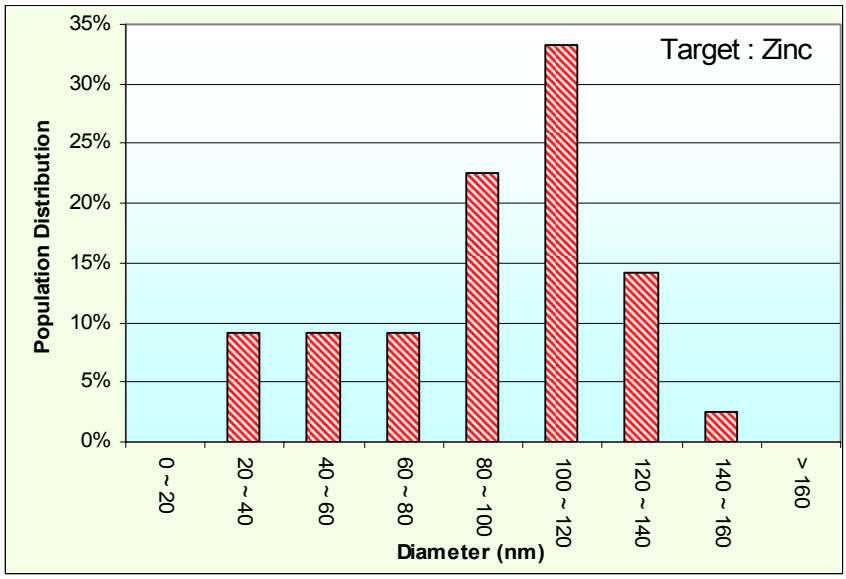

Figure 4- 70 Graph of experimental results of nanoparticle population distribution vs. diameter range of experiment 25 : Target Material Zinc

4.5.6 Experimental results of various Carrier Gas

Experiment	26		
Laser Power (mW)	220	Pressure (Pa)	34,000
Carrier Gas	Helium	Flow Rate (SLM)	0.60
Target Material	Titanium	Temperature (K)	297.3

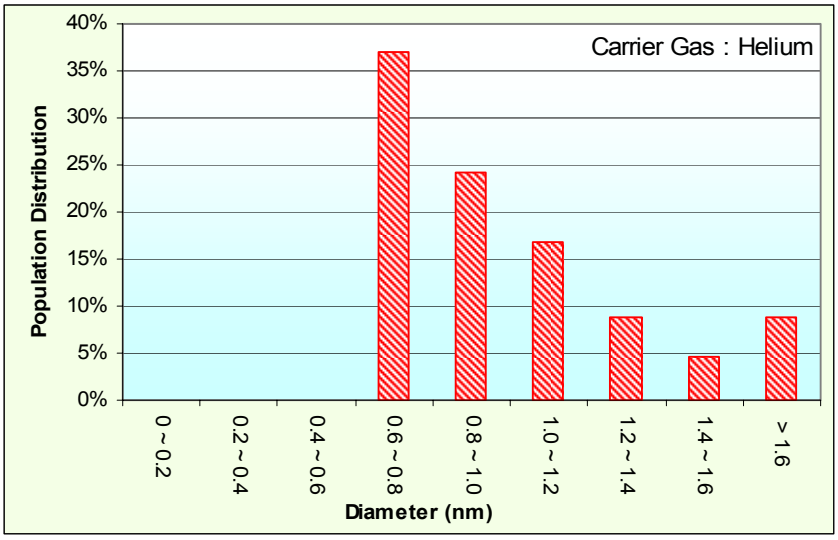

Figure 4- 71 Graph of experimental results of nanoparticle population distribution vs. diameter range of experiment 26 : Helium gas

Experiment	27		
Laser Power (mW)	220	Pressure (Pa)	34,000
Carrier Gas	Argon	Flow Rate (SLM)	0.60
Target Material	Titanium	Temperature (K)	297.3

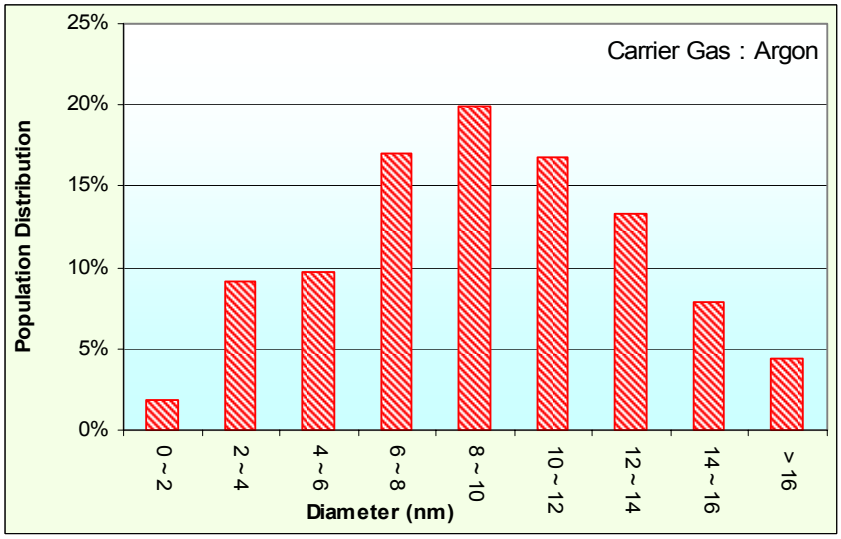

Figure 4- 72 Graph of experimental results of nanoparticle population distribution vs. diameter range of experiment 27 : Argon gas

Experiment	28		
Laser Power (mW)	220	Pressure (Pa)	34,000
Carrier Gas	Nitrogen	Flow Rate (SLM)	0.60
Target Material	Titanium	Temperature (K)	297.3

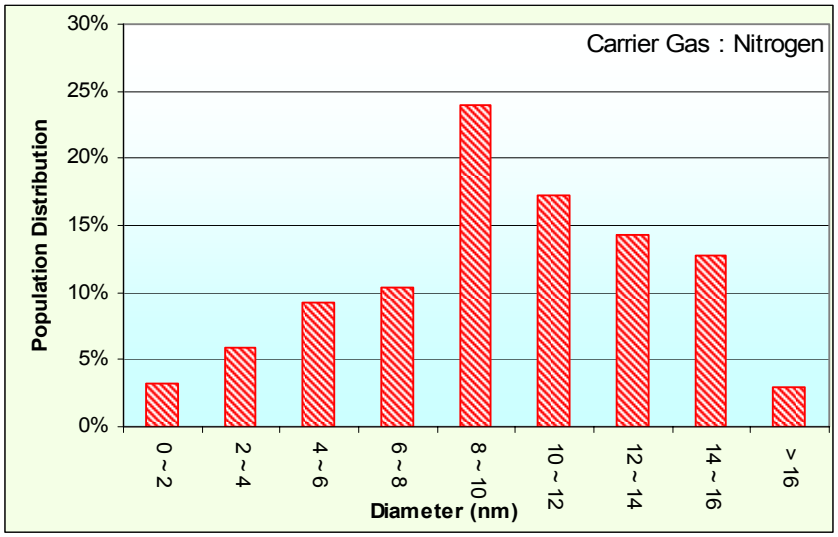

Figure 4- 73 Graph of experimental results of nanoparticle population distribution vs. diameter range of experiment 28 : Nitrogen gas

4.6 Summary

The equipment and experimental procedure were described in this chapter. Both the simulation data and experiment results were presented in graphs. Detail discussion of these results will be carried out it the next chapter.

5. Discussion

In this chapter, the results of the simulation model data and experimental results are discussed. All the forecasted simulation models data and collected experimental results are a huge collection of discrete values In order to have a meaningful analysis of these values; they are treated as population distributions. Naturally, statistical representative values of population distributions are used to quantify and present these data and results. The two statistical values used to help in the analysis were the *mean* and the *standard deviation*. The particle size diameter *mean* gives a representation of the diameter size of the population. Though it is a common aim for most researchers to achieve the smallest possible diameter, it is not the greatest concern to the industry. The properties of the nanoparticles are related to diameter sizes and more than often, industries are seeking a certain specific size , rather than the smallest diameter. The *standard deviation* of population gives a good indication of the spread of the distribution. The lower the standard deviation number, the narrow the range of the nanoparticle population. In contrast to mean, lower standard deviation range is sought after by both researchers and industry. A narrow range of nanoparticle sizes, ensures more consistent properties of the nanoparticles population as a whole.

The discussion is separated into six sub-sections as according to the six parameters. In each sub-section , the parameters are varied at different levels , and each level is consider as a experimental run. For every experimental run, the mean of each simulation distribution data is calculated and plotted against the variable parameters. A second set of curves of the mean of each of the corresponding experiment distribution results were plotted on the same graph. The trends of the each of the graphs are further explained as according to the model. The discrepancies between the model and experimental results are accounted for in this chapter. The same was done for the standard deviation of each experimental run as well.

In addition, *histograms* of both the simulation model data and experiments results were plotted together to aid in the study of the difference in the population distribution of the model and experimental data.

5.1 Effect of Laser Power

According to the model proposed, the diameter of the nanoparticle is directly proportional to the laser fluence as indicated in equation

$$d \propto (ln(F))^3$$ **Equation 5- 1**

The fluence (F) is in turn directly proportional to power (P). Thus,

$$d \propto (\ln(P))^3$$ **Equation 5- 2**

This relation between power and diameter was shown in good agreement to the model diameter mean, as well as in the experimental mean.

5.1.1 Comparison between model and experimental diameter mean of Laser Power variation

As mentioned above, the value of the diameter means for varying levels of laser power were computed. The resulting diagram is shown below in Figure 5-1. The general trend of both graphs shows that the higher the laser power, the larger the diameter of the nanoparticles. According to the proposed model, with higher laser power, more target metal material will be ablated. The greater the mass which was ablated into vapour, the larger the monomer population, which in turn increased the rate of particle growth. This reasoning is further strengthened by the results obtained from the experiments.

However, the values of the diameter mean measured from the experiments were generally larger than the model prediction, as seen in figure 5-2. A table of this difference is shown in table 5-1.

Laser Power (mW)	Varies	Pressure (Pa)	32,000
Carrier Gas	Argon	Flow Rate (SLM)	0.60
Target Material	Titanium	Temperature (K)	297.3

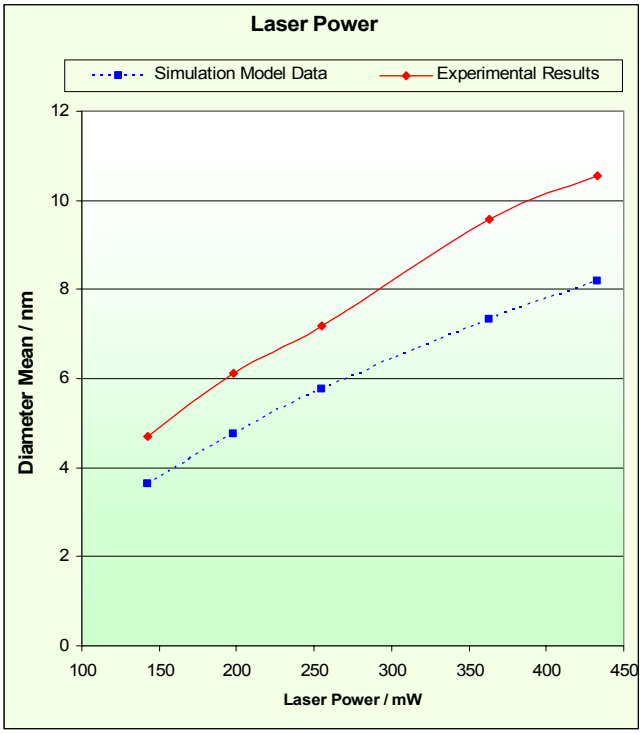

Figure 5- 1 Graph of diameter mean of model and experimental vs. variation in Laser Power.

A paired-test was conducted on the difference of the diameter mean of the model data and experimental results. The null hypothesis was set that there is no difference in the diameter mean. In other words, both model data and experimental results coincide with each other. The alternative hypothesis was set as otherwise. The paired-test value of each of the difference is computed and tabulated in table 5-1. A trial test for two tails at 95% confidence limit was performed against each of the paired–test value. The corresponding critical points of Z-distribution value of two tails test at 95% confidence limit is given in table 5-1 as well. If the value of the paired-test is greater than the critical point,

than the value of the paired-test falls outside the confidence limit and the hypothesis is failed. It is observed that all the five experiment runs with laser power variation failed the hypothesis that both the model data and experimental results has the same diameter mean.

Table 5-1 Table of paired Z-test of diameter mean difference of Laser Power variation of two tails trial test at 95% confidence limit.

Experiment Run number	Laser Power (mW)	Diameter mean difference (nm)	Paired - Test Value	Critical point of 2 tails Z-distribution at 95 % confidence limit
1	143	1.0654	0.461225	1.959964
2	198	1.3453	0.396641	1.959964
3	255	1.4132	0.370113	1.959964
4	363	2.2409	0.331401	1.959964
5	433	2.3693	0.350987	1.959964

This discrepancy could be explained by the assumptions 16 and assumption 17 stated for the proposed model. As recalled from chapter 3 :

Assumption 16

In the condition of laminar flow, the effect of particle growth by coalescence / and coagulation is much lesser than by the absorption of atomic vapour (monomer).

Assumption 17

Absorption of atomic vapour (monomer) is the only mechanism of nucleus growth.

In the absence of consideration for coagulation and coalescence, partial of the particular growth mechanism was not taken into account. Consequentially, the model predicted a lower value for diameter. These phenomena and discrepancies will be discussed more in depth later in this chapter, sub-section 5.4. In some of the experimental runs, environmental conditions were set to reduce the occurrences of coagulation and coalescence to the minimum.

During these runs, when the carrier flow rate is above 0.5 SLM, the differences between simulation and experiment were found to be very small.

Laser Power (mW)	Varies	Pressure (Pa)	32,000
Carrier Gas	Argon	Flow Rate (SLM)	0.60
Target Material	Titanium	Temperature (K)	297.3

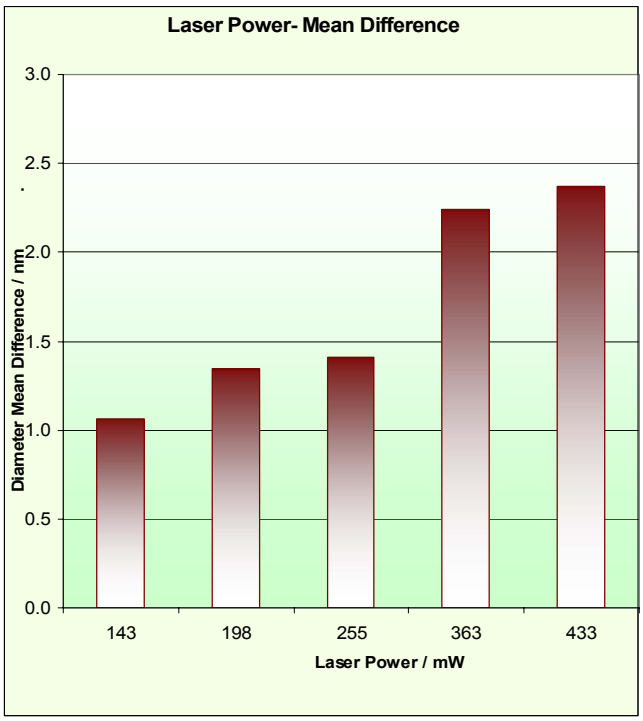

Figure 5- 2 Graph of diameter mean differences vs. variation in Laser Power.

5.1.2 Comparison between model and experimental standard deviation of Laser Power variation

As mentioned above, with the increase in laser power, the larger the population of monomers formed, the higher probability of collision between the monomers and the growing nucleus. With a larger population of monomers, the greater number of permutation of collisions between monomers and the different sizes of growing nuclei. Thus the collision frequency between the monomers and each growing nuclei were no longer the same as the others. Eventually the rate

of each nuclei growth deviated from each other. The larger the differences, the greater the range of nanoparticle sizes existing in a single population.

Likewise to the diameter mean of the nanoparticles, the standard deviation calculated from the simulation shows a positive proportional relationship with the laser power level. From figure 5-3, it is seen that the higher the laser power, the greater the standard deviation. The values obtained from the experiments also agree with this trend.

Laser Power (mW)	Varies	Pressure (Pa)	32,000
Carrier Gas	Argon	Flow Rate (SLM)	0.60
Target Material	Titanium	Temperature (K)	297.3

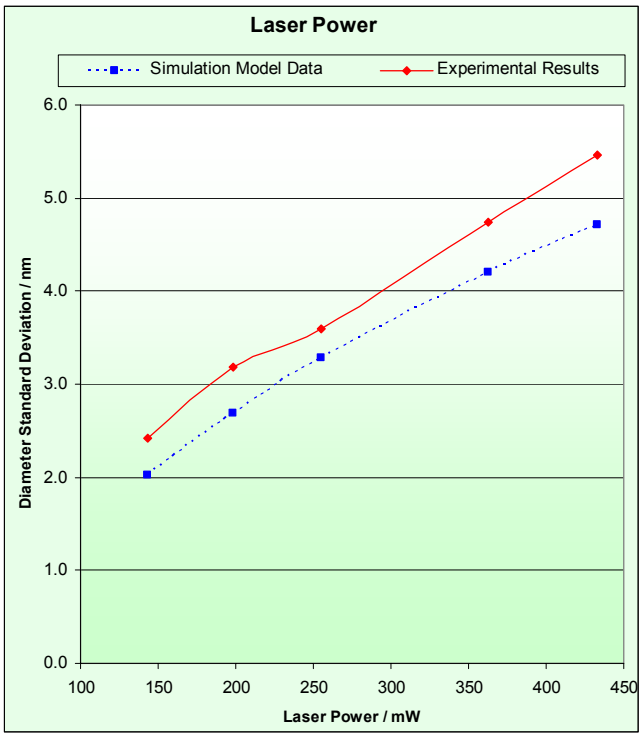

Figure 5- 3 Graph of standard deviation of model and experimental diameter vs. variation in Laser Power.

Similarly to the diameter means, the values of the standard deviation measured from experiments are generally higher than that of the model, as shown in

figure 5–4. These differences could be accounted for again by the two assumptions taken by the proposed model as explained earlier.

Laser Power (mW)	Varies	Pressure (Pa)	32,000
Carrier Gas	Argon	Flow Rate (SLM)	0.60
Target Material	Titanium	Temperature (K)	297.3

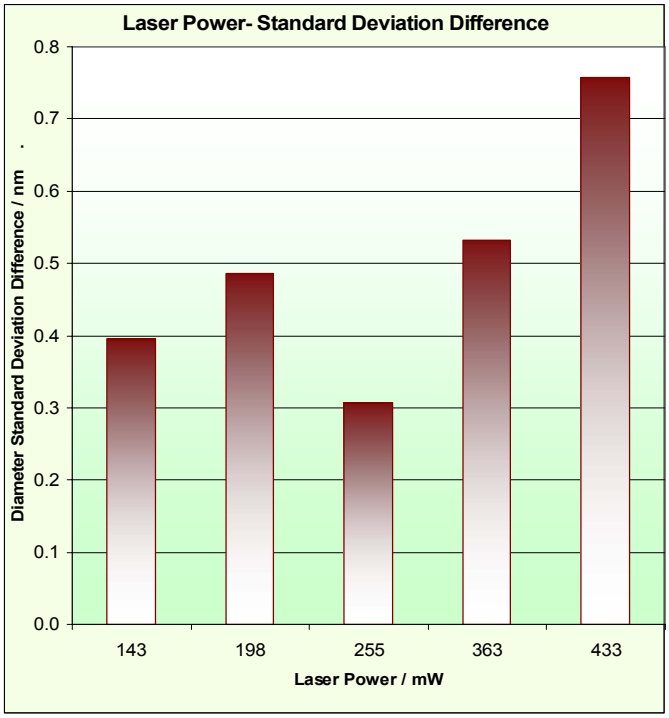

Figure 5- 4 Graph of diameter standard deviation differences vs. variation in Laser Power.

5.1.3 Nanoparticle population distribution obtained by various Laser Powers

Nevertheless, the *standard deviation* is still unable to reflect the shape of the distribution curve. In order to present the shape of the distribution histograms were plotted. Following, in figures 5-5 (a) to (e), it is shown that the spread of the distribution of both the model and experiments are different. While the model predicts an undulating distribution with two peaks, the experiments yields curves of close resemblance to that of an Erlang distribution with shape

parameters of 2 to 5. They all have only a single peak, and are skewed towards the lower distribution of the population. Table 5-2 below shows the skewness of each graphs. The value of skew for the model data and its corresponding experimental results are not the same as expected as both have different distribution spread. However, both the data and results share the common trend of increasing skewness as the laser power increases. Generally, when the value of the skew of a distribution curve increases, it indicates that the mode of the distribution is becoming larger than its mean. In this case of the histogram, it also indicates both the mean and standard deviation of the nanoparticles population are increasing as well. This is in coincidence to the explanations given in discussion of higher laser power results in lager diameter mean. In the five histograms graphs of figures 5-5 (a) to (e), the population with larger diameter mean has more positive skew number for its histogram graph.

Table 5-2 Table of skew of the histogram graphs of difference of Laser Power variation.

Experiment Run number	Laser Power (mW)	Model Data Histogram Skewness	Experimental Results Histogram Skewness
1	143	0.378	0.178
2	198	-0.448	0.336
3	255	-0.438	0.266
4	363	-1.029	0.198
5	433	-1.036	0.725

One interesting consistency to note is that the *mode* of the experiments results and the *mean* of the simulation data, both fall in the same *range* in the histogram. This observation is of interest because the same trend is observed for most of the experimental runs, as will be presented later in this chapter.

Figure 5- 5 Histogram Graphs of nanoparticle population obtained from simulation model data and experimental results of Laser Power at (a)143mW, (b)198mW, (c)255mW, (d)363mW, (e)433mW.

Laser Power (mW)	Varies	Pressure (Pa)	32,000
Carrier Gas	Argon	Flow Rate (SLM)	0.60
Target Material	Titanium	Temperature (K)	297.3

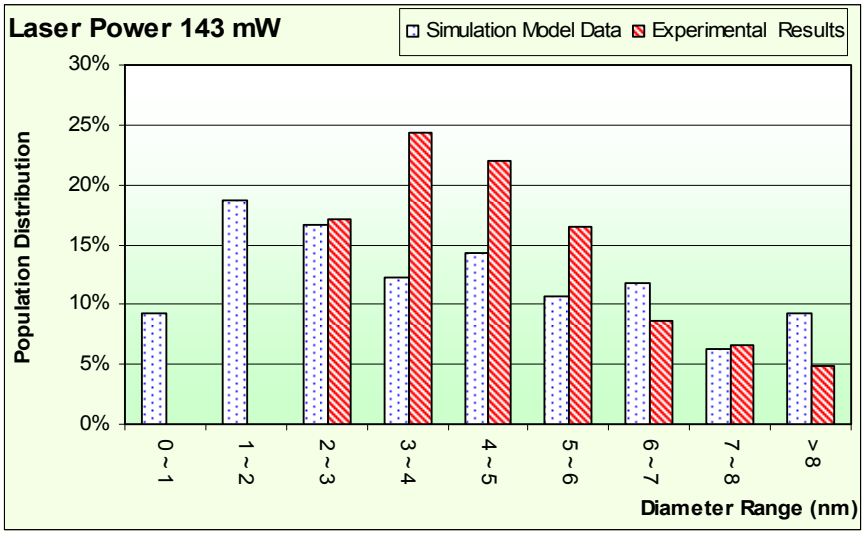

(a)

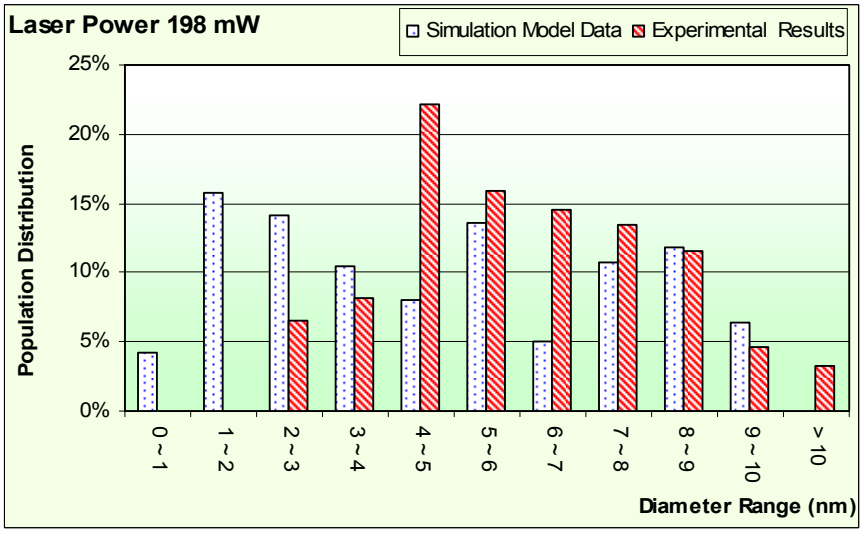

(b)

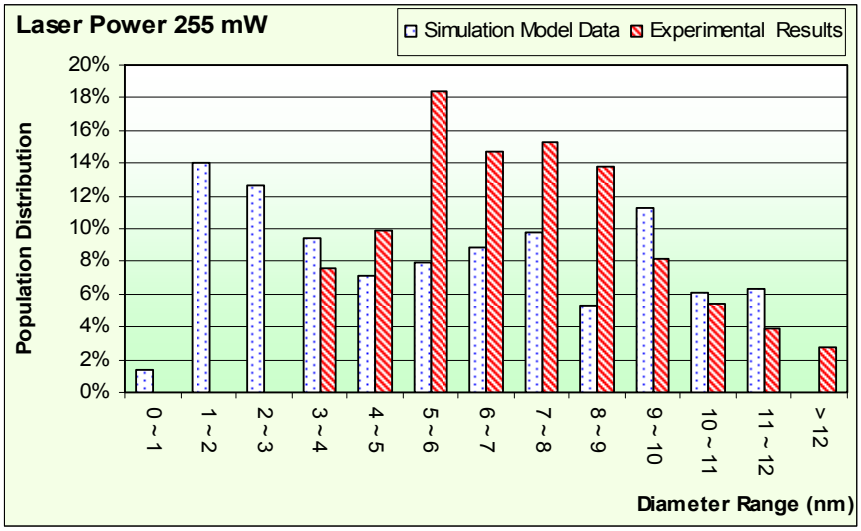
Laser Power 255 mW
Simulation Model Data
Experimental Results
Population Distribution
20%
18%
16%
14%
12%
10%
8%
6%
4%
2%
0%
0 ~ 1
1 ~ 2
2 ~ 3
3 ~ 4
4 ~ 5
5 ~ 6
6 ~ 7
7 ~ 8
8 ~ 9
9 ~ 10
10 ~ 11
11 ~ 12
> 12
Diameter Range (nm)

(c)

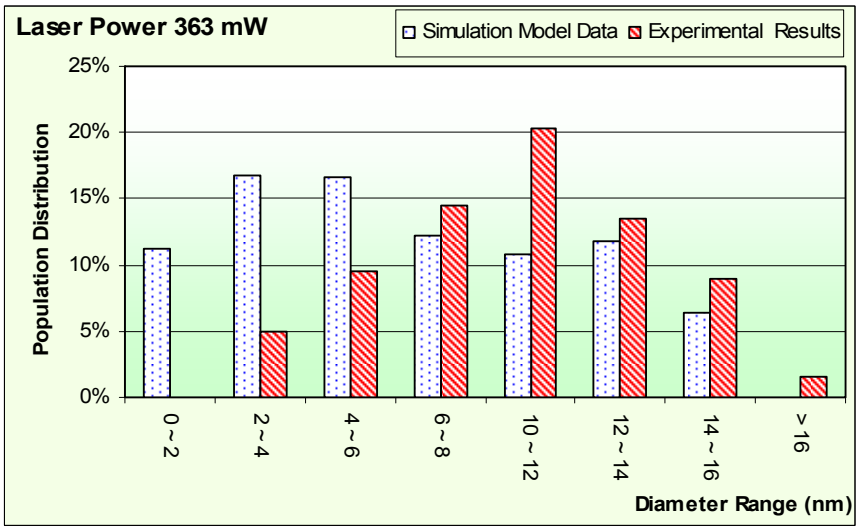
Laser Power 363 mW
Simulation Model Data
Experimental Results
Population Distribution
25%
20%
15%
10%
5%
0%
0 ~ 2
2 ~ 4
4 ~ 6
6 ~ 8
10 ~ 12
12 ~ 14
14 ~ 16
> 16
Diameter Range (nm)

(d)

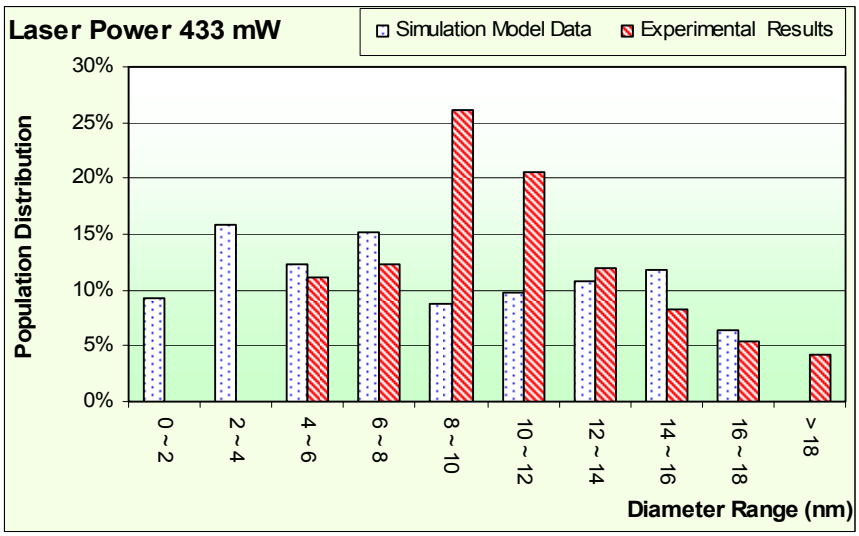
Laser Power 433 mW
Simulation Model Data
Experimental Results
Population Distribution
30%
25%
20%
15%
10%
5%
0%
0 ~ 2
2 ~ 4
4 ~ 6
6 ~ 8
8 ~ 10
10 ~ 12
12 ~ 14
14 ~ 16
16 ~ 18
> 18
Diameter Range (nm)

(e)

5.2 Effect of Pressure

Data computed from the simulation and results collected from the experiments were plotted against each other in the same graph, as shown in figures 5-6. Figure 5-7 displays the mean difference between the two graphs. By rearranging the proposed model and expressing the nanoparticle diameter in terms of pressure, the resulting expression will prove to be very complex. Instead , a crude but fairly accurate approach of *dimensional analysis* could be considered to establish a relationship between the diameter mean and pressure. By use of *dimensional analysis*, an empirical relationship was found between the diameter and pressure,

$$d \propto P \qquad \textbf{Equation 5- 3}$$

5.2.1 Comparison between model and experimental diameter mean of Pressure variation

The positive direct proportional relationship between diameter and pressure was clearly shown in figure 5-6. However, the graph plotted in figure 5 - 6 does not reveal the linear relationship as predicted by the dimensional analysis. Nevertheless, both the analysis and graph show that the pressure has a positive effect on both the diameter mean as well as its standard deviation. That is, an increase in pressure will result in an increase in diameter mean and standard deviation. This effect is more pronounced when the pressure exceeds 35,000 Pa. The graphs on figure 5-6 show that the actual relationship between diameter mean and pressure is more similar to that of an exponential curve with a power of two.

According to the *Ideal Gas Law*, an increase in carrier gas pressure results in more carrier gas molecules in the nucleus growth chamber. With larger population of carrier gas molecules, the number of collisions between these gas molecules and monomers will increase. These elevated collisions lead to

more interaction probabilities between these monomers and the growing nuclei. These intensified interactive activities amplified the growth rate of the nuclei into larger nanoparticles. As a result the higher pressure leaded to larger nanoparticles diameter.

Laser Power (mW)	198	Pressure (Pa)	Varies
Carrier Gas	Argon	Flow Rate (SLM)	0.60
Target Material	Titanium	Temperature (K)	297.3

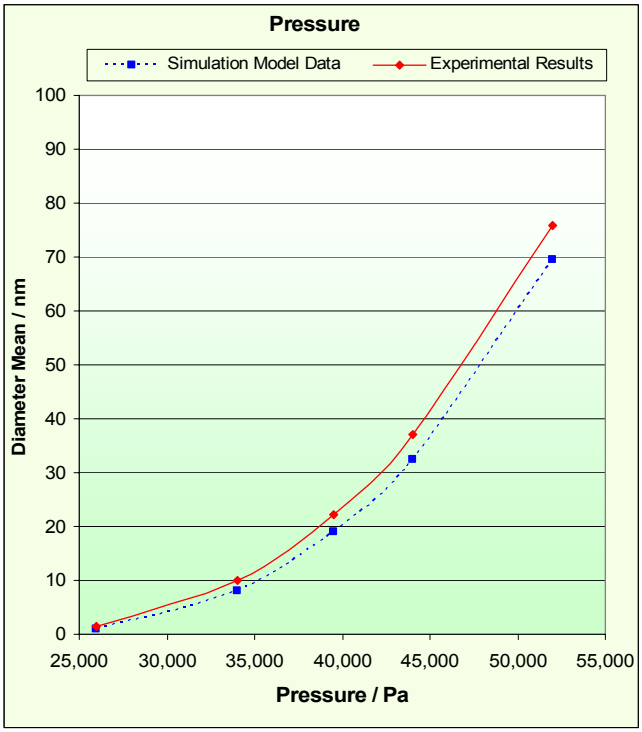

Figure 5- 6 Graph of diameter mean of model and experimental vs. variation in Pressure.

Figure 5-7 shows a graph of the diameter mean difference of the actual experimental results and computer simulated data. Similar to the previous experimental set with *Laser Power* variation, the actual experiment results of the diameter mean and standard deviation are larger than the prediction of the computer simulation.

A table of this diameter mean difference is shown in table 5-2. The same set of hypothesis was used as in subsection 5.1 of *Laser Power* variation. The paired-test values for the difference were computed together with the corresponding critical points of their two tails Z-distribution at 95% confidence limit. Based on

the Z-test , there is no enough evidence to conclude that there is any significant difference between the model data and experimental results.

Table 5-3 Table of paired Z-test of diameter mean difference of Pressure variation of two tails trial test at 95% confidence limit.

Experiment Run number	Pressure (KPa)	Diameter mean difference (nm)	Paired-Test Value	Critical point of 2 tails Z - distribution at 95 % confidence limit
6	26	0.5660	1.234668	1.959964
7	34	2.1062	0.350043	1.959964
8	39.5	3.0407	0.402559	1.959964
9	44	4.6429	0.619628	1.959964
10	52	6.4271	1.700825	1.959964

Laser Power (mW)	198	Pressure (Pa)	Varies
Carrier Gas	Argon	Flow Rate (SLM)	0.60
Target Material	Titanium	Temperature (K)	297.3

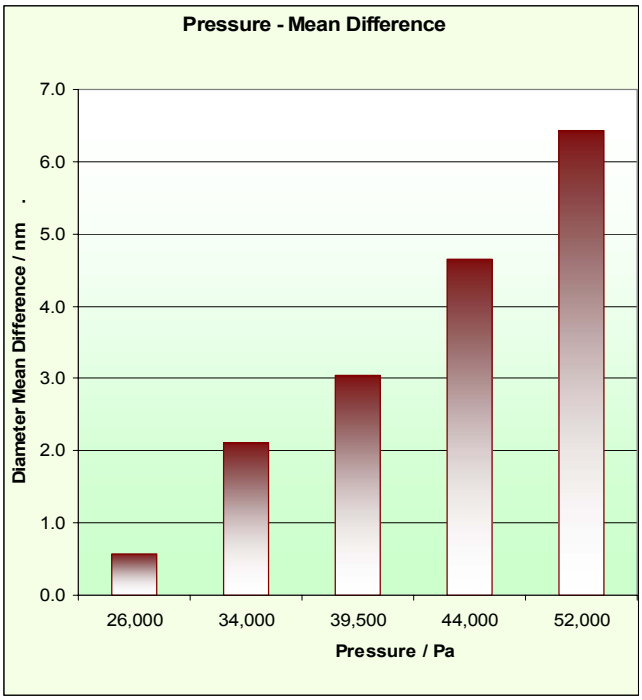

Figure 5- 7 Graph of diameter mean differences vs. variation in Pressure

The discrepancies will be explained later in the report and the details will be discussed in sub-section *5.4* of *Flow Rate* variation. The predication of the computed simulation model has two assumptions that ignore the process of coagulation and coalescence.

5.2.2 Comparison between model and experimental diameter standard deviation of Pressure variation

In the same way, the standard deviation of both model and experiments under higher pressure conditions are larger than for lower pressure. According to *Kinetic Ideal Gas Theory*, higher pressure carrier gas contains more gas molecules. This leads to more collisions between growing nuclei and monomers. With higher number of interactions, the probabilities of different permutations of collisions between growing nuclei and monomers of various energy level increases. Thus as shown in the graphs in figure 5-8 , higher pressure resulted in a wider standard deviation for the nanoparticle population.

Laser Power (mW)	198	Pressure (Pa)	Varies
Carrier Gas	Argon	Flow Rate (SLM)	0.60
Target Material	Titanium	Temperature (K)	297.3

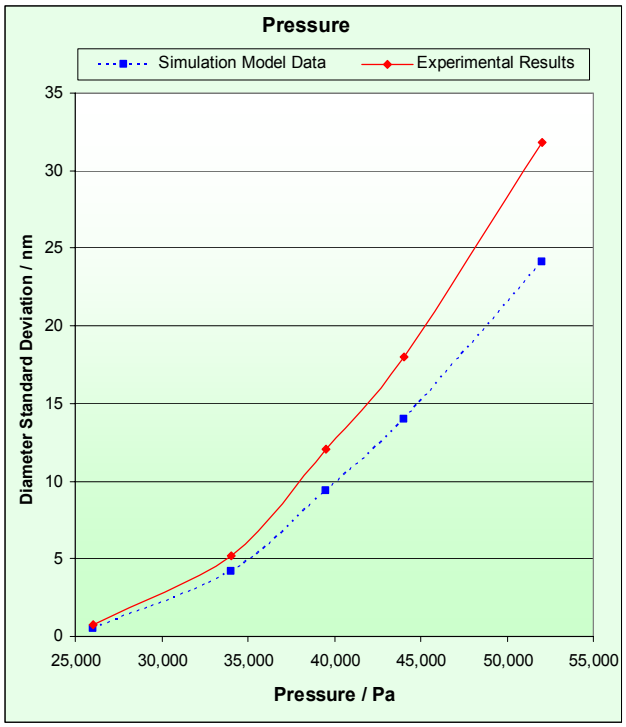

Figure 5- 8 Graph of standard deviation of model and experimental diameter vs. variation in Pressure

Figure 5-9 below, shows the difference between the diameter standard deviation of the model and experimental results. It can be observed from the graph, the differences increases more as the pressure variation goes higher. This observation coincides with the explanation offered before. When the pressure is higher, coagulation and coalescence are more pronounced, and have larger effects on the rate of growth for the nuclei population. In the model, coagulation and coalescence were not included. Thus, the lower growth rates of the model than experimental results are responsible to the difference between the model data and the experimental results. As predicated, the difference widened as the pressure increases.

Laser Power (mW)	198	Pressure (Pa)	Varies
Carrier Gas	Argon	Flow Rate (SLM)	0.60
Target Material	Titanium	Temperature (K)	297.3

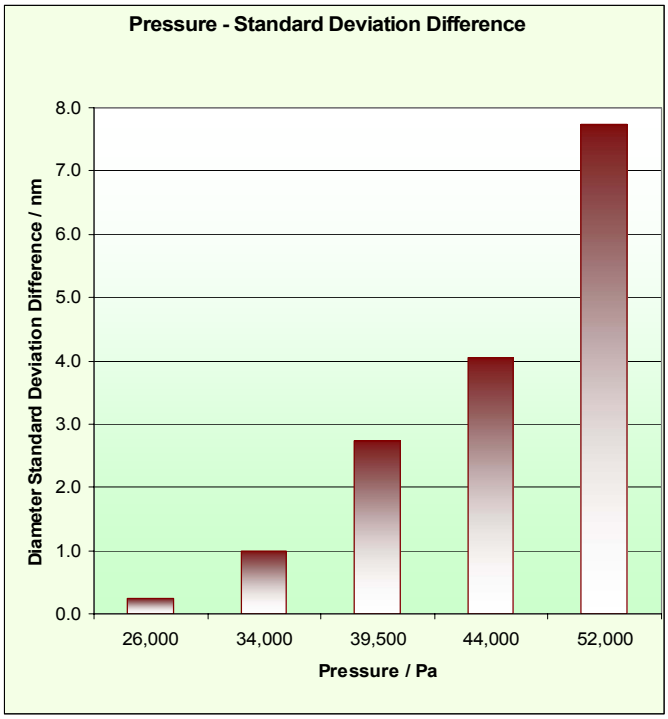

Figure 5- 9 Graph of diameter standard deviation differences vs. variation in Pressure

5.2.3 Nanoparticle population distribution obtained by various Pressure

Following in figures 5-10 (a) to (e), the histograms of the nanoparticles populations of pressure variation from 26KPa to 52KPa are presented. In each of these histograms, both the simulation model data and experiments results were plotted against each other. As explained earlier, the histograms were used to study the actual distribution of the different populations. One interesting observation is that the skew of the population is seen to lean towards the right as the pressure increases. The trend is most significant when the pressure reaches 52,000 Pa. The same reasoning offered before could account for this observation. The greater pressure leads to more collisions, which in turn increases the growth rate, resulting in larger nanoparticles and wider spread of diameters variation.

Table 5-4 below shows the skewness of each of the histogram graphs of various pressures. Similar to the graphs of laser power variation, both the model data and experimental results share the common trend of increasing skewness as the pressure increases. This is in tally to the explanations given in discussion of higher pressure results in larger diameter mean. For the graphs in figures 5-10 (a) to (e), graphs with lager diameter have more positive skew number. However, the histograms each have different numbers of ranges, it is not able to draw a conclusive comparison between each skew values.

Table 5-4 Table of skew of the histogram graphs of difference of Pressure variation.

Experiment Run number	Pressure (KPa)	Model Data Histogram Skewness	Experimental Results Histogram Skewness
6	26	-1.361	-0.462
7	34	-0.491	0.376
8	39.5	-0.367	0.507
9	44	-0.789	1.265
10	52	0.134	0.637

The same interesting consistency found in section *5.1 Effect of Laser Power*, is again observed here. The *mode* of the experiments results and the *mean* of the simulation data, both fall in the same *range* in the histograms.

Figure 5- 10 Histogram graphs of nanoparticle population obtained from simulation model data and experiments results of Pressure (a) 26KPa, (b) 34KPa, (c) 39.5KPa, (d) 44KPa, (e) 52KPa.

Laser Power (mW)	198	Pressure (Pa)	Varies
Carrier Gas	Argon	Flow Rate (SLM)	0.60
Target Material	Titanium	Temperature (K)	297.3

(a)

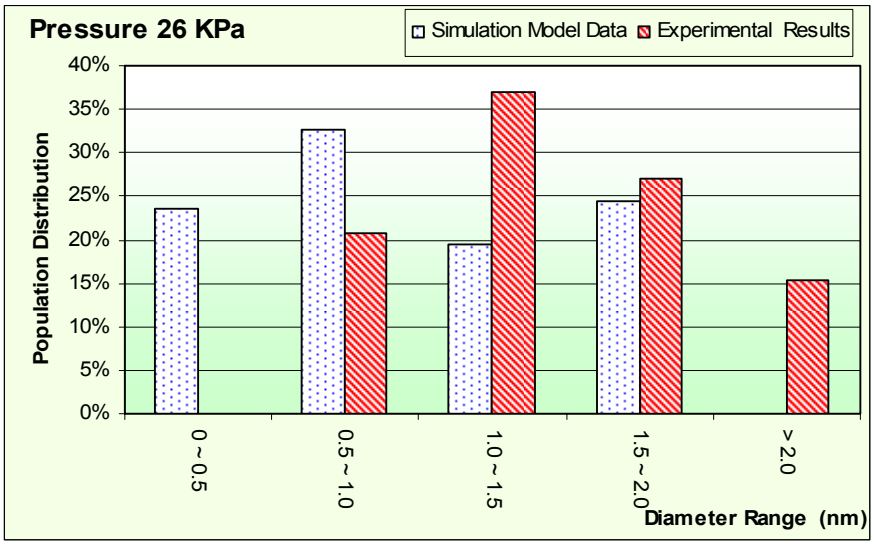

(b)

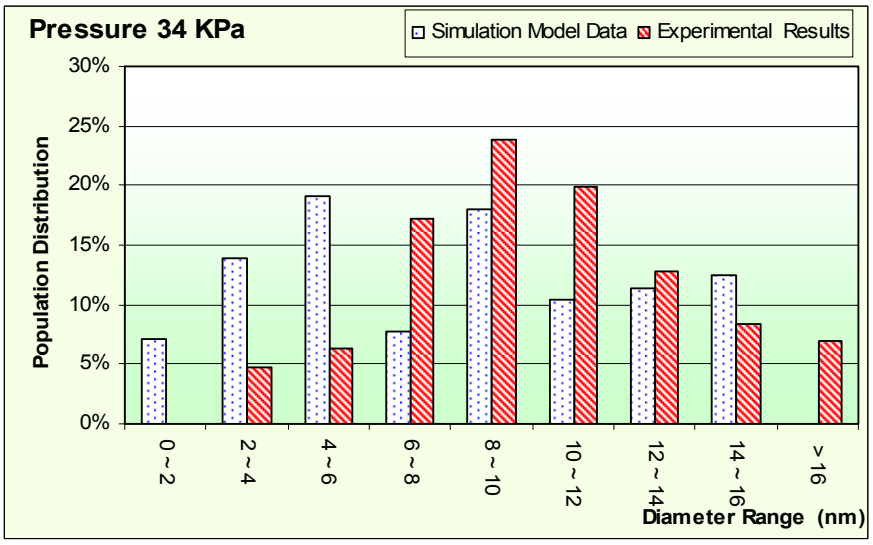

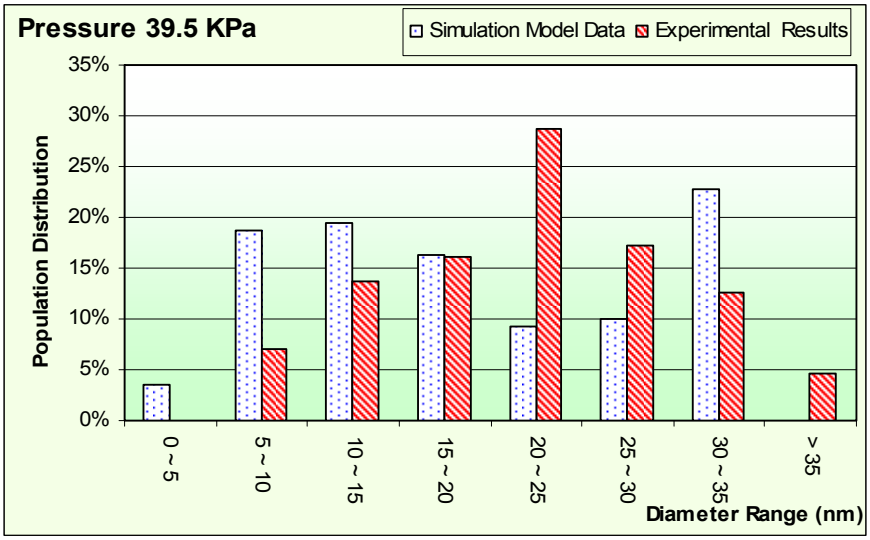
Pressure 39.5 KPa
Simulation Model Data
Experimental Results
Population Distribution
35%
30%
25%
20%
15%
10%
5%
0%
0 ~ 5
5 ~ 10
10 ~ 15
15 ~ 20
20 ~ 25
25 ~ 30
30 ~ 35
> 35
Diameter Range (nm)

(c)

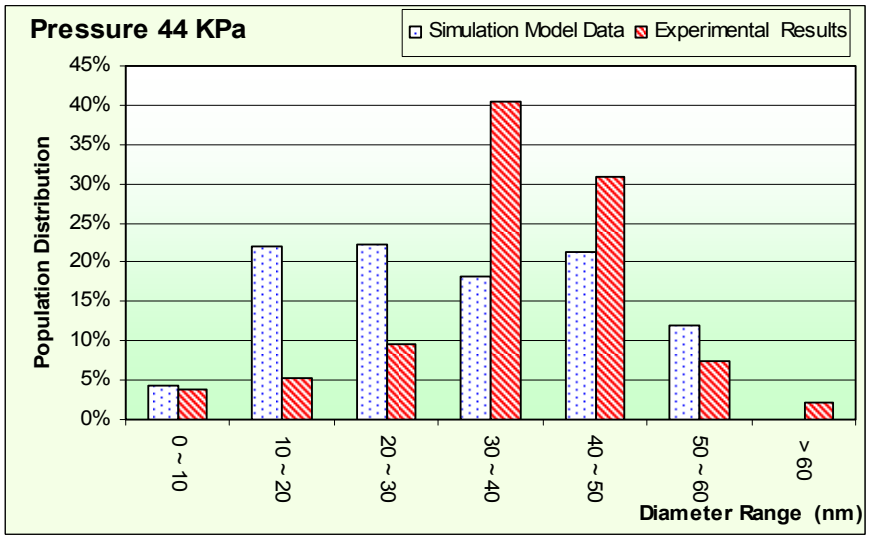
Pressure 44 KPa
Simulation Model Data
Experimental Results
Population Distribution
45%
40%
35%
30%
25%
20%
15%
10%
5%
0%
0 ~ 10
10 ~ 20
20 ~ 30
30 ~ 40
40 ~ 50
50 ~ 60
> 60
Diameter Range (nm)

(d)

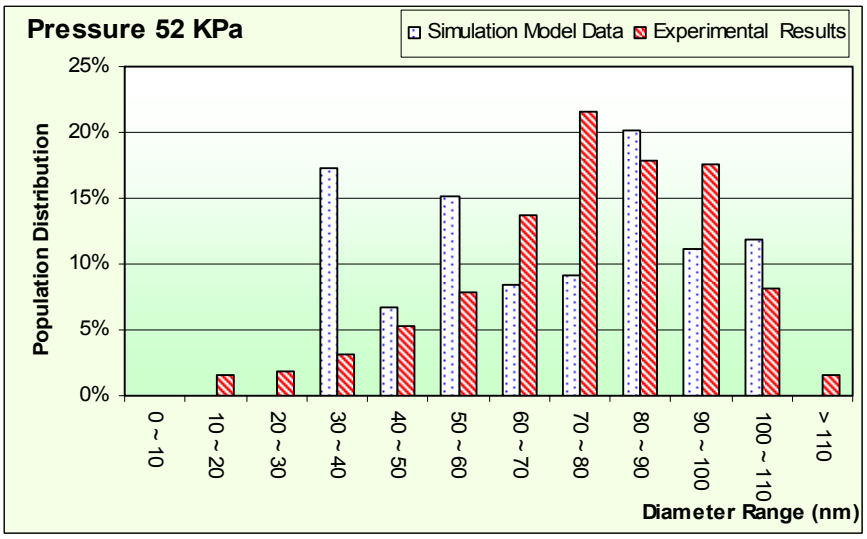
Pressure 52 KPa
Simulation Model Data
Experimental Results
Population Distribution
25%
20%
15%
10%
5%
0%
0 ~ 10
10 ~ 20
20 ~ 30
30 ~ 40
40 ~ 50
50 ~ 60
60 ~ 70
70 ~ 80
80 ~ 90
90 ~ 100
100 ~ 110
> 110
Diameter Range (nm)

(e)

5.3 Effect of Temperature

Following the same investigation approach of dimension analysis as in section 5.2, the relation between the nanoparticle diameter and temperature of the chamber can be expressed by a simplified relationship of proportion,

$$d \propto T \qquad \textbf{Equation 5- 4}$$

From the above relationship, we expect to find the diameter mean and standard deviation to have positive relationship to the temperature of the chamber.

5.3.1 Comparison between model and experimental diameter mean of Temperature variation

Figure 5-11 displays the diameter mean of the nanoparticles formed under various chamber temperature conditions. As predicted, both the curves of mean and standard deviation increase as the temperature is elevated. However, different from pressure variation, the curves for both the mean and standard deviation have relative smaller variation within the range of research 290 K to 340 K.

As proposed by James Clerk Maxwell in 1866, the kinetic energy of a gas molecule is directly proportional to its temperature. With higher chamber temperature, the kinetic energy levels of the carrier gas molecules are higher. Each time there is a collision with the carrier gas molecules, these kinetic energies were transferred to the monomers by momentum exchange. With higher kinetic energy in the monomers, there are more collisions resulting in more monomers successfully adhering to the growing nuclei. The high success rate gives rise to the growth rate of the nucleus into a nanoparticle. The faster growth rate yields larger nanoparticles of larger diameter.

Alternatively, the phenomena could be accounted for from the perspective of simple energy transfer. The greater thermal energy, from higher temperature, is transformed in to greater kinetic energy which lead to more collision. In additional, higher kinetic energy collision provides the binding energy requires for the monomer adhesion onto the nuclei. Thus, with a higher chamber temperature, the nanoparticles formed have a larger diameter mean.

Laser Power (mW)	218	Pressure (Pa)	31,000
Carrier Gas	Argon	Flow Rate (SLM)	0.60
Target Material	Titanium	Temperature (K)	Varies

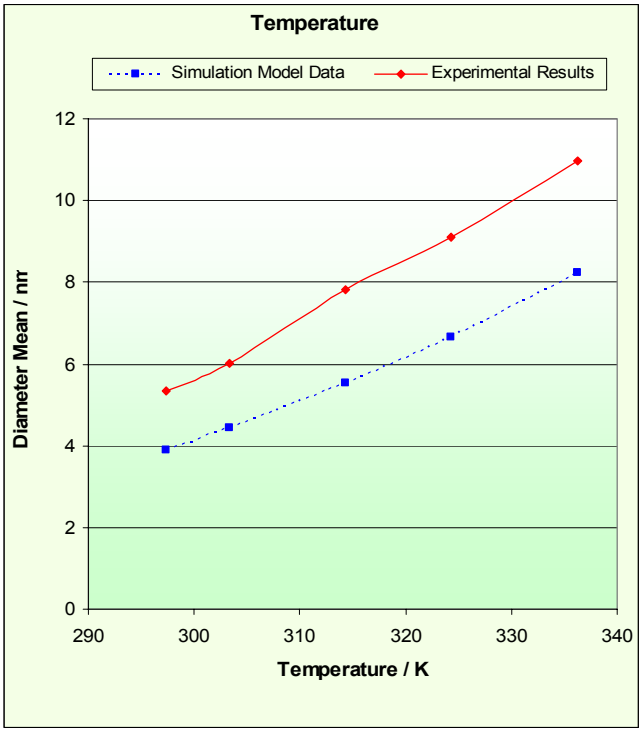

Figure 5- 11 Graph of diameter mean of model and experimental vs. variation in Temperature

Figure 5-12 below shows the graph of the difference of diameter mean between the data of model simulation and results of experiments. Displayed in table 5-3 below is the value of paired-test the diameter mean difference with critical points of two tails Z-distribution trial at 95% confidence limit. The hypothesis used is the same as in subsection 5.1 *Effects of Laser Power*. Based on the Z-test, there is no evidence to suggest that there is any significant difference

between the model data and experimental results for diameter mean of the nanoparticles.

Table 5-5 Table of paired Z-test of diameter mean difference of Temperature variation of two tails trial test at 95% confidence limit..

Experiment Run number	Temperature (K)	Diameter mean difference (nm)	Paired -Test Value	Critical point of 2 tails Z -distribution at 95 % confidence limit
11	297.3	1.4610	0.446131	1.959964
12	303.3	1.5950	0.408958	1.959964
13	314.3	2.3032	0.380002	1.959964
14	324.3	2.4233	0.342700	1.959964
15	336.3	2.7532	0.308889	1.959964

The difference in diameter mean is due to assumptions 16 and 17 taken in the model. The assumptions omitted the consideration of coagulation and coalescence. Though these two processes exist in reality, the effects are not so significant in the case of temperature variation. Detail of the discussion of both coagulation and coalescence will be done in section *5.4 Effect of Flow Rate*.

Laser Power (mW)	218	Pressure (Pa)	31,000
Carrier Gas	Argon	Flow Rate (SLM)	0.60
Target Material	Titanium	Temperature (K)	Varies

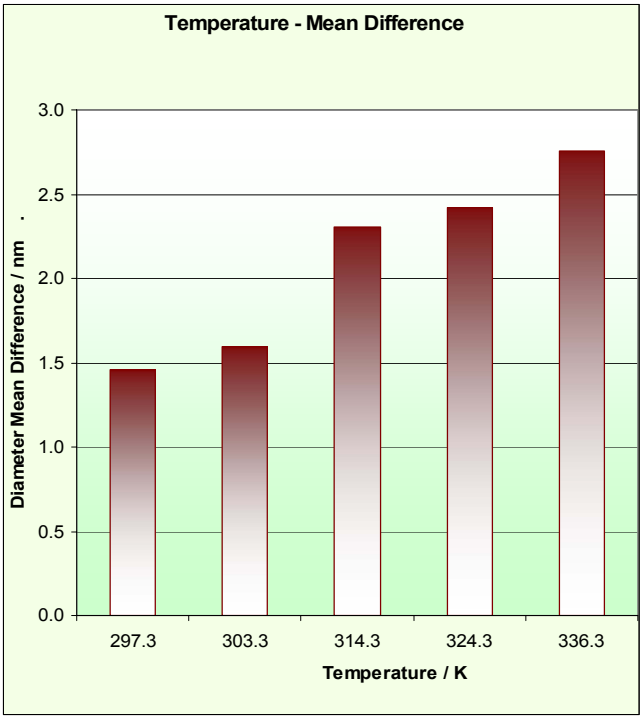

Figure 5- 12 Graph of diameter mean difference vs. variation in Temperature

5.3.2 Comparison between model and experimental diameter standard deviation of Temperature variation

The *Maxwell-Boltzmann distribution function* gives a good description of how the distribution of velocities of gas molecules is dependent on the temperature. According to the function relationship, the higher chamber temperature will have a more even distribution spread of gas molecules velocities. On the other hand, lower chamber temperature, will have gas molecules with narrower distribution of velocities concentrated at the lower velocities. Consequently, in the experiments, higher chamber temperature had the distribution of the kinetic energy of the monomers more evenly spread, which gave rise to a wider range of different growth rates of nuclei. This resulted in a wider range of nanoparticle diameters formed, which in turn yielded a larger range of nanoparticle diameter standard deviation as shown in figure 5-13.

Laser Power (mW)	218	Pressure (Pa)	31,000
Carrier Gas	Argon	Flow Rate (SLM)	0.60
Target Material	Titanium	Temperature (K)	Varies

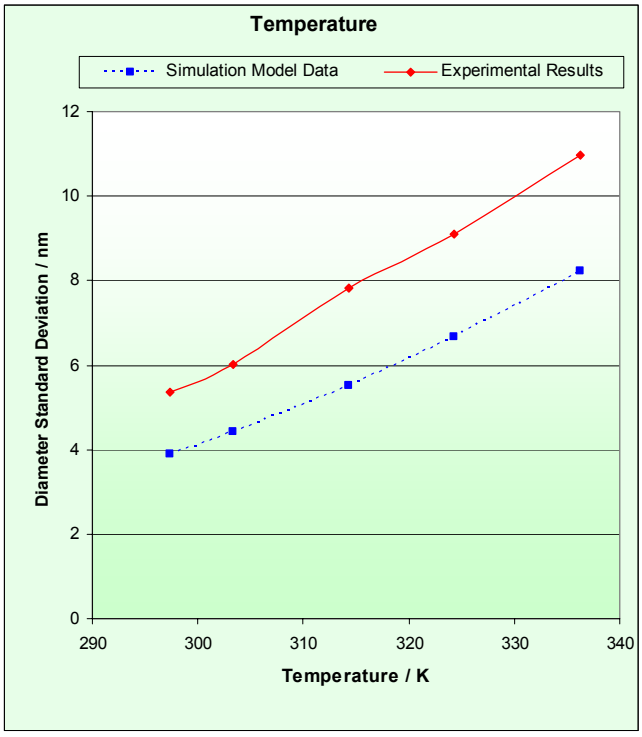

Figure 5- 13 Graph of standard deviation of model and experimental diameter vs. variation in Temperature

Figure 5-14, show the graphs of the difference of diameter standard deviation between model data and experimental results. Likewise, the difference varies very little with temperature variation. This is so for the same reason that the effects of coagulation and coalescence are almost the same within the temperature range of 290 K to 340 K.

Laser Power (mW)	218	Pressure (Pa)	31,000
Carrier Gas	Argon	Flow Rate (SLM)	0.60
Target Material	Titanium	Temperature (K)	Varies

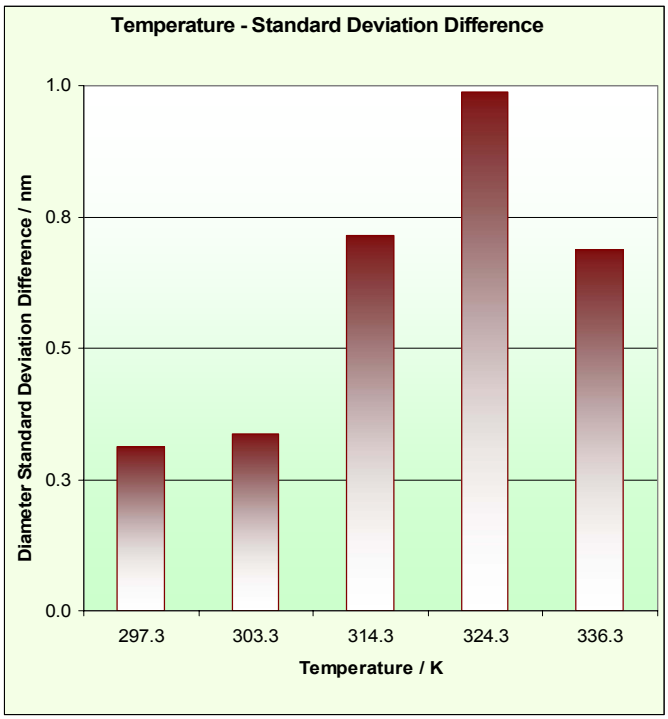

Figure 5- 14 Graph of diameter standard deviation difference vs. variation in Temperature

5.3.3 Nanoparticle population distribution obtained by various Temperature

Below in figures 5-15 (a) to (e), the histograms of nanoparticles population of various temperatures are shown. The distributions of the nanoparticles show a close resemblance to that of the Maxwell-Boltzmann distribution curve. The

lower temperature populations are skewed more towards the left hand side (smaller diameter), and have a higher percentage of lower diameter nanoparticles. The higher temperature populations are more evenly distributed, and skew more towards the right hand side (bigger diameter).

Following in table 5-6 gives the skew value of each of the histogram graphs of various pressures. Unlike the previous two sets of graphs of laser power and pressure variation, the graphs of temperature variation of both the model data and experimental results share the common trend of decreasing skewness as the temperature increases. This is in tally to the explanations given in discussion of elevated temperature results in larger diameter mean and wider standard deviation. Wider standard deviation distribution curve has more higher magnitude skew number. Same as pervious, the histograms each have different numbers of ranges; thus it is not possible to draw a conclusive comparison between each skew values within table5-6.

Table 5-6 Table of skew of the histogram graphs of difference of Pressure variation.

Experiment Run number	Temperature (K)	Model Data Histogram Skewness	Experimental Results Histogram Skewness
11	297.3	-1.004	-0.056
12	303.3	-0.798	0.404
13	314.3	-1.454	0.265
14	324.3	-1.661	0.084
15	336.3	-1.305	-0.365

Like the previous two sets of experimental runs, this set of experimental run of temperature variation has histograms with the *mode* of the experiments results and the *mean* of the simulation data, both belong to the same *range* in the histograms.

Figure 5- 15 Histogram graphs of nanoparticle population obtained from simulation model data and experiments results of Temperature (a) 297.3K, (b) 303.3K, (c) 314.3K, (d) 424.3 K, (e) 336.3K.

Laser Power (mW)	218	Pressure (Pa)	31,000
Carrier Gas	Argon	Flow Rate (SLM)	0.60
Target Material	Titanium	Temperature (K)	Varies

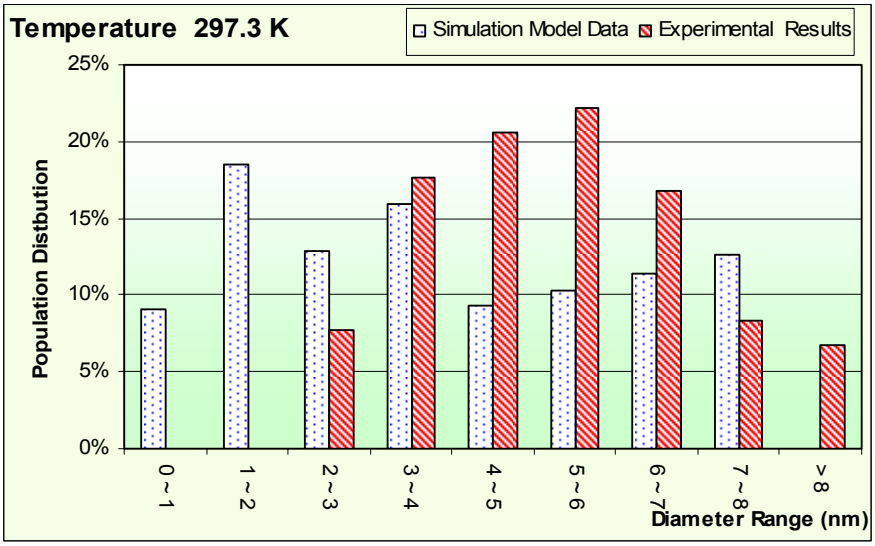

(a)

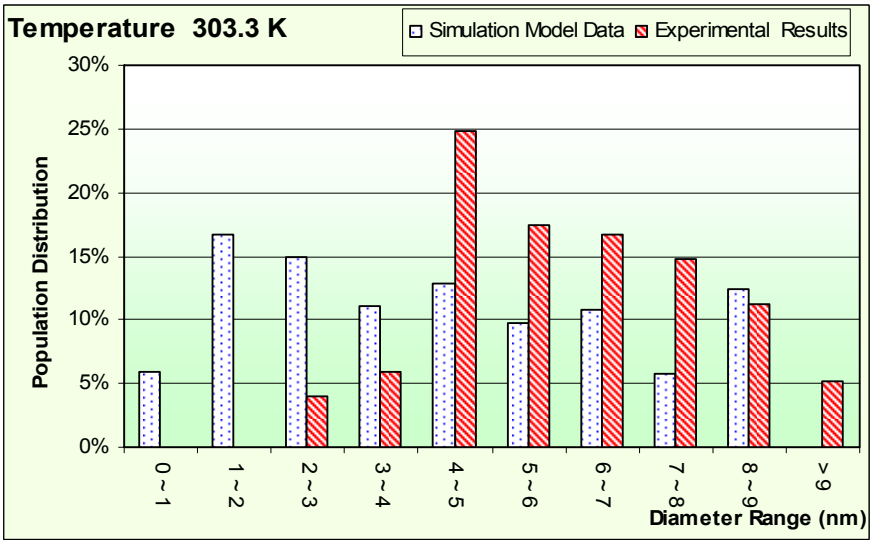

(b)

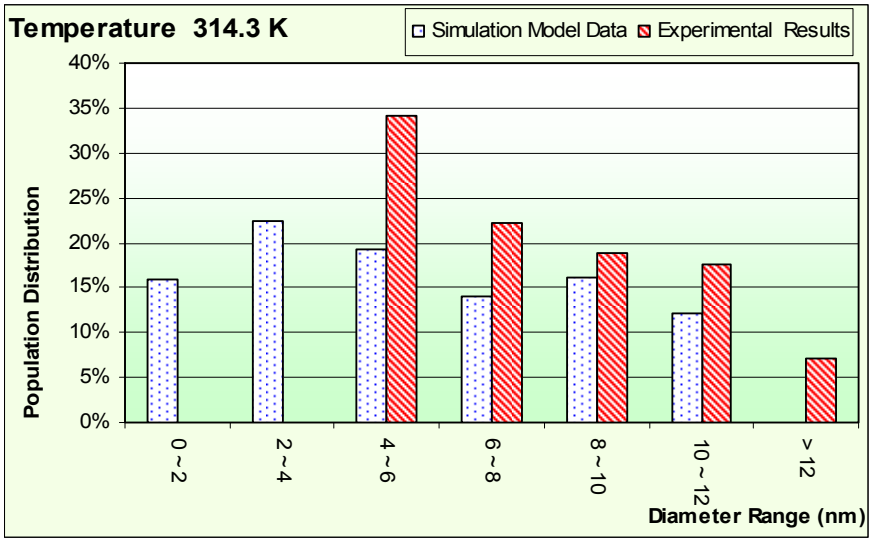
Temperature 314.3 K
Simulation Model Data
Experimental Results
Population Distribution
40%
35%
30%
25%
20%
15%
10%
5%
0%
0 ~ 2
2 ~ 4
4 ~ 6
6 ~ 8
8 ~ 10
10 ~ 12
> 12
Diameter Range (nm)

(c)

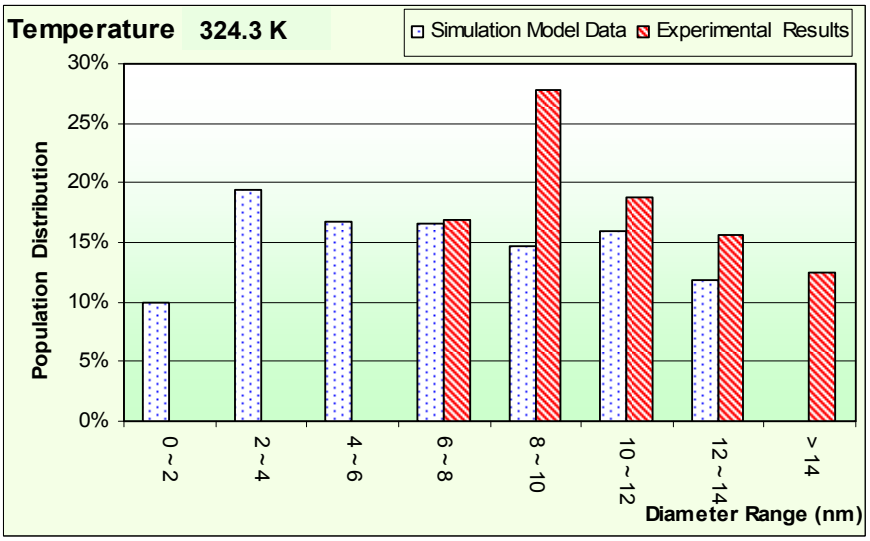
Temperature 324.3 K
Simulation Model Data
Experimental Results
Population Distribution
30%
25%
20%
15%
10%
5%
0%
0 ~ 2
2 ~ 4
4 ~ 6
6 ~ 8
8 ~ 10
10 ~ 12
12 ~ 14
> 14
Diameter Range (nm)

(d)

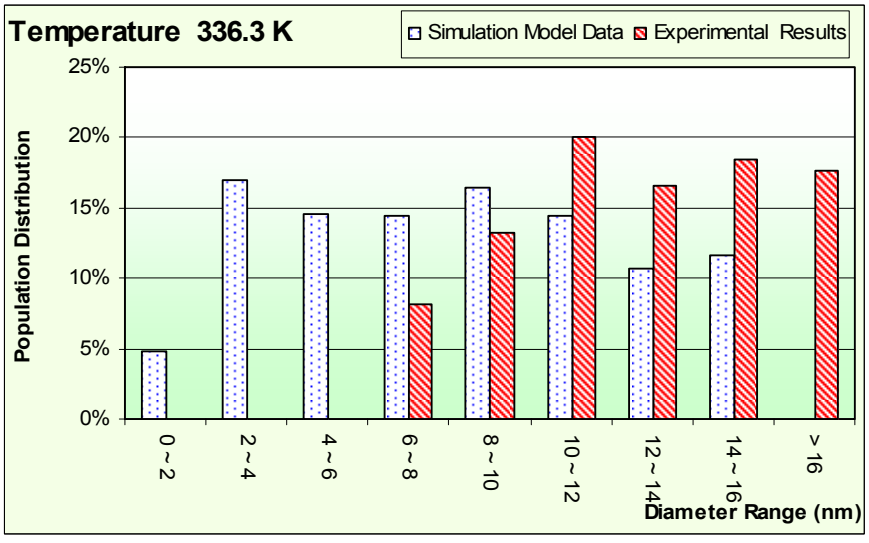
Temperature 336.3 K
Simulation Model Data
Experimental Results
Population Distribution
25%
20%
15%
10%
5%
0%
0 ~ 2
2 ~ 4
4 ~ 6
6 ~ 8
8 ~ 10
10 ~ 12
12 ~ 14
14 ~ 16
> 16
Diameter Range (nm)

(e)

5.4 Effect of Flow Rate

The flow rate of the carrier gas, *f* , in the growth chamber is directly inverse to the time span the growing nucleus had for growth , $f \propto \frac{1}{t}$.

From the proposed model ,

$$d = 2\sqrt{2}\frac{m_A}{\rho N_A}\frac{v_1}{V}\left[(n_1)\times p(n_1)\right]^2\times 10^{-2}\times t + d^* \qquad \textbf{Equation3-44}$$

it is easily deduced that the diameter of nanoparticle is inversely proportion to the flow rate ,

$$d \propto \frac{1}{f} \qquad \textbf{Equation 5- 5}$$

5.4.1 Comparison between model and experimental diameter mean of Flow Rate variation

The diameter mean of the nanoparticles of the various carrier gas flow rates were plotted in the graph shown in figure 5-16. Holding all other parameters constant, the flow rate of the carrier gas determines the amount of time the aerosols monomers and nuclei were kept in growing channel. Indirectly, the flow rate determined the time available for nuclei growth. The faster the flow rate, the smaller the nanoparticle diameter. This relationship is well reflected in figure 5-16. Secondly, the flow rate also affected the monomers concentration in the aerosol. The amount of monomers dispersed into the aerosol was generated at a stable and continuous rate by femto-second laser ablation. With faster flow rate, the aerosol was effectively more diluted into lower concentration. With a lower concentration of monomers, the opportunities of monomers colliding with growing nuclei were reduced as well. Both factors discussed above, contributed to the deterrent of nuclei growth. The resulting conditions of faster carrier gas flow rates yielded smaller diameter mean nanoparticles. On the other hand, when the flow rate was slow, the concentration of the monomers increased, and the nuclei had more time for

growth. These two factors complemented each other to produce larger diameter mean. As observed in figure 5-16, the diameter mean size increased exponentially when the flow rate reduced.

Laser Power (mW)	210	Pressure (Pa)	31,000
Carrier Gas	Argon	Flow Rate (SLM)	Varies
Target Material	Titanium	Temperature (K)	297.3

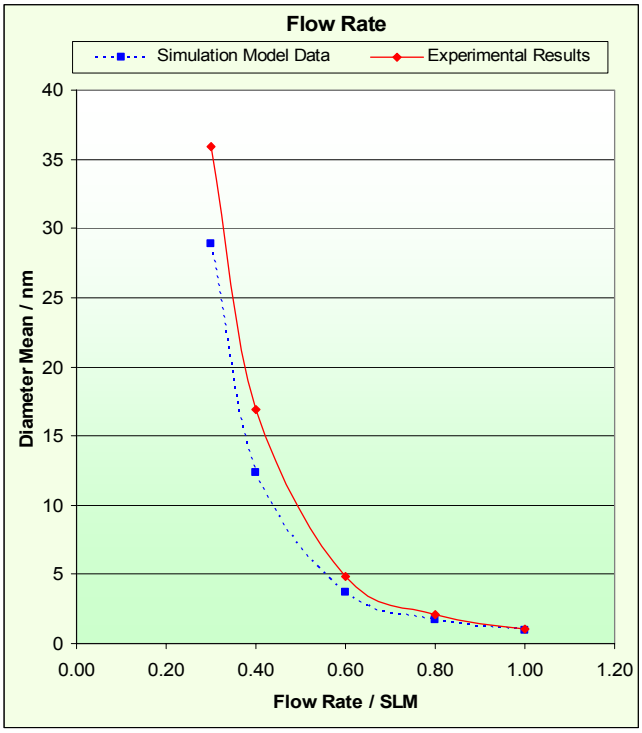

Figure 5- 16 Graph of diameter mean of model and experimental vs. variation in Flow Rate

Figure 5-17, shows the difference of the diameter mean as the flow rate varied. As mentioned before in the previous three sections, two assumptions were taken during the building of the model, in which the events of coalescence and coagulation were simplified from the model. With the absent of coalescence and coagulation being considered in the model, the model growth rate of nucleus to nanoparticle is lower than that in reality. Thus, the diameter mean of nanoparticles simulated by the model was smaller than those obtained from experiment runs.

Under the condition of high flow rate, that is 0.5 SLM (*Standard Liter per Minute*) and above, the aerosol concentration of monomers was very low. In addition, there was shorter time for nuclei growth. The growing nuclei were so well dispersed, due to their low concentration in the aerosol, that the probabilities of their interactions were reduced to a minimum. As a consequence of these control environmental conditions, the assumptions 16 and 17 were realized in these experimental runs. In reality, under these conditions, the nanoparticle yield behaved closely to that predicted by the proposed model.

As shown in following table 5-4 is the values for a paired-test of diameter mean difference of a two tails trial at 95% confidence limit of various *Flow Rate.* Using the same hypothesis as before, there is no evidence to suggest that there is any significant difference between the model data and experimental results for all the experiment runs. However, for experiment runs 16, 17 and 18, the diameter mean differences are much more significant than experiment run 19 and 20.

Table 5- 7 Table of paired Z-test of diameter mean difference of Flow Rate variation of two tails trial test at 95% confidence limit.

Experiment Run number	Flow rate (SLM)	Diameter mean difference (nm)	t-Test Value	Critical point of 2 tails Z-distribution at 95 % confidence limit
16	0.3	7.0229	0.474428	1.959964
17	0.4	4.6347	0.37995	1.959964
18	0.6	1.2119	0.403007	1.959964
19	0.8	0.4100	0.595856	1.959964
20	1.0	0.0955	0.601848	1.959964

Also, shown in figure 5-17, the differences of the diameter mean of the experiment results and simulation data were at their minimum when the flow rate was at it fastest. The experiment sets began to behave very closely to the model when the flow rate exceeded above 0.5 SLM. Naturally, the difference dropped sharply and approached zero when the flow rate was increased towards its peak of 1.0 SLM in this research.

Laser Power (mW)	210	Pressure (Pa)	31,000
Carrier Gas	Argon	Flow Rate (SLM)	Varies
Target Material	Titanium	Temperature (K)	297.3

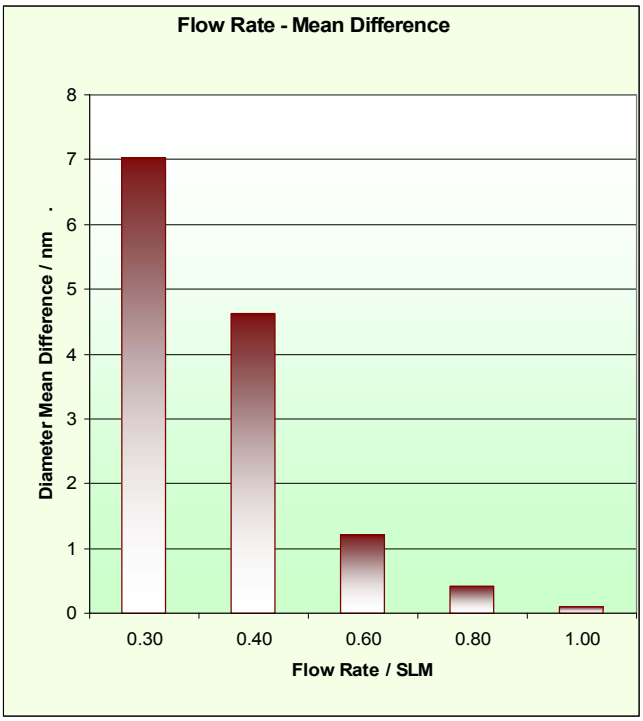

Figure 5- 17 Graph of diameter mean difference vs. variation in Flow Rate

5.4.2 Comparison between model and experimental diameter standard deviation of Flow Rate variation

Like the previous experiment runs in sub-section 5.1, 5.2 and 5.3 , the diameter standard deviation of both the model and experimental of various flow rates were plotted, in figure 5-18. The graph exhibits a similar shape to that of figure 5-16. The fundamental principle of the flow rate affecting both the (i) monomers aerosol concentration and, (ii) time span in the growth chamber, had the same effect on the standard deviation. When the flow rate increased, the growing nuclei had less monomers of different velocities to be absorbed into themselves. This leaded to the formation of nanoparticles with fewer variations in diameter which resulted in a smaller standard deviation range for the faster flow rate, as seen in figure 5-18

Laser Power (mW)	210	Pressure (Pa)	31,000
Carrier Gas	Argon	Flow Rate (SLM)	Varies
Target Material	Titanium	Temperature (K)	297.3

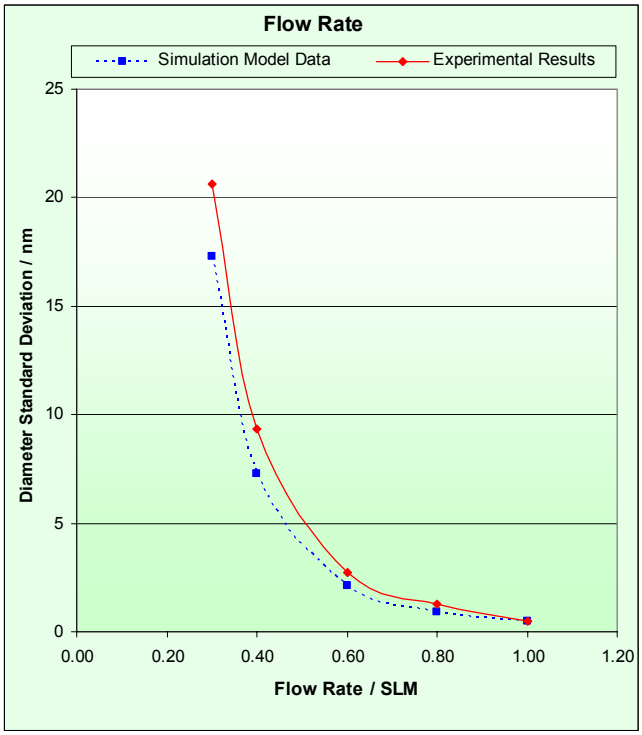

Figure 5- 18 Graph of standard deviation of model and experimental diameter vs. variation in Flow Rate

Figure 5-19, shows the difference of the diameter standard deviation as the flow rate varied. As explained earlier, the difference of standard deviation between the experiments and model, dropped sharply when the flow rate increased beyond 0.5 SLM. With the effects of coagulation and agglomeration reduced to nearly zero, when the flow rate was at its highest of 1.0 SLM, so does the difference of diameter standard deviation approached zero.

Laser Power (mW)	210	Pressure (Pa)	31,000
Carrier Gas	Argon	Flow Rate (SLM)	Varies
Target Material	Titanium	Temperature (K)	297.3

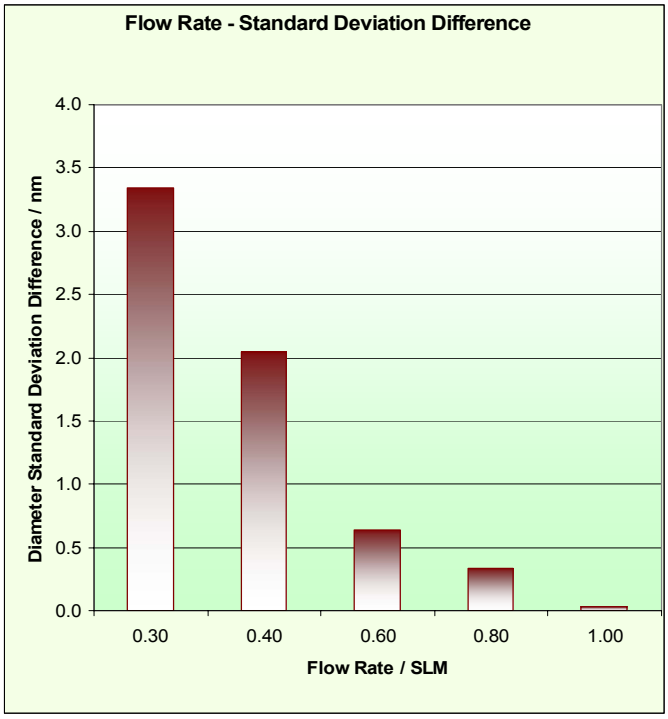

Figure 5- 19 Graph of diameter standard deviation difference vs. variation in Flow Rate

5.4.3 Nanoparticle population distribution obtained by various Flow Rate

Below in figures 5-20 (a) to (e),, are histograms graphs of the nanoparticle population for both model and experiment of different level of flow rate. Because the temperature and pressure of these experimental runs were kept constant, the shapes of the histograms of these runs were all quite similar. The main dissimilarities between these histograms are their ranges and values.

In table 5-8 below, the skew value of each of the histogram graphs of various flow rates, in figures 5-20 (a) to (e), are presented. Unlike the all the previous three sets of graphs of laser power, pressure and temperature variation, the graphs of flow rates variation do not have a general increment nor decrement

trend as the flow rates increase. Little conclusion could be drawn from the values of skew.

Table 5-8 Table of skew of the histogram graphs of difference of Pressure variation.

Experiment Run number	Flow rate (SLM)	Model Data Histogram Skewness	Experimental Results Histogram Skewness
16	0.3	-0.756	0.909
17	0.4	-0.818	-0.437
18	0.6	-0.713	-0.709
19	0.8	-0.43	0.751
20	1.0	-0.671	0.637

Like the previous three effects, of (i) laser power (ii) pressure (iii) temperature, the effect of flow rate has histograms that the *mode* of the experiments results and the *mean* of the simulation data, both fall in the same *range* in the histogram, seen in figures 5-20 (a) to (e) below.

Figure 5- 20Histogram graphs of nanoparticle population obtained from simulation mold data and experiments results of Flow Rate (a) 0.3 SLM , (b) 0.4 SLM, (c) 0.6 SLM, (d) 0.8 SLM, (e) 1.0 SLM.

Laser Power (mW)	210	Pressure (Pa)	31,000
Carrier Gas	Argon	Flow Rate (SLM)	Varies
Target Material	Titanium	Temperature (K)	297.3

(a)

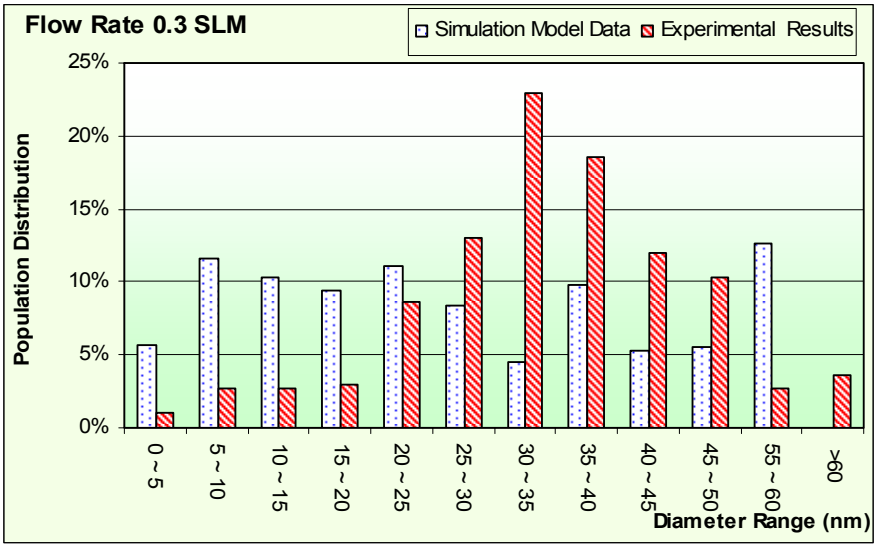

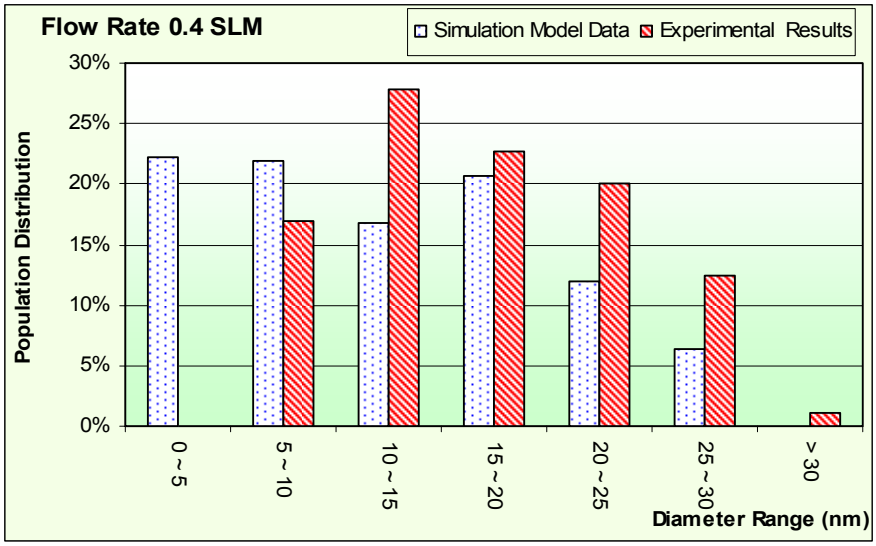
Flow Rate 0.4 SLM
Simulation Model Data
Experimental Results
Population Distribution
30%
25%
20%
15%
10%
5%
0%
0 ~ 5
5 ~ 10
10 ~ 15
15 ~ 20
20 ~ 25
25 ~ 30
> 30
Diameter Range (nm)

(b)

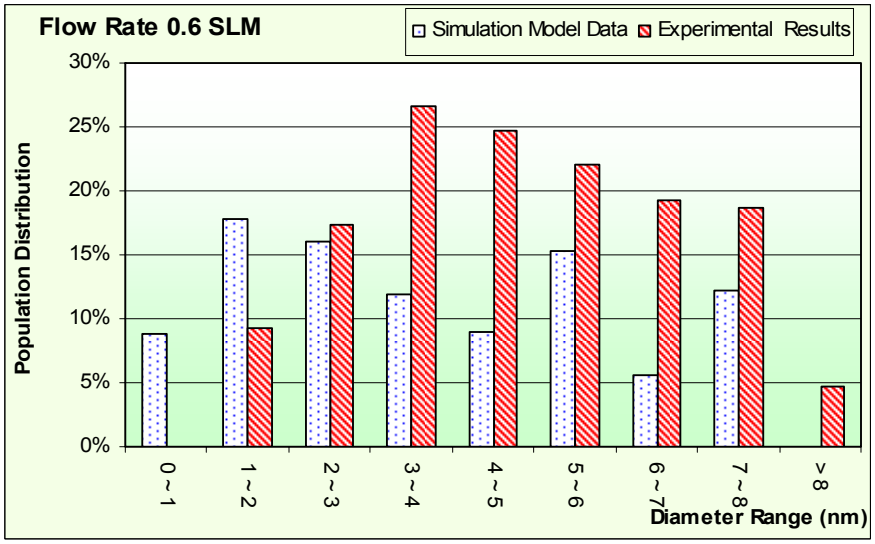
Flow Rate 0.6 SLM
Simulation Model Data
Experimental Results
Population Distribution
30%
25%
20%
15%
10%
5%
0%
0 ~ 1
1 ~ 2
2 ~ 3
3 ~ 4
4 ~ 5
5 ~ 6
6 ~ 7
7 ~ 8
> 8
Diameter Range (nm)

(c)

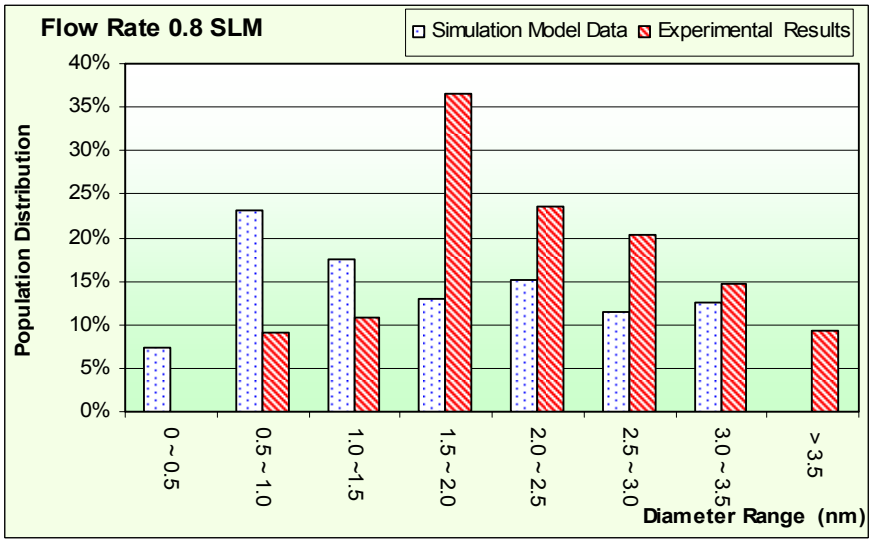
Flow Rate 0.8 SLM
Simulation Model Data
Experimental Results
Population Distribution
40%
35%
30%
25%
20%
15%
10%
5%
0%
0 ~ 0.5
0.5 ~ 1.0
1.0 ~1.5
1.5 ~ 2.0
2.0 ~ 2.5
2.5 ~ 3.0
3.0 ~ 3.5
> 3.5
Diameter Range (nm)

(d)

(e)

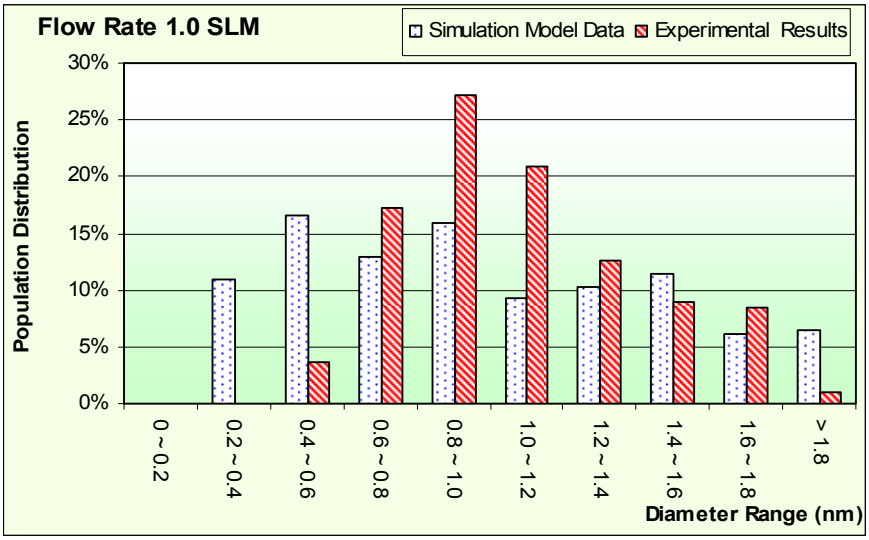

5.5 Effect of Target Material

The relationship between target material and nanoparticle diameter is more complex than for the previous four effects of (i) laser power irradiation, (ii) temperature of the chamber, (iii) pressure of the chamber, and (iv) flow rate of the carrier gas. The target materials under consideration in this research are five transition metal elements found across row 3 of the periodic table.

A simplification of model equation 3-44,

$$d = 2\sqrt{2}\,\frac{m_A}{\rho\, N_A}\,\frac{v_1}{V}\left[(n_1)\times p(n_1)\right]^2 \times 10^{-2} \times t + d^{*} \qquad \textbf{Equation 3-44}$$

results in the relation of

$$d \propto \left(d_1 + d_g\right)^2 \cdot \frac{1}{\rho} \cdot \frac{1}{m_1} \cdot \left(\frac{n_a}{k}\right)^3 \cdot \left[\ln \frac{1}{(\varepsilon_b + \varepsilon_{esc})(n_e)}\right]^3 \qquad \textbf{Equation 5- 6}$$

where ε_b binding energy

ε_{esc} work function

d_1 diameter of monomer

d_g diameter of gas molecule

n_a number of atoms per unit volume

n_e number of electrons per unit volume

m_1 mass of monomer (equivalent to atomic mass)

k imaginary part of refractive index

ρ density of material

It can be seen from equation 5-6 that there is no direct relationship between the properties of the target material and the diameter of the nanoparticle. These properties, binding energy , work function, diameter of monomer, number of electron density, number of atom density, mass of monomer and density, are all interrelated. The metals of interest in this research are :

- Titanium,
- Iron,
- Nickel,
- Copper,
- Zinc,

listed in ascending order of their atomic numbers. A table of the physical properties of the metal elements are show below in table 5-1.

Table 5- 9 Physical Properties of Metal Elements

	Atomic Number	Atomic Weight	Density g/cm3	Melting Point ^{O}C	Boiling Point ^{O}C	Entropy of fusion kJ / mol	Entropy of vapour. kJ / mol
Titanium	22	47.88	4.5	1668	3285	18.8	425
Iron	26	55.85	7.87	1538	2750	13.8	340
Nickel	28	58.69	8.9	1455	2920	17.2	375
Copper	29	63.55	8.96	1084.6	2570	13	307
Zinc	30	65.39	7.14	419.5	907	7.28	115.5
	Entropy of atomizat^{n} kJ / mol	number of atoms per kg	Atomic Binding energy, ε_a eV / atom	Therm. Binding energy, ε_b eV / atom	Work function ε_{esc} eV / atom	number of electons n_e / cm^3	number of atoms per kg

Titanium	469	1.26E+25	4.860842	4.4048	4.33	1.13E+23	1.26E+25
Iron	398	1.08E+25	4.124979	3.5239	4.70	8.49E+22	1.08E+25
Nickel	429	1.03E+25	4.446271	3.8866	5.15	1.83E+23	1.03E+25
Copper	337	9.48E+24	3.492759	3.1818	4.65	8.49E+22	9.48E+24
Zinc	129.3	9.21E+24	1.3401	1.1971	4.33	1.32E+23	9.21E+24

	number of neutral atoms n_a / cm^3	Molecular Volume cm^3 / mol	Atomic volume V_1 nm^3	Imaginary part of reflective index , k
Titanium	5.66E+22	10.640	0.0177	4.845
Iron	8.49E+22	7.100	0.0118	3.600
Nickel	9.13E+22	6.590	0.0109	4.310
Copper	8.49E+22	7.100	0.0118	3.300
Zinc	6.58E+22	9.200	0.0153	4.620

A general guide for these five metal target is that as the atomic mass increases , there is a decrease in their

- binding energy ,
- work function,

While on the other hand,

- diameter of monomer ,
- number of electron density ,
- number of atom density,
- mass of monomer,
- imaginary part of refractive index ,

increase with their atomic numbers, as shown by the data in table 5-1. However, in most instances, Nickel behaves with great exception with respect to the general trend and Zinc has properties being in the most extreme of all these five metal elements. Being a transition metal, they could exist relatively stable as a single atom structures under normal room conditions. These stable single atoms entities are in fact the equivalent to the monomers as defined. Thus, the mass of a single monomer of metal element could be closely estimated as its atomic mass.

5.5.1 Comparison between model and experimental diameter mean of Target Material variation

Figure 5-23 displays the diameter mean of the nanoparticles of the five different target materials. It is shown that there is no general trend for the atomic mass with respect to the nanoparticle diameter. However, there are two significant properties of the target material that could be used to forecast the diameter of the nanoparticles synthesized. The nanoparticles formed will have larger diameters if the metal material has lower binding energy (either atomic binding energy or thermal binding energy). This general relationship is displayed in figure 5-21. Secondly, if the metal material has a larger atomic volume, the nanoparticles formed will be bigger as well, as shown in figure 5-22.

Laser Power (mW)	224	Pressure (Pa)	32,000
Carrier Gas	Argon	Flow Rate (SLM)	0.60
Target Material	Varies	Temperature (K)	297.3

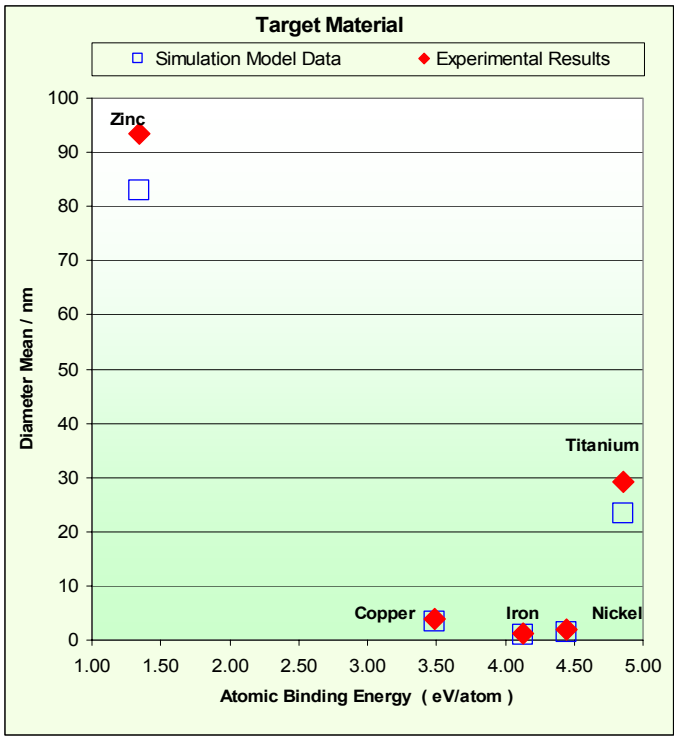

Figure 5- 21 Graph of diameter mean vs. variation in atomic binding energy

Laser Power (mW)	224	Pressure (Pa)	32,000
Carrier Gas	Argon	Flow Rate (SLM)	0.60
Target Material	Varies	Temperature (K)	297.3

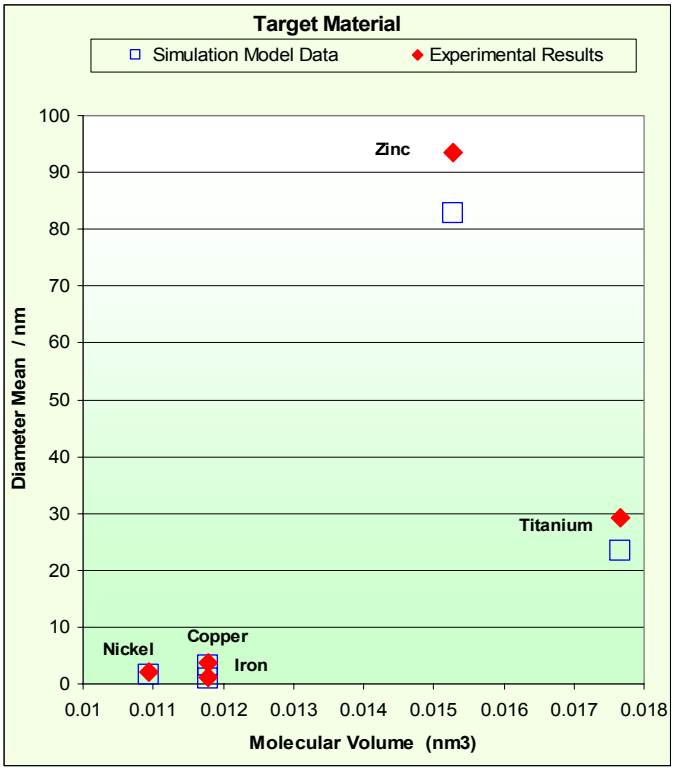

Figure 5- 22 Graph of diameter mean vs. variation in molecular volume

From both figures 5-21 and 5-22, it can be seen that these two general trends were shared by both the simulation data and experimental results. It is clearly revealed that both binding energy and molecular volume of the metal material do not have a direct relation to the size of the nanoparticles. Instead, these two physical properties of the metal have an inter-active relationship. To be able to model accurately the nanoparticle size of other metals in term of these physical properties, more research will be required. However, this is beyond the scope of this current research.

With the ambient conditions, carrier gas pressure, chamber temperature, carrier gas flow rate, remaining constant and the same amount of laser power energy applied, the numbers of collisions is very much dependent on the nature

of monomers and growing nuclei. In other words, both the quantity and characteristic of these monomers and growing nuclei were more significant to diameter growth rate. With the amount of laser power applied to all material controlled to be the same, the difference in the physical material properties will determine the amount of mass ablated, and subsequently, the amount of monomers generated for nanoparticle formation. Metals with lower binding energy, work function and refractive index, are able to convert laser power into bond breaking energy with higher efficiency. With the same amount of laser power applied to all the different metal materials, the amount of monomers generated depends very much on the physical properties of these target materials. Metals with lower binding energy, work function and refractive index, will yield more monomers. With more monomers, the more successful adhesive collisions between the growing nuclei and monomers will occur, and thus the larger the nanoparticle diameter will be.

However, it could be seen that Zinc, Copper, Nickel, and Iron follow quite closely to this relation with the exception of Titanium. As mentioned above, the nanoparticle diameter does not depend solely on any one of the physical properties of metal, but a more complex relation of combined effects of several factors. The second significant physical atomic property is the atomic volume.

As observed in figure 5-22, the larger the atomic volume of the metal, the bigger the nanoparticle diameter yielded. For transition metals, all the monomers are equivalent to a single atom. The larger monomer, with its bigger surface area, has a higher probability of collision onto growing nuclei, resulting in larger nanoparticle diameters. This relationship is well obeyed by Copper, Nickel, Iron, and Titanium, with the exception of Zinc. Nanoparticles formed by Zinc had a relatively much larger diameters than the other four metals. Again, this observation displays the combined effects of several physical properties of the metal are the main factors that affects the size of nanoparticles, rather than any individual property. This further enforced the fact that the effects of physical properties of the metal are more complex than that expressed in the proposed model. However these relationships are not included in the scope of the current research.

Laser Power (mW)	224	Pressure (Pa)	32,000
Carrier Gas	Argon	Flow Rate (SLM)	0.60
Target Material	Varies	Temperature (K)	297.3

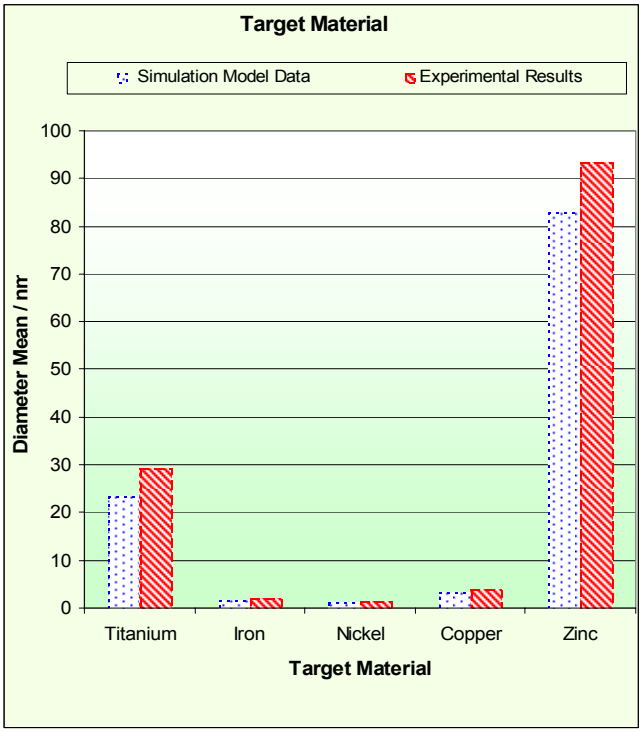

Figure 5- 23 Graph of diameter mean of model and experimental vs. variation in Target Material

In figure 5-24 is a graph showing the difference between the diameter mean of simulation model data and experiment results. As shown in following table 5-6 are the values of paired-test the diameter mean difference, and the critical points of the two tails Z-distribution at 95 % confidence limit of various *Target Materials.* The set of hypothesis are the same as previous Z-test. Based on these, there is enough evidence to suggest that there is no significant difference between the model data and experimental results for all the various Target Material expect for Zinc.

Table 5- 10 Table of paired Z-test of diameter mean difference of Target Material variation of two tails trial test at 95% confidence limit..

Experiment Run number	Target Material	Diameter mean difference (nm)	Z-Test Value	Critical point of 2 tails t-distribution at 95 % confidence limit
21	Titanium	5.7737	0.385765	1.959964
22	Iron	0.4755	0.262922	1.959964
23	Nickel	0.2587	0.587292	1.959964
24	Copper	0.4946	0.348136	1.959964
25	Zinc	10.5115	2.971063	1.959964

Also observe is the common trend shared by the various nanoparticles synthesis conditions, is that the differences of the diameter mean are proportional to the diameter mean. The smaller diameter mean generally has less difference. During the conditions in which the nuclei growths were suppressed, so were the conditions for coagulation and coalescence. In these conditions whereby nucleus growth is less favorable, the nanoparticles yield would have smaller diameter. As a result, the smaller diameter mean populations had a narrower difference between the simulation data and experimental results. On the other hand, when nucleus growth conditions were more favorable, the nanoparticles yield would be larger. Naturally, the larger diameter mean populations had a wider difference.

Laser Power (mW)	224	Pressure (Pa)	32,000
Carrier Gas	Argon	Flow Rate (SLM)	0.60
Target Material	Varies	Temperature (K)	297.3

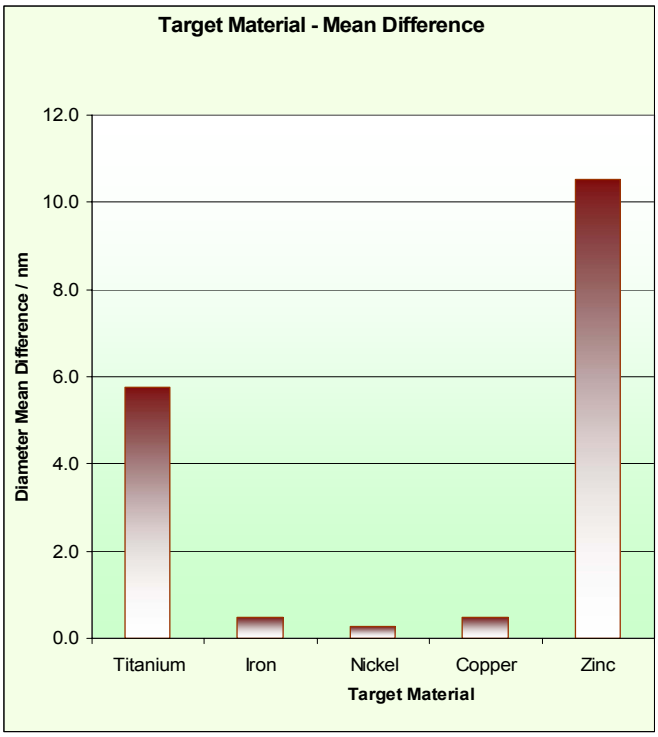

Figure 5- 24 Graph of diameter mean difference vs. variation in Target Material

5.5.2 Comparison between model and experimental diameter standard deviation of Target Material variation

Similar to previous experiments, the difference in standard deviation between the simulation model data and experimental results are directly proportional to the diameter mean. As explained earlier, the same ambient and physical conditions that promote nuclei growth, which resulted in larger diameter mean, also promote coagulation and coalescence. With more coagulation and coalescence, there existed alternative nanoparticle growth mechanisms, which leaded to larger diameter mean. The same conditions that were favorable for nuclei growth, inherited a higher permutation of different monomers with

different velocities interacting with the growing nuclei. As a result, the spread of the nanoparticle population, along with its standard deviation, was wider.

It should be noted that physical ambient conditions, chamber pressure, carrier gas flow rate, ambient temperature, laser power applied and carrier gas type for these series of experiments were kept constant. It could be seen from the large variation of the standard deviations of the five different target materials, displayed on the graph in figure 5-25. It shows that nucleus growth rate is much more sensitive to the properties of metal as compared to the difference in surrounding environmental conditions.

Laser Power (mW)	224	Pressure (Pa)	32,000
Carrier Gas	Argon	Flow Rate (SLM)	0.60
Target Material	Varies	Temperature (K)	297.3

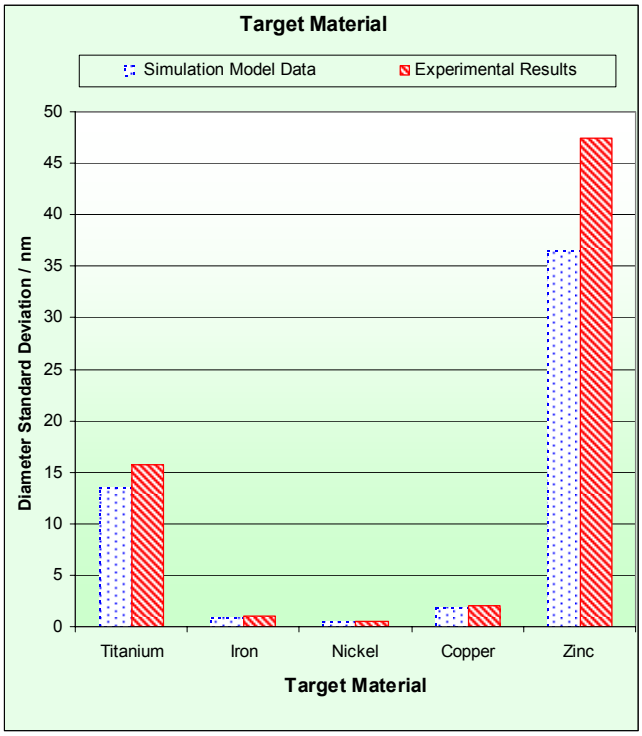

Figure 5- 25 Graph of standard deviation of model and experimental diameter vs. variation in Target Material

A second interesting observation is that the diameters standard deviation difference between the model and experiment varied greatly across the five metals. Likewise, the more favorable the condition for nucleus growth, the more

predominate the effects of coagulation and agglomeration. As these effects were more pronounce, so will be the difference between diameter standard deviation. Though the ambient conditions of all the experiment runs were keep constant, the graph in figure 5-26 shows that the difference still varied greatly across the five target materials. This observation indicates again that the growth rate is much more sensitive to the properties of metals as compared to the difference in ambient conditions.

Laser Power (mW)	224	Pressure (Pa)	32,000
Carrier Gas	Argon	Flow Rate (SLM)	0.60
Target Material	Varies	Temperature (K)	297.3

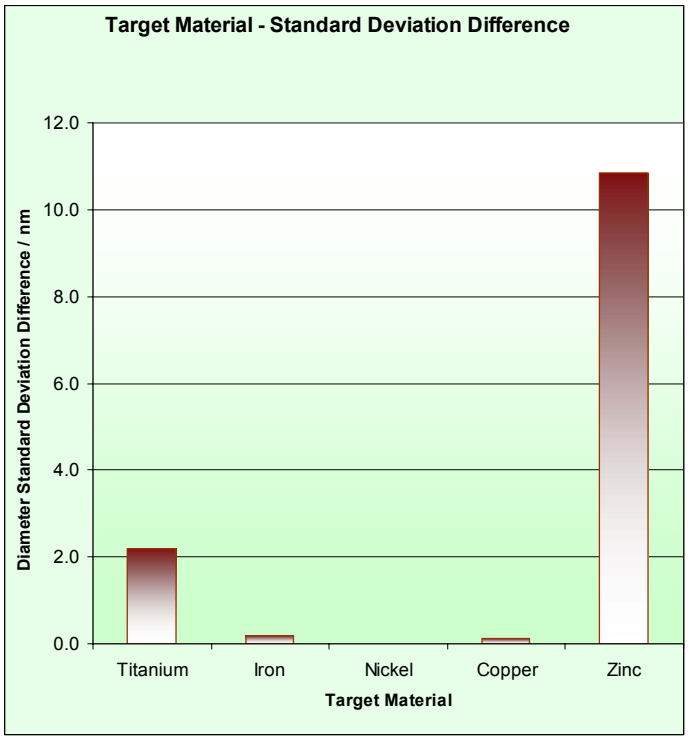

Figure 5- 26 Graph of diameter standard deviation difference vs. variation in Target Material

5.5.3 Nanoparticle population distribution obtained by various Target Material

Figures 5-27 (a) to (e) below are histograms of the nanoparticle population of both simulation and experiment of different metal materials. Although the temperature, pressure, flow rate, laser power and gas type of these experiments run were kept constant, unlike the previous experimental runs, the shape of the histograms were all different when compared against each other. This again indicates that nanoparticles diameter synthesized is the most sensitive to the physical properties of the metals

Shown in table 5-11 is the skewness of each of the histogram graphs of various target materials. As the parameter of target materials variation is the most sensitive parameter, explained earlier, the fluctuation of the skewness across table 5-11 is higher than the other variations. There exit no general trend within the skew value with respect to target materials variation. Like the variation of flow rates, little conclusive statement could be drawn from these values of skew.

Table 5-11 Table of skew of the histogram graphs of difference of Pressure variation.

Experiment Run number	Target Material	Model Data Histogram Skewness	Experimental Results Histogram Skewness
21	Titanium	-0.866	0.769
22	Iron	-0.713	1.011
23	Nickel	0.191	0.486
24	Copper	-1.578	1.442
25	Zinc	-0.932	1.1

However, likewise to the previous all four experimental runs, the *mode* of the experiments results and the *mean* of the simulation model data, both fall in the same range in the histogram.

Figure 5- 27 Histogram graphs of nanoparticle population obtained from simulation model data and experimental results of Target (a) Titanium , (b) Iron, (c) Nickel, (d) Copper, (e) Zinc .

Laser Power (mW)	224	Pressure (Pa)	32,000
Carrier Gas	Argon	Flow Rate (SLM)	0.60
Target Material	Varies	Temperature (K)	297.3

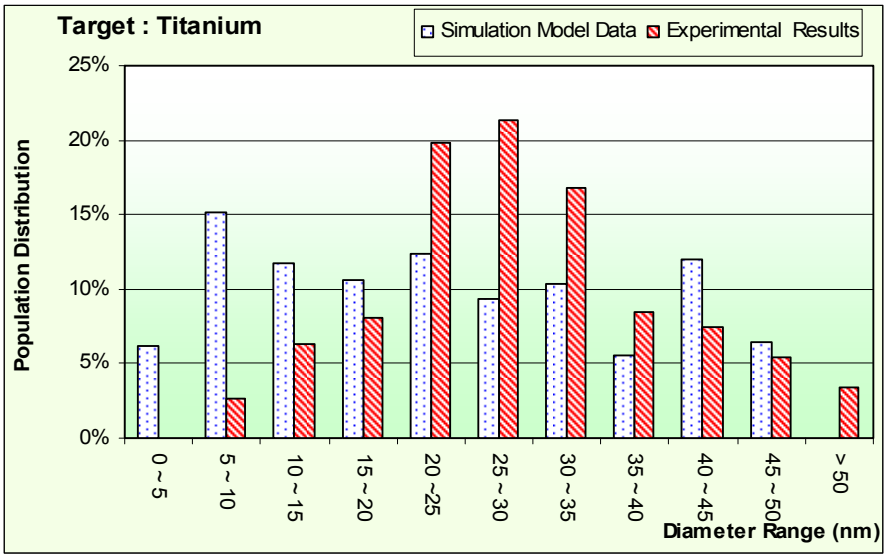

(a)

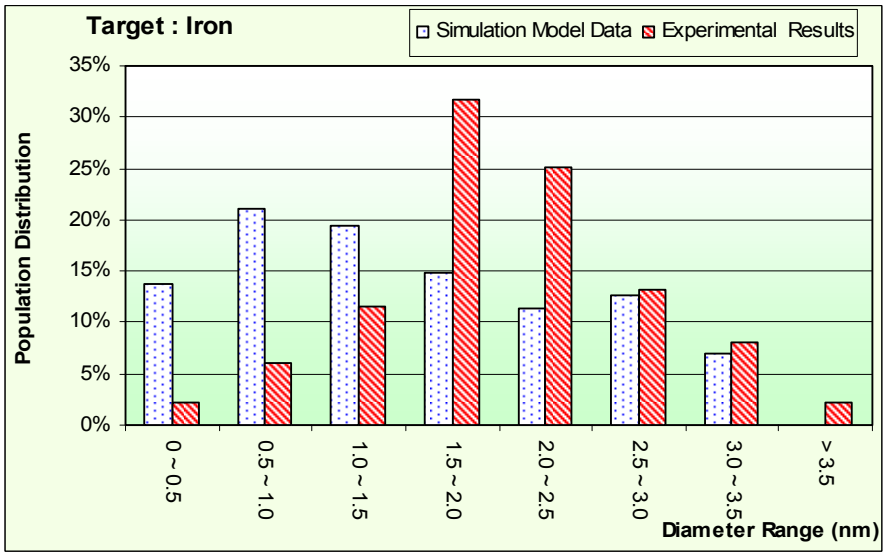

(b)

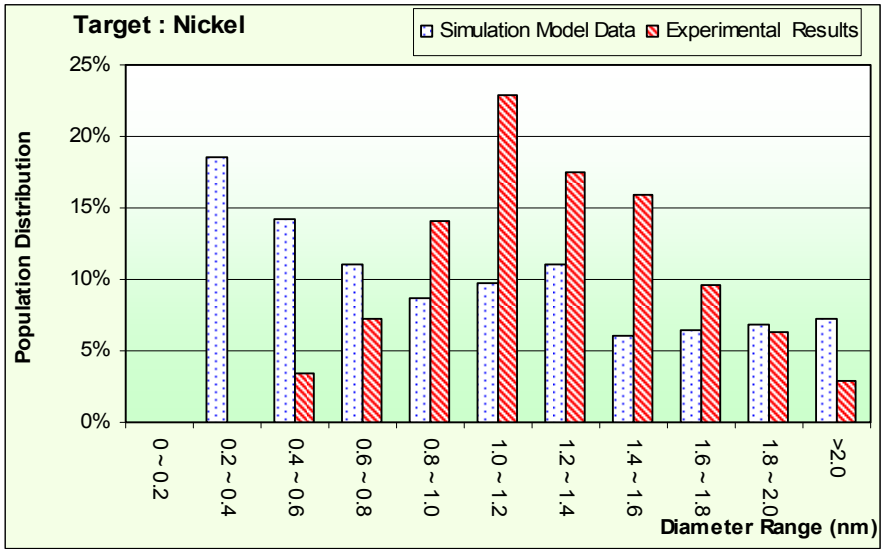
Target : Nickel
Simulation Model Data
Experimental Results
Population Distribution
25%
20%
15%
10%
5%
0%
0 ~ 0.2
0.2 ~ 0.4
0.4 ~ 0.6
0.6 ~ 0.8
0.8 ~ 1.0
1.0 ~ 1.2
1.2 ~ 1.4
1.4 ~ 1.6
1.6 ~ 1.8
1.8 ~ 2.0
>2.0
Diameter Range (nm)

(c)

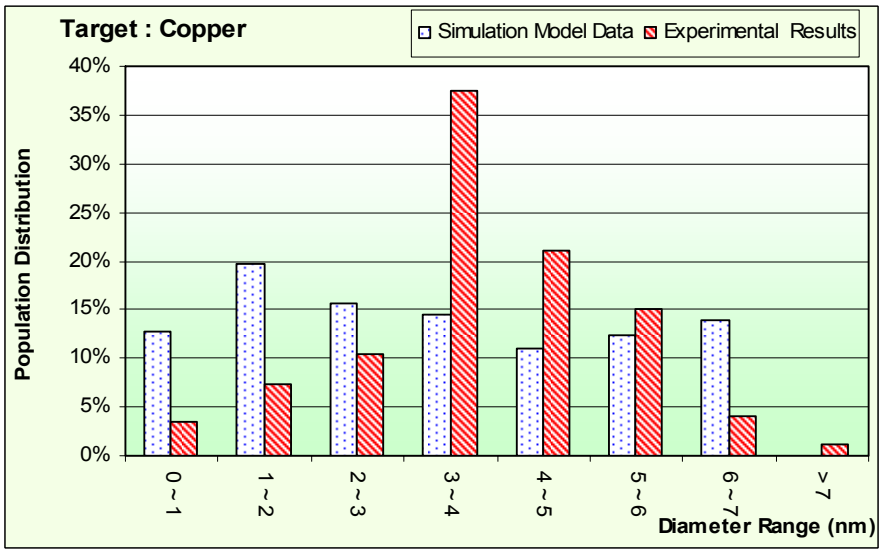
Target : Copper
Simulation Model Data
Experimental Results
Population Distribution
40%
35%
30%
25%
20%
15%
10%
5%
0%
0 ~ 1
1 ~ 2
2 ~ 3
3 ~ 4
4 ~ 5
5 ~ 6
6 ~ 7
> 7
Diameter Range (nm)

(d)

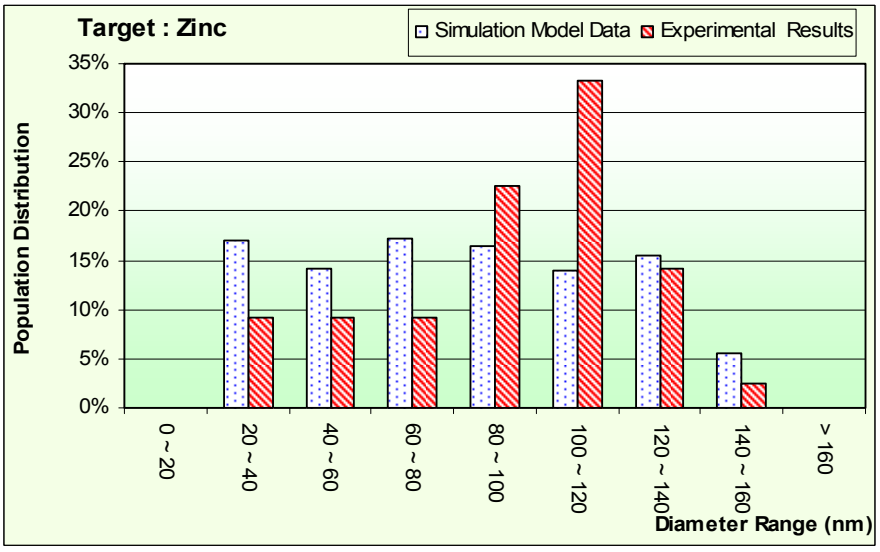
Target : Zinc
Simulation Model Data
Experimental Results
Population Distribution
35%
30%
25%
20%
15%
10%
5%
0%
0 ~ 20
20 ~ 40
40 ~ 60
60 ~ 80
80 ~ 100
100 ~ 120
120 ~ 140
140 ~ 160
> 160
Diameter Range (nm)

(e)

5.6 Effect of Carrier Gas

In section 5.4, the effect of the flow rate of the carrier gas, *f*, was discussed. According to the proposed model, Equation 3-44 , it can be inferred that the diameter of the nanoparticle is related to the gas atom/ molecule diameter and it atomic/ molecular mass,

$$d \propto \left(d_1 + d_g\right)^2 \qquad \textbf{Equation 5- 7}$$

where d diameter of nanoparticle
d_1 diameter of monomer
d_g diameter of gas atom / molecule
m_g atomic/ molecular mass of carrier gas

For the three carrier gases, Helium, Argon and Nitrogen, the atomic number , N_A , increase with the ratio of $\left(d_1 + d_g\right)^2$ as shown in table 5-2 below

Table 5- 12 Physical Properties of Gas Elements

Carrier Gas	Atomic Number N_a	Atomic Weight	atomic / molecule size d_g (nm)	$\left(d_1 + d_g\right)^2$ (nm^2)
Helium (He)	2	4	0.031	0.125419
Argon (Ar)	18	39.95	0.071	0.155350
Nitrogen (N)	14	14.003	0.065	0.150656

In other words, the diameter of nanoparticle (d) synthesized is directly proportional to the atomic number (N_a) of the carrier gas.

$$d \propto N_a \qquad \textbf{Equation 5- 8}$$

5.6.1 Comparison between model and experimental diameter mean of Carrier Gas variation

Figure 5-28 shows the diameter mean of the nanoparticles synthesized in the different carrier gases. The graph follows a general trend of nanoparticle diameter increasing with atomic number. This agrees well with the proposed model. In reality, the experimental results also follow the same trend. As the atomic numbers increase, so does the atomic / molecular diameters and the atomic / molecular mass. With larger atomic / molecular diameters, the carrier gas atoms/ molecules have more collision interaction with the monomers. With higher atomic / molecular mass, the momentum transferred to the monomers also increases. The combined effects of higher momentum and higher collisions frequency, the monomers had more successful adhesion collisions with the growing nuclei, leading to larger nanoparticle diameters.

Laser Power (mW)	224	Pressure (Pa)	32,000
Carrier Gas	Varies	Flow Rate (SLM)	0.60
Target Material	Titanium	Temperature (K)	297.3

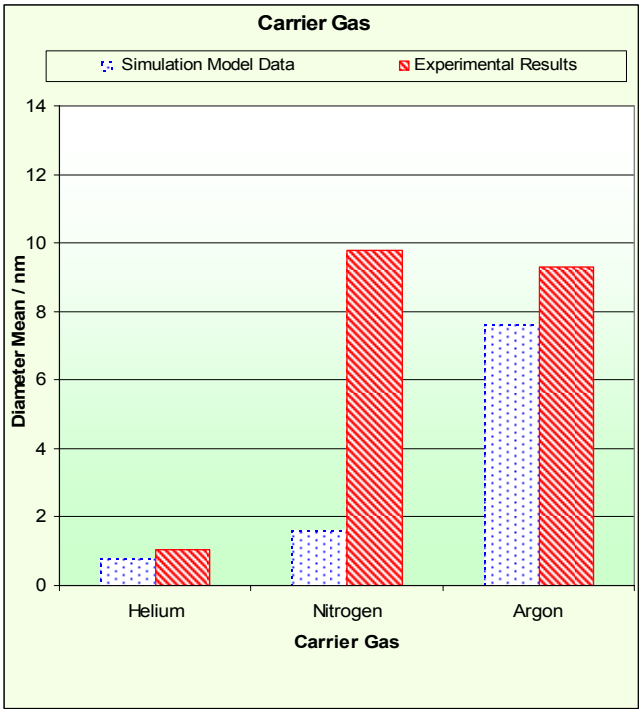

Figure 5- 28 Graph of diameter mean of model and experimental vs. variation in Carrier Gas

One noteworthy observation is that the difference of the diameter mean of the nanoparticle between the simulation model data and experimental data for the Nitrogen carrier gas is relativity very high. This huge difference is reflected visibly the graph in figure 5-29. Also, shown in table 5-13 is this difference. In the table are the values of paired-test the diameter mean difference with two tail Z-distribution critical points at 95% confidence limit of various *Carrier Gas.* Using the same hypothesis, it is shown that there is no enough evidences to prove that there is any significant difference between the model data and experimental results. However, it is observed that the diameter difference between the model data and experimental results for Nitrogen is very great.

Table 5- 13 Table of paired Z-test of diameter mean difference of Carrier Gas variation of two tails trial test at 95% confidence limit.

Experiment Run number	Carrier Gas	Diameter mean difference (nm)	Z-Test Value	Critical point of 2 tails Z-distribution at 95 % confidence limit
26	Helium	0.2559	1.431779	1.959964
27	Nitrogen	8.1517	0.345483	1.959964
28	Argon	1.6463	1.759907	1.959964

The reason is that the proposed model is not suitable to describe this method of synthesis utilizing Nitrogen as carried gas in because of *Assumption 20* taken in model.

Assumption 20

All the assumptions as stated in the Kinetic Theory of Ideal Gas hold for this model, in which

- *The molecules of gas are in constant random motion. They travel at high speed in straight lines unless they collide with the wall of the container or other molecules.*
- *The molecules are separated by relatively large distances as compared to the diameter of the molecules, which is considered to be negligible.*
- *The forces of attraction between molecules are negligible.*

- *The temperature of molecules is a measure of the average kinetic energy of the molecules of gas.*

Under *Assumption 20*, all carrier gas atoms / molecules were assumed to be point mass and are considered to be of a perfect spherical shape. Therefore, no correction factors were introduced into the proposed model for the momentum exchanges between the carrier gas atoms / molecules and the monomers. Nitrogen, which exists as duo-atoms molecules in the experimental conditions, failed to abide to these assumptions. In addition, the duo-atom molecules have a wider effective diameter than perfect sphere geometry as used in the proposed model. Consequently, the nanoparticles diameter formed in reality are much larger than that predicted by the proposed model.

Laser Power (mW)	224	Pressure (Pa)	32,000
Carrier Gas	Varies	Flow Rate (SLM)	0.60
Target Material	Titanium	Temperature (K)	297.3

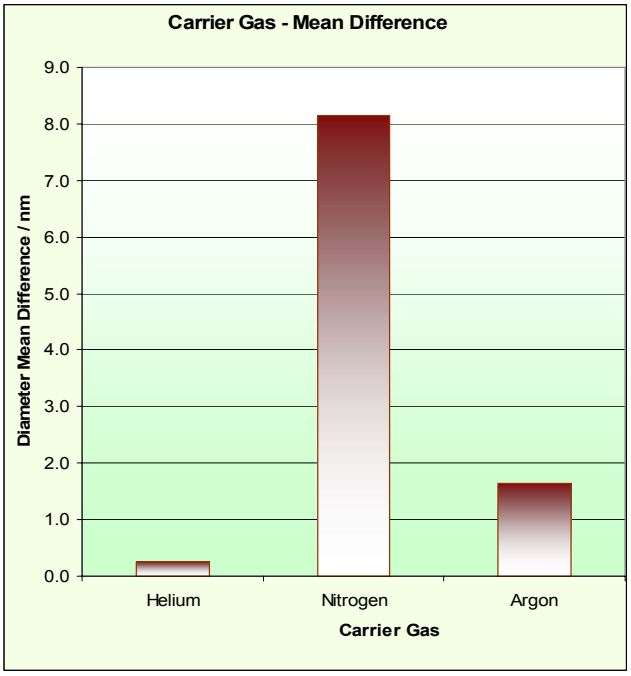

Figure 5- 29 Graph of diameter mean of model and experimental vs. variation in Carrier Gas

5.6.2 Comparison between model and experimental diameter standard deviation of Carrier Gas variation

Likewise, the standard deviation of the nanoparticle populations of the three carrier gases, widen with the increasing atomic number of the carrier gas, as seen in figure 5-30. The same bases that promoted nuclei growth rate, monomers with higher momentum and higher collisions, also increased the permutations of monomers with different velocities to interact with growing nuclei. The outcome of these higher interaction permutations is a wider spread of nanoparticle diameter populations.

Laser Power (mW)	224	Pressure (Pa)	32,000
Carrier Gas	Varies	Flow Rate (SLM)	0.60
Target Material	Titanium	Temperature (K)	297.3

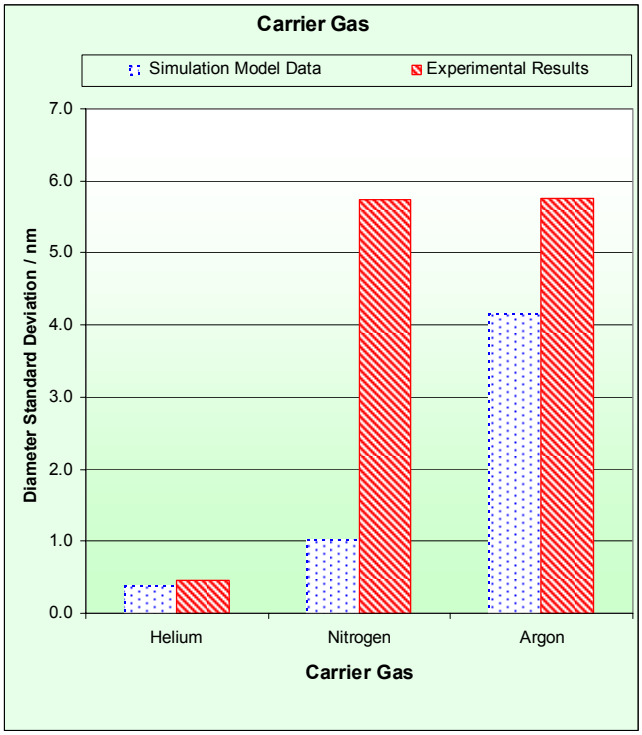

Figure 5- 30 Graph of standard deviation of model and experimental diameter vs. variation in Carrier Gas

Following in figure 50-31, its graph shows the differences of the diameter mean and standard deviation respectively between simulation data and experimental

data. Similar, for the same reason of the assumption taken in the model, there is a relatively large difference in the standard deviation between simulation data and experimental results.

Laser Power (mW)	224	Pressure (Pa)	32,000
Carrier Gas	Varies	Flow Rate (SLM)	0.60
Target Material	Titanium	Temperature (K)	297.3

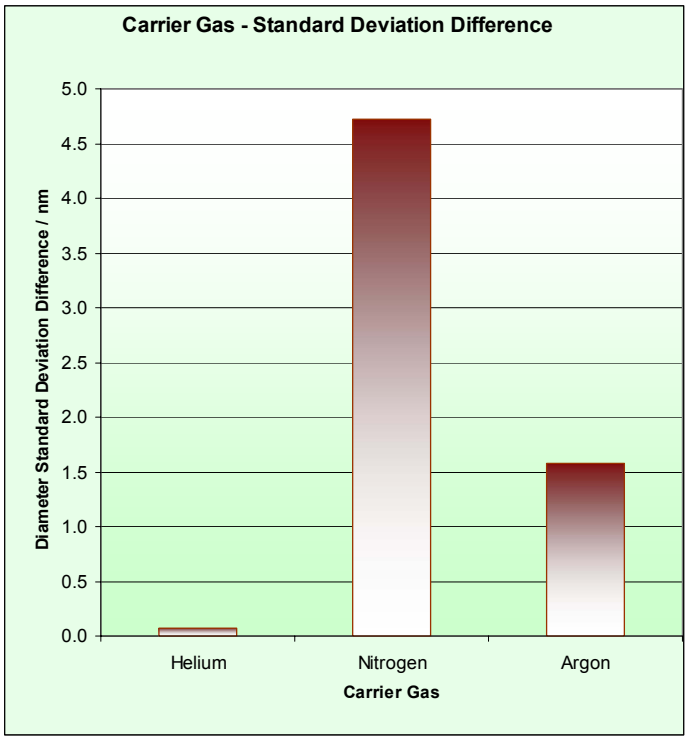

Figure 5- 31 Graph of diameter standard deviation difference vs. variation in Carrier Gas

5.6.3 Nanoparticle population distribution obtained by various Carrier Gases

Table 5-14 below is the values of skew each of the histogram graphs of various carrier gases. Discussed earlier, the proposed model is not able to explain the experiment run 27 with the use of Nitrogen as carrier gas. With the elimination of experiment run 27, there left with only 2 variations of carrier gaes. No tend could be seen from only 2 data entries. Again the value of skew is unable to give conclusive statement.

Table 5- 14 Table of skew of the histogram graphs of difference of Pressure variation.

Experiment Run number	Carrier Gas	Model Data Histogram Skewness	Experimental Results Histogram Skewness
26	Helium	-0.431	1.19
27	Nitrogen	-1.169	-0.046
28	Agron	1.999	0.625

Figure 5-32 (a) to (c) are the histograms of the nanoparticle population of the three different carrier gases. Except for Nitrogen, Helium and Argon both shows the same trends as the other experiments. The *mode* of Helium and Argon experiments results and the *mean* of the simulation data, both fall in the same *range* in the histogram. Due to the assumptions taken in the proposed model, the actual behavior of Nitrogen as carrier gas in the experiments differed from what was expected in the model.

Figure 5- 32 Histogram graphs of nanoparticle population obtained from simulation data and experiments results of Carrier Gas (a) Helium, (b) Nitrogen, (c) Argon.

Laser Power (mW)	224	Pressure (Pa)	32,000
Carrier Gas	Varies	Flow Rate (SLM)	0.60
Target Material	Titanium	Temperature (K)	297.3

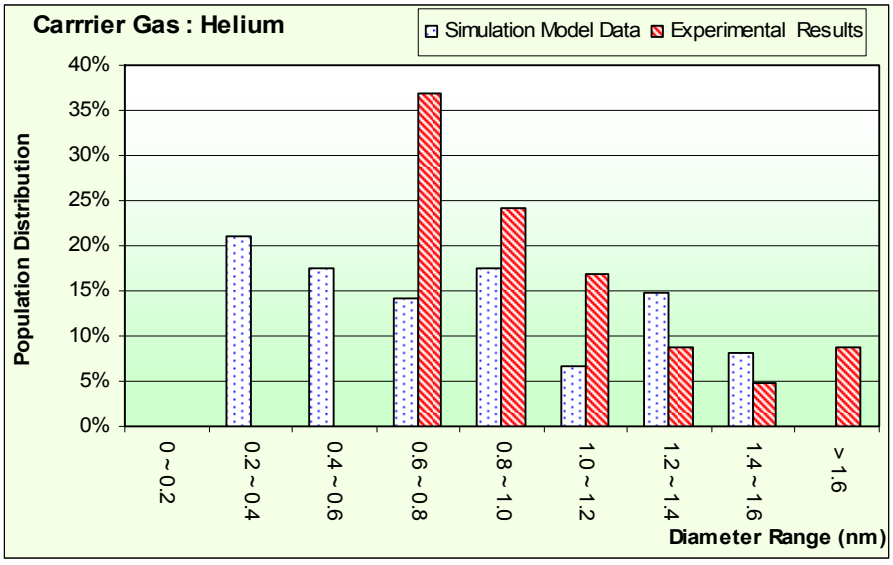

(a)

(b)

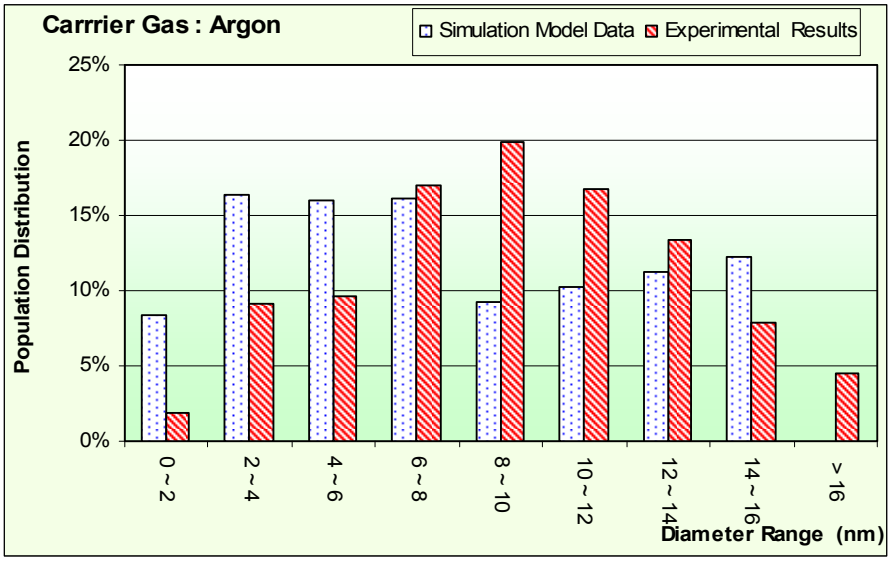

(c)

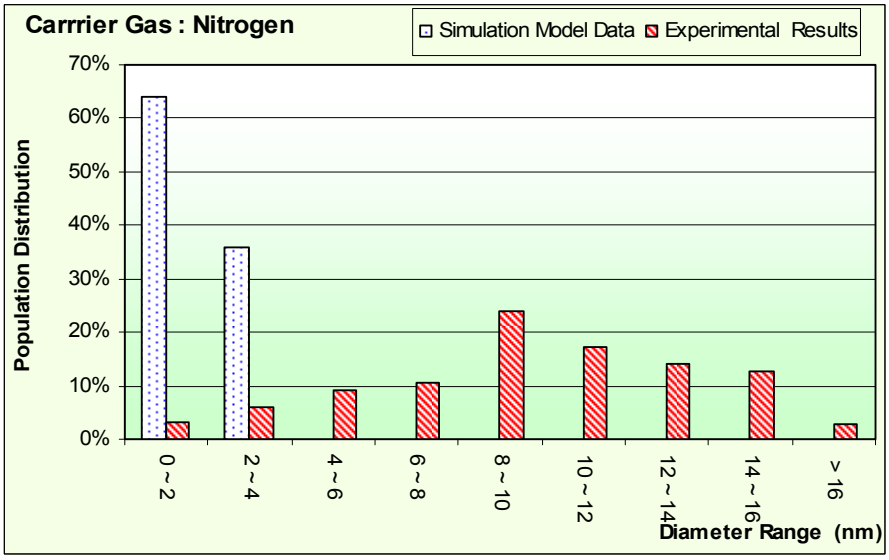

5.7 Correlation between Model Data and Experimental Results

In order to investigate the correlation between model data and experimental results, a two-tails *t-test*, of two samples with different variances, at 95% confidence limits was performed on the diameter mean from both groups. Also,

a two tails pair *t-test*, at 95% confidence limits was performed on the diameter standard deviation from both groups as well. The summary of both tests are show in table 5-15. As seen from the results of both the tests, there is a good fit between the diameter mean and standard deviation of model data and experimental results. From these, it can be seen that the model is able to predict the experiment results correctly within the confidence limits.

Table 5- 15 Summary of t-test on diameter mean and standard deviation of model data and experiential results

***t-test,* two-tails, two samples different variances, at 95% confidence limits** H_0 : both mean are the same H_1 : both mean are different t-test value = 0.6260 t-distribution percentage at t-test values = 53.67% critical point, 2 tails @ 95% = 2.3788 as t-test < critical point , there is not enough evidence to reject H_0
***t-test,* two-tails, pair test, at 95% confidence limits** H_0 : both standard deviation are the same H_1 : both standard deviation are different t-test value = 0.0014 t-distribution percentage at t-test values = 99.89% critical point, 2 tails @ 95% = 2.3788 as t-test < critical point , there is not enough evidence to reject H_0

5.8 Summary

In depth studies of the simulation data and experiment results were carried out, and completed with discussions. The writer attempted to account for each of the results by the use of the proposed model. Explanations were offered for each of the deviations in the two sets of results. The conclusion to the research will be drawn in the next chapter.

6. Conclusion

In the last chapter of the thesis, the conclusions of the discussion of the previous chapters are put forward. The achievements of the objectives are listed as well. The chapter ends with several suggestions for future work to improve this research.

6.1 Achievement of Objectives

In conclusion to the thesis, the three main objectives of the research were met as follow,

1. A model that accounts for the formation of metallic nanoparticles, in gaseous medium, impelled by femto-second laser energy, was established.
2. The proposed model is expressed as a function of
    (i) laser power,
    (ii) ambient temperature,
    (iii) chamber pressure,
    (iv) carrier gas flow rate,
    (v) physical properties of metal target material, and
    (vi) physical properties of the carrier gas.

    All these six parameters are simple-to-measurable and easy-to-manipulate parameters, as shown by table 3-1. With these parameters manipulation, it is easy to attain the necessary set up to achieve the desirable nanoparticles size with great ease.
3. A set of equipments was designed and built to replicate the environmental condition as described in the model. Simulation data was computed from the model, while experiments were conducted with the equipments to obtain

experimental results. Both the data and results were compared against each other to verify the model.

The experimental results were found to match well with the proposed model in most of experiment runs within the limit of scope of the research. Though some deviations were observed, explanations to these divergences were given. The scope of the research limited the model to following conditions:

- The model developed in this research is limited to the application of femto-second laser ablation on metallic target material.
- Of the six parameters studied in this research, they were restricted to the range as stated in table 6-1:

Table 6- 1 Range of the six parameters used in model.

Pressure	100 ~ 900 mBar
Laser Power	00 ~ 600 mW
Temperature	20 ~ 60 ^{0}C
Flow rate	0.1 ~ 1.0 SLM
Target material type	Ti, Cu , Fe, Zn , Ni
Carrier Gas	N_2 , He , Ar

- Only the physical dimensions of spherical diameter of the nanoparticles are used to quantify the proposed model in this research.

6.2 Knowledge Gained

In the verification of the proposed model, the simulation data was compared against the experimental results. As shown in all the figures in Chapter 5, good fits were displayed between the simulation model data and experimental results,

with a few exceptions. The good fits between the model data and experimental results displayed in the graphs in chapter 4 indicate that the proposed model is viable.

The model was developed based on the mechanism of nuclei growth as a process of monomers collection in the aerosol medium. Any physical factors that can promote and accelerate this process of collection will results in nanoparticles of larger diameter being formed, as well as the widening of the distribution spread of the nanoparticles populations in the aerosol. These arguments are well supported by the results from the experiments.

The diameters of the nanoparticle increase with

(i) an increase in laser power ,
(ii) an increase in chamber pressure ,
(iii) a decrease in carrier gas flow rate ,
(iv) an increase in chamber temperature ,
(v) a decrease in atomic binding energy and increase in atomic volume of the metal material ,
(vi) an increase in atomic / molecular volume of the carrier gas.

When laser power is high, it will ablate more mass of target material into the aerosol, forming more monomers. With the increase in monomer populations, the probability of more monomers collected by growing nuclei increases as well. As a result of more monomers adhering to the nucleus, larger nanoparticle diameter is synthesized.

If the pressure of the chamber is increased, it contains more carrier gas atoms /molecules. These atoms/molecules interact more with the monomers, transferring their momentum to the monomers. Higher momentum monomers will accelerate the collection process, yielding larger diameter nanoparticles.

In the situation of slower flow rates of the carrier gas, monomers formed by ablation have little time to be diffused, thus resulting in a higher concentration of monomers per unit volume. Furthermore, the slow flow rate gives the

growing nuclei more time to grow. The combined effects of these two factors will improve the collection process of the growing nuclei, leading to the formation of larger nanoparticles.

Similarly, an elevation in the temperature of the chamber excites the carrier gas atoms/molecules. The excessive kinetic energy of these atoms/molecules are transmitted to the monomers. There will be more successful adhesive collision with growing nuclei, making the nanoparticles grows bigger.

The atomic physical properties of the metallic material have the most significant effect on the nanoparticle diameters. This is displayed in figure 5-21 on chapter 5. The difference of diameters yielded by different metals under the same ambient conditions is wide. Metals with low atomic binding energy will liberate more monomers when ablated by the same laser power. On the other hand, metals with relatively larger atomic volume, produced larger monomers. Bigger monomers interact more with nuclei, and lower binding energy allow more successful adhesion collisions. All these factors come together to yield larger nanoparticles diameter.

In conditions when bigger atomic/molecular gases are used as carrier medium in the chamber, these bigger gas atoms/molecules will have a higher collision rate with the monomers. The more collisions, the more kinetic energy will be transferred to the monomers. The more monomers with higher energy, the more pronounce the collection of monomers by the nuclei, and the greater the nanoparticles diameter will be.

Based on the mechanism of nuclei growth, the six parameters have similar effects on the distribution spread of the nanoparticle populations. The same positive effects of these six parameters that yield larger diameter, are also the same effects that widen the distribution spread of the nanoparticles population. However, in the event when the *loading*, concentration of nanoparticles in a fixed volume of aerosol, is low, the effects of coagulation and coalescence will be minimized.

The condition of little coagulation and coalescence was replicated in several of the experiment runs, when

- the laser power is at its lowest,
- the metal target has the highest binding energy,
- the carrier gas flow rate at its highest,

The first two conditions ablated the lowest amount of the monomers, and the third condition reduced the loading greatly. All these factors greatly diminish the possibility of coagulation and coalescence occurring, making the distributions spread at their narrowest in this condition.

The effect of pressure and temperature is the next most significant effect on the spread of distribution. As according to the *Ideal Gas Law*, with lower pressure and temperature, the kinetic energy of the carrier gas atoms / molecules are at the lowest. The spread of atoms/molecules kinetic energy distribution is at its narrowest. These low kinetic energy and narrow distribution profile of the carrier gas in turn cause the monomer population to be the same of the similar profile of low kinetic energy and narrow distribution. With more uniform kinetic energy, these monomers yield a population of nanoparticles of a narrow distribution spread.

All in all, under synthesis of metallic nanoparticle using femto second laser ablation in a low pressure chamber, the following general rules hold :

For smaller nanoparticle diameter,

(i) the laser power used is to be lower ;
(ii) pressure of chamber is to be lower ;
(iii) flow rate of he carrier gas is to be faster ;
(iv) temperature within the chamber is to be lower ;
(v) utilize metal with atomic higher binding and smaller atomic volume ;
(vi) utilize carrier gas with smaller atomic /molecular diameter.

For a narrower distribution spread of nanoparticle population,

(i) utilize lower loading aerosol, i.e. lower concentration of monomers to grow nanoparticles ;

(ii) utilize carrier gas type with lower temperature and pressure.

One point to remember is that the physical atomic properties of the material cannot be changed as they are fixed as a constant. Whenever, a new metal is considered as target material, the other ambient parameters have to be altered to compensate for the difference accordingly.

6.3 Suggested Future Work

Although the proposed model was able to explain the phenomena of nanoparticle formation under lower pressure condition femto second laser ablation, the experimental results were not in perfect correlations with data simulated based on the proposed model. These deviations are caused by some of the assumptions taken in the proposed model.

6.3.1 Coagulation and Coalescence

Under the assumption 16 and 17, the mechanism of the sub-process of coagulation and coalescence were omitted in the model. In several experimental runs, the environmental conditions favoured more coagulation and coalescence than others. In these experiment runs, the difference of the diameters between simulated data and experiment results were the greatest. Figure 6-1 below shows the difference of the mean diameters of various nanoparticle diameters yield.

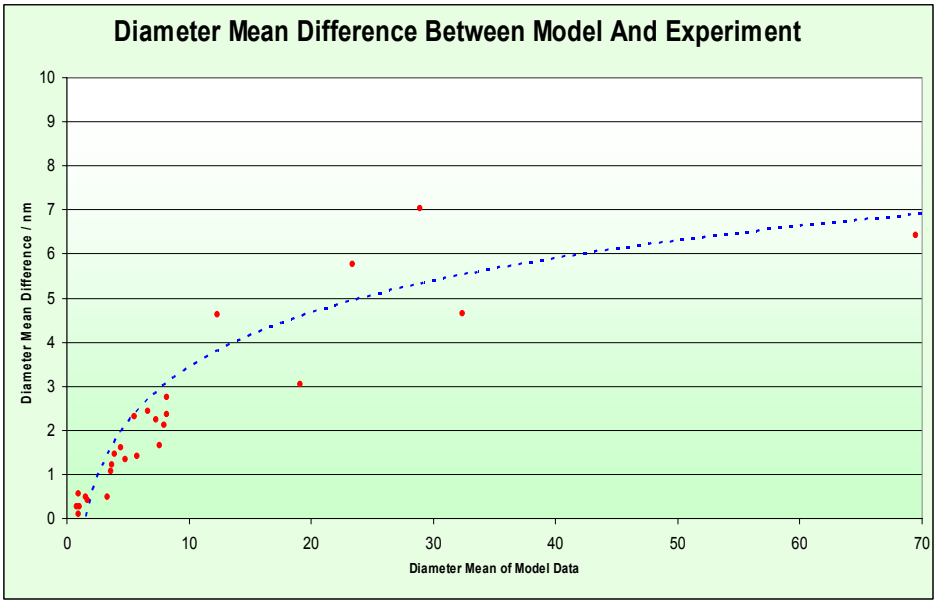

Figure 6- 1 Graphs of diameter difference between Model and Experiments vs. diameter mean

Assume that coagulation and coalescence, other than monomers collections, are the other main mechanism of nuclei growth. The difference in diameter mean could be used as an indication of amount nuclei growth by coagulation and coalescence. As the diameter of the nanoparticles get bigger, so will the effects of coagulation and coalescence become more significant. Due to the assumptions taken in the model, the sub-process of coagulation and coalescence were not included. The writer acknowledges the limitation of the proposed model with respect to coagulation and coalescence and suggests that further work could be undertaken in these areas to improve the robustness of the model.

6.3.2 Metal Target Material

In the discussion of Chapter 5, it was indicated that the model is the most sensitive to the atomic physical properties of the metal, namely the atomic binding energy and atomic volume. It was shown in Chapter 5 , that when the chamber ambient conditions were kept constant the nanoparticles formed by different metal target materials varied greatly. However, no direct mathematical

equation between these physical properties and the nanoparticles was documented in the research. Though the general trend and these relationships were account for in descriptive manner, it was not explained nor quantified by equations. As the scope of this research dose not cover these aspects, the detail study of the sensitivity of these physical atomic properties to nanoparticles diameter was not studied in depth. Future work could be explored into these aspects of the metal material properties to the size formation of nanoparticles.

6.3.3 Correction factor for Carrier Gas

Based on the assumption 20 of *Kinetic Theory of Ideal Gas* and adhering to the *Ideal Gas Law*, all the carrier gas atoms/molecules were taken to be a perfect spherical shape. In reality, as shown in the experiment runs with Nitrogen , a di-atomic molecule, the proposed model could not account for the formation of nanoparticle size accurately. Due to the shape difference of nitrogen gas molecules, the interaction between carrier gas and monomers are different. A correction factor will need to determined and included into the model to make it more accurate and sensitive to the different carrier gas types. As the scope of this research was limited to only three different carrier gas, little conclusion of the correction factor could be deduced form this research. More future work is suggested to determine this correction factor for other types of carrier gases.

6.3.4 Partial Use of the Model

The proposed model could be broken into three parts. The first part of the model explains the laser ablation of metal material. The second part accounts for the formation of monomers. The third describes the growth of nuclei (monomers) into nanoparticle. These three parts could be broken up and used as individual to help build future models.

Example, if evaporation of the metal was done directly by other means. All that is required is to know the amount of metal that is evaporated. Understanding the ambient conditions in which the metal vapour is in, the ratio of monomers and nuclei formed could be determined. The growth rate of the nuclei into nanoparticles can next be determined using the proposed model.

If the medium, in which the monomers and nuclei are to be suspended, is to changed from gaseous to liquid, the same basis could be used for future works. However, correction factors to the denser medium will need to be determined first for this proposed model to work.

Reference

[1] Chokshi, A.H., Rosen, A., Karch, J., Gleiter, H., **"On the validity of the hall-petch relationship in nanocrystalline materials** " *Scripta Met*. 23 (1989) pp.1679

[2] Nieman, G.W., Weertman, J.R., Siegel, R.W., "**Microhardness of nanocrystalline palladium and copper produced by inert-gas condensation**," *Scripta Met*. 23 (1989) pp. 2013

[3] Sanders, P.G., Eastman, J.A. and Weertman, J.R., "**Elastic and tensile behavior of nanocrystalline copper and palladium**" , *Acta mater.* 45, No. 10 (1997) pp. 4019-4025

[4] Nanomat Inc. , North Huntingdon, PA , USA ; http://www.nanomat.com

[5] Technanogy Material's Development , Santa Ana,. CA, USA ; http://www.technanogy.net

[6] Nyacol Inc. Ashland, MA , USA ; http://www.nyacol.com

[7] Ichinose, N., Ozaki, Y., & Kashu, S. (1992). Superfine particle technology. Berlin: Springer

[8] Kodas T.T. & M. Hampden-Smith, "**Aerosol Processing of Materials"**. *Wiley-VCH, New York* 1999.

[9] TiongLiu, Huaiyu Shao and Xingguo Li "**Oxidation behaviour of Fe Al nanoparticles prepared by hydrogen plasma-metal reaction** " *Nanotechnology* 14 (2003) p 542-545.

[10] N.Glumac, Y.Chen and G.Skandan."**Diagnostics and modeling of nanopowder synthesis in low pressure flames**" *J. Mater. Res.* **13** (1998), p. 2572.

[11] A.Singhal, G. Skandan, N.Glumac and B. H. Kear, "**Minimizing aggregation effects in flame synthesized nanoparticles**" *Scr. Mater.* **44** (2001), p 2203-2207

[12] Li X.G. ,Chiba A and Takahashi S , "**Preparation, oxidation and magnetic properties of Fe-Cr ultrafine powders by hydrogen plasma-metal reaction**" *J. Magn. Mater.* **173** (1997) p 101

[13] Perez R J and Lavernia E.J. , "**Grain growth of nanocrystalline Fe–Al alloys produced by cryomilling in liquid argon and nitrogen**" *Mater. Sci. Eng.* **255** (1998) p 124

[14] Liu T, Zhang Y H and Li X G , "**Synthesis of Fe–Al nanoparticles by hydrogen plasma–metal reaction**" *Scr. Mater.* **48** (2003) p403

[15] Source Washington University In St. Louis. ; http:/www.sciencedaily.com/release/2001/02/010227074244.htm

[16] Nieman, G.W., Weertman, J.R., Siegel, R.W., "**Microhardness of nanocrystalline palladium and copper produced by inert-gas condensation**," *Scripta Met*. **23** (1989) pp. 2013

[17] H.Srikanth, R.Hajndl, C.Chirinos, and J. Sanders, " **Magnetic studies of polymer-coated Fe nanoparticles synthesized by microwave plasma polymerization** "*App. Phy. Lett.* **79** (2001), p 3503–3505.

[18] Askeland DR. **The science and engineering of materials.** *Boston, MA: PWS-Kent Publishing Company*; (1989). p. 123

[19] J.R. Groza and R.J. Dowding , "**Nanoparticulate materials densification**". *Nanostruct. Mater.* **7** (1996), pp. 749–76

[20] N.Janakiraman, M.Weimenn, J. Schuhmacher, Kmuller, J.Bill, F. Aldinger and P. Singh, **"Thermal Stability, Phase Evolution, and Crystallization in Si-B-C-N Ceramics**

Derived from a Polyborosilazane Precursor" *Jour. America Ceram. Soc.* **85** (2002) p 1807

[21] Source form AMR International Corp. Toronto, Ontario, Canada

[22] R. K. Kalyanaraman 1, S. H. Yoo 1, M. S. Krupashankara 1, T. S. Sudarshan 1 and R. J. Dowding, " **Novel technique for synthesis and consolidation of aluminium nitride nanopowders**" *Powder Metallurgy*, **43** (2000), p380–385.

[23] Lian Gao, Jingguo Li, Takafumi Kusunose and Koichi Niihara "**Preparation and properties of TiN–Si_3N_4 composites**" Jour. Euro. Cer. Soc. ,**24** (2004), p 381-386

[24] T. C. Rojas and M. Ocaña, "**Uniform nanoparticles of Pr(III)/Ceria solid solutions prepared by homogeneous precipitation**" Scr.Mater., **46** (2002), p655-660

[25] J.F. Chen, Z.G. Shen, F.T. Liu, X.L. Liu and Jimmy Yun, **"Preparation and properties of barium titanate nanopowder by conventional and high-gravity reactive precipitation methods**" *Scr. Mater.*, **49** (2003), p 509-514

[26] J.F. Chen, L.Shen, F.Guo and X.M. Wang, "**Synthesis of nano-fibers of aluminum hydroxide in novel rotating packed bed reactor**" *Chem. Eng. Sci.*, **58** (2003) p 569-575

[27] R. Zauner and A.G. Jones, "**On the influence of mixing on crystal precipitation processes – application of the Segregated Feed Model (SFM)**" *Chem. Eng. Sci.* **57** (2002), p 823–831.

[28] V. Raman, R.O. Fox, A.D. Harvey and D.H. West, "**CFD analysis of premixed methane chlorination reactors with detailed chemistry**" *Ind.& Eng. Chem. Res.* **40** (2001), p 5170–5176.

[29] Schwarzer, H. C., & Peukert, W. (2002). "**Nanoparticle precipitation: Exp. Invest., model. & process simul**." *15th international symposium on industrial crystallization*, Sorrento, Italy.

[30] J.F. Chen and L.Shao, "**Mass production of nanoparticles by high gravity reactive precipitation technology with low cos**t "*China Particuology*, **1** (2003) P 64-69

[31] Source form Nanophase Technologies Corporation , Romeoville, IL , USA

[32] Liguang Wang and Rodney O. Fox, "**Application of in situ adaptive tabulation to CFD simulation of nano-particle formation by reactive precipitation,**" *Chem. Eng. Sci. ,***58** (2003) p 4387-4401

[33] K. Chakrabarti, C.M. Whang , "**Structural and physical properties of Ag doped poly(dimethylsiloxane) modified silica xerogels** "*J. Appl. Phys.* 90 (2001) p 6493

[34] Edited by R.Weast , *CRC HandBook of Cemistry and Physics*, **62nd Ed**. (1981)

[35] K. Masuda, M. Yamamoto, M. Kanaya, and Y Kanemitsu, , "**Fabrication of Ge nanocrystals in SiO_2 films by ion implantation: control of size and position** " *J. Non-Cryst. Solids* **299** (2002) p1097

[36] A.Henglein, T. Linnert, and P. Mulvaney , "**Controlling the Spontaneous Precipitation of Silver Nanoparticles in Sol-Gel Materials** " *Ber. Bunsenges Phys. Chem*. **94** (1990) p1449

[37] P.W. Wei, Bruce Dunn, Vinh Doan, Ben. J. Schwartz, Eli Yablonovitch and M. Yamane, "**Controlling the Spontaneous Precipitation of Silver Nanoparticles in Sol-Gel Materials "** *Jour. Sol-Gel Sci .and Tech.,* **19** (2000) p 249-252

[38] F.S. Li, L. Wang, J.B. Wang, Q.G. Zhou, X.Z. Zhou, H.P. Kunkel and G. Williams, "**Site preference of Fe in nanoparticles of $ZnFe_2O_4$,**' *Jour. Of Mag.and Mag. Mater.* **286** (2004) p 332-339.

[39] X.P Zhao, J.B. Yin, "**Preparation and Electrorheological Characteristics of Rare Earth Doped TiO_2 Suspensions**" *Chem. Mater.* **14** (2002) p 2258-2263

[40] H.Q. Yang, X.J. Wang, H.Z. Shi, F.J. Wang, X.X. Gu and X. Yao, "**Sol–gel preparation of Ge nanocrystals embedded in SiO_2 glasses**" *Jour. Of Crystal Growth,* **236** (2002) p 371-375

[41] Jianrong Zhang and Lian Gao " *Synthesis of SnO2 Nanoparticles by the Sol-gel Method From Granulated Tin*" *Chemistry Letters* **Vol. 32 No. 5** (2003) , p.458 .

[42] Source from Nanogate Technologies GmbH , Saarbrücken, Germany

[43] Erik Pitoniak, Chnag-Yu Wu, Danielle Londeree,David Mazyck, Jean-Claude Bonzongo, Kevin Powers and Wolfgang Sigmund, "**Nanostructured silica-gel doped with TiO_2 for mercury vapor control**", *Journal of Nanoparticle Research* **5** (2003), 281-292

[44] Uyeda R.,**"Progress in Materials Science**" *Pergamon, Oxford,* Vol. **35,** (1991)p. 1.

[45] Ryogo Kubo, "**Electronic Properties of Metallic Fine Particles.** ", *J. Phys. Soc. Jpn.* Vol.**17**, No.**6,** (1962) p 975-986

[46] Chihiro Kaito, "**Formation of double oxides by coalescence of smoke particles of different oxides**" , Journal of Crystal Growth Vol. **55**, Iss. **2**, (Nov. 1981), p 273-280

[47] Chihiro Kaito, Yoshio Saito and Kazuo, "**Studies on the structure and morphology of ultrafine particles of metallic sulfides**" ,*Journal of Crystal Growth*, Vol. **94**, Iss. **4**, (Apr 1989), p 967-977

[48] K.A. Higginson, M.Kuno, J. Bonevich, S.B. Qadri, M. Yousuf and H. Mattoussi, "**Synthesis and characterization of colloidal-HgS quantum dots**" *J. Phys. Chem. B* **106** (2002) p9982

[49] M.Green, N.Allsop, G.Wakefield, P.J. Dobson and J.L. Hutchison, "**A simple metalorganic route to organically passivated mercury telluride nanocrystals** " *J. Mater. Chem.* **12** (2002) p 2671

[50] A. Schild. A. Gutsch,, H. Muhlenweng, and S.E. Partsins, "**Simulation of Nanoparticle Production in Premixed Aerosol Flow Reactors by Interfacing Fluid Mechanics and Particle Dynamics**" *J. Nanoparticl Research* **1** (1999) p560

[51] L.Fulcheri, N.Probst, G.Flamant, F.Fabry and E.Grivei, "**Plasma processing: a step towards the production of new grades of carbon black**" *3rd Int Conf. On Carbon Black, Mulhouse*, (2000) p 11-20

[52] A. Gutsch, M. Krämer, G. Michael, H. Mühlenweg, M. Pridőhl and G. Zimmermann , "**Gas-Phase Production of Nanoparticles**" *KONA Powder and Particle* **20** (2002) p 24-35

[53] Mark Green, Gareth Wakefield and Peter J. Dobson "**Trialkylphosphine oxide/amine stabilised silver nanocrystals-the importance of steric factors and Lewis basicity in capping agents**", *Jour. Mater. Chem.* **13** (2003) p 1076-1078

[54] X.L. Dong, C.J. Choi and B.K. Kim, **"Chemical synthesis of Co nanoparticles by chemical vapor condensation**" Scr.Mater., **47** (2002) p 857-861

[55] F. E. Kruis, H. Fissan, and A. Peled, "**Synthesis of nanoparticles in the gas phase for electronic, optical and magnetic applications - a review**," *Journal of Aerosol Science*, vol. **29**, no. **5-6**, (1998) pp. 511–535

[56] Zhou H, Cai W, Zhang L. , "**Photoluminescence of indium–oxide nanoparticles dispersed within pores of mesoporous silica** " *Appl Phys Lett* **75** (1999) p 495.

[57] Sato S, Murakata T, Ohgawara T.,"**Control of pore size distribution of silica gel through sol-gel process using water soluble polymers as additives**" *J Mater Sci* **25** (1990) p4880.

[58] Kreibig U, Gartz M, Hilger A, Hoovel H., "**Advances in Metal and Semiconductor Clusters**"*Adv Met Semicond Clusters* **4** (1998) p345.

[59] Yasuda T, Komiyama H, Tanaka K. "**Gas-sensitive electrical conduction and its mechanism in a Ag-insulator system with locally discontinuous structure**," *Jpn J Appl Phys* 26 (1987) p818

[60] Jingzhang Gao Youli Qi, Wu Yang, Xiaojun Guo, Shengyin Li and Xien Li, "**Shape control of CeO_2 nano-particles and synthesis of nano-metric solid acid SO_4^{2-} / CeO_2**" *Mater. Chem. and Phy.* **82** (2003) p 602-607

[61] Chrisitian Janzen, Jorg Knipping, Bernd Rellinghaus and Paul Roth, "**Formation of slica-embbed iron-oxide nanoparticles in low-pressure flames**", *Journal of Nanoparticle Research* **5** (2003), 589-596

[62] A.Vital, U. Klotz, T.Graule, .R.Mueller, H.k. Kammler and S.E. Pratsins, "**Synthesis of spherical , non-agregated silica nanoparticles**" *NATO Advanced Research Workshop on Nanostructured Materials and Coatings*, (Aug. 2002) Kiev, Ukraine

[63] Aiguo Liu, Kafui Nyavora, Zhimin Lib and Nosa O.Egiebora," **Effects of composition and calcinations temperature on morphology and structure of barium modified zirconia nanoparticles** " *Mater. Sci. and Eng. A* **, 366** (2004) p66-73

[64] Mansoo Choi, **"Research in Korea on gas phase synthesis and control of nanoparticles",** *Journal of Nanoparticle Research* **3**: (2001) p201–211,

[65] Huaming Yang, Yuehua Hu, Xiangchao Zhang and Guanzhou Qiu **, "Mechanochemical synthesis of cobalt oxide nanoparticles"** Mater. Let., **58** (2004), P 387-389

[66] Huaming Yang, Aidong Tang, Xiangchao Zhang, Wuguo Yang and Guanzhuo Qiu "**In_2O_3 nanoparticles synthesized by mechanochemical processing**"*, Scr. Mater.* , **50** (2004) , p 413-415

[67] Wei Chen and Junying Zhang, " **Ag nanoparticles hosted in monolithic mesoporous silica by thermal decomposition method** " *Scr. Mater.* ,**49** (2003),p 321-325

[68] Zhijian Wang,Haiming Zhang, Ligong Zhang, Jinshan Yuan, Shenggang Yan and Chunyan Wang "**Low-temperature synthesis of ZnO nanoparticles by solid-state pyrolytic reaction**. " *Nanotechnology,* **14** (2003), 11-15

[69] P. A. Chernavskii, N. V. Peskov, A. V. Mugtasimov and V. V. Lunin, "**Oxidation of metal nanoparticles: Experiment and model**." *Russian Journal of Physical Chemistry B, Focus on Physics* Volume **1**, Number **4** (2007) , 1990-7931

[70] Y.B. Pithawalla, M.S. El-Shall, S.C. Deevi, V. Strom and K.V. Rao "**Synthesis of Magnetic Intermetallic FeAl Nanoparticles from a Non-Magnetic Bulk Alloy"** *J. Phys. Chem.* **105** (2001), p. 2085

[71] A. Puretzky, D.B. Geohegan, X. Fan and S.J. Pennycook "**In situ imaging and spectroscopy of single-wall carbon nanotube synthesis by laser vaporization**" *Appl. Phys. Lett.* **76** (2000), p. 182

[72] K.R. Chen, T.C. King, J.H. Hes, J.N. Leboeuf, D.B. Geohegan, R.F. Wood *et al "***Theory and numerical modeling of the accelerated expansion of laser-ablated materials near a solid surface***" .Phys. Rev. B* **60** (1999), p8373

[73] Y. B. Pithawallaa, M. S. El-Shall and S. Deevib "**Laser based synthesis of intermetallic Cu-Zn nanoparticles and filaments**", *Scr. Mater.* **48** (2003) , p 671-676

[74] Dietz T.G., M.A. Duncan, D.E. Powers & R.E. Smalley, "**Laser production of supersonic metal cluster beams**" . *J. Chemi. Phys.* **74,** (1981) p6511–6512.

[75] Lowndes D.H., D.B. Geohegan, A.A. Puretzky, D.P. Norton & C.M. Rouleau, "**Synthesis of novel thin-film materials by pulsed laser deposition**". *Science* **273** (1996) p898–903.

[76] William T. Nichols, Gokul Malyavanatham, Dale E. Henneke, James R. Brock, Michael F. Becker , John W. Keto and Howard D. Glicksman , "**Gas and pressure dependence for the mean size of nanoparticles produced by laser ablation of flowing aerosols** ", *Journal of Nanoparticle Research* **2**: (2000) p141–145,

[77] Becker M.F., J.R. Brock, H. Cai, D.E. Henneke, J.W. Keto, J. Lee,W.T. Nichols & H.D. Glicksman, "**Metal nanoparticles generated by laser ablation**". *Nanostruc. Mat*. **10,** (1998) p 853–863.

[78] M.V. Allmen. In:" **Laser-Beam Interactions with Materials** " *Springer-Verlag, New York* (1987), p. 158.

[79] Deirdre L. Olynick, J. Murray Gibson and Robert S. Averback. "**In situ ultra-high vacuum transmission electron microscopy studies of nanocrystalline copper,**"*Mater. Sci. Eng. A* **204** (1995), p. 54.

[80] Changsheng Xie, Junhui Hua, Run Wua and Hui Xia **,** "**Structure transition comparison between the amorphous nanosize particles and coarse-grained polycrystalline of cobalt, Nanostructured Materials**" *Nanostruct. Mater.* **8** (1999), p. 1061-1066

[81] El-Shall, Samy S. and Li, Shoutian "**Synthesis of nanoparticles by a laser-vaporization-controlled condensation technique**" *Proc. SPIE Vol.* **3123**,(07/1997) p. 98-109

[82] T. Takeichi, Y. Eguchi, Y. Kaburagi, Y. Hishiyama, and M. Inagaki, "**Carbonization and graphitization of BPDA/PDA polyimide films: effect of structure of polyimide precursor** " *Carbon* **37** (1999) p569

[83] B. Wolff-Rottke, J. Ihlemann, H. Schmidt, A. Scholl**, "Influence of the laser-spot diameter on photo-ablation rates"** *Appl. Phys*. A **60** (1995) p13.

[84] Z . A. Misra, A. Mitra, and R.K. Thareja, "**Diagnostics of laser ablated plasmas using fast photography** " *Appl. Phys. Lett.* **74** (1999) p 929

[85] Gurav A., T. Kodas, T. Pluym & Y. Xiong, 1993. "**Aerosol processing of materials**". *Aerosol Sci. Technol*. **19**, 411–452.

[86] K.C.Yung and D.W. Zeng , "**Laser ablation of Upilex-S polyimide: influence of laser wavelength on chemical structure and composition in both ablated area and halo**" *Surf. And Coat. Tech.,* **145** (2001) , p 186-193

[87] Danny Perez and Laurent J. Lewis, " **Ablation of solids under femtosecond laser pulses** ", *Physics Review Letter*, **Vol.89 No. 25** (2002) 255504

[88] K. Sokolowski-Tinten, J. Bialkowski, A. Cavalleri, D. von der Linde ,A. Oparin J. Meyer-ter-Vehn and S. I. Anisimovet, "**Transient States of Matter during Short Pulse Laser Ablation** " , *Physics Review Letter*, **81** (1994) 224

[89] Sylvie Noel, Jorg Hermann, Tatiana Itina, "**Investigation of nanoparticle generation during femtosecond laser ablation of metals** "*Applied Surface Science* **253** (2007) p6310–6315

[90] S. Eliezer, N. Eliaz, E. Grossman, D. Fisher, I. Gouzman, Z. Henis, S.Pecker, Y. Horovitz, M. Fraenkel, S. Maman, Y. Lereah, " **Synthesis of nanoparticles with femtosecond laser pulses** " *Phys. Rev. B* **69** (2004) p144119.

[91] S. Amoruso, G. Ausanio, R. Bruzzese, M. Vitiello, X.Wang, "**Femtosecond laser pulse irradiation of solid targets as a general route to nanoparticle formation in a vacuum**" *Phys. Rev. B* **71** (2005) p033406.

[92] D. Scuderi, O. Albert, D. Moreau, P.P. Pronko, J. Etchepare, "**Interaction of a laser-produced plume with a second time delayed femtosecond pulse**" *Appl. Phys. Lett*. **86** (2005) p071502.

[93] T.E. Itina, J. Hermann, Ph. Delaporte, M. Sentis, " **Modeling of metal ablation induced by ultrashort laser pulses** ",*Thin Solid Films* , **453 –454** (2004) p513–517

[94] T.E. Itina, F. Vidal, PH. Delaporte, M.Sentis, "**Numerical study of ultra-short laser ablation of metals and of laser plume dynamics** ", *Appl. Phys. A* **79**, (2004) p1089–1092

[95] E. Gamaly, A. Rode, B. Luther-Davies, V. Tikhonchuk "**Ablation of solids by femtosecond lasers: Ablation mechanism and ablation thresholds for metals and dielectrics** ", *Phys. Plasm*. **9**, (2002) p949

[96] P. Lorazo, L.J. Lewis, M. Meunie, "**Short-Pulse Laser Ablation of Solids: From Phase Explosion to Fragmentation** " *Phys. Rev. Lett*. **91**, (2003) 225502

[97] B.J. Garrison, T.E. Itina, L.V. Zhigilei, "**Limit of overheating and the threshold behavior in laser ablation** " *Phys. Rev. E* **68**, (2003) 041501

[98] Danny Perez and Laurent J. Lewis, " **Molecular dynamics study of ablation of solids under femtosecond laser pulses** ",*Physical Review B*, , (2003).

[99] D Danny Perez and Laurent J. Lewis. " **Ablation of solids under femto-second laser pulses.**" *Physical Review Letters*, **89**: (2002) p255504

[100] Ya. B. *Zel'dovich* and Yu. P. Raizer, "**Physics of Shock Waves and High-Temperature Hydrodynamic Phenomena**", *Dover Publications*, **Vol 8** (2002), p 585 - 596

[101] M. Kuwata a B. Luk'yanchuk b, T. Yabe , "**Nanoclusters formation within the vapor plume, produced by ns-laser ablation: Effect of the initial density and pressure distributions**" , *Japan J. Appl. Phys.* **Vol 40** (2001) p4262-4268

[102] B. Luk'yanchuk, W. Marine, "**On the delay time in photoluminescence of Si-nano-clusters, produced by laser ablation**" *Applied Surface Science* **154–155** (2000) p314–319

[103] Tatiana E. Itina , Karine Gouriet , Leonid V. Zhigilei , Sylvie Noel, Jorg Hermann , Marc Sentis, "**Mechanisms of small clusters production by short and ultra-short laser ablation"** *Applied Surface Science* **253** (2007) p7656–7661

[104] W. Marine, L. Patrone , B. Luk'yanchuk, M. Sentis, "**Strategy of nanocluster and nanostructure synthesis by conventional pulsed laser ablation** *" Applied Surface Science* **154–155** (2000) p345–352

[105] L.C. Chen, in: D.B. Chrisey, G.K. Hubler., "**Pulsed Laser Deposition of Thin Films**", *Wiley*, *Eds* (1994) p. 195.

[106] Marc Ullmann, Sheldon K. Friedlander and Andreas Schmidt-Ott**,** "**Nanoparticle formation by laser ablation**", *Journal of Nanoparticle Research* **4**: (2002) p499–509

[107] Ready J.F., **Effects of High-Power Laser Radiation.** (1971) *.Academic Press.*

[108] S. Amoruso, R. Bruzzese, M. Vitiello , N. N. Nedialkov, P. A. Atanasov ,"**Experimental and theoretical investigations of femtosecond laser ablation of aluminum in vacuum**", *Journal of Applied Physics* **98** (2005) 044907

[109] D. Scuderi, R. Benzerga, O. Albert, B. Reynier, J. Etchepare, " **Spectral and temporal characteristics of metallic nanoparticles produced by femtosecond laser pulses** " *Appl. Surf. Sci.* **252 (13)** (2006) p 4360–4363

[110] L.V. Zhigilei, B.J. Garrison**,** " **Microscopic mechanisms of laser ablation of organ.** " *J. Appl. Phys*. **88** (3) (2000) p 1281.

[111] G.A. Bird, "**Molecular Gas Dynamics and the Direct Simulation of Gas Flows**", *Clarendon, Oxford,* 1994.

[112] T.E. Itina, J. Hermann, P. Delaporte, M. Sentis, "**Laser-generated plasma plume expansion: Combined continuous-microscopic modeling**" *Phys. Rev. E* **66** (2002) 066406.

[113] M.I. Zeifman, B.J. Garrison, L.V. Zhigilei, "**Combined molecular dynamics–direct simulation Monte Carlo computational study of laser ablation plume evolution**", *J. Appl. Phys*. **92** (2002) 2181.

[114] H. Mizuseki, Y. Jin, Y. Kawazoe, L.T.Wille, **"Cluster growth processes by direct simulation monte carlo method** " , *Appl. Phys*. A **73** (2001) 731-735

[115] B. Briehl, H.M. Urbassek, "**Monte Carlo simulation of growth and decay processes in a cluster aggregation source**" , *J. Vac. Sci. Technol. A* **17** (1999) 256.

[116] Sproson, D. W., Messing, G. L.. "**Ceramic powder synthesis by thermal reaction of atomized solutions**" *Advances in Ceramics*. Vol. 21 (1987) C, Inc.,Westerville. P 99-108.

[117] Messing, G. L., Zhang, S.-C., Jayanthi, G. V.. "**Ceramic powder synthesis by spray pyrolysis**" . *J. Am. Ceram. Soc.*, Vol. **76** (1993) p. 2707.

[118] Gurav, A., T. Kodas, T. Pluym, Y. Xiong.. "**Aerosol processing of materials**". *Aerosol Sci. Tech.*, Vol. **19**, (1993) p. 411.452.

[119] Kodas, T. T."**Generation of complex metal oxides by aerosol processes : superconducting ceramic particles and films**". *Angewandte Chemie International Edition,* Vol. **28**, (1989) p794-807.

[120] S. Krishnadasan, J. Tovilla, R. Vilar, A. J. deMello and J. C. deMello, "**On-line analysis of CdSe nanoparticle formation in a continuous flow chip-based microreactor** ", *Journal of material chemistry.* Vol **14** , (2004) p2655-2660

[121] Koch, W. and Friedlander, S. K. "**The effect of particle coalescence on the surface-area of a coagulating aerosol**". *J. Colloid Interface Sc*i. (1990) **140**, p419-427.

[122] Xiong, Y., Akhtar, M. K. and Pratsinis, S. E." **Formation of agglomerate particles by coagulation and sintering II : The evolution of the morphology of aerosol-made titania, silica, and silica doped titania powders**".*J. Aerosol Sci.* **24** (1993), p301-313.

[123] Girshick, S., Rao, N., Haberlein, J., McMurry, P., Jones, S., Hansen, D. and Micheel, B. "**Nanoparticle formation using a plasma expansion process**". *Plasma Chem. Plasma Process*. **15**, (1995) p581-607.

[124] Friedlander, S. K. and Wu, M. K." **Linear rate law for the decay of the excess surface-area of a coalescing solid particle**." *Phys. Rev. B* **49** (1994), p3622-3624.

[125] Zachariah, M. R., Aquino-Class, M., Shull, R. D. and Steel, E. "**Formation of superparamagnetic nanocomposites from vapor phase condensation in a flame**". *Nanostructured Mater*. **5**, (1995) 383-392.

[126] Kingery, W. D. and Berg, M. "**Study of the initial stages of sintering solids by viscous flow, evaporation-condensation, and self-diffusion**". *J*. *Appl*. *Phys*. **26**, (1955) 1205 - 1212.

[127] Kari E.J. Lehtinen, Michael R. Zachariah, "**Energy accumulation in nanoparticle collision and coalescence processes**", *Aerosol Science* **33** (2002) 357–368

[128] Gokul Malyavantham, Daniel T.O'Brien, Micheal F. Becker, Johon W.Keto adn Desiderio Kovar, "**Au-Cu nanoparticles produced by laser ablation of mixture of Au and Cu mircoparticles**" *Journal of Nanoparticle Research* **6** ,(2004) p661-664

[129] E. Ozawa, Y. Kawakami and T.Seto "**Formation and size contol of tungsten nanoparticle produced by Nd:YAG laser irradiation**" *Scripta Materialia* **44** (2001) p 2279-2283

[130] T. Seto, Y. Kawakami, N.Suzuki, M.Hirasawa and N. Aya, "**Laser synthesis of Uniform Silicon single nanodots** ", *Nano Letters* , Vol.**1** No.**6** (2001), 315-318

[131] T.Seto, Y. Kawakami, N.Suzuki, M. Hirasawa, S. Kano. N.Aya S. Saskai and H. Shimura, "**Evaluation of morphology and size distribution of silicon and titanium oxide nanoparticles generated by laser ablation** ", *Journal of Nanoparticle Research* **3** ,(2001) p185-191

[132] Sergiy Libert, Dan V.Goia and Egon Matijevic, "**Internally composite uniform colloidal cadmium sulfide sphere**" *Langmuir* **19** (2003) 10673-10678

[133] H. Cai, N. Chaudhary,t J. Lee,s M. F. Becker, J. R. Brock,t J. W. Keto "**Generation of metal nanoparticle by laser of microspheres**" *J*. *Aerosol Sci*. Vol. **29**, No. **5/6**, (1998) 627-636

[134] Toshihito Miyama and Yoshiro Yonezawa. "**Photoinduced formation and aggregation of silver nanoparticle at the surface of carboxymethlcellulose films**", *Journal of Nanoparticle Resaerch ,* **6**(2004), 457-465.

[135] Sudipa Panigrahi, Subrata Kundu, Sujit Kumar Ghosh, Sudip Nath and Tarasankar Pal "**General method of synthesis for metal nanoparticles**", *Journal of Nanoparticle Research* **6** (2004), 411–414,.

[136] Ulikra Backman, Jorma K.Jokiniemi, Ari Auvinen and Kari E.J.Lehtine, "**The Effect of Boundary Conditions on Gas–Phase Synthesized Silver Nanoparticles**" ,*Journal of Nanoparticle Research* , **4** (2002), 325-335

[137] Y. J. Lee, H. T. Kim and K. W. Lee, "**Development of monitoring technology for airborne particulate matter**", *Environmental Monitoring and Assessment* **70 (**2001), 3–20

[138] S.B. Kwon, M.C. Kim, K.W. Lee, "**Effects of jet configuration on the performance of multi-nozzle impactors**" , *Journal of Aerosol Scienc*e, Vol **336** Iss **6**,(2002) , 859-869

[139] H. T. Kim, Y. T. Han, Y. J. Kim, K. W. Lee, and K. J. Chun, "**Design and test of 2.5 μm cut off size inlet based on a particle cup impactor configuration**" *Aerosol Science and Technology* **36** (2002)136–144

[140] Yogendra Singh, JuileR.N. Javier, Sheryl H. Ehrman, Martin H. Magnusson, Knut Deppert, " **Approaches to increasing yield in evapourtaion / condensation nanoparticle generation**", *Journal of Aerosol Scienc*e, **33**,(2002) ,1309-1325,

[141] Gurav A., T. Kodas, T. Pluym & Y. Xiong,. "**Aerosol processing of materials**." *Aerosol Sci. Technol.* (1993) **19**, 411–452.

[142] Dietz T.G. , M.A. Ducan, D.E. Powers and R.E. Samelly, "**Laser production of supersonic metal cluster beam** ", *Journal of Chemistry and Physics* **74**, (1981), 6511-6512

[143] Lowndes D.H. , D.H. Geohegan, A.A. D.P. Norton and C.M. Rouleau, "**Synthesis of novel thin film material by pulsed laser deposition**", Science,**273**, (1996) 898-903

[144] M.V. Allmen. In: **Laser-Beam Interactions with Materials**, *Springer-Verlag, New York* (1987), p. 158.

[145] Deirdre L. Olynick, J. Murray Gibson and Robert S. Averback. "**In situ ultra-high vacuum transmission electron microscopy studies of nanocrystalline copper,**"*Mater. Sci. Eng. A* **204** (1995), p. 54

[146] Changsheng Xie, Junhui Hua, Run Wua and Hui Xia **,** "**Structure transition comparison between the amorphous nanosize particles and coarse-grained polycrystalline of cobalt, Nanostructured Materials**" *Nanostruct. Mater.* **8** (1999), p. 1061-1066

[147] J. Heitz, J.T. Dickinson, " **Characterization of particulates accompanying laser ablation of pressed polytetrafluorethylene (PTFE) targets**" *Appl. Phys.* A **68** (1999) 515.

[148] T. Takeichi, Y. Eguchi, Y. Kaburagi, Y. Hishiyama, and M. Inagaki, "**Carbonization and graphitization of BPDA / PDA polyimide films: effect of structure of polyimide precursor** " *Carbon* **37** (1999) p569

[149] B. Wolff-Rottke, J. Ihlemann, H. Schmidt, A. Scholl**, "Influence of the laser-spot diameter on photo-ablation rates"** *Appl. Phys*. A **60** (1995) p13

[150] Z . A. Misra, A. Mitra, and R.K. Thareja, "**Diagnostics of laser ablated plasmas using fast photography** " *Appl. Phys. Lett.* **74** (1999) p 929

[151] Igor S.Altman, Igor E.Agranovski and Mansoo Choi, "**Nanoparticle Generation : The Concept of A Stagnation Size Region For Condensation Growth**", *Physical Review E* **70** (2004) 062603

[152] Michael R.Zachariah and Michael J.Carrier, "**Molecular Dynamics Computation if Gas-Phase nanoparticle Sintering : A Comparison With Phenomenological Models**." *Journal of Aerosol Science,* Vol **30** , No **9**, (1999), pp1139-1151

[153] Yasuo Kousaka, Toshiyuki Nomura and Manuel Alonso, "**Simple Model of Particle Formation By Homogeneous and Heterogeneous Nucleation**" ,*Advance Powder Technology*, Vol**12**, No**3**, (2001), pp291-309

[154] N.Suzuki, T.Makino, Y.Yamada, Takehito and T.Seto, "**Monodispersed, non-agglomerated silicon nanocrystallites** " , *Applied Physics Letter* Vol **78** Nbr **14** (2001), p2043-2045

[155] P.Heszler, K.Elihn, L.Landstrom and M.Boman, "**Formation and Emission Spectroscopy of Laser Generated Nanoparticle**" , *Proc. SPIE* Vol **4590,** pp251-262.

[156] S.Veintemillas-Vergauer, O.Bomati-Miguel and M.P.Morales ,"**Effect of Process Conditions On The Structural And Magnetic Properties of γ–Fe_2O_3 Nanoparticles Produced By Laser Pyrolysis**" , *Scripta Materialia*, 47(2002) p589-593

[157] Carls, J.C. and J.R. Brock "**Propagation of laser breakdown and detonation waves in transparent droplets**". *Opt. Lett.,* **13**, (1988) p273.

[158] Carls, J.C. and J.R. Brock "**Explosive vaporization of single droplets by lasers: comparison of models with experiments**". *Opt. Lett*., **13**, (1988) p919.

[159] Mansoo Choi, **"Research in Korea on gas phase synthesis and control of nanoparticles",** *Journal of Nanoparticle Research* **3**: (2001) p201–211,

[160] R. Wolfe "**The Theory of the Reflectivity of Metals**", *Proc. Phys. Soc. A* **68** (1955) 121-127

[161] P. Gonzales, R. Bernath, J. Duncan , T. Olmstead , M. Richardson , " **Femtosecond ablation scaling for different materials** " , *Proceeding of SPIE* Vol **5458** (265-272)

[162] Y.Lawrence Yao, Hongqiang Chen , Wenwu Zhang, "**Time scale effects in laser removal : a review** ", *International Journal Advance Manufacturing Technology* (24-Nov-2004) DOI 10.1007/s 000170-003-2026-y

[163] A. Gutsch, M.Kramer , G.Micheal, H.Muhlenweg, M. Pridohl and G.Zimmermann, "**Gas-Phase Production of Nanoparticle**", *KONA* No.**20** (2002) pp24-35

[164] Motoaki Adachi,Shigeki Tsukui and Kikuo Okuyama, "**Nanoparticle formation mechanism in CVD reactor with ionization of source vapour**", *Jounral of Nanoparticle Research* **5** (2003) 31-37

[165] Muramoto J, Nakata Y, Okada T and Maeda M , "**Influences of Preparation Conditions on Laser Ablated Si nanoparticle formation processes observed by imaging laser spectroscopy**", *Applied Surface Science*, **129** (May 1998) p373-377

[166] Krinke, T.J , K. Deppert , M.H. Magnusson , F. Schmidt and H. Fissian "**Microscopic aspects of the deposition of nanoparticles from gas phas**e", *Journal of Aerosol Science* , **33** (2002), 1341-1359

[167] Yasuo Kousaka, Toshiyuki Nomura and Manuel Alonso, "**Simple Model of Particle Formation By Homogeneous And Heterogeneous Nucleation**", *Advance Powder Technology,* Vol**12**, No**3**, (2001) pp291-309,

[168] László Mihály , Michael C. Martin "**Solid State Physics: Problems and Solutions**" , *Wiley-Interscience* (1996)

[169] D. Perez and L. Lewis, "**Ablation of Solids under Femtosecond Laser Pulses**" *Phys. Rev. Lett.* **89**, (2002) 255504

[170] L. V. Zhigilei, P. B. S. Kodali, and B. J. Garrison, "**A Microscopic View of Laser Ablation**."*J. Phys. Chem. B* **102** (1998) 2845

[171] L. V. Zhigilei, "**Dynamics of the plume formation and parameters of the ejected clusters in short-pulse laser ablation** " *Appl. Phys. A* **76** (2003) 339

[172] M. Lenzner, F. Krausz, J. Kruger, and W. Kautek," **Photoablation with sub-10fs laser pulses**" *Appl. Surf. Sci.* **11** (2000) 154–155

[173] N. Nedialkov, P. A. Atanasov, S. E. Imamova, A. Ruf, P. Berger, and F. Dausinger, "**Dynamics of the ejected material during ultrashort laser ablation of metals** " *Appl. Phys.* A **79** (2004) 1121

[174] J. Hohlfeld, S.-S. Wellershoff, J. Gudde, U. Conrad, V. Jahnke, and E. Matthias "**Electron and lattice dynamics following optical excitation of metals**", *Chem. Phys*. **251** (2000) 237

[175] N. M. Bulgakova, R. Stoian, A. Rosenfeld, and I. V. Hertel, E. E. B. Campbell, "**Electronic transport and consequences for material removal in ultra-fast pulsed laser ablation of materials** " *Physical Review B* **69**, (2004) 054102

[176] R.Stoian, D. Ashkenasi, A. Rosenfeld, and E. E. B. Campbell, "**Coulomb explosion in ultrashort pulsed laser ablation of Al_2O_3**" , *Phys. Rev. B* **62**, (2000) 13167-

[177] E. M. Logothetis and P. L. Hartman, " **Three-Photon Photoelectric Effect in Gold** " *Phys. Rev. Lett.* **18** (1967) 581

[178] E. M. Logothetis "**Two-Photon Photoelectric Spectroscopy in CsI**" *Phys. Rev. Lett*. **19**, (1967) 1470-1472

[179] E. M. Logothetis and P. L. Hartman, " **Laser-Induced Electron Emission from Solids: Many-Photon Photoelectric Effects and Thermionic Emission** " *Phys. Rev.* **187** (1969) 460

[180] Changrui Cheng and Xianfan Xu "**Mechanisms of decomposition of metal during femtosecond laser ablation"** *Physical Review B* **72**,(2005) 165415

[182] B. Rethfeld, A. Kaiser, M. Vicanek, G. Simon "**Ultrafast dynamics of nonequilibrium electrons in metals under femtosecond laser irradiation** " *Phys. Rev. B 65*, (2002) 214303

[183] P. Maine, D. Strickland, P. Bado, M. Pessot, and G. Mourou "**Generation of ultrahigh peak power pulses by chirped pulse amplification** " *, IEEE Journal of Quantum Electronics* **24** (1988) 398-403

[184] S.K.Friedlander, "**Smoke , Dust and Haze : Fundamentals of Aerosol Behavior**", *John Wiley & Sons* (1963)

[185] Fred Gelbard, Yoram Tambour John H. Sinfeld , "**Sectional representations for simulation aerosol dynamics** " , *Journal of Colloid and Interface Science* **76** no **2** (1980) p541–556

[186] Vanja Margetic, "**Femto Second Laser Ablation** ", *Dissert. Erlangung Dr. , Fach. Phy. Univ. Dortmund*, December 2002

[187] Srinivas Vwemury, Karl A. Kusters and Sotiris E. Pratsinis, "**Time-lag for attainment of self preserving particle size distribution by coagulation**" *Journal of Colloid and Interface Science* **165** (1994) p53-59

[188] Anisimov, S. I., Kapeliovich, B. L., and Perel'man, T. L., ''**Electron Emission From Metal Surfaces Exposed to Ultra-Short Laser Pulses**,'' *Sov. Phys. JETP*, **39**, (1974) p. 375–377.

[189] Chowdhury, I. H., and Xu, X., ''**Heat Transfer in Femtosecond Laser Processing of Metal**,'' *Numer. Heat Transfer, Part A*, **44**, (2003), pp. 219–232.

[190] Xianfan Xu, Changrui Cheng and Ihtesham H. Chowdhury, " **Molecular Dynamics Study of Phase Change Mechanisms During Femtosecond Laser Ablation** "*Journal of Heat Transfer* Vol. **126** (2004) p727-734

[191] N. N. Nedialkov and P. A. Atanasov , S. Amoruso, R. Bruzzese, and M. Vitiello "**Experimental and theoretical investigations of femtosecond laser ablation of aluminum in vacuum**", *Journal of Applied Physics* **98** (2005) p044907

[192] Xu, X., ''**Heat Transfer and Phase Change in Pulsed Excimer Laser Ablation of Metal**,'' *Annual Review of Heat Transfer, 12, C.-L. Tien, V. Prasad, and F. P. Incropera, eds., Bell House, New York*, (2001), pp. 79–115.

[193] Kelly, R., and Miotello, A. ''**Comments on Explosive Mechanisms of Laser Sputtering**,'' *Appl. Surf. Sci.,* **96–98**, (1996) pp. 205–215.

[194] Song, K. H., and Xu, X. ''**Explosive Phase Transformation in Pulsed Laser Ablation**'' *Appl. Surf. Sci*., **127** (1998), pp. 111–116

[195] J. König, S. Nolte, and A. Tünnermann, "**Plasma evolution during metal ablation with ultrashort laser pulses**" *Optics Express, **Vol.** **13,*** Issue **26**, (2005) p.10597-10607

[196] Siders, C. W., Cavalier, A., Sokolowski-Tinten, K., Toth., Cs., Guo, T., Kammler, M., Horn von Hoegen, M., Wilson, K. R., von der Linde, D. and Barty, C. P. J. , ''**Detection of Nonthermal Melting by Ultrafast X-Ray Diffraction**,'' Science, 286, (1999) p1340–1342.

[197] Henyk, M., Wolfframm, D., and Reif, J., ''**Ultra Short Laser Pulse Induced Charged Particle Emission From Wide Band-gap Crystals**,'' *Appl. Surf. Sci*., **168**, (2000) p. 263–266.

[198] Russo, R.E. Mao X.L. and Mao, S.S , "**The physics of laser ablation in microchemical analysis**", *Analytical Chemistry* **74**[**3**], (2-1-2002) 70A-77A.

[199] Mott, N. F. (Nevill Francis) **,"Sir Nevill Mott : 65 years in physics",** *World Scientific*, 1995.

[200] Philip B.Allen, "**Theory of Thermal Relaxation of Electrons In Metal**", *Physical review Letter,* Iss **13**, vol **59** , (1987) p1460-1463

[201] Zhang, W., Yao, Y. L., and Chen, K., "**Modeling and Analysis of UV Laser Micromachining of Copper**," *Int. J. Advanced Manufacturing Technology, Pergamon*, Vol. 18, (2001) pp.323-331

[202] D.Y.Tzou and Emily J.Pfautsch, "**Ultra heating and thermomechanical coupling induced by femtosecond lasers**", *J.Eng. Math*., DOI 10.1007 / s10665-007-9181-3 (2007) 0022-0833 (Print) 1573-2703 (Online)

[203] M. Wolf and M. Aeschlimann," **Femtosekundendynamik in Metallen - Das kurze Leben heißer Elektronen / The femto second dynamic in metals - the short life of hot electrons**" *Phys. B*. **54**, (1998) p45.

[204] D.Bäuerle, "**Laser Processing and Chemistry, 3rd ed"**., *Springer, Berlin, 2000.*

[205] F.Vidal, T.W. Johnston, S. Laville, O. Barthélemy, M. Chaker, B. Le Drogoff, J. Margot, and M. Sabsabi," **Critical-Point Phase Separation in Laser Ablation of Conductors**" *Phys. Rev. Lett*. **86**, (2001) 2573 - 2576

[206] B.Luther-Davies, E. G. Gamaly, Y. Wang, A.V.Rode, and V.T. Tikhoncuk "**Matter in Ultrastrong Laser Fields**" *Sov. J. Quantum Electron. 22(*4), 289-325 (1992).

[207] E. M. Lifshitz and L. P. Pitaevskii, ***Physical Kinetics,*** *Pergamon Press, Oxford*, 1981.

[208] V.Yu. Bychenkov, V.T. Tikhnonchuk and S.V. Tolokonnikov, "**Nuclear reactions triggered by laser-accelerated high-energy ions**" *JETP* **88**, (1999)1137-1142,

[209] E.G. Gamaly, A.V. Rode, and B Luher-Daviers , "**Ultrafast ablation with high-pulse-rate lasers. Part I: Theoretical considerations** " *Journal of Applied Physics*, Volume **85**, Issue **8**, (1999) pp. 4213-4221

[210] A.V. Rode , B Luher-Daviers and E.G. Gamaly, "**Ultrafast ablation with high-pulse-rate lasers. Part II: Experiments on laser deposition of amorphous carbon films**" *Journal of Applied Physics*, Volume **85**, Issue **8**, (1999) pp 4222-4330

[211] F.Drewnick, "**Airbone Nanoparticles : Properties, measurement and Atmospheric Relevance**", Wintersemester Lecture Series , *Max-Plank Institut fuer Chemie/ Institut fuer Physik der Atmosphere*, Uni Mainz 2004

[212] Hinds, W.C, "**Aerosol Technology – Properties, Behavior, and Measurement of Airborne Particles; 2nd edition** ", *John Wiley & Sons, New York* (1999)

[213] N.A.Fuchs ,"**The Mechanics of Aerosols**", *Pergamon Press Book* , 1964

[214] Serway, Raymond, "**Physics for Scientists and Engineers with Modern Physics, 3rdEd**", *Saunders College Publishing* (1990)

[215] Kari E.J. Lehtinen and Michael R. Zachariah, "**Energy accumulation during the coalescence and coagulation processes**" , *Journal of Aerosol Science*, **33** (2002) 357-368

[216] Kari E.J. Lehtinen and Michael R. Zachariah,"**Energy accumulation during the coalescence and coagulation of nanoparticles**" , *Physical Letter Review B* **63(20)** (2001) 205420/1-205402/7

[217] Sotiris E.Pratsinis, "**Simultaneous Nucleation, Condensation, and Coagulation in Aerosol Reactors**" , *Journal of Colloid and Interface Science*, Vol. **124**, No. **2**, (Aug1988) 416–427

[218] Richard B.McClurg and Richard C.Flagan ,"**Critical Comparsion of Droplet Models in Homogeneous Nucleation Theory**", *Journal of Colloid and Interface Science,* Vol. **201**, (Aug 1988) 194-199

[219] Yang Zhang, Christian Seigneur, John H Seinfeld, Mark Z. Jacobson and Francis S.Binkowski, "**Simulation of Aerosol Dynamics : A comparative review of algorithms used in air quality control,**" *Aerosol Science and Technology* **31** (1999) 487-514

[220] Yogendra Singh, Julie R.N.Javier , Sheryl Ehrman, Martin H.Magnusson and Knut Deppert, "**Approaches to increasing yield in evapouration / condensation nanoparticle generation**", *Journal of Aerosol Science* , 33 , (2002) 139-1325

[221] Tatiana E. Itina and Leonid V. Zhigilei ,"**Generation of nanoparticles by laser ablation : Combined MD-DSMC computational study**" *Journal of Physics conference series* **59** (2007) 44-49

[222] Tatiana E. Itina, Marc Sentis, Wladimir Marine, "**Synthesis of nanoclusters by nanosecond laser ablation : Direct simulation Monte Carlo modeling** " *Applied Surface Science* **252** (2006) 4433–4438

[223] Tatiana E. Itina , Karine Gouriet, Leonid V. Zhigilei, Sylvie Noel, Jorg Hermann , Marc Sentis ,"**Mechanisms of small clusters production by short and ultra-short laser ablation**" , *Applied Surface Science* **253** (2007) 7656–7661

[224] Gert Callies, Henrik Schittenhelm, Peter Berger, Helmut Hűgel, **"Modeling of expansion of laser-evaporated matter in argon helium and nitrogen and the condensation of cluster** ", *Applied Surface Science* **127-129** (1998) 134-141

[225] B.S.Luk'yanchuk, W.Marine, S.I.Anisimov, G.A.Simakina, "**Condensation of vapor and nanoclusters formation within the vapor plume, produced by ns-laser ablation of Si, Ge and C**", *SPIE Conference* **Vol.3618** (1999) p434-452

[226] B.S.Luk'yanchuk, W.Marine, S.I.Anisimov, "**Condensation of vapor and nanoclusters formation within the vapor plume, produced by ns-laser ablation of Si** ", *Journal of Laser Physics*, **Vol.8** (1998) p291

[227] M. Kuwata, B.Luk'yanchuk, T.Yabe, " **Nanoclusters formation within the vapor plume, produced by ns-laser ablation : Effect of the initial density and pressure distributions** " *SPIE Conference* **Vol.4065** (2000) p441-451

[228] Luis de Juan and Fernandezde la Mora, " **Sizing nanoparticles with a focusing impactor : Effect of the collector size**", *J. Aerosol Sci.* **Vol.29 No. 5/**6 (1998) p 589-599

[229] P. Liu. , P. Ziemann, D. Kittleson and P. McMurry "**Generating particles beam controlled dimensions and divergence: Theory of particles motion in aerodynamics lenses and nozzle expansions**", *Aerosol Sci. Technol* .**Vol. 22** (1998) p293-313